Nanostar Based Platforms for Enhanced Blood Brain Barrier Crossing

Rosália Cristina Lopes Rodrigues

Department of Materials

Imperial College London

A thesis submitted for the degree of

Doctor of Philosophy

2018

Declaration

I declare that this thesis is a result of my work and that external contributions to this work have been acknowledged.

The copyright of this thesis rests with the author and is made available under a Creative Commons Attribution Non-Commercial No Derivatives licence. Researchers are free to copy, distribute or transmit the thesis on the condition that they attribute it, that they do not use it for commercial purposes and that they do not alter, transform or build upon it. For any reuse or redistribution, researchers must make clear to others the licence terms of this work.

Abstract

The availability of drugs to treat diseases of the central nervous systems is severely restricted by the presence of the blood brain barrier (BBB). The blood-brain barrier prevents the passage of more than 98% of small molecules and 100% of large molecule pharmaceutics. With the rapid progression of neurodegenerative conditions arising with the increase in life expectancy, central nervous system disorders are now the leading cause of death in the United Kingdom, highlighting the urgent need to develop new strategies to effectively cross the blood brain barrier.

Nanoscale particles have shown great potential for specifically identifying and binding to the BBB and are currently being investigated for enhanced brain penetration. In this work, the effect of a complex multispiked nanoparticle morphology on BBB penetration is investigated as an alternative to the conventionally used spherical nano-vehicles. Specifically, a platform matrix of plasmonic gold nanoparticles in the shape of gold stars were designed for specific brain targeting and effective transcytosis. The nanostars were synthesised with a highly controllable spectrum of properties including size, surface spikiness and morphology. Successful conformal surface biofunctionalisation with the BBB targeting protein transferrin was achieved for the complex stars and conformational changes due to packing was observed at high concentration of protein. The shape and functional properties of the nanostars was thus preserved after coating. The high surface area of the nanostars enabled superior loading capacity with the transferrin targeting moieties.

In transwell transport studies the human brain endothelial cell line hCMEC/D3 showed preferential uptake of AuStrs over spherical nanoparticles. It was found that AuStrs with high aspect ratio, and spiky surface topology constituted the best transcytotic agents. TEM analysis demonstrated that AuStrs penetrate through

the cells, not through the tight junctions, thus validating a transcellular transport mechanism. It is demonstrated that the extent of transcytosis and cell uptake can be tuned based on nanostructure geometry and surface biofunctionalization. This thesis provides important insights of the nano-bio interface for the future design of BBB penetrating agents.

Acknowledgements

I would like to thank my supervisors, Professor Mary Ryan and Professor Alexandra Porter, for the guidance. I am truly grateful to you for giving me the opportunity to complete a project that I truly feel passionate about and to have benefited from your expertise.

For collaborating on this project with STEM imaging I want to thank Dr Jiahui Qi. We have shared many microscopy sessions and great images at 23:59. Thank you Angela, Catriona, Pakatip and the staff from the Harvey Flowers characterization suit, Mahmoud and Cati, for all the knowledge and assistance with the imaging and instrumentation.

I thank all the members of the Porter-Ryan group for the learning experience. Thank you to the wonderful friends I made the last few years. Thank you Eleonora and Emma for being my friends and for supporting me for countless times. Thank you Giuseppe for your wise advice, and Milly, Daphne and all my office friends for the fun times.

I dedicate this thesis to my family, Sissa, Fabião and Felix for being my pillars and always encouraging me to do my best and enjoy life. To Mãe, Henriqueta, for all your love. To Miguel, o melhor Monstro das Bolachas.

In loving memory of our father Dr Francisco Adão Rodrigues for we are *Filhos de Ouro*.

Contents

Page no

1 Introduction **21**

1.1 Research objectives 24

1.2 Organization of the thesis 25

2 Literature Review **27**

2.1 Drug specificity and delivery systems 27

2.2 The blood brain barrier as a challenging site for drug delivery . . . 29

2.2.1 The blood brain barrier 29

2.2.2 The neurovascular unit 30

2.2.3 BBB transvascular transport pathways 33

2.3 Nanoparticles as promising delivery vehicles for BBB delivery . . 40

2.3.1 Nanoparticles based delivery vehicles 40

2.3.2 Synthesis of AuNP vehicles 41

2.3.3 Gold nanoparticle clearance and toxicology 47

2.4 Tailoring of nanoparticles for BBB crossing 49

2.4.1 Nanoparticle-ligand complexes for brain access 49

2.4.2 Effect of geometry in cell uptake and trafficking 55

2.5 Gold nanostars as a candidate platform for BBB targetting and permeability 60
2.6 *In Vitro* models of the BBB as a validation tool 65
2.6.1 Non-cell based *in vitro* models of the BBB 65
2.6.2 Cell based *in vitro* models of the BBB 66
2.6.3 Reported nanostructure efficiencies in *in vitro* BBB models 68
2.7 Scope of the work and Project Outline 75
2.7.1 Project motivation 75
2.7.2 Project aims 75
2.7.3 Criteria followed for nanoparticle design 75
2.7.4 Study Outline 78

3 Characterization techniques 79
3.1 Microscopy techniques 79
3.1.1 Transmission electron microscopy 79
3.1.2 Scanning Electron Microscope 84
3.1.3 Focused Ion beam-SEM 84
3.2 Spectroscopy techniques 85
3.2.1 Energy Dispersive X-ray Spectroscopy 85
3.2.2 Inductively Coupled Plasma-Optical Emission Spectroscopy(ICP-OES) 86
3.2.3 Dynamic Light Scattering (DLS) 87

4 Development of AuStr Vehicles 89
4.1 Introduction 89
4.2 Experimental 91
4.2.1 Materials: 91

4.2.2 Gold nanostructure synthesis: 91
4.2.3 AuStr and AuNP Characterization: 91
4.2.4 Elemental Quantification: 92
4.2.5 Chapter contributions 92
4.3 Results: Nanoparticle Synthesis 93
4.3.1 Effect of total amount of metal precursor 93
4.3.2 Effect of metallic precursor ratio (Au:Ag) 97
4.3.3 Effect of seed addition for a mediated synthesis 100
4.3.4 Effect of hydrochloric acid (HCl) concentration 105
4.3.5 Nanostar Elemental Analysis 107
4.3.6 Experimental characterization of nanostar Au mass 110
4.4 Results: Nanoparticle surface stabilization 113
4.4.1 Passivation of the gold nanoparticles by PEGylation . . . 113
4.4.2 Bioconjugation of the gold nanoparticles with transferrin protein 115
4.5 Results: Monitoring and Quantification of controlled protein attachment to AuNP 124
4.6 Discussion 138
4.6.1 Controlled synthesis of AuStrs 138
4.6.2 Nanostar elemental analysis 144
4.6.3 Formation of tunable protein coronas on the AuNPs 144
4.6.4 Conformal protein coating of the AuStrs 145
4.7 Conclusions 148

5 *In Vitro* Evaluation of AuStr Crossing **149**

5.1 Introduction 149

5.2 Experimental 154
5.2.1 Cell Culture 154
5.2.2 Immunofluorescence Staining 155
5.2.3 Gold nanostructure toxicity 156
5.2.4 Statistical Analysis 157
5.2.5 Transport assay 158
5.3 Results 160
5.3.1 Nanoparticle Selection for the BBB studies 160
5.3.2 Establishing an *in Vitro* BBB model to study nanoparticle transcytosis 161
5.3.3 Evaluation of nanoparticle cytotoxicity 164
5.3.4 TEM Investigation of Nanoparticle Uptake and Transport events 167
5.3.5 Quantification of nanostructure transcytosis across the BBB 188
5.4 Discussion 196
5.4.1 Establishing an *in Vitro* BBB model to study nanoparticle transcytosis 197
5.4.2 Evaluation of nanoparticle cytotoxicity 199
5.4.3 TEM Investigation of Nanoparticle Uptake and Transport events 200
5.4.4 Quantification of nanostructure transcytosis across the BBB 210
5.4.5 Evaluation transcytosis efficiency in correlation with geometry 220
5.5 Conclusions 223

6 Conclusions and Future work **225**

List of Figures

1.1 Percent deaths caused by different conditions in between 2005 and 2016 22

2.1 Scheme of drug tissue interactions 28

2.2 Schematic representation of the BBB.(a) brain capillary and associated supporting astrocyte cels, (b) components of the neurovascular unit (c) molecular complexes at the BBB tight junctions. Adapted from (Chen and Liu, 2012). Copyright 2012 Elsevier 31

2.3 Overview of the transport pathways across the blood brain barrier. Pathways a) to f) are commonly for solute molecules; and the route g) involves monocytes, macrophages and other immune cells. Adapted with permission from (Chen and Liu, 2012). Copyright 2012 Elsevier 34

2.4 Graph of BBB permeability (cm/sec) as a function of lipid solubility determined in an octanol/water partition system for several solutes. The open points represent solutes that fit the correlation between lipid solubility and BBB penetration. The filled points represents the outliers to the correlation with higher transport verified for substrates of facilitated diffusion above the regression line (e.g. glucose) and efflux pumps below the regression line (e.g. cyclosporine). Suc, sucrose; Cre, creatinine; PCNU, 1-(2-chloroethyl)-3-(2,6-dioxo-1-piperidyl)1-nitrosourea; BCNU, 1,3-bis(2-chloroethyl)-N-nitrosourea; d-Glu, d-glucose; Ble, bleomycin; Adr, adriamycin (doxorubicin); Epi, epipodophyllotoxin (etoposide); Cycl, cyclosporin A; Vcr, vincristine. Adapted from Levin (1980). Copyright 1980 American Chemical Society 36

2.5 Illustration of the Trojan horse concept showing the combination of antibodies and proteins ligands known to cross the BBB to nanoparticle substrates to mediate their specific entry. A nanoparticle(NP) combined with a monoclonal antibody (mAb) for receptor R crosses the BBB into the brain by the Trojan horse approach. The NP, with a ligand targeting the BBB (dark triangle), traverses the BBB by receptor-mediated transcytosis. The ligand (light triangle) docks on a cancer cell receptor and the NP delivers its anticancer payload to the cancer cell in glioblastoma multiforme (GBM). Adapted from (Jain, 2012) with permission from Future Medicine (2012) 7(8) 38

2.6 LaMer curve describing three stages of metal nanocrystal formation in solution system. Stage I: atom production, stage II: nucleation, and stage III: seed formation and growth. Cs = saturation concentration, Cmin = critical concentration and Cmax = critical concentration representing the limiting state of supersaturation Adapted from (You and Fang, 2016). Copyright 2016 Elsevier 42

2.7 Schematic illustration for the proposed process of gold nanoparticle formation. Adapted with permission from Polte et al. (2010). Copyright 2010 American Chemical Society 44

2.8 Focusing size distribution through separation of nucleation and growth. The growth process of nanocrystals can occur in two different modes, focusing and defocusing, depending upon the concentration of the monomer present. Adapted with permission from Yin and Alivisatos (2005). Copyright 2004 Springer Nature 45

2.9 The transferrin cycle. Fully iron loaded transferrin (holotransferrin, HOLO-TF) binds to transferrin receptors (TFR) on the cell surface. The complexes localize to clatherin-coated pits, which invaginate to initiate endocytosis. Specialized endosomes form, and become acidified through the action of a proton pump. Acidification leads to protein conformational changes of that release iron from transferrin. Acidification also enables proton-coupled iron transport out of the endosomes through the activity of the divalent metal transporter 1 protein (DMT1). Subsequently, iron-free transferrin (apotransferrin, APO-TF) and the transferrin receptor both return to the cell surface, where they dissociate at neutral pH. Both proteins participate in further rounds of iron delivery. In non-erythroid cells, iron is stored as ferritin and haemosiderin. Adapted with permission from Andrews (2000). Copyright 2000 Springer Nature . 52

2.10 Schematic showing the angle (Φ) between the long axis of the particle and the bilayer normal (a). Computer-simulated diagram showing the translocation of ellipsoid nanoparticles across a lipid bilayer with vertical (b) and horizontal (c) starting orientations. Adapted with permission from Yang and Ma (2010). Copyright 2010 Springer Nature 57

2.11 Uncoated silica particles of different shapes (discoidal, spherical, hemispherical and cylindrical) were intravenously injected in mice and the relative Si content is presented for each organ. The bar chart shows clearly a shape-dependent accumulation in the major organs. The star symbol identifies differences between the discoidal and the other particles with $p < 0.001$. Adapted with permission from Decuzzi et al. (2010). Copyright 2009 Elsevier 58

2.12 Intracellular trafficking of nanoparticles with different morphologies: (a) particles with low sharpness enter the cell by endocytosis, reside in endosomes which evolve into lysosomes and exits the cells via exocytosis with the lysosome as a vehicle; (b) sharp-shaped nanoparticles enter the cell by endocytosis, escapes the endosome by rupturing the endosomal membrane before the lysosome is formed and accumulate in the cytosol. Adapted from Chu et al. (2014). Copyright 2014 Springer Nature 59

2.13 Design of Fe_3O_4@SiO_2-Tat nanoparticles for BBB crossing (a);TEM images of Fe_3O_4@SiO_2 NPs (b); transport efficiency of Fe_3O_4@SiO_2-Tat and Fe_3O_4@SiO_2-Amino NPs. Adapted from Zhao et al. (2016). Copyright 2016 Springer Nature 69

2.14 TEM images of MWNTs-NH3^{+} (a) and DTPA-MWNTs (b). MWNTs-NH3^{+}that crossed the PBEC layer was quantitatively assessed using radioactive tracers. DTPA-MWNTs were synthesised from MWNTs-NH3^{+} and radioactively labelled with [^{111}Indium] . The radioactivity of [^{111}In]-DTPA-MWNTs was measured in the basal chamber at different time points and a maximum of 13.0 $\pm$ 1.1% was reached after 72 hours. The incubation at 4 C significantly decreased the uptake of [^{111}In]-DTPA-MWNTs . [^{111}In]EDTA was used as a marker to ensure that [^{111}In] was due to [^{111}In]-DTPA-MWNTs transport and not [^{111}In]EDTA.(One way ANOVA test; *p < 0.05, ***p < 0.001, ****p < 0.0001, n = 3). Adapted from Kafa et al. (2015). Copyright 2015 Elsevier 71

2.15 Proposed scheme of transcytosis mechanism for transferrin containing nanoparticles with an acid-cleavable linkage(a). Following endocytosis the transferrin ligand separates from the nanoparticle core due to rapid acidification of the endosome, allowing the nanoparticle to freely transcytose into the brain. Graph showing the percentage of injected nanoparticles reaching the basal well of bEnd.3 coated transwells 8 h after introduction (b). The number in the formulation name indicates the number of ligands per nanoparticle, -N indicates noncleavable PEG conjugate, and -C indicates cleavable PEG conjugate. 120Tf-C and 200Tf-C show greater ability to cross the transwells compared with 200Tf-N. Error bars given are SE. *P < 0.001. Adapted from Clark and Davis (2015). Copyright 2015 PNAS 73

2.16 Schematic representation of the study outline showing the different stages of nanostructure assembly for BBB targeting 78

3.1 Schematic representation of some of secondary signals generated when a beam of high speed electrons interacts with a thin sample. Adapted from (Williams and Carter, 2009) 81

3.2 Schematic representation of the mechanism by which differences in mass or thickness generate image contrast in a bright field TEM image. Adapted from (Williams and Carter, 2009) 82

4.1 UV-VIS spectra of AuStrs synthesised at different $HAuCl_4$ concentrations. 94

4.2 TEM images of AuStrs synthesized with different concentrations of $HAuCl_4$: (a) 0.05, (b) 0.10, (c) 0.15 and (d) 0.20 mM. Graph (e) shows the AuStr size distribution as a function of $HAuCl_4$ concentration. The size of the nanoparticles was determined using the image J software. 96

4.3 UV-Vis spectra of nanostars synthesised at different gold to silver ratios. 97

4.4 Bright field TEM images of AuStrs synthesised at different Au:Ag ratios of 3 (a), 10 (b), 20 (c), 40 (d) and 80:1 (e). Graph (f) shows the spike count per AuStr as a function of Au:Ag ratio. The nanostructures spike count was analysed using the image J software. . 99

4.5 UV-Vis spectra of AuStrs synthesised with different volumes of seed 100

4.6 Bright field TEM images of AuStrs synthesised at 0.2 mM $HAuCl_4$ concentration in the absence (a) or presence (b) of gold seeds. Graph (c) shows the size distribution of nanostructures as a function of the seedless or seed-mediated synthesis mechanism . The nanostructures size distribution was analysed using the image J software. 101

4.7 Bright field TEM images of AuStrs synthesised at 0.1 mM $HAuCl_4$ concentrations in the absence (a) or presence (b) of gold seeds. TEM images AuStrs synthesised at 0.05 mM $HAuCl_4$ concentrations in the absence (c) or presence (d) of gold seeds. 102

4.8 Bright field TEM images of AuStrs synthesised with increasing seed solution volumes of 6 (a), 12.5 (b), 50 (c), 100 (d) and 400 (e) μL. Graph (f) shows the size distribution of the AuStrs as a function of the seed volume. The nanostructures size distribution was analysed using the image J software. 104

4.9 Bright field TEM images of AuStrs synthesised with increasing volumes of 1N Hydrochloric acid of 1.5 (a), 2.5 (b) and 3.5 (c) μL. Graph (d) shows the peak wavelength of the AuStr (λmax) and spike *aspect ratio* as a function of volume of HCl. The nanostructures spike aspect ratio was analysed using the image J software. 106

4.10 Bright field TEM images of AuStrs depicting both the secondary spike and body regions. 107

4.11 EDS spectra of AuStrs (a) AuStr spike(b) and AuStr body (c) synthesised in the presence of HCl. Both spike and body regions have a similar composition of gold and silver. The samples are supported in a TEM copper grid as indicated by the presence of a Cu peak 108

4.12 STEM-EDS elemental mapping of AuStrs showing the spatial distribution of Au (blue) and Ag (red) elements in the nanostructure. 109

4.13 Schematic representation of the substrate silanization with MPTS molecules. Scheme drawn in ChemDraw software 111

4.14 Schematic representation of the self-assembly of gold nanoparticles on the thiol functionalized substrate.Scheme drawn in ChemDraw software 111

4.15 Surface characterization of 100nm AuStr substrates. SEM images of 100 nm AuStr monolayers formed on glass following 24 (a) and 48 (b) hours incubation in nanoparticle solution. Atomic Force Micrograph (AFM) of the 48 hour substrate surface. 112

4.16 TGA curve of 100 nm AuStrs conjugated with polyethylene glycol polymer. The graph shows two mass loss regions, the first (20-90 °C) corresponding to solvent loss and the second (90-650 °C) corresponding to PEG degradation, followed by the plateau of the curve, indicating no further mass changes. 114

4.17 Bright field TEM image of monodisperse 100 nm PEG-AuStr. . . 114

4.18 Chemical structure of the NHS-PEG-OPSS molecule with the orange square marking the NHS (N-hydroxysuccinimide) group and blue square the OPSS group (orthopyridyl disulfide) 115

4.19 High perfomace liquid chromatography (HPLC) analysis showing successful protein PEGylation. Top graph shows the elution time of non PEGylated transferrin control and bottom graph shows the elution time of PEGylated Tf samples. The signal was recorded at 280 nm using a UV-Vis detector. 116

4.20 NaCl based titration of Tf-AuNPs synthesised at different Tf concentration (a).(b) Spectrophotometric evaluation of Tf-AuNP stability. Tf-AuNP bioconstructs dispersed in water were read across a range of wavelengths and the wavelength at which the signal is the highest is identified as the peak wavelength position (λmax). The wavelength spectra peaks were fitted to filter out interfering background noise. The λmax of the different Tf-AuNP bioconstructs dispersed in water is taken as a reference and is subtracted from that of Tf-AuNP biconstructs reacted in the presence of NaCl to obtain the LSPR shift. (c) UV-VIS spectra of AuNPs before and after bioconjugation with Tf. 119

4.21 Bright field TEM images (a) and (b) showing negatively stained unconjugated AuNP 120

4.22 Bright field TEM images (a-d) showing negatively stained Tf-AuNPs with black arrows pointing to Tf coronas. 121

4.23 NaCl based titration of 100 nm Tf-AuStrs synthesised at different Tf concentration. (a) UV-VIS spectra of AuStrs reacted at different NaCl concentrations (b) Graph of AuStr λ max as a function of NaCl concentration, (c) UV-VIS spectra of Tf-AuStrs synthesised with different volumes of Tf, (d) Uv-Vis spectra of different Tf-AuStr constructs in the presence of NaCl and (e) Graph of LSPR shift as a function of Tf-AuStrs sysntehsised with increasing volumes of Tf. 123

4.24 Schematic illustration of the procedure used quantify Tf binding to AuNPs. Tf (blue triangles) react with AuNPs (red spheres) for 18 hours following which the solution is centrifuged to separate the unreacted protein from the Tf-AuNPs pellet. The unreacted Tf in the supernatant is concentrated in spin columns and the recovered volume is measured by UV-VIS spectroscopy to determine the protein concentration in solution. The formed Tf-AuNP constructs are further characterised by dynamic light scattering (DLS). 124

4.25 UV-VIS calibration curve of transferrin taken at 269 nm 125

4.26 Quantification of Tf loading for biconstructs reacted at fixed Tf concentrations but with different amounts of AuNPs. Tf-AuNP2 were reacted with double the amount of gold to that of standard Tf-AuNP constructs. The graph shows that decreasing the Tf to AuNP ratio decreases protein binding. 126

4.27 Figure summarising the Tf-AuNP reactions that affect protein binding 127

4.28 Hydrodynamic diameter measured through Dynamic Light scattering (DLS) for uncoated AuNP (a), Tf-AuNP2 (b) and Tf-AuNP (c). Figure (d) shows the superimposed size distribution curve of the three nanoparticle formulations. 128

4.29 Quantification of Tf loaded to AuNPs following a 2 hour and a 18 hour reaction. The graph shows similar protein loading for both reaction times. 129

4.30 Evaluation of Tf-AuNP bioconstruct hydrodynamic size as a function of reaction time measured by dynamic light scattering. 130

4.31 TEM of a Tf-AuNP biocunstruct with black arrows showing the presence of surface protein layer with an average thickness of 2.15 $\pm$ 0.29 nm. 130

4.32 Bright field TEM micrographs of negatively stained 100 nm Tf-AuStrs with black arrows showing the presence of a surface protein layer with an average thickness of 2.28 nm 131

4.33 Bright field TEM micrographs of negatively stained 25 nm Tf-AuStrs with black arrows pointing at Tf protein coronas on the nanoparticles surfaces 132

4.34 Bright field TEM micrographs of negatively stained 50 nm Tf-AuStrs with black arrows pointing at Tf protein coronas on the nanoparticles surfaces. 132

4.35 Bright field TEM micrographs of negatively stained 100 nm Tf-AuStrs conjugated at high Tf to AuStr ratios [10x]. 133

4.36 Corona thickness on the surface of AuStrs reacted in standard protein concentrations [1Tf] and at high protein concentrations [10Tf]. Thickness measurement analysis were performed in Image j. . . . 134

4.37 Hydrodynamic diameter measured through Dynamic Light scattering (DLS) for AuStrs reacted at high tf concentrations Tf-AuStr[10Tf] (b) and standards tf concentrations Tf-AuStr [1Tf]. Figure (c) shows the superimposed size distribution curve of the two AuStr formulations. The graphs show that changing the Tf to AuStr ratio did not affect bioconstruct size. 135

4.38 TEM image showing the presence of a conformal protein coating surrounding the AuStr reacted at standard Tf concentration [1Tf] (a and b). The thickness of this coating (c and d) increased when the standard amount of reacting protein is raised by a factor of ten [10Tf]. At the tip of the spikes the protein thickness remained unaltered. 136

4.39 Graph showing Tf loading on AuStrs increased when the standard amount of reacting protein [1Tf] is raised by a factor of ten [10Tf]. 137

4.40 Summary of the systematic tailoring of AuStrs to identify the synthesis parameters responsible for particle size and structure. All TEM images are representative of the resulting samples and are individually identified in the corresponding graphs of reaction conditions vs effects on the nanoparticle (I-V). AuStr synthesis was performed in the presence or absence of gold seeds. In absence of gold seeds, nanoparticle size control (I) was achieved by varying the total amount of metal precursor (a-c). Spike count per AuStr (II) was controlled by increasing the Au:Ag ratio (from d to e). Introducing seeds in the reaction dramatically improved the AuStr size homogeneity (III) as evidenced by images taken before (f) and after (g) seed addition. Further varying the seed concentrations (IV) proved effective in fine tuning the AuStr final size (k-l). Spike morphology (III) was tailored by increasing HCl in the reaction system (j-l). By changing spike morphology the nanoparticles λ_{max} was tuned in the NIR (V). 143

4.41 Manipulation of the orientation of Transferrin on the surface of AuStrs. Tf changes binding orientation from horizontal (a) at standard Tf concentrations [1Tf] to a double layer (b) or vertical orientation (c) at high Tf concentrations [10Tf]. 146

5.1 Scheme illustrating the transwell based *in vitro* model of the BBB setup. 159

5.2 Synthesis of gold nanoparticles for transcytosis studies. Monodispersed AuStrs were synthesised with 25 (a), 50 (b) and 100 nm (c) in diameter and AuNPs were 12 nm in diameter (d). 160

5.3 Gold nanostars conjugated to transferrin. (a) 25 nm (b) 50 nm (c) 100 nm diameter Tf-AuStr 161

5.4 Evaluation of the *in vitro* hCMEC/D3 blood brain barrier model. The formation of non overlapping cell monolayers was shown by confocal microscopy of DAPI stained nuclei, shown in blue (a). The formation of tight junctions was confirmed by the positive staining of cells with the tight junction protein Occludin, shown in green (b) and by transmission electron microscopy, indicated by the red arrows (c). (d) Evolution of BBB transendothelial electrical resistance during 200 hours (10 days) of culture. (e) The cells model showed low paracellular permeability as evidenced by both 70kDa and 4 kDa dextran molecules. 163

5.5 LDH viability assay of hCMEC/D3 cell cells treated with increasing doses of gold nanostructures of 5, 10, 25 and 50 μg/mL for 24 hours. hCMEC/D3 cell membrane integrity was unaffected by neither the nanostructures morphologies (AuStr and AuNP) over the treatment period. Triton was used as the positive control for toxicity and untreated cells were used as negative controls.(*p <0.05,**p <0.01,***p <0.001,****p <0.0001, n=3) 165

5.6 MTS viability assay of hCMEC/D3 cells treated with increasing doses of gold nanostructures of 5, 10, 25 and 50 μg/mL for 24 hours. The hCMEC/D3 cell viability was unaffected by the different AuStrs nor AuNP morphologies following 24 hr nanostructure exposure. Triton was used as the positive control for toxicity and untreated cells were used as negative controls.(*p <0.05,**p <0.01,***p <0.001,****p <0.0001, n=3) 166

5.7 Bright field TEM images of uptake, transport and transcytosis events of 100 nm PEG-AuStrs in hCMEC/D3 cells monolayers. Cells were exposed to 50 μg/mL in assay medium containing 2.5% FBS for 24 hours. Panels a-d are representative images uptake events. Red arrows in panel a shows three AuStrs inserted into the cell membrane and a large cylindrical vesicle inside the cell. Panel b and c are higher magnification images of panel a. Panel d shows a AuStr aggregate interacting with cellular membrane protrusions (red arrow) prior to uptake. Panels e-l are representative images of intracellular transport events, with red arrows showing nanoparticles in the cytoplasm close to transport vesicles. Panels m-t are representative images of transcytosis events, with red arrows showing AuStrs in the cytoplasm close to the filter surface. 169

5.8 TEM images of uptake, transport and transcytosis events of 100 nm Tf-AuStrs in hCMEC/D3 cells monolayers. Panels a-i were obtained in HAADF-STEM mode and panels j-o were obtained in bright field mode. Cells were exposed to 50 μ g/mL in assay medium containing 2.5% FBS for 24 hours. Panels a-e are representative images of uptake events. Panel b and e are higher magnification images of the AuStr entry events observed in panel a and d respectively. Panels f-i are representative images of intracellular transport events, with red arrows showing nanoparticles attached to the vesicle wall. Panels m-o are representative images of transcytosis events, with red arrows showing nanoparticles between the basolateral membrane and the filter surface. 171

5.9 Bright field TEM images of uptake, transport and transcytosis events of 50 nm PEG-AuStrs in hCMEC/D3 cells monolayers. Cells were exposed to 50 μg/mL in assay medium containing 2.5% FBS for 24 hours. Panel a and b are representative images of uptake events, with panel b being a higher magnification image of panel a. Panels c-f are representative images of intracellular transport events, with panels d and f being higher magnification images of panels c and e, respectively. Panels g and h are representative images of transcytosis events. 173

5.10 Bright field TEM images of transcytosis events of 50 nm PEG-AuStrs in hCMEC/D3 cells monolayers. In panel a-c red circles highlight nanoparticles surrounded in a dark halo following crossing of the basolateral membrane. Panel d shows the EDS spectra of the nanoparticle in panel c. The detected osmium signal is due to the AuStr proximity to the osmium stained cells. 174

5.11 TEM images of uptake and transport events of 50 nm Tf-AuStrs in hCMEC/D3 cells monolayers. All panels except f and i were obtained in bright field mode and panels f and i were obtained in HAADF-STEM mode. Cells were exposed to 50 μg/mL in assay medium containing 2.5% FBS for 24 hours. Panel a-f are representative images of uptake events, with panels b and d being a higher magnifications images of panels a and c, respectively. Panel f is a representative HAADF-STEM image of panel e. Panels g-i are representative images of intracellular transport events, with panels h and i being higher magnification images of panels g in bright field and HAADF-STEM modes, respectively. Panel j is a representative image of pre-transcytotic events with panel k and l being higher magnification images of panel j. 176

5.12 TEM images of uptake and transport events of 25 nm PEG-AuStrs in hCMEC/D3 cells monolayers. Panels c, f and i were obtained in HAADF-STEM mode, with the remaining panels being obtained in bright field mode. Cells were exposed to 50 μg/mL in assay medium containing 2.5% FBS for 24 hours. Panel a-f are representative images of uptake events. Panels b and c are higher magnifications images of panel a in bright field and HAADF-STEM modes, respectively. Panels g-i are representative images of intracellular transport events, with panels h and i being higher magnification images of panel g in bright field and HAADF-STEM modes, respectively. 178

5.13 TEM images of uptake, transport and transcytosis events of 25 nm Tf-AuStrs in hCMEC/D3 cells monolayers. Panels a-f were obtained in bright field mode, with panels g and h being obtained in HAADF-STEM mode. Cells were exposed to 50 μg/mL in assay medium containing 2.5% FBS for 24 hours. Panel a and b are representative images of uptake events, with panel b being a higher magnification image of panel a. Panels c and d are representative images of intracellular transport events, with panel d being a higher magnification images of panel c. Panels e-h are representative images of transcytotic events. Panels f and h are higher magnification images of panels e and g, respectively. 180

5.14 HAADF-STEM images of PEG-AuNPs in hCMEC/D3 cells monolayers. Cells were exposed to 50 μg/mL in assay medium containing 2.5% FBS for 24 hours. Panels a-f are representative images of transport events and intracellular distribution of the nanoparticles. Panels b, d and f are higher magnification images of panels a, c and e, respectively. 182

5.15 HAADF-STEM images of uptake and transport events of Tf-AuNPs in hCMEC/D3 cells monolayers. Cells were exposed to 50 μg/mL in assay medium containing 2.5% FBS for 24 hours. Panel a is a representative image of uptake and transport events. Panel b is a higher magnification image of panel a, showing a cell membrane indentation. Panel c and d are higher magnification images of panel a, showing vesicular transport. Panels e and f are representative images of transport events. 184

5.16 (a) 3D tomographic reconstructution model of hCMEC/D3 monolayers exposed to 50 μg/mL of 100 nm PEG-AuStr for.The cells are shown in blue and the areas of high intensity corresponding to the AuStrs are shown in gold. (b) A large cell in the monolayer with AuStrs aggregates on the cell membrane surface and inside the cell close to the basolateral membrane. (c) SEM image of the cell in planel (b). (d) Lateral view of the 3D cell monolayer model. 186

5.17 Tomographic investigation of uptake, transport and transcytosis of 100 nm PEG-AuStrs across hCMEC/D3 cells following 24 hour exposure. The 3D reconstrution was performed in the software Avizo lite. Panels (a) to (d) show 3D volume reconstructions of the cell monolayer (I) to (V) show the corresponding FIB-SEM images of the depicted 3D events. The 3D volume reconstructions and the FIB-SEM images revealed AuStrs at different stages of interaction with the cells. (a) and (I) nanoparticles closely engaged with the apical side of the blood brain barrier and crossing the cell monolayer (a). b) and II) Nanoparticles are observed enveloped in the plasma membrane lipid bilayer. A group of AuStrs can also was also found intracellularly close to the basolateral membrane (b). (c) and (III) Nanoparticles enclosed in transport vesicle.AuStr transcytotic events can also be observed in the volume reconstruction (c). (d) and (III- IV) Nanoparticles successfully found on the basolateral side of the blood brain barrier The red arrows in 3D BBB volume reconstruction represent the multiple transcytosis events. The cell cytoplasm is shown in blue and the areas of high intensity shown in yellow represent the AuStrs. 187

5.18 Transcytosis of PEGylated and transferrin conjugated gold nanostructures across hCMEC/D3 monolayers cultured on transwell filters. Graphs showing the effect of particle morphology, diameter and surface conjugation (Tf or PEG) in: (a) transcytosis, (b) cell association, (c) apical, (d) summed cell association and transport and (e) total Au recovered (*p<0.1, **p<0.01, ***p<0.001, ****p<0.0001). Nanoparticles were added to the apical compartment and incubated for 24 hours. Cells were treated with 50 μg/mL nanostructure solution for 24 hours. The amount of gold in the apical, cellular and basolateral compartments were quantified by ICP-OES. The values are expressed as percentage of the administered dose of gold. . . 189

5.19 Graph showing the paracellular permeability (cm/min) of 70 KDa dextran across hCMEC/D3 cells following 24 hour nanostructure exposure at a concentration of 50 μg/mL. The D3 control group consists of untreated hCMEC/D3 cell samples. Where, PS25 is 25 nm PEG-AuStr, TS25 is 25 nm Tf-AuStr,PS50 is 50 nm PEG-AuStr, TS50 is 50 nm Tf-AuStr, PS100 is 100 nm PEG-AuStr, TS100 is 100 nm Tf-AuStr, PP is PEG-AuNP and TP is Tf-AuNP 193

5.20 Brigth field TEM images showing AuStrs found apically above cell regions containing intact tight junctions. Panel shows (a) 50 Tf-AuStrs and panel b is a high magnification image of panel a. Panel c shows 100 nm Tf-AuStr. 194

5.21 Representative cryo-TEM images of the dispersity state of PEGylated AuStrs of 25 (a-e) 50 (f-j) and 100 nm (k-o) in diameter and PEG-AuNPs (p-t) in cell culture media supplemented with 2.5 % FBS. The gold nanostructures were found mainly as single particles in cell culture medium. Gold nanostructure aggregates were occasionally observed (e, j and o) 195

5.22 Evaluation of nanoparticle aggregation in cell culture media. (a)Graph of percent aggregation as a function of gold nanostructure type. The percent aggregation was below 5% for all the nanoparticle samples.(b) Graph showing the aggregation profile of 25, 50 and 100 nm diameter AuStr samples in the form of a frequency distribution. The majority of the stars exist in the form of single particles independently of AuStr diameter. 196

5.23 Graphs showing the average spike length (a) and average spike *aspect ratio* as a function of AuStr diameter. The AuStr spike measurements determined using the image J software. 214

5.24 Image showing two proposed models of iron transport through the BBB without (left) or with (rigth)transcytosis of transferrin (Skjørringe et al., 2015).Copyright 2015 Skjorringe, Burkhart, Johnsen and Moos. 217

5.25 Transcytosis as a function of zeta potential for PEGylated (a) and Tf coated nanostructures (b), with slope deviation from zero being not significant (p=0.6 and p=0.06, for graphs a and b respectively. 220

5.26 Transcytosis as a function of AuStr diameter for PEGylated (a) and Tf coated nanostructures (b), with slope deviation from zero only being significant for Tf coated nanostructures (p=0.13 and p=0.04, for graphs a and b respectively). Transcytosis as a function of spike *length* for PEGylated (c) and Tf coated nanostructures (d), with slope deviation from zero only being significant for PEGylated nanostructures (p=0.004 and p=0.09, for graphs c and d respectively). Transcytosis as a function of spike aspect ratio for PEGylated (e) and Tf coated nanostructures (f), with slope deviation from zero being significant for Tf coated nanostructures (p=0.06 and p=0.03, for graphs e and f respectively). 222

5.27 Summary of nanostructures geometrical features and their effect in transcytosis. 223

1 LDH and MTS cytotoxicity assays of N27 cells exposed to 100 nm PEG AuStrs at the concentration of 50 μg/mL. The figure shows that the nanostars were not toxic in neuronal cells with statistical significance. 231

List of Tables

2.1 Literature review of nanostar synthesis mechanisms. 62

2.2 Literature review of nanostar synthesis mechanisms (continued). . 63

2.3 Literature review of nanostar synthesis mechanisms (continued). . 64

2.4 Summary of reported transcytosis efficiencies in *in vitro* BBB models 74

5.1 Zeta potential of gold nanostructures in media+FBS (pH = 7). . . 161

Chapter 1

Introduction

Neurodegenerative diseases are characterised by a group of conditions that are debilitating for causing a progressive degeneration or death of nerve cells. Neurodegenerative conditions including Alzheimer's disease and other dementias, Parkinson's disease and multiple sclerosis affect different parts of the nervous system but are in general associated with a set of symptoms including loss of memory, mood changes, problems with communication and reasoning and a compromised motor ability. Alarmingly, the incidence of dementia increases exponentially with age (from the age of 65 years) and doubles at about every 5 years (Corrada et al., 2010). Between the years of 1990 and 2010, the number of death related to neurodegenerative conditions more than tripled, and years lived with disability attributed to these disorders increased by more than 70% (Neurology, 2013). The World Health Organisation predicts that the numbers of people affected by neurodegenerative conditions will continue to increase as the life expectancy of the population increases. According to the United Nations, Europe has the world's highest proportion of older people in the world with 16% of the population being older than 60 years, a percentage that is predicted to increase to 30% by 2030 (Nations, 2017).

Alzheimer's disease and other dementias are now the leading cause of death in the United Kingdom having surpassed in the last decade the other leading causes of death including ischaemic heart diseases, cerebrovascular diseases, chronic lower respiratory diseases and lung cancer (Figure 1.1). The incidence of neurodegenerative diseases imposes not only a major impact on the patients quality of life but also a very large economic cost burden on society. In the UK alone, 850 thousand people suffer from a sort a dementia costing the health care system about 26 billion pounds per year (Lewis et al., 2014).

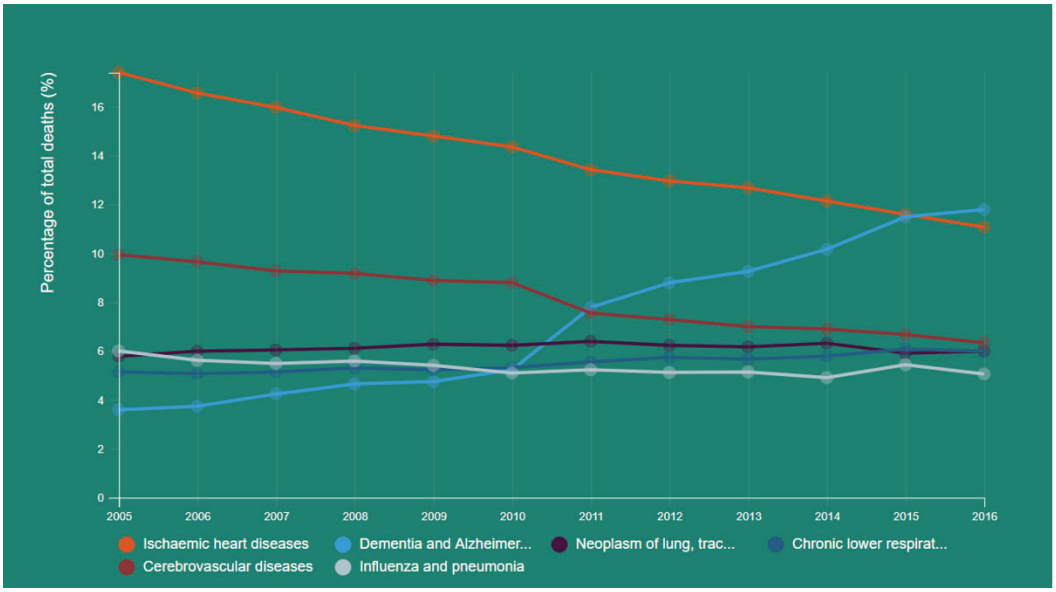


Figure 1.1: Percent deaths caused by different conditions in between 2005 and 2016. The graph shows the increase in the proportion of deaths due to Alzheimer's disease and other forms of dementia over the last several years, compared to several other leading causes of death.Dementia is currently the leading cause of death in the UK (Alzheimers UK, 2016)

Unlike any other condition in the top 10 causes of death, dementia is the only one without a treatment to prevent, cure or slow its progression (Alzheimer's Research UK, 2018). Unlike cancer and cardiovascular diseases, the pace of the development of drugs to tackle neurodegenerative diseases has been almost stagnant.

There are only a few drugs approved to treat neurodegeneration and the majority of which are limited to mitigating the symptoms rather than acting on its underlaying cause. Hence the need for promising therapies remains almost entirely unmet.

The transport of diagnostics and therapeutics across the blood brain barrier (BBB) has been recognised as one of the most challenging fields of biomedical research and is considered the bottleneck in brain drug development (Pardridge, 2005). In particular, the impermeability of the BBB is considered to be the single most important factor limiting the future growth of neurotherapeutics (Pardridge, 2007).

Therefore, the knowledge and insights gained from the successful identification of parameters and or agents to challenge BBB impermeability have a great potential to be implemented for diagnostics and therapeutics delivery for the treatment of several brain and neurological diseases thus benefiting the scientific and industrial communities.

Nanotechnology has great potential to revolutionise the diagnostic and therapeutic approaches towards neurodegenerative conditions. More specifically, because nanotechnology devices (*i.e.* nanocarriers or vehicles) containing at least one dimension in the nanoscale (1-100 nm), they can be produced controllably to cross the BBB, could play a vital role in the early molecular diagnosis of pathologies and have potential in the development of effective target specific drug therapies.

To reach sites of difficult access such as the brain, it is imperative to develop vehicles with characteristics that are beneficial for cell penetration and can do so in efficient doses and in a targeted manner. These vehicles should specifically target diseased cells, whilst also causing minimal toxic side effects. Over the last few years, gold nanostars have attracted a great deal of attention in the field of nanomedicine due to their remarkable optical and theranostic properties.(Schütz

et al., 2011; Chen et al., 2013; Sasidharan et al., 2016)

The exact role of a multispiked nanovehicle's underlying geometry on BBB crossing ability (*i.e.* transcytosis) has not yet been investigated. Part of the reason for this is that the current methods to synthesise gold nanostars (AuStrs) have limited control over their geometries - a prerequisite required to potentially optimize their penetrating capabilities. In addition, potential use of these materials in medical applications such as cell-targeting, are limited by the ability to tailor the surface conformation of the peptides or proteins coated on their surface, at the molecular level. This lack of control limits our fundamental understanding of the behavior of gold nanostars at the nano-bio interface.

1.1 Research objectives

The main aim of this thesis was to evaluate the *in vitro* efficiency of multispiked AuStr as penetrating vehicles for the BBB. The specific objectives of this project are to:

1. To synthesise biocompatible AuStrs with controlled geometry, transferrin (Tf) surface coverage and optical properties for testing in biological systems.

2. To evaluate whether AuStrs cross the BBB more efficiently that spherical Au nanoparticles.

3. To evaluate the effect of AuStr diameter on their rates of translocation across the BBB

4. To evaluate whether conjugation of Tf to the surface of both the AuStr and spherical nanoparticles increases their uptake inside the brain endothelial cells and their rates of translocation across the BBB.

5. To image the pathways of each nanostructure (varied diameter, geometry, Tf) across the BBB to understand the mechanism by which each parameter alters this pathway.

6. To correlate the intracellular distribution and transcytosis efficiency of the different nanostructure formulations to the different nanoparticle morphologies and Tf surface coverage.

1.2 Organization of the thesis

This thesis presents the work that was carried out for this PhD. *Chapter 2* presents a review of the literature relevant to this project. *Chapter 3* describes the experimental techniques and instrumentation employed in this work. *Chapter 4* presents the results of the size and shape controlled synthesis of AuStr and the controlled bioconjugation of gold nanostructures (stars and spheres) with the targetting protein transferrin. *Chapter 5* presents the results from the toxicity, TEM intracellular imaging and transport studies of gold nanostructures in hCMEC/D3 brain cells. Finally, conclusions and suggestions of future work are presented in *Chapter 6*.

Chapter 2

Literature Review

2.1 Drug specificity and delivery systems

The delivery of therapeutics in a controllable way to target cells and tissues of interest represents the major focus of drug delivery system research. New ways of delivering drugs are being developed as a result of the unveiled knowledge on the physiological obstacles to drug delivery (*i.e.* transport in the circulation and through tissue). The inability of drugs to distinguish between healthy and unhealthy tissue is causing major limitations in administering therapeutically effective doses(Allen, 2002) (Figure 2.1). Additionally, the unwanted side effects of non-specific drug interactions hinder the development of new drugs.(Kuhn et al., 2016) The specific targeting of unhealthy tissues can be achieved by functionalizing the surface of the drugs, or their carriers (*i.e.* vehicles) with molecules, like proteins able to recognize specific binding sites on the target tissue.(Wronska et al., 2016; Kumar et al., 2012; Zhang et al., 2013; Richardson et al., 2016)

The fine tuning of drug delivery systems relies on controlling the sites where the drugs are released and the rate at which the release happens. Strategies for drug

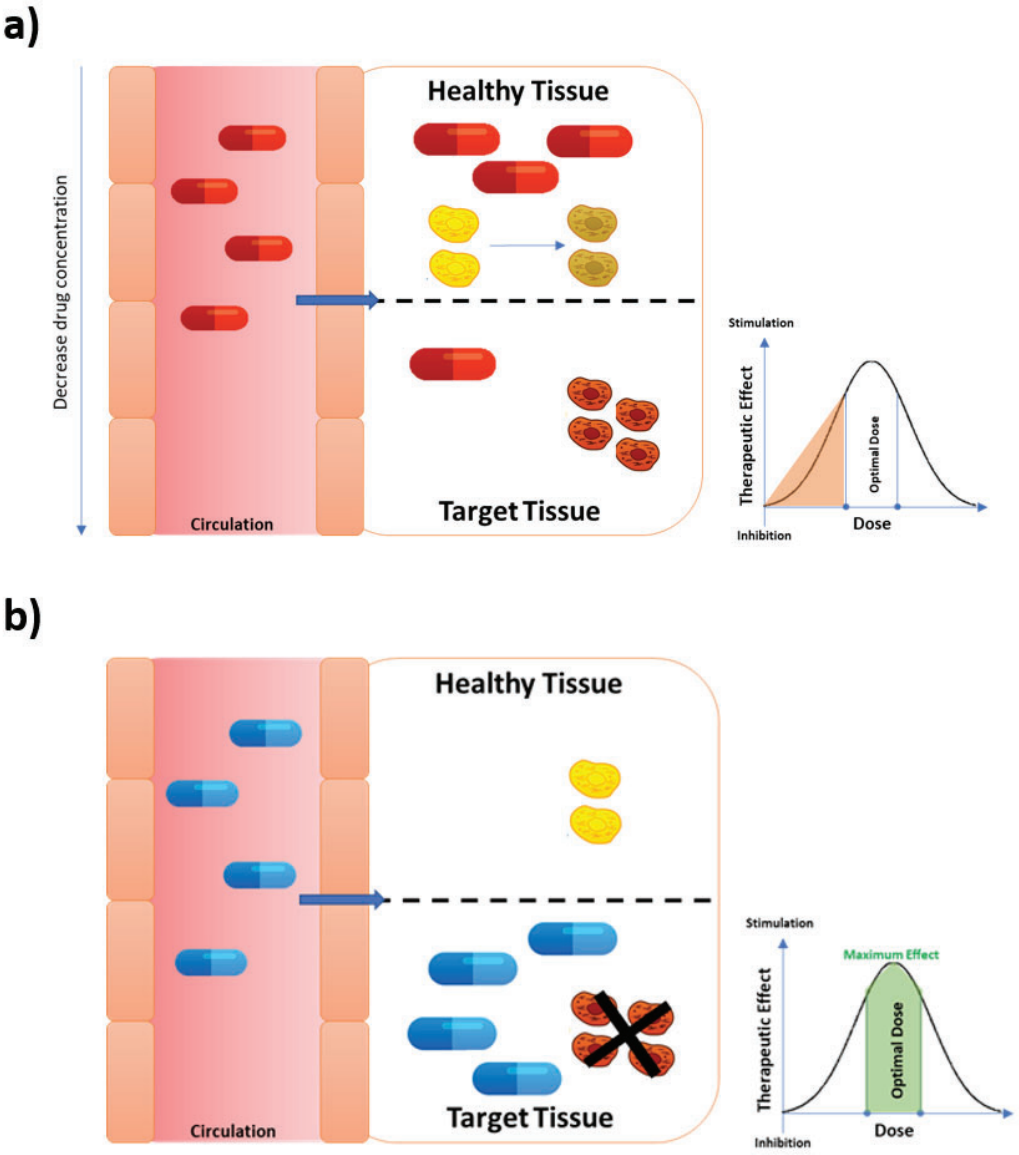


Figure 2.1: Scheme of drug tissue interactions. Systematically administered non-specific drugs diffuse into healthy tissue, compromise healthy cells (yellow) due to off target effects and reach target tissues in sub-optimal amounts (a). Targeted drugs specifically recognize target tissues, reach target sites in optimal concentrations and exert the intended effect in diseased cells (red) without compromising the healthy tissue.original figure.

delivery vary according to the target site and thus the drug should be appropriately modified to cope with the respective target specific challenges. The following sec-

tion provides an overview of one of the most challenging sites for drug delivery, the blood brain barrier.

2.2 The blood brain barrier as a challenging site for drug delivery

2.2.1 The blood brain barrier

The protection that the brain is given, highlights not only its delicate nature but also its importance. The skull protects the brain from physical damage whilst the blood brain barrier (BBB) protects the brain from potentially harmful agents present in the blood stream.

The brain's biochemical environment needs to be tightly regulated as several external stimuli can induce fluctuations of the blood levels of amino acids, hormones and potassium amongst other substances. Since some of these molecules are involved in neuronal excitability it is paramount to maintain the central nervous system (CNS) interstitial fluid stable after routine activities such as food intake and exercise. This stability ensures the accurate synaptic transmissions that enable the CNS to perform its complex integrative functions (Levin, 1980). A highly specialised and selectively permeable membrane between the blood and the brain is therefore required.

The concept of the existence of a blood-brain barrier was first introduced in 1900 by Lewandowsky (Ribatti et al., 2006). In their work, it was demonstrated that the injection of compounds known to be toxic to the nervous tissue would only cause harm when directly introduced to the brain as opposed to administration through the vascular system. Similar behaviour had previously been reported in

1885 by Paul Ehrlich (Ribatti et al., 2006) after observing that the intravenously administered dye Trypan blue, was able to stain all organs except for the brain and spinal cord. Later, Reese and Karnovsky (1967), through electron-microscopy observed that the BBB was localized at the endothelial cells of the capillaries in the cerebral cortex.

2.2.2 The neurovascular unit

The brain vascular network comprises more than 100 billion capillaries constituting a total surface area of about 20 m^2 spread of a length of about 400 miles (Pardridge, 2007). The BBB consists of the brain the microvasculature endothelial cells and their supporting cells namely, astrocytes, pericyte and nerve endings at the vascular surface level (Figure 2.2). However, the vascular permeability of the BBB is solely dependent on the endothelium barrier of the brain capillaries.

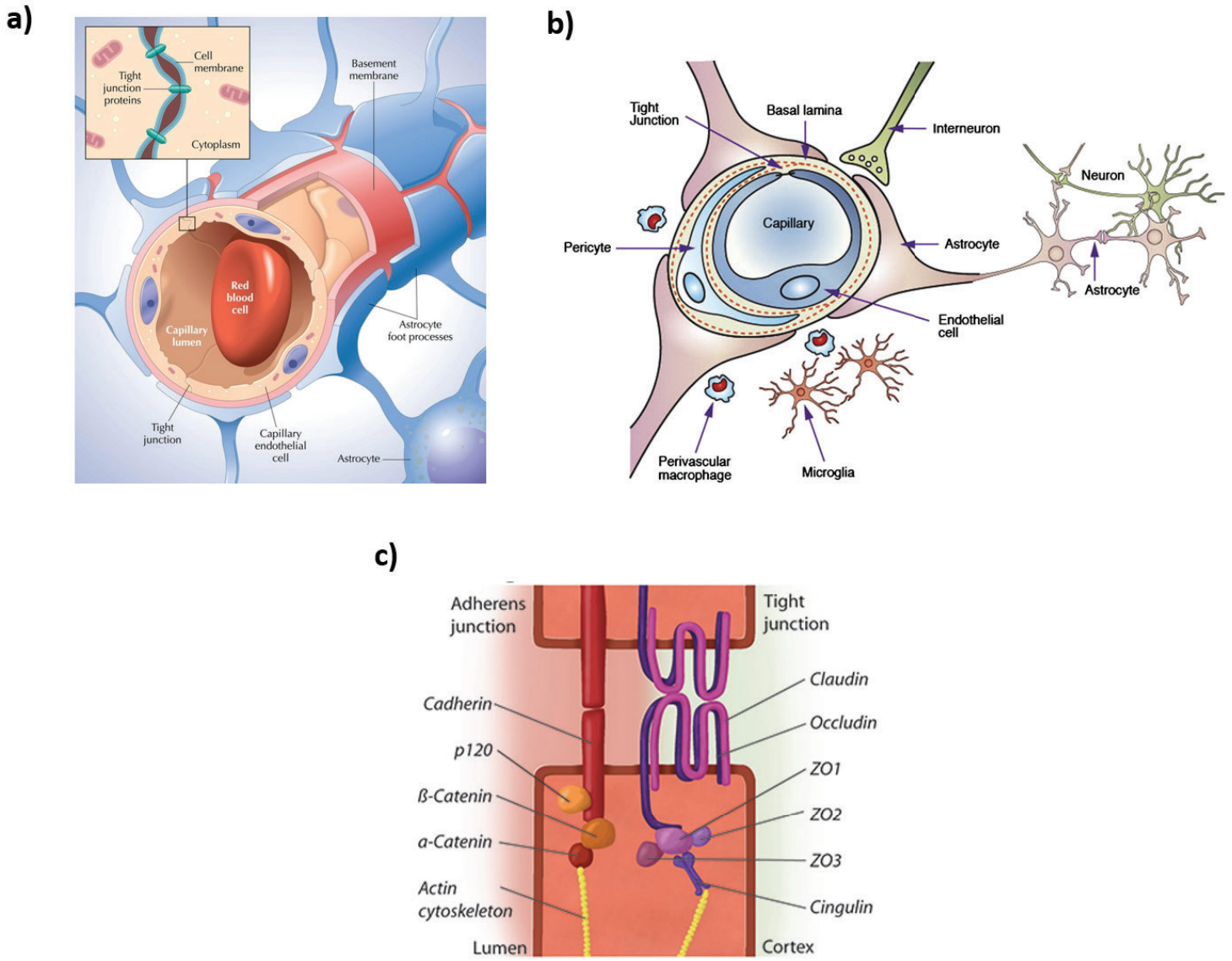


Figure 2.2: Schematic representation of the BBB.(a) brain capillary and associated supporting astrocyte cels, (b) components of the neurovascular unit (c) molecular complexes at the BBB tight junctions. Adapted from (Chen and Liu, 2012). Copyright 2012 Elsevier

The brain endothelial cells are brought into very close proximity and are tightly stitched together by tight junctions. The tight junctions consist of transmembrane and cytoplasmic proteins including zona occludens (ZO1, ZO2 and ZO-3), junction adhesion molecules (JAMs), occludin, claudins and accessory proteins. Together these proteins form a cohesive system that keeps the cells tightly connected (Figure 2.2 c).

These tight junctions are extremely close to one another, with separating gaps of about 4 nm thus rendering a paracellular transport route highly improbable (Guerrero et al., 2010). Therefore, substances of interest carried in the blood need to pass through two consecutive membranes (luminal and abluminal) in order to reach the brain. Initially, the solute passes from the blood through the luminal membrane of the capillary endothelial cell into the endothelial cytoplasm. From here, the solute only needs to travel a distance of at least 200 nm and cross the abluminal membrane to reach the brain.

The presence of tight junctions turns the membrane selectively permeable, allowing the passage of substances needed for normal brain functioning including glucose, water and oxygen whilst restricting pathogenic microorganisms and toxic solutes. However, this very same barrier is also refusing access to most of the pharmaceutics designed to tackle diseases of the central nervous system (CNS). More than 98% of small drugs and virtually all biologics (peptides, antibodies, genes) are blocked from crossing the BBB in pharmacological relevant concentrations (Pardridge, 2005).

Several approaches have been investigated to enhance brain access in a safe and efficient way (Patel et al., 2009). Conventional strategies used to evade this barrier range from osmotic disruption of the BBB for increasing capillary permeability, to direct intracerebral or cerebrospinal fluid drug injections (Pardridge, 2007). How-

ever, such approaches may cause serious risks to patients by allowing immune cells and toxins to access the brain when the BBB is temporarily opened Pardridge (2012). There is an urgent need to dwell upon new drug delivery vehicles to target and penetrate the BBB.

Alternatively, biological delivery strategies can be used in which the cargo is engineered to utilize the existing surface receptors on the brains endothelial cells to cross the BBB, in a manner that mimics physiological transport mechanisms. By understanding the physiology of the BBB, one can take advantage of these influx pathways to deliver drugs of interest to the brain (Prades et al., 2012).

2.2.3 BBB transvascular transport pathways

The blood brain barrier expresses numerous transport systems on the luminal side of the BBB that together provide a dynamic barrier. Broadly these pathways regulate the efflux of substances from the brain, the migration of immune cells to the brain, the transport of various small molecules through protein mediated transport or lipophilic diffusion, transport of larger molecules through endocytosis (receptor or adsorptive mediated transcytosis), as well as the efflux of substances (Figure 2.3). These pathways can be specific or non-specific in nature. Lipophilic diffusion, protein mediated transport and adsorptive endocytosis are non-specific transport routes whilst receptor mediated endocytosis constitutes a specific type of transport. A brief overview of the different pathways is provided below.

Efflux mechanisms

Active efflux transport systems work towards removing substances out of the brain as part of a detoxification mechanism. The ATP binding cassete (ABC) transporter family (e.g. P-glycoprotein) are known to be involved in this type of trans-

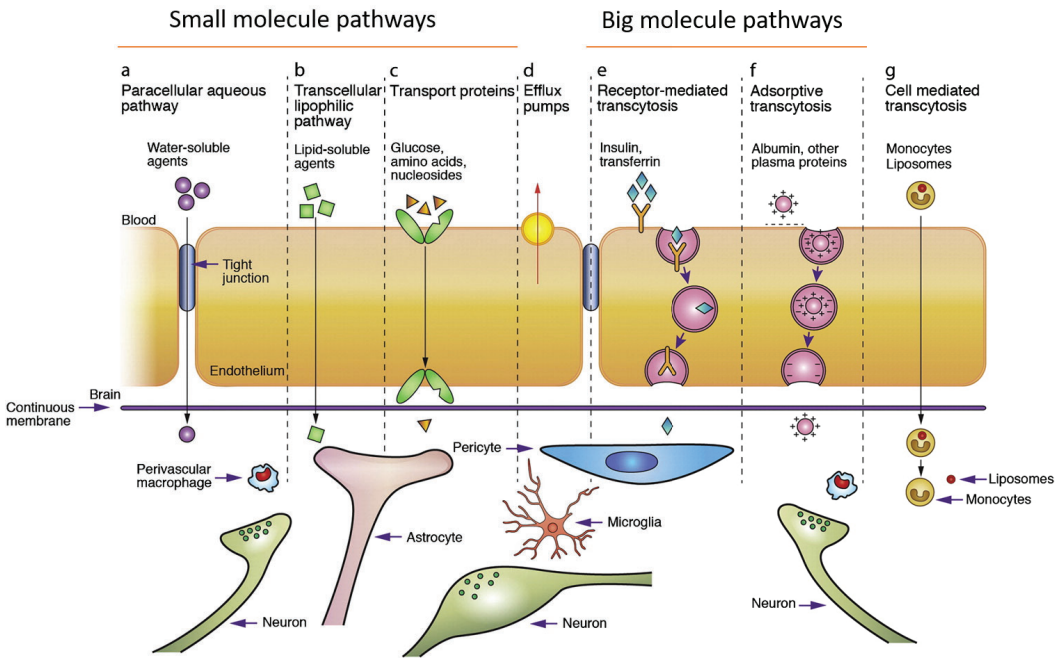


Figure 2.3: Overview of the transport pathways across the blood brain barrier. Pathways a) to f) are commonly for solute molecules; and the route g) involves monocytes, macrophages and other immune cells. Adapted with permission from (Chen and Liu, 2012). Copyright 2012 Elsevier

port (Kusuhara and Sugiyama, 2005).

Immune cell migration

Whilst the resident microglia constitute the first and predominant line of defence in the central nervous system, a small amount of immune cells can also migrate into the CNS to provide non-pathological surveillance (e.g. scavenging plaques and damaged cells). In conditions like multiple sclerosis, there is an abnormally high migration of immune cells to the CNS (Lawrence Steinman, 1996). The potential use of immune cells for CNS drug delivery(Xue et al., 2017) would require efficient immune cells engineering with molecules to be delivered, immune cell extravasation across the barrier and release into the CNS.

Carrier-mediated transport

Carrier-mediated transport makes use of protein transporters (e.g. glucose transporter GLUT1) to mediate a bidirectional movement of relatively small and water soluble nutrients (Chen and Liu, 2012).

Lipophilic diffusion for the transport of small molecules

Levin (1980) reported on the link between a molecule's lipidic solubility and BBB penetration (Figure 2.4). Moreover, it is possible to estimate the probability of free diffusion of molecules through the BBB based on their molecular weight (Fischer et al., 1998) and number of hydrogen bonds.

The passage of molecules with up to 400 Da were thought to be able to diffuse through the barrier due to the presence of thermal molecular motions of the BBB phospholipid hydrocarbon tails (Träuble, 1971). These motions generate, for a finite period, pores of strict sizes that set the threshold for molecular weight at 400 Da.

Furthermore, the number of hydrogen bonds can also be used as a measure of lipid solubility as this influences the passage of substances across the BBB barrier. Compounds are more likely to diffuse in sufficient amounts if they form less than 8 hydrogen bonds with water. Not many molecules can meet both criteria for a low molecular weight and low number of hydrogen bonds. Strategies to increase lipid solubility can involve conversion chemistry in which hydrogen bonds can be blocked. However, conversion chemistry is extremely challenging. In fact, one of the only successful conversion reactions that led to crossing of the BBB in sufficient amounts was the production of heroin by the modification of morphine's hydroxyl groups with acetyl functional groups (Oldendorf et al., 1972).

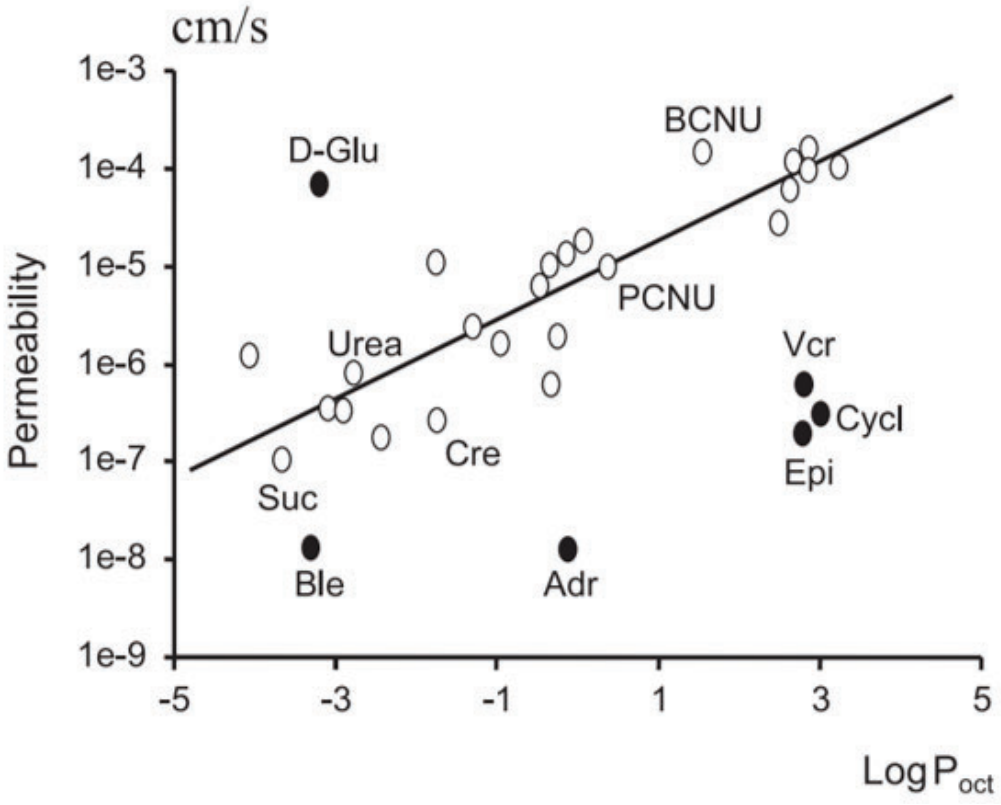


Figure 2.4: Graph of BBB permeability (cm/sec) as a function of lipid solubility determined in an octanol/water partition system for several solutes. The open points represent solutes that fit the correlation between lipid solubility and BBB penetration. The filled points represents the outliers to the correlation with higher transport verified for substrates of facilitated diffusion above the regression line (e.g. glucose) and efflux pumps below the regression line (e.g. cyclosporine). Suc, sucrose; Cre, creatinine; PCNU, 1-(2-chloroethyl)-3-(2,6-dioxo-1-piperidyl)1-nitrosourea; BCNU, 1,3-bis(2-chloroethyl)-N-nitrosourea; d-Glu, d-glucose; Ble, bleomycin; Adr, adriamycin (doxorubicin); Epi, epipodophyllotoxin (etoposide); Cycl, cyclosporin A; Vcr, vincristine. Adapted from Levin (1980). Copyright 1980 American Chemical Society

Increasing lipid diffusion is however linked to a few drawbacks for being unsuitable to larger molecules and due to its non-specific nature. Solubilised compounds in circulation can virtually diffuse across any biological membranes on their way to the brain. Thus, the lack of specificity associated to this approach may ultimately affect the compound's critical concentration making it suboptimal for

brain permeability.

Endocytic transport of large molecules

The endothelium of the brain microvasculature supports endocytic or vesicular based transport mechanisms. These transport systems are initiated by the envelopment of the substrate/cargo by invaginations of the cell membrane, giving rise to membranous spherical structures that bud off forming a transport vesicle. Once formed, these vesicles undergo sorting and can be recycled back to the cell surface or undergo degradation via a lytic pathway (Mellman, 1996). Alternatively, the vesicle can be transported to the opposite membrane, in a process known as transcytosis. It is argued that the frequency of transcytotic events is lower at the blood-brain barrier than at other continuous endothelium tissues (Reese and Karnovsky, 1967).

Transcytosis can be triggered by adsorptive endocytosis or by receptor mediated endocytosis. Adsorptive endocytosis occurs through the binding of usually strongly cationic cargo molecules to the negatively charged glycocalyx at the endothelium cell membrane (Hervé et al., 2008) . In the receptor-mediated transport, peptides and proteins in the circulating blood are taken in via peptide-specific receptors (e.g. leptin, insulin and transferrin receptors). This transport can be uni or bidirectional (Pardridge, 2002). This route allows the passage of relatively larger molecules than the previously mentioned systems. In fact, the passage of the immunoglobulin G, from the brain to the blood, occurs through this route via the Fc receptor (Zhang and Pardridge, 2001). Unlike lipidic diffusion, receptor dependant passage through the BBB is known to increase the specificity of the pathway to and from the brain. Molecules known to trigger receptor-mediated transcytosis include transferrin, apolipoproteins and insulin.

Strategies to cross the BBB: Nanoparticle ligand complexes for BBB crossing

Despite its protective effectiveness, the BBB still needs to allow the passage of substances carried by the blood and essential for normal brain functioning and integrity. By understanding the physiology of the BBB, one can take advantage of these influx pathways to deliver drugs of interest to the brain (Prades et al., 2012). Receptor mediated pathways are of particular interest as these allow for the specific targeting of the BBB. Moreover, It is possible to conjugate molecules known to enter the brain by receptor mediated endocytosis to the surface of drugs or their vehicles to gain access to the brain. This strategy is commonly known as the 'trojan horse' approach (Figure 2.5). Drug vehicles in the nanoscale are currently being used to complement this delivery approach.

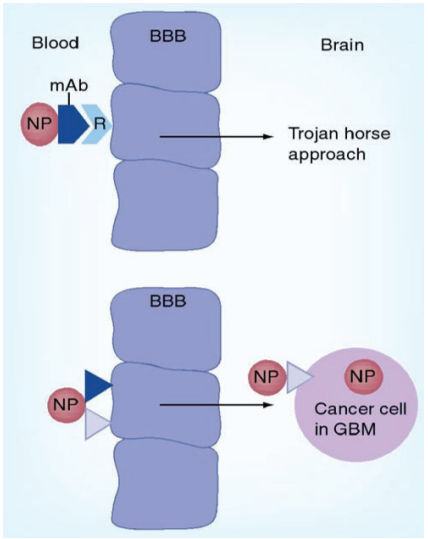


Figure 2.5: Illustration of the Trojan horse concept showing the combination of antibodies and proteins ligands known to cross the BBB to nanoparticle substrates to mediate their specific entry. A nanoparticle(NP) combined with a monoclonal antibody (mAb) for receptor R crosses the BBB into the brain by the Trojan horse approach. The NP, with a ligand targeting the BBB (dark triangle), traverses the BBB by receptor-mediated transcytosis. The ligand (light triangle) docks on a cancer cell receptor and the NP delivers its anticancer payload to the cancer cell in glioblastoma multiforme (GBM). Adapted from (Jain, 2012) with permission from Future Medicine (2012) 7(8)

It is known that ligands mounted onto nanoparticles show more *in vitro* efficacy in different types of cancer cells compared to the ligands free form counterpart, even when the latter is used at higher concentrations (Dam et al., 2014a). The mounting of ligands onto gold nanoparticles is commonly achieved by exposing these NP to thiol modified biomolecules and their self assembly on the nanoparticle surface (Dam et al., 2014a).

It is hypothesised that the presence of a localised dense layer of ligands (Mammen et al., 1998) in the nanoparticle interface allows it to support multiple simultaneous interactions with multiple receptors on the target membrane. This type of interaction, known as polyvalency, can allow for more robust interactions with the target comparatively to the monovalent biological interaction of the ligand in its free form (Mammen et al., 1998). Fundamentally, when considered collectively these interactions are qualitative different than their individual components. This may account in part for some of the difference in efficiency between the *in situ* and free flowing forms of ligands. Furthermore, it was proposed in kinetic studies that the enhancement observed in high affinity polyvalent interactions is predominately owing to a decay in the dissociation rate in lieu of an increment in the association rate (Mammen et al., 1998).

2.3 Nanoparticles as promising delivery vehicles for BBB delivery

2.3.1 Nanoparticles based delivery vehicles

Major focus is currently on the use of nanoparticle based systems as several studies have reported the ability of nanoparticles to cross the BBB and accumulate in the CNS (Andrieux et al., 2009; Kreuter, 2001; Calvo et al., 2001; Kreuter et al., 2002; Ulbrich et al., 2009). Vehicles in the nanoscale offer great delivery advantages ranging from overcoming biological barriers and increasing cell internalization, to the stable delivery of hydrophobic drugs. In particular nanovehicles have a large surface area to volume (SA/V) ratio which allows significant loading of surface molecules (*e.g.* proteins), facilitating the local delivery of effective drug doses.

The way in which a nanoparticle interacts with its surrounding environment is dependent on its properties including the shape, size, surface charge, chemistry and material (Nel et al., 2009a; Sau et al., 2010; Alexandridis, 2011). By specifically tailoring these parameters it should be possible to control interactions at the materials biology interface for specific BBB delivery.

The shape, size and charge of nanoparticles are properties reported to influence their cellular uptake. For instance, the nanoparticle's charge can induce repulsive or attractive interactions with the negatively charged phospholipids of cell membranes which ultimately impact the nanoparticle's cell penetration. Furthermore, the particles' charge determines the type of endocytosis involved in the cellular internalization. Harush-Frenkel et al. (2007) experiments in HeLa cells revealed that clatherin mediated endocytosis is the uptake pathway for positively charged

nanoparticles whilst negatively charged particles are unable to trigger this specific route and are taken up by the cells relatively slowly. On the other hand, the density of charges on nanoparticles also directly correlates with membrane damage and particle uptake (Lin et al., 2010).

Gold is one the most attractive materials for biomedical applications due to its high stability and quantum properties. Gold is an inert metal, very stable in biological environments and biocompatible in human cells. Additionally, gold nanoparticles support surface plasmons which can be tuned according to the particle's size, shape and structure and are highly relevant for advanced therapeutic and diagnostic applications. Since the properties of noble metal nanoparticles are intrinsically linked to their shape and size, a tight control of these properties is necessary (Niu and Xu, 2011). Understanding the mechanisms through which these particles grow is of great significance for a controlled synthesis.

2.3.2 Synthesis of AuNP vehicles

Whilst many synthesis methods for gold nanoparticles have been reported over the years (Daniel and Astruc, 2004), the exact mechanism through which a nanoparticle is originated is on ongoing research. This is mainly due to the limited time-resolution and *in situ* information about the conversion of reaction precursors into particles. Many of the currently applied principles are based on the LaMer's theory for the controlled growth of monodispersed colloids (LaMer and Dinegar, 1950; Mer, 1952). In solution-phase systems, particles can arise as a result of precipitation reactions (Figure 2.6). In conditions where the concentration of the reaction species reaches a critical supersaturation point, small nucleation bursts occur. These nucleation events are halted when the species concentrations drops bellow the critical threshold. Subsequently, solutes from the solution diffuse to the

surface of the formed nuclei until the concentration of solute is lowered to close to its solubility level. The final particle size is thus achieved.

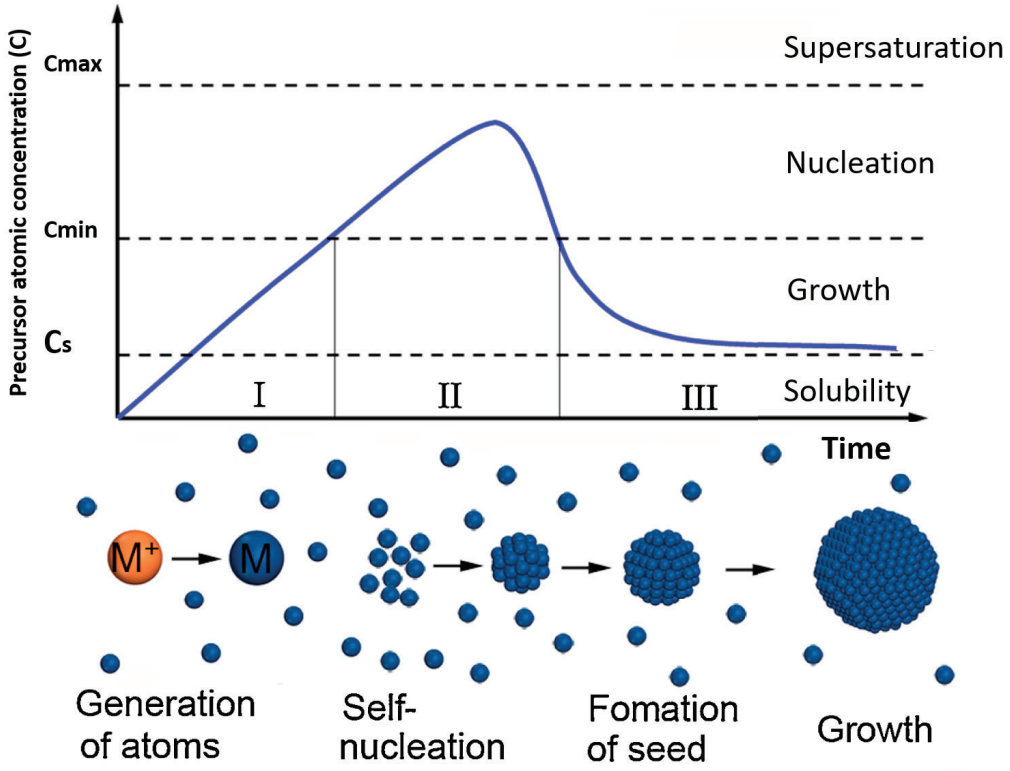


Figure 2.6: LaMer curve describing three stages of metal nanocrystal formation in solution system. Stage I: atom production, stage II: nucleation, and stage III: seed formation and growth. Cs = saturation concentration, Cmin = critical concentration and Cmax = critical concentration representing the limiting state of supersaturation Adapted from (You and Fang, 2016). Copyright 2016 Elsevier

The separation of growth and nucleation stages is thus key to achieve monodispersity. For transcytosis studies , monodisperse nanoparticle batches are desirable as they allow for a more controlled study of the nanoparticle's size and geometry related effects without interference from heterogeneous nanoparticle aggregates. Furthermore, for crossing cell membranes size uniformity is of great importance as cellular uptake mechanisms are size dependent. Nucleation and growth processes can be artificially separated by introducing pre-formed particles in a solution where

the monomers concentration is below critical supersaturation. This is known as seeding. Otherwise, to achieve uniform growth, the solute concentration should be kept at slightly above the critical concentration required to initiate nucleation. In this way, short single burst of nucleation can instantly decrease the solute concentration below the nucleation threshold, making further nucleation events that would cause polydispersed particle growth less likely. In theory, forming all the nuclei at the same time should guarantee that the particles formed follow a narrow size distribution.

Based on the LaMer's theory, gold salts are reduced in solution and when the concentration of Au_0 atoms saturates the solution the atoms merge into small nanometer sized particles which serve as nucleation points.

Pong et al. (2007) suggested a more complex growth mechanism. It was proposed that the reduction of tetrachloroauric acid ($HAuCl_4$) by trisodium citrate, leads to the formation of clusters of about 5 nm that assemble into chains and intermediate networks of nanowires interconnected by amorphous gold. Over time, the chains increase in diameter and eventually collapse and cleave, and simultaneously individual particles grow through Ostwald ripening to a final size of about 15 nm. Ostwald ripening is a phenomenon in which small particles grow at the expense of the dissolution of even smaller particles to generate nanocrystals with improved thermodynamic stability as a result of lowered surface area to volume ratio and thus lowered surface energy.

Polte et al. (2010) monitored the direct precursor reduction and nanoparticle formation by employing synchrotron radiation. It was found that nanoparticle formation was a multistep process in which initially, small nuclei ($\sim$2 nm) are quickly formed and then coalesce into bigger particles ($\sim$3 nm). Subsequently, the particles grow ($\sim$5 nm) slowly supported the ongoing reduction of gold precursor

and further coalescence events followed by fast particle growth to their final size (7.7 nm), with complete precursor consumption (Figure 2.7).

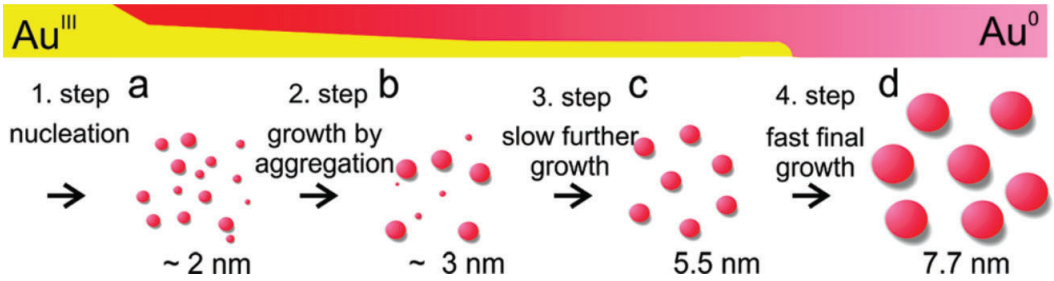


Figure 2.7: Schematic illustration for the proposed process of gold nanoparticle formation. Adapted with permission from Polte et al. (2010). Copyright 2010 American Chemical Society

Polte's arguments counter LaMer's theory by defending that after nucleation the number of particles decreases with the particles growing in size but with minimal Au (III) consumption, suggesting the coalescence of particles. The formation of networks as reported by Pong et al. (2007) were not observed by Polte et al. (2010).

Size Control

In order to be able to more accurately predict and control nanoparticle application in *in vitro* or *in vivo* environments, it is important to produce nanoparticle batches with a relatively narrow size distribution that exhibit properties that are reproducible.

As previously mentioned, the duration of the nucleation stage is a key determinant of the colloid size distribution. During particle growth, the consumption of monomers may give rise to concentration gradients where supersaturation is lower at the colloid surface than in the bulk solution. Moreover, following the partial depletion of the monomer concentration, the amount of monomers that diffuse from the bulk solution is lower than the monomer adsorption to the colloid/nanocrystal surface. Consequently the monomer diffusion becomes a limiting step.

In a diffusion-limited regime, the growth rate is found to dependent on the nanocrystal size. Thus, nanoparticles which size fall bellow a critical value eventually dissolve, thus having a negative growth rate. This is understandable considering that small particles have greater surface curvature, higher SA:V ratio, high surface energy and thus are unstable due their large fraction of active surface atoms (Yin and Alivisatos, 2005).

The growth rate of particles larger than the critical size, initially increases and then decreases gradually after reaching a maximum of double the critical size. The monomer concentration determines the critical size, being that a larger critical size is favoured by low monomer concentrations.

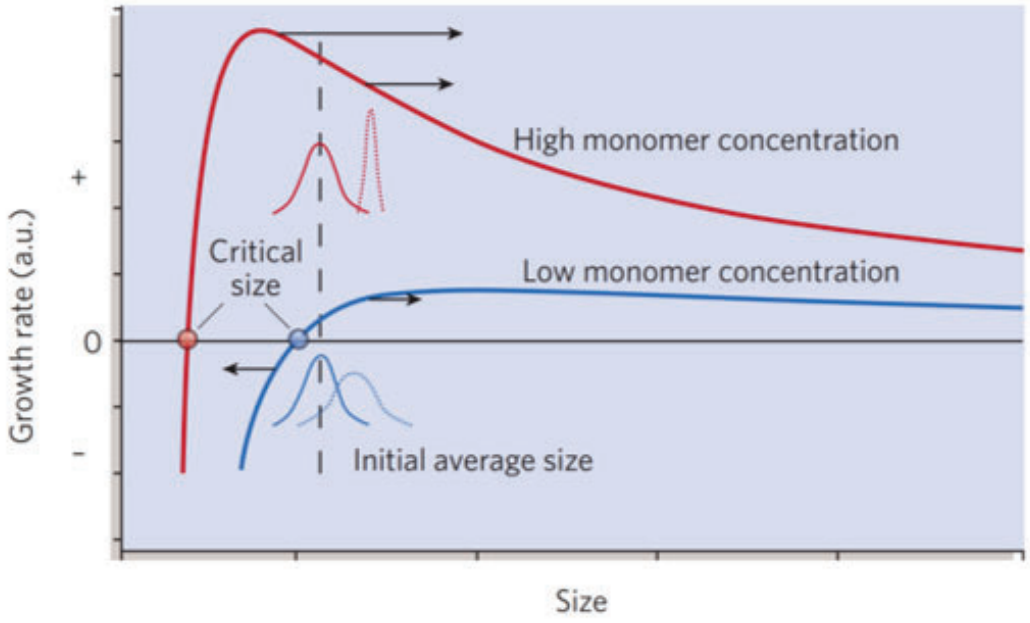


Figure 2.8: Focusing size distribution through separation of nucleation and growth. The growth process of nanocrystals can occur in two different modes, focusing and defocusing, depending upon the concentration of the monomer present. Adapted with permission from Yin and Alivisatos (2005). Copyright 2004 Springer Nature

Moreover, according to the LaMer theory, the growth of nanoparticles can occur in two different regimes, namely focusing and defocusing according to the con-

centration of monomer present (Figure 2.8). During focusing, the average radius of the particles increases rapidly and the resulting size distribution is narrower. A focusing regime occurs at high monomer concentration which favours a small critical size, allowing all particles to grow. In this regime, the size distribution can be focused down to one that is mainly monodispersed because small particles grow faster than the larger ones. Terminating the synthesis in this stage thus yields monodispersed spherical particles. Conversely, a defocusing regime occurs in the presence of low monomer concentration. Here, the size distribution broadens due to the growth of small particles at the expense of depletion of even smaller particles (Ostwald ripening), thus skewing the size distribution (Yin and Alivisatos, 2005).

Whilst the previously mentioned parameters affect the particle size distribution, the surface kinetics of the nanocrystals will determine the shape that they grow into.

Shape Control

Asymmetric (anisotropic) shaped particles can be obtained when the growth rate is increased above that of a focusing regime which yields nearly round but faceted shapes. At equilibrium, the particle assumes a low aspect ratio shape as this minimizes the surface energy and allows the adjacent crystal facets to have similar energies. Anisotropic shapes, for existing in high energy forms, are metastable (Yin and Alivisatos, 2005). Here surface energy of individual facets determines the individual facet growth rate such that low-energy facets grow slower than high-energy facets. A particles shape can be kinetically controlled through the introduction of surfactants that selectively adsorb to particular facets during growth thus altering their respective surface energy (Jana, 2005). Consequently, as the surfactant exchange rate may vary across facets, the selective adhesion of ligands causes growth rate differences across different facets. Moreover, binding of ligands lowers the

surface energy of a particular facet thus slowing growth on that facet whilst growth is accentuated in other crystallographic directions.

Furthermore, by strategically adjusting between a kinetic and thermodynamic growth regime through the control of monomer concentration and temperature, it is possible to further control the shape. In fact, whilst low monomer concentration and high temperatures are typical of a thermodynamic regime, high monomer concentrations characterizes the kinetic growth regime (Yin and Alivisatos, 2005; Niu and Xu, 2011).

Over the last decade, research in the field of anisotropic nanoparticles has seen considerable advances and progress. These advances were made possible due to the development of the seed-mediated method by Murphy group (Jana et al., 2001). In terms of anisotropic morphologies, gold nanoparticles have been more extensively investigated. In fact, these particles may have so far yielded the largest variety of shapes (Li et al., 2014).

2.3.3 Gold nanoparticle clearance and toxicology

The intravenous administration of nanoparticles allows them to be transported to peripheral tissues and organs (Yang et al., 2017a). Within the blood, the nanoparticles can interact with different cellular components (e.g. erythrocytes and platelets), serum proteins and coagulation factors. In particular, during transport, the immune system recognizes the presence of foreign particles based on the adsorption of opsonins to the surface of the nanoparticles. Opsonization effectively increases the nanoparticles *in vivo* hydrodynamic size which limits their ability to be cleared by glomerular filtration in the kidneys being that for renal clearance the nanoparticle size should be less than 10 nm (Longmire et al., 2008). The surface modification of nanoparticles with polyethylene glycol molecules (PEGylation) is

one of the widely used strategies to control the particle half-life in the blood, distribution and clearance by limiting the adsorption of opsonins to the surface of nanoparticles(Hamidi et al., 2006; Longmire et al., 2008).

Ultimately, the propensity for such interactions that affect clearance, are determined by the nanoparticles' intrinsic characteristics such as composition, dimension, morphology, surface chemistry and charge. When it comes to particle composition, gold is an excellent choice of material for being biocompatible and resistant to oxidation. Gold nanoparticles can be easily synthesised with different dimensions, they are being used in very small sizes (1.9 nm) for X-ray contrast (Hainfeld et al., 2006) as well as in larger sizes (50-500 nm) for optical resonance applications (Oldenburg et al., 1998). Studies by De Jong et al. (2008) show that hepatobiliary system is the primary site for the clearance of gold nanoparticles in a size range between 10 and 250 nm in *in vivo* rat models. In fact, the hepatobiliary system constitutes the primary route of excretion of particles that are not removed by renal clearance (Longmire et al., 2008). Physiologically the liver cells (hepatocytes) uptake and enzymatically catabolise blood born and foreign particles and excrete them through the biliary system. This clearance action is complemented by the presence of Kupffer cells which degrade opsonised particles extracellularly. Finally, the surface chemistry and charge of gold nanoparticles can be easily modulated via thiol bonding to favour excretion.

Even though the clearance of more complexly shaped naoparticles such as gold nanocages (Chen et al., 2005) needs further investigation , its is assumed that they may behave analogously to conventional gold colloids. Nonetheless, an equilibrium should be reached and thus the nanoparticles should be formulated in such a way that allows them adequate circulation times for their intended diagnostic or therapeutic function before immunoclearance.

2.4 Tailoring of nanoparticles for BBB crossing

Tailoring of nanoparticles for BBB crossing can be achieved by attaching proteins associated with receptor-mediated pathways to the surface of the nanoparticles. Additionally, the nanoparticles baseline characteristic can also be selected to promote an efficient BBB penetration.

2.4.1 Nanoparticle-ligand complexes for brain access

When it comes to crossing the BBB by taking advantage of the brain's surface receptors, nanoparticles can be specifically coated with ligands, such as antibodies or proteins, that can selectively interact with the mentioned receptors. Due to their relatively large size, antibodies have low mobility *in vivo* (Kumari and Yadav, 2011). Hence, despite some of the reported use of Abs across the BBB the use of proteins may be more advantageous.

Using nanoparticle-protein complexes may facilitate the crossing of the BBB due to a few effects. The combination of proteins with nanoparticles may generate complexes with beneficially lowered zeta potentials. This may improve the complex availability as a consequence of decreased retention by the RES (Prades et al., 2012). The diffusion across the BBB may be improved due to the improved amphipatic character of the assembled complex. Finally, interactions of the complex with particular plasma proteins (Giljohann et al., 2007) may aid in the process of receptor-mediated transcytosis. There are a few examples of proteins that have been reported to enter the BBB, including transferrin, apolipoproteins and leptin.

Transferrin

Transferrin is non-haem glycoprotein which chief physiological function is in transport of iron (Aisen and Listowsky, 1980). Tranferrin is composed of two metal-binding sites located in its N-terminal and C-terminal domains which give the protein a prolate ellipsoid shape. Transferrin is composed of 678 aminoacid residues and two glycan moieties which together amount to a molecular weigh of about 79550 Da (MacGillivray et al., 1982). In the presence of bicarbonate ions, Iron (III) transferrin combines with two Fe^{3+} to form complexes with a characteristic absorbance between 465 and 470 nm. The binding and dissociation of iron is a pH dependent reaction with complete dissociation occuring at pH 4.5, partial dissociation at 6.5 and maximum association between pH 7.5-10.At physiological conditions, for the specific binding of Fe^{3+} to transferrin to occur an anion such as carbonate or bicarbonate must be present. For every Fe^{3+} bound to transferrin, one bicarbonate ion binds cuncurrentely and three protons are released. The protons released are believed to originate from the ionization of three tyrosine residues of the protein (Harris et al., 1985). Equations 2.1 and 2.2 represent the reaction of iron binding to transferrin(Chung, 1984):

$$Fe^{3+} + H_6\mathrm{Tf} + HCO_3^- \Leftrightarrow [Fe - H_3\mathrm{Tf} - HCO_3]^- + 3H^+ \tag{2.1}$$

$$Fe^{3+} + [Fe - H_3\mathrm{Tf} - HCO_3]^- + HCO_3^- \Leftrightarrow [Fe_2 - \mathrm{Tf} - (HCO_3)_2]^{-2} + 3H^+ \tag{2.2}$$

Following binding iron at the places of absorption (e.g.intestinal mucosal cells) transferrin transports the iron to sites of utilization such as the brain (Figure 2.9).

The brain endothelium is know to overexpress transferrin receptors. As the iron is very tightely bound to transferrin, the binding of the protein to its receptor on the cell surface constitutes the first stage to transfer the iron from the protein to the cell. Upon binding, the the ligand-receptor complex is internalised by the cell via receptor mediated endocytosis. The exact pathway followed by the protein-receptor complex is unknown. The differic transferrin releases the iron to the cells in a non-lysososmal acidic compartment (pH 5.4) as a result of reduced affinity at low pH. Iron is transported across the vesicular membrane and the apotransferrin and its receptor are recycled back to the plasma membrane and re-utilized.

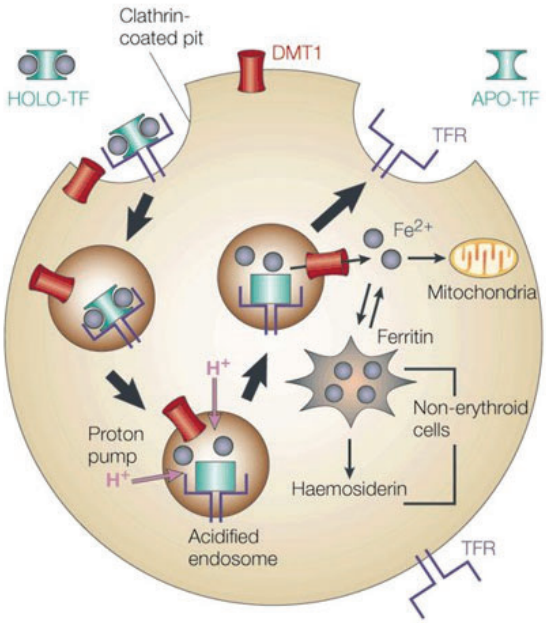


Figure 2.9: The transferrin cycle. Fully iron loaded transferrin (holotransferrin, HOLO-TF) binds to transferrin receptors (TFR) on the cell surface. The complexes localize to clatherin-coated pits, which invaginate to initiate endocytosis. Specialized endosomes form, and become acidified through the action of a proton pump. Acidification leads to protein conformational changes of that release iron from transferrin. Acidification also enables proton-coupled iron transport out of the endosomes through the activity of the divalent metal transporter 1 protein (DMT1). Subsequently, iron-free transferrin (apotransferrin, APO-TF) and the transferrin receptor both return to the cell surface, where they dissociate at neutral pH. Both proteins participate in further rounds of iron delivery. In non-erythroid cells, iron is stored as ferritin and haemosiderin. Adapted with permission from Andrews (2000). Copyright 2000 Springer Nature

Alternatively it has also been argued that transferrin receptors are responsible for the transport of tranferrin across the endothelial cells of the BBB via transcytosis and their accumulation in the brain. Similarly to the insulin receptor, transferrin receptors are involved in transport events to and from the brain parenchyma. Wiley et al. (2013) demonstrated that the accumulation of transferrin conjugated to gold nanoparticles in the brain was dependent on the nanoparticles' transferrin content. In mice models, a moderate gold nanoparticle tranferrin coating led to effective penetration and accumulation of the nanoparticles in the brain. It was proposed that nanoparticles with high transferrin contents fail to be released from the endothelium following trancytosis, as the complex remains engaged with the receptor. On the other hand, a scarce transferin coating prevents the nanoparticles to effectively interact with the receptor to initiate transcytosis.

Apolipoproteins

After transferrin, low density lipoprotein receptor-related protein 1 (LRP1) is the most extensively studied transcytotic system at the BBB. This receptor is expressed in both apical and basolateral membranes of the BBB and participates in the transport of LDLs (low density lipoproteins) across the blood-brain barrier (Herz and Marschang, 2003). Since LRP1 is expressed in a variety of CNS cells including neurons, astrocytes, pericites and microglia, targeting this receptor may cause side effects.

Leptin

Leptin is a polypeptide composed of 146 amino acids. After being released by the fat storage cells (adipocytes), leptin is transported in the blood to the central nervous system where it acts on cells that express the leptin receptor in the brain

and on the hypothalamus. Due to its size, the passive diffusion of leptin across the BBB is not a possibility.

Since the receptor interacting regions of leptin have been associated with brain uptake, it is possible that by identifying the peptide fragments containing these regions of interest one can synthesise constructs for enhanced/selective brain uptake. In fact, some fragments have so far solely been linked to a transport role. This is the case for the 61-90 fragment which is thought to be involved in the unidirectional transcytosis across the BBB (Barrett et al., 2009). Whilst being considerably smaller than the full size leptin, the 61-90 fragment showed a comparable brain uptake to the parent protein. Further attempts to decrease the size of the peptide negatively affected it's uptake properties (Barrett et al., 2009).

Other peptides have also been shown to have the ability to target the brain. In an *in vivo model*, Guerrero et al. (2010) was able to increase the concentration of citrate gold nanoparticles delivered to the brain by four fold by conjugating these particles with the amphipatic peptide CLPFFD. This peptide was derived from the β-amyloid peptide and was able to cross the BBB on its own and to identify toxic aggregates of β-amyloid. With this conjugation, the author was able to obtain conjugates with decreased negative charge and greater lipid solubility, which was argued to decrease the nanoparticle retention by the reticuloendothelial system. Importantly the integrity of the BBB after exposure to nanoparticles seemed unaltered.

In a previous *in vitro* study, Araya et al. (2008) demonstrated the ability of GNP-peptide conjugate to specifically bind to β-amyloid toxic aggregates and their dissolution upon the release of heat by the GNPs when irradiated with microwaves. This was a valuable proof of concept for tackling Alzheimer's disease with great potential if the particle conjugates can effectively cross the BBB.

Ruan et al. (2015) engineered gold nanoparticles to cross the BBB and target glioma cells. Initially the particles were conjugated with the anticancer drug doxorubicin (DOX) via the acid-responsive linker hydrazone. To mediate BBB crossing these particles were then PEGylated and functionalized with angiopep-2, a substrate for the BBB receptor low density lipoprotein receptor-related protein 1 (LRP1). Since LRP1 is also overexpressed in glioma cells the particles synthesised have a dual targeting functionality. In the acidic glioma microenvironment the hydrazone link is hydrolysed and the drug released. Administration of DOX on its own was much less effective than attaching the drug to AuNPs. On the other hand when DOX was conjugated to the NP but without the angiopep-2 component shows improved but still low glioma targeting.

2.4.2 Effect of geometry in cell uptake and trafficking

The nanoparticle's morphology is recognised as being a key factor influencing cellular uptake and distribution. A number of studies have shown how a nanoparticle's shape strongly influences the particle's internalization and functional behaviour (Champion et al., 2007; Geng et al., 2007). Whilst the interaction of cells with spherical nanoparticles has been widely investigated, much focus is now being placed in elongated and anisotropic morphology due to their versatility and very attractive properties such as cell specific uptake and enhanced circulation times (Wang et al., 2018). Several studies have provided valuable insights on geometrical traits that make particular shapes more prone to cellular uptake. In general, shape related effects are hypothesised based on the principles of particle surface curvature (Chithrani et al., 2006), membrane contact angle, surface area, organ specific preferential accumulation (Decuzzi et al., 2010) and intracellular trafficking (Chu et al., 2014).

It has been speculated that the curvature difference between two shapes governs the binding to the cell surface. Chithrani et al. (2006) showed that elongated particles block more membrane receptor sites when bound longitudinally and thus are less internalised than nanospheres.

The particles' angle of contact with the membrane affects the particle penetration (Champion and Mitragotri, 2006) (Figure 2.10). An ellipsoidal particle whose major axis meets the cell membrane normal in a perpendicular angle benefits from increased penetration (Yang and Ma, 2010) and hence the synthesis of particles with numerous short protruding features could further enhance the nanoparticle's penetrating ability. The effect of sharp features was investigated and it was found that rod-shaped nanoparticles with high aspect ratio were internalised by cells to a greater extent than rod shaped particles of lower aspect ratio (Huang et al., 2010; Gratton et al., 2008). Particles with larger surface area are able to accommodate more multivalent interactions to promote particle endocytosis (Gratton et al., 2008; Hao et al., 2012). In this context, anisotropic nanoparticles are able to achieve larger SA/V ratios to support such multivalent bonds.

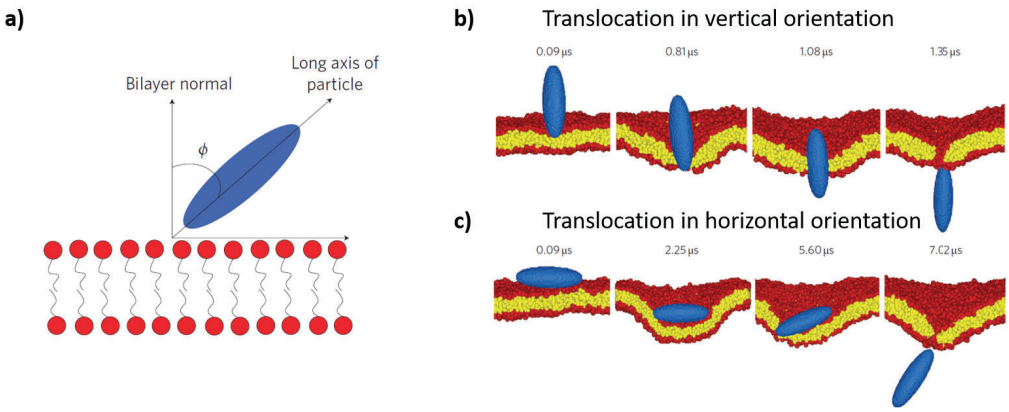


Figure 2.10: Schematic showing the angle (Φ) between the long axis of the particle and the bilayer normal (a). Computer-simulated diagram showing the translocation of ellipsoid nanoparticles across a lipid bilayer with vertical (b) and horizontal (c) starting orientations. Adapted with permission from Yang and Ma (2010). Copyright 2010 Springer Nature

Furthermore, a particle's preferential accumulation in particular organs is influenced by the nanoparticle's shape Decuzzi et al. (2010) (Figure 2.11). In fact, elongated nanoparticles have been reported to exhibit a 7-fold increase in brain accumulation compared with their spherical nanoparticle counterparts (Kolhar et al., 2013).

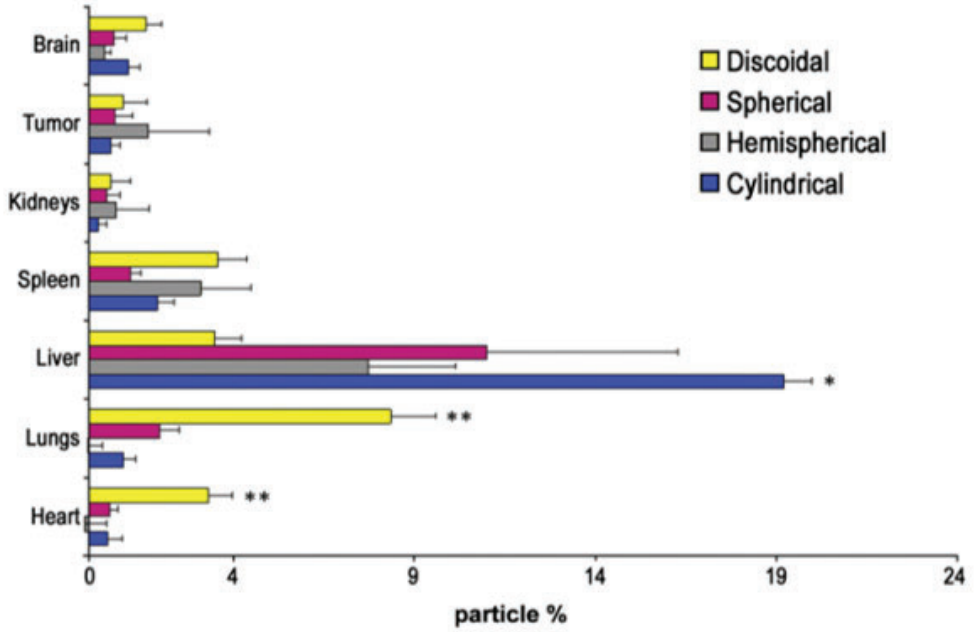


Figure 2.11: Uncoated silica particles of different shapes (discoidal, spherical, hemispherical and cylindrical) were intravenously injected in mice and the relative Si content is presented for each organ. The bar chart shows clearly a shape-dependent accumulation in the major organs. The star symbol identifies differences between the discoidal and the other particles with $p < 0.001$. Adapted with permission from Decuzzi et al. (2010). Copyright 2009 Elsevier

The particle's shape also influences their intracellular trafficking (Chu et al., 2014) (Figure 2.12). Following endocytosis, particles with a round morphology preferentially remained in the endosome and were later cleared by exocytosis when the enclosing vesicle matured into a lysosome (Chu et al., 2014). Conversely, nanoparticles that are sharp could escape the endosome and thus avoided the lysosomal pathway and its mediated excretion (Chu et al., 2014).

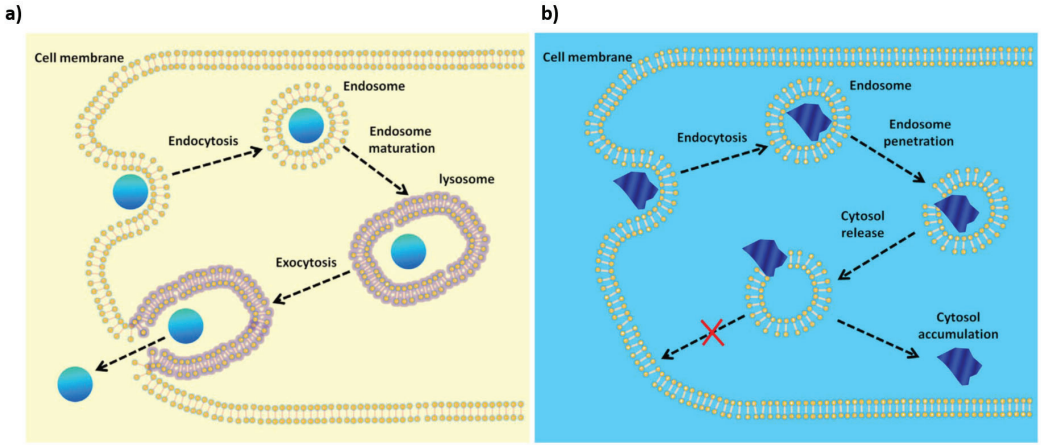


Figure 2.12: Intracellular trafficking of nanoparticles with different morphologies: (a) particles with low sharpness enter the cell by endocytosis, reside in endosomes which evolve into lysosomes and exits the cells via exocytosis with the lysosome as a vehicle; (b) sharp-shaped nanoparticles enter the cell by endocytosis, escapes the endosome by rupturing the endosomal membrane before the lysosome is formed and accumulate in the cytosol. Adapted from Chu et al. (2014). Copyright 2014 Springer Nature

It is important to point out that these shape related effects are very complex and thus bring about discrepancies between studies. These are frequently linked to the nanoparticles' baseline bio-activity and the differences in cellular systems used for the uptake studies. In fact, the mechanism of uptake of the same nanoparticle by different cell types can vary possibly due to different structures in the cell membranes (Santos et al., 2011; Kuhn et al., 2014; Yameen et al., 2014). Therefore, it is important to establish a link between the nanoparticles' geometry and their

penetrating and uptake efficiency directly on BBB models, so that nanocarriers can be efficiently engineered for BBB interactions. Furthermore, shape influences the nanomaterials' preferential accumulation in particular cell types, thus increasing selectivity.

Currently, the most effective nanoparticle shape to mediate BBB transcytosis has not yet been identified. In particular, knowledge about the performance of more complex anisotropic shapes in BBB transcytosis is lacking, although these shapes could be advantageous to mediate the currently poor transport of macromolecule drugs across the BBB (Pardridge, 2014).

In summary, the previous studies suggest that features for best BBB penetration include multiple sharp features of high surface curvature, fixed angle of contact to the cell membrane and high surface area to volume ratio. A nanostar morphology could be therefore a promising candidate for effective BBB penetration.

2.5 Gold nanostars as a candidate platform for BBB targetting and permeability

Nanostars are particles in the nanometer range which consist of branches that radially protrude from a central body (core). This morphology provides them with multiple sharp features which ensure fixed perpendicular angles to interact with cell membranes.

Gold nanostars are advantageous delivery vehicles as they offer large surface areas that allow for a great loading capacity. This has been shown to be an important factor in affecting the rate and quantity of aptamer coated gold nanostar uptake in pancreatic cancer and fibrosarcoma cells (Dam et al., 2014b). Their morphology also allows them to support plasmonic bands in the NIR that when appropriately

exposed to lasers generate heat that can be used for photothermal treatment. Taking advantage of the latter, Yin et al. (2016) group made use of the cell penetrating peptide Penetratin coated onto gold nanostars to gain access to the brain via the BBB. This nanoconstruct was able to permeate the Brain and in an enhanced manner comparatively to controls and prevent the formation of Alzheimers's related aggregates and to dissociate pre-formed aggregates following photothermal treatment.

It is important to note that whilst nanostars have a more complex morphology, their shape does not necessarily have an adverse effect on cell uptake. In fact, computational studies (Li et al., 2015b) have shown that the membrane wrapping time of nanostars is similar to that of nanospheres. Li et al. (2015b)'s study was aimed at clarifying the role of shape of PEGylated nanoparticles during cellular uptake, considering simulated particles with the same surface area and grafting density. The results revealed that spherical gold nanoparticles demonstrated the highest endocytic rate comparatively to cube rod and disk morphologies due to their lower membrane binding energy than the other morphologies. Star shaped nanoparticles were also quickly enclosed by the cell membrane similarly to spheres. The entry of asymmetric particles (cube, rod and disk morphologies) was dependent on the entry angle, with gold nanospheres and gold nanostars, by being relatively symmetric, become free of unfavorable docking orientation effects that could increase the membrane wrapping time. This indicates that the membrane bending potential is not an adverse factor for nanostars.

Several seed-mediated and one-pot synthesis methods have been used in the literature to synthesize AuStrs. A review of the literature is presented in tables 2.1, 2.2 and 2.3.

Seed Mediated Nanostar Synthesis		
Study (Reference)	**Reaction conditions**	**Observations**
Yuan et al. (2012a)	Seed solution: heated $HAuCl_4$ solution reduced by citrate Growth solution: $HAuCl_4$, HCl, $AgNO_3$, ascorbic acid	The resulting stars were about 60 nm in size Plasmon peak could be shifted to the red when stars grew in the presence of concentrations of silver.
Kuo and Huang (2005)	Seed solution: 2.5 nm seeds were synthesized with $HAuCl_4$ in the presence of $NaBH_4$ and sodium citrate. Growth solution: $HAuCl_4$, sodium dodecyl sulphate as a surfactant and ascorbic acid as a reducing agent	The stars were about 40 nm in size containing 1-5 spikes. Ascorbic acid promoted branching and red-shifted the absorption band.
Pallavicini et al. (2013)	Seeds: $HAuCl_4$ treated with NaBH4 in a Triton X-100 solution. Growth solution: $HAuCl_4$, $AgNO_3$, and ascorbic acid in Triton X-100/water was added to the seeds.	Stars were 70-100 nm in size containing five spikes. High amounts of ascorbic acid promoted the formation of longer spikes and red-shifted the absorption bands. Two LSPR bands were observed in the following ranges: 600-900 and 1100-1600nm. It was hypothesized that this extreme red-shift was caused by coupling between the spikes of the nanostars through the collinear arrangement of some branches.
Barbosa et al. (2010)	Seeds : $HAuCl_4$ was reduced in either: $NaBH_4$, Polyvinylpyrrolidone (PVP) and N, N-dimethulformamide (DMF)/H2O to form 3 nm size seeds; Citrate, Ethanol and PVP to form 15 nm seeds; PVP/DMF to from 30 nm colloids Growth solution: $HAuCl_4$ in PVP/DMF	The stars were 30-80 nm in size with smaller stars being associated to smaller seeds. Monodispersity was achieved when the seeds were added only once the Au^{3+} had been completely reduced to Au^{+} by DMF (in the presence of PVP). A low $HAuCl_4$ to seed molar ratio led to small rounded particles. Higher temperatures led to rounded particles.
Kumar et al. (2008)	Seeds: 15 nm PVP-coated seeds in ethanol were Growth solution: $HAuCl_4$, PVP, and DMF.	Stars were about 60 nm in size. The size distribution improved when seeds were as opposed to when they were not used. Higher concentration of PVP lead to more branched structures.
Yuan et al. (2007)	Seeds: 14 nm gold seeds were synthesized by boiling $HAuCl_4$ with sodium citrate. Growth solution: $HAuCl_4$, NH_2OH and a $AgNO_3$	Stars were150-300 nm in size. The concentration of $AgNO_3$ affected spike morphology. At a certain $AgNO_3$ concentration, the spikes reached a length of 100 nm. Thorny multilevel nanostructures were obtained with repeated growth.

Table 2.1: Literature review of nanostar synthesis mechanisms.

Seed Mediated Nanostar Synthesis (continued)		
Study (Reference)	**Reaction conditions**	**Observations**
Yuan et al. (2011)	Seeds: 8nm silver seeds were synthesized by adding $NaBH_4$ and sodium citrate to a solution of $AgNO_3$ under heating. Growth solution: $HAuCl_4$ and NH_2OH	Stars were 100-500 nm in size. The redox displacement of silver by gold produced AgCl, which precipitated on the surface of the nanospheres and promoted the growth of spikes. Changing the solution volume altered the surface morphology. Smoother particles were obtained at higher temperature, possibly because both the rate of gold deposition and the solubility of AgCl increased.
Schütz et al. (2011)	Seeds: 10 nm seeds were synthesized with $HAuCl_4$, sodium citrate, and $AgNO_3$, under boiling . Growth Solution: $HAuCl_4$, glycerol, sodium citrate, and $AgNO_3$. Hydroquinone was added as a reducing/-capping agent.	The stars were 60 nm in size Glycerol slowed the formation of nanostars and led to monodisperse particles. Larger seeds yielded larger stars.
Nehl et al. (2006)	Seeds: commercial colloid seeds and surfactant-stabilized seeds prepared by reduction of $HAuCl_4$ in the presence of CTAB. Growth solution: For the commercial seeds: CTAB, $HAuCl_4$, $AgNO_3$, and ascorbic acid. For the surfactant-stabilized seeds: CTAB, $HAuCl_4$, and $AgNO_3$, followed by the addition of ascorbic acid and NaOH. The nanostars were PEGylated.	The stars were 100 nm in size

Table 2.2: Literature review of nanostar synthesis mechanisms (continued).

One pot-synthesis of Nanostars		
Study (Reference)	**Reaction conditions**	**Observations**
Umadevi et al. (2013)	Synthesis performed in a hexagonal liquid crystal template $HAuCl_4$ was treated with $AgNO_3$ and ascorbic acid	The resulting stars were about 100 nm in size and had long spikes. The amount of $AgNO_3$ affected spike morphology.
Kedia and Kumar (2013)	$HAuCl_4$ was treated with PVP and DMF in the presence of NaOH	The resulting stars were 50-100 nm in size. Lower [NaOH] led to sharper tips.
Bakr et al. (2006)	$HAuCl_4$ reacted in the presence of H_2O_2, sodium citrate, and various ligands (11-mercapto-1-hexanol, 3-mercacpto-propanoic acid, and 11-mercaptoundecanoic acid).	The resulting nanoparticles were about 40 nm in size and contained more than 4 spikes. The rate of addition of $HAuCl_4$ affected the size and morphology of the particles.
Kedia and Senthil Kumar (2012)	$HAuCl_4$ reacted in the presence of PVP, DMF, and HCl.	The nanostars were about 100 nm in size HCl mediated spike formation, but when in high concentrations it drove the reaction towards the thermodynamic route, producing spherical particles. It was proposed that PVP complexes to DMF to reduce $AuCl^-$ ions.
Xie et al. (2007)	$HAuCl_4$ was treated in HEPES buffer at room temperature	The stars were about 40 nm in size containing 1-8 spikes. High temperatures led to the formation of spherical particles
Cheng et al. (2012)	$HAuCl_4$ was mixed with $AgNO_3$ and ascorbic Chitosan was used as a stabilizer	Stars were 60-150 nm in size The concentration of silver nitrate affected spike morphology. It was proposed that silver ions were reduced on the surface of the gold through underpotential deposition.

Table 2.3: Literature review of nanostar synthesis mechanisms (continued).

Currently there are no studies that elucidate the effect of surface spikiness on BBB penetration ability.

2.6 *In Vitro* models of the BBB as a validation tool

Considering the BBB impermeability, several *in vitro* screening methods were developed to prognosticate the efficiency of forefront drug delivery systems in crossing the BBB and accumulating in the target sites *in vivo*. These constitute a strong tool that can be introduced early in the drug delivery development process, thus potentially preventing latter failure of drug candidates. Failure comes at a heavy economic and time cost being that on average 1 billion dollars are required for the development of a treatment for a CNS disorder, which frequently requires more than a decade of research (Nutt, 2011). These *in vitro* models are roughly categorised into cell-based and non-cell based.

2.6.1 Non-cell based *in vitro* models of the BBB

Non-cell based models include PAMPA (parallel artificial membrane permeability assay), an assay in which a donor and acceptor compartments are separated by a lipid artificial membrane dissolved on non-polar solvent and supported onto a porous filter. Following membrane exposure to nanomedicines for a set period of time, both compartments are quantified. This assay is thus used as a measure of passive transcellular permeability. Ideally, the physiological lipid composition of this membrane should closely resemble that of the BBB as this was shown to more accurately reflect the permeability of control substances know to cross (BBB positive) or to be restricted (BBB negative) by the BBB in *in vivo* data (Mensch et al., 2010). Additionally, they should be sufficiently dense as to prevent the formation

water pores (Tsinman et al., 2011), a structure that symbolically represents paracellular transport and is thus non-representative of *in vivo* BBB transport. These models are simplistic compared to the real BBB membrane dynamics. Apart from transcellular passive diffusion, this model excludes all other transcellular transport mechanisms reported *in vivo*. Finally, the presence of an organic solvent and lack of a bilayer configuration also come as disadvantages. Nontheless, Prades et al. (2012) was able to use a PAMPA model, as a complement to a BBB cellular in vitro model, to demonstrate that Transferrin receptor targeted gold nanoparticles were unable to cross the BBB by passive diffusion.

2.6.2 Cell based *in vitro* models of the BBB

Cellular models allow the evaluation of the permeability of compounds that pass by passive diffusion or by active transport. This constitutes a more thorough model with the possibility of providing mechanistic insights into the BBB crossing mechanism by compounds. The characteristics of different cellular *in vitro* models depend, amongst other factors, on the type of cells employed. Different cell types have different expression levels of cellular receptors and form cellular monolayers of particular tightness. In particular, the tightness of the monolayer is evaluated by measuring the transendothelial electrical resistance (TEER). This consists on the appliance of an electrical current on both sides of the transwell and registration of the barrier resistance on a voltmeter.

Before nanomedicine exposure, TEER is used to validate tight junction expression by evaluating whether the paracellular route is being appropriately restricted, similarly to the physiological conditions. After exposure, TEER can also be used to demonstrate that the nanoparticles did not compromise the membrane integrity.

As part of their maintenance, primary brain capillary endothelial cells for these

in vitro models need to be subcultured periodically and passed onto fresh growth media. It is known that cells of low passage bear the closest phenotypic resemblance to *in vivo* BBB cells. Hence, to minimize batch to batch variability overtime (e.g. loss of transporter expression), these cells were genetically engineered to generate immortalised cell models.

The most commonly used, and thus most extensively characterised, human origin BBB immortalised cell line for drug uptake studies is the hCMEC/D3 (Weksler et al., 2013), reported for the first time by Weksler et al. (2005). This cell line is derived from human temporal lobe microvessels obtained during surgery. These cells form contact-inhibited monolayers on collagen (type I and IV) coated substrates. This cell line also expresses a number of important BBB characteristic junction associated proteins, transporters (e.g Glut 1 and LAT-1), receptors (e.g transferrin and insulin), endothelial cell markers (e.g. CD31 and CD40), and ABC efflux transporters (e.g. P-gp) (Banerjee et al., 2016; Helms et al., 2016).

Monolayers of this cell line form an effective barrier for the passage of molecules of high molecular weight. Conversely, low molecular weight compounds may experience enhanced permeability through paracellular route. In fact, whilst in mammalian systems (e.g rat) (Butt et al., 1990) the TEER value is commonly accepted to be above 1000 Ω cm ^{2}, in hCMED/D3 nonolayers low TEER values around 9-50 Ω cm ^{2} are reported (Biemans et al., 2016; Weksler et al., 2005, 2013).

In this regard, optimization work is still being employed in order to improve their relatively low junctional tightness for low molecular weight compounds. Strategies include co-culture with other cell types of the neurovascular unit (Hatherell et al., 2011) and stimulation of the Wnt/β-catenin pathway (Paolinelli et al., 2013), the signalling pathway involved in the regulation of expression of tight junction proteins.

Recently, microfluidic based models of the BBB have started to emerge. Similarly to the mentioned examples, in these systems, cells are grown in a porous filter support membrane. However, here the filter sits in between two microfluidic channels trough which culture media circulates. Unlike transwell systems, these allow the introduction of fluidic shear stress (Booth and Kim, 2012) to closely represent the dynamic interface of the BBB *in vivo*.

2.6.3 Reported nanostructure efficiencies in *in vitro* BBB models

Different nanoparticle based carrier systems are being developed and their performance tested in *in vitro* BBB transwell models.

Zhao et al. (2016) produced magnetic nanoparticles and conjugated them with the cell penetrating peptide Tat (SiO_2@Fe_3O_4-Tat) (Figure 2.13 a and b).

A U251/hCMEC/D3 co-culture transwell based cell model was used for the permeability studies. It was found that SiO_2@Fe_3O_4-Tat nanoparticles were able to pass through the BBB however this was greatly facilitated by the aid of an external magnetic field for magnetically mediated dragging (Figure 2.13 c). The nanoparticles performance was attributed to a synergetic effect of Tat conjugation and magnetic field.

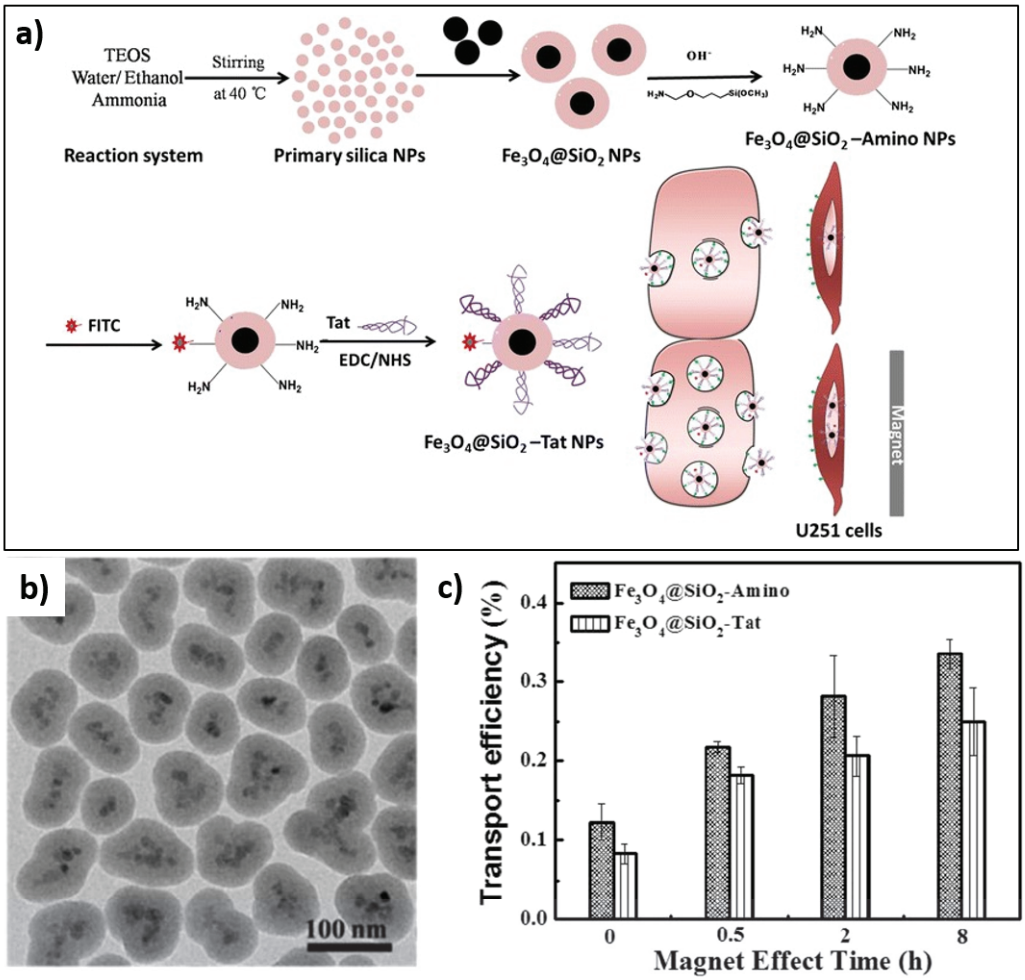


Figure 2.13: Design of Fe_3O_4@SiO_2-Tat nanoparticles for BBB crossing (a);TEM images of Fe_3O_4@SiO_2 NPs (b); transport efficiency of Fe_3O_4@SiO_2-Tat and Fe_3O_4@SiO_2-Amino NPs. Adapted from Zhao et al. (2016). Copyright 2016 Springer Nature

Kafa et al. (2015) used primary porcine brain endothelial cells (PBEC) and primary rat astrocytes co-culture BBB model to investigate the transcytosis ability of amino-functionalized multi-walled carbon nanotubes (MWNTs-$NH3^{+}$) (Figure 2.14). A complete crossing of the nanostructures was only achieved after 48 hours of exposure. The maximum transport achieved was 13 $\pm$ 1.1 % following 72 hours of exposure. It was hypothesised that MWNTs-$NH3^{+}$ could be taken into endothelial cells by adsorptive-mediated endocytosis due to their slight cationic nature.

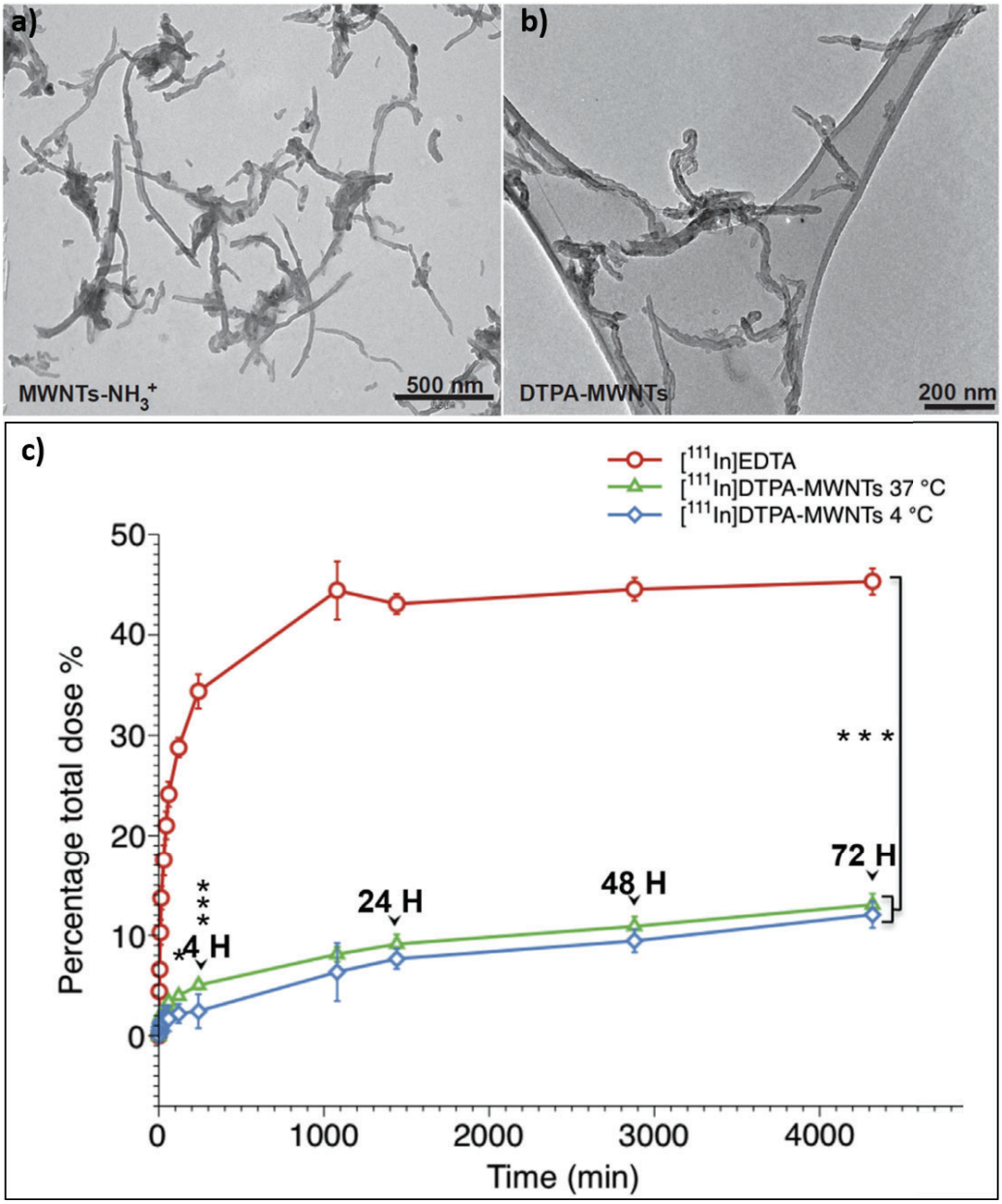


Figure 2.14: TEM images of MWNTs-NH3^{+} (a) and DTPA-MWNTs (b). MWNTs-NH3^{+}that crossed the PBEC layer was quantitatively assessed using radioactive tracers. DTPA-MWNTs were synthesised from MWNTs-NH3^{+} and radioactively labelled with [^{111}Indium] . The radioactivity of [^{111}In]-DTPA-MWNTs was measured in the basal chamber at different time points and a maximum of 13.0 $\pm$ 1.1% was reached after 72 hours. The incubation at 4 C significantly decreased the uptake of [^{111}In]-DTPA-MWNTs . [^{111}In]EDTA was used as a marker to ensure that [^{111}In] was due to [^{111}In]-DTPA-MWNTs transport and not [^{111}In]EDTA.(One way ANOVA test; *p < 0.05, ***p < 0.001, ****p < 0.0001, n = 3). Adapted from Kafa et al. (2015). Copyright 2015 Elsevier

Clark and Davis (2015) applied a murine endothelial cell line (bEnd.3) transwell BBB model to evaluate the transcytosis of spherical 80 nm gold nanoparticles conjugated to transferrin via an acid cleavable linkage (DAK-PEG-OPSS). In the presence of this cleavable group, the nanoparticles were capable of more efficiently undergoing transcytosis comparatively to control transferrin gold conjugates (Figure 2.15). The difference in transcytosis capacity was attributed to the the ability of high avidity (densely loaded) transferrin conjugated gold nanoparticles to completely detach from transferrin receptors following hydrolysis of the DAK group in the transport vesicles acidic pH. In these conditions the nanoparticles were able to completely detach from the endothelial cells at the basolateral membrane whilst control Tf conjugated gold nanoparticles remained attached to the endothelium.

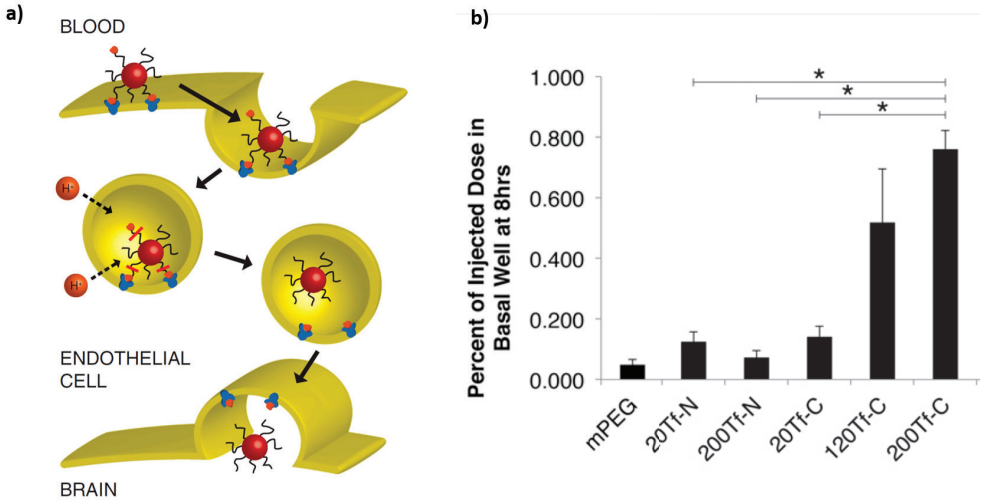


Figure 2.15: Proposed scheme of transcytosis mechanism for transferrin containing nanoparticles with an acid-cleavable linkage(a). Following endocytosis the transferrin ligand separates from the nanoparticle core due to rapid acidification of the endosome, allowing the nanoparticle to freely transcytose into the brain. Graph showing the percentage of injected nanoparticles reaching the basal well of bEnd.3 coated transwells 8 h after introduction (b). The number in the formulation name indicates the number of ligands per nanoparticle, -N indicates noncleavable PEG conjugate, and -C indicates cleavable PEG conjugate. 120Tf-C and 200Tf-C show greater ability to cross the transwells compared with 200Tf-N. Error bars given are SE. *P < 0.001. Adapted from Clark and Davis (2015). Copyright 2015 PNAS

A summary of reported nanoparticle efficiencies is provided in table 2.4.

Nanoparticle shape	Materials and Formulation	Administered dose	Type of Cell in monolayer	Size (nm)	% Transcytosis (maximum reported)	Reference
Spherical	PEG-Silica (PSiNPs)	200 μg/ml	Mouse cerebral endothelial cells (bEnd.3)	25	26.1	(Liu et al., 2014)
				50	19.2	
				100	10.6	
	LF-Silica (PSi-Lf NPs)	ND	Rat brain VECs	25	21.3	(Song et al., 2017)
				50	11.6	
				100	5.8	
	Amino-Fe3O4@SiO2 NPs	200 μg (under 8h magnetic effect)	hCMEC/D3	76.4	0.34	(Zhao et al., 2016)
	TAT-Fe3O4@SiO2 NPs			87.6	0.25	
	Phosphorylcholine coated iron oxide nanoparticles (IONP-PC)	50 μg/ml	hCMEC/D3	112	17	(Ivask et al., 2018)
	LPFFD and TGN conjugated Selenium nanoparticles (L1T1-SeNPs)	0.1 mg/ml DMEM + 10%FBS	bEnd.3 cells	103.12	68	(Yang et al., 2017b)
	200Tf-C gold nanoparticle	1×10^{10} AuNPs in serum-free DMEM	bEnd.3-coated	80	75	(Clark and Davis, 2015)
Nanocluster	Dopa@GQC (Glutathione stabilized gold quantum cluster functionalized with L-Dopa)	1 mg/ml vehicle not disclosed	bEnd.3 cells	0.7-1.4	>90	(Nair et al., 2017)
Nanotubes	carbon MWNTs-NH3+	20 μg/ml	Primary porcine brain endothelial cells (PBEC) in co culture	L=500 nm, ϕ=18.9 nm	13	(Kafa et al., 2015)

Table 2.4: Summary of reported transcytosis efficiencies in *in vitro* BBB models

2.7 Scope of the work and Project Outline

2.7.1 Project motivation

The blood brain barrier (BBB) is arguably the main obstacle for the administration of therapeutic and diagnostic compounds for conditions such as brain cancer, Alzheimer's and Parkinson's diseases. Nanoparticles are being investigated as agents to cross this barrier, however further understanding of cell-nanoparticle interactions are needed to enable the effective design of these agents.

2.7.2 Project aims

The work in this thesis will focus on the development of a nanoparticle-based vehicle capable of selectively targeting and efficiently crossing the BBB. Assessment of the available literature suggests that highly structured nanovehicles, with spiky protrusions, could have many beneficial features for efficient BBB penetration. However, the effect of a nanovehicle with designed and controllable surface spikiness on BBB penetration and transcytosis has not yet been studied.

2.7.3 Criteria followed for nanoparticle design

In summary, the design of the nanoparticles for BBB penetration should meet particular design criteria to maximise the nanoparticles potential *in vivo* use. Amongst the factors for consideration for nanoparticle design are a low toxicity material, stability and circulation time, appropriate size, active targeting and efficient cell penetration.

Low toxicity material

As the nanomaterial is to be implemented in a biological environment it should be made of a biocompatible/bio-inert material to avoid toxic effects. For this work gold was chosen for being a known biocompatible material (Shukla et al., 2005). Ideally, the nanovehicle should be designed for long circulation times and be physically stable to allow them sufficient time to reach the target sites and perform their designed function. These desired properties can be controlled based on the choice of surface coating (and its stability in biological media) and size.

Stability and circulation time

In this work we opted for conjugating the gold nanostars with the biocompatible polymer polyethylene glycol (PEG). PEG provides physical stability to the nanostructures, preventing them from aggregating in biological media through steric repulsion forces. Additionally, PEG is reported to considerably increase nanoparticles circulatory retention time by evading the reticuloendotheliul system, as nanoparticles are prone to uptake by macrophages (Owens and Peppas, 2006). Specifically, PEG creates a hydrophilic protective layer around the nanostructure surface that prevents or delays the binding of blood serum proteins known as opsonins (Owens and Peppas, 2006). Opsonins binding to nanoparticles would otherwise mediate macrophage recognition and removal from circulation before the nanostructures have the chance to perform their function.

Appropriate size range

The size of the nanoparticle influences its fate within the system. For nanocarrier applications, nanoparticles are typically designed with diameters ranging

between 40 to 150 nm. This range promotes a greater nanoparticle retention. Particles with smaller dimensions are removed from the blood circulation by kidneys, whilst bigger than 150 nm are removed by the liver's reticuloendothelial system. (Kumar, 2010).

In this project the main nanoparticles were synthesized with a target diameter of 100 nm. Being that the size limit for brain penetration is 100 nm (Nance et al., 2012), using nanoparticles in this upper limit should allow for the administration of versatile payloads of targeting molecules for efficient brain targeting. Additionally, 100 nm nanoparticles can pass through the fenestrae in liver endothelial cell (Snoeys et al., 2007) and have been previously reported to spontaneously accumulate in tumours following a systemic injection due to enhanced permeability and retention (EPR) effect (Maeda et al., 2000). Whilst beneficial, this size-dependent accumulation occurs passively.

Active targeting

To promote promote the active recognition and attachment to the BBB cells the nanoparticles should display a targeting molecule on their surface. Here, the gold nanostructures are bioconjugated with transferrin molecules to target and encourage the crossing of the nanoparticles through the BBB. As discussed in the literature review, transferrin molecules can enter the endothelium *via* transferrin receptor mediated pathways.

Efficient cell penetration

Finally, the nanocarrier should be able to cross the plasma membrane and avoid intracellular entrapment to successfully complete BBB transcytosis. From the assessment of the literature, it is clear that nanoparticle shape influences the cel-

lular penetration (Yang and Ma, 2010) and intracellular trafficking (Chu et al., 2014, 2015). In this thesis, a nanostar morphology is explored as their high aspect ratio features and large surface areas could be beneficial for effective BBB trafficking and transcytosis. A transwell-based *in vitro* model of the BBB employing hCMEC/D3 cells was used here to evaluate the BBB crossing ability of the nanoparticle candidates. This cell line is well-characterised and known to express transferrin receptors (Weksler et al., 2013).

2.7.4 Study Outline

The first experimental studies focus on the shape controlled synthesis of candidate nanostar morphologies and their respective stabilization and bioconjugation with transferrin proteins (Figure 2.16). Spherical nanoparticles are also studied for comparison purposes.

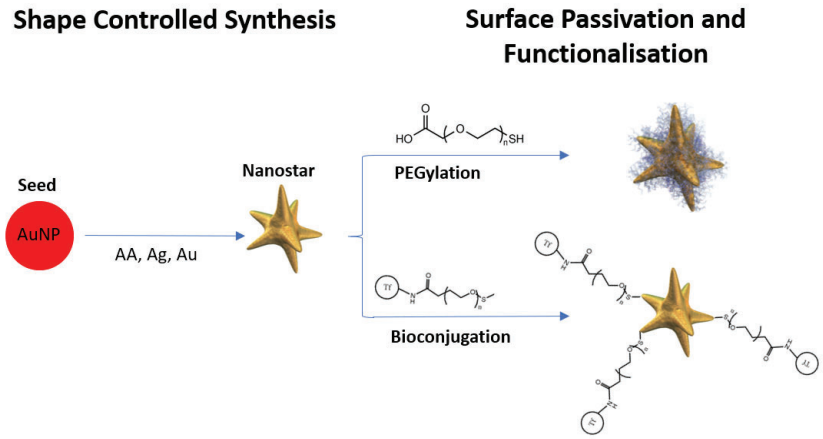


Figure 2.16: Schematic representation of the study outline showing the different stages of nanostructure assembly for BBB targeting

The second experimental section focuses on the evaluation of AuStr transcytotic performance across an *in vitro* BBB model: a transwell based *in vitro* model of the BBB using the hCMEC/D3 cell line is used for this study.

Chapter 3

Characterization techniques

The present chapter provides a theoretical overview of the main analytical techniques used to characterise the study samples prepared in chapters 4 and 5. Sample preparation details are provided in the respective experimental chapters 4 and 5.

3.1 Microscopy techniques

3.1.1 Transmission electron microscopy

Transmission electron microscopy is a valuable analytical technique for the visualisation of samples at the nanometre level. By making use of a focused beam of electrons, it is able to reach resolution and magnification levels beyond the capability of light microscopes. Moreover, the ability to distinguish the shortest distance between two separate points defines the resolution of the microscope. Resolution depends on the wavelength of the electron beam. Being that electrons have particle and wave-like properties, their wavelength can be defined by the Broglie's theory on wave particle duality by taking into account the particles momentum, p,

through the Plank's constant, h (Williams and Carter, 2009).

$$\lambda = \frac{h}{p} \tag{3.1}$$

To achieve higher resolutions shorter wavelengths are required. This implies that the electrons require a high momentum. High momentum is achieved in electron microscopes through the acceleration of the electrons through a potential, V, thus imparting them with kinetic energy:

$$\lambda = \frac{h}{\sqrt{2m_o eV}} \tag{3.2}$$

where m_0 is the rest mass of the electron. However, at such velocities, it is important to take into account the relativistic effects and thus the equation (Williams and Carter, 2009):

$$\lambda = \frac{h}{\sqrt{2m_o eV + (1 + \frac{eV}{2m_o c^2})}} \tag{3.3}$$

where c is the speed of light.

From the above relationship (Equation 1.3), it is shown that by increasing the acceleration voltage, the electron momentum can be increased and thus decreasing the wavelength. Whilst the wavelengths in an electron microscope are typically in the range of 10^{-3} to 10^{-2} nm, light microscopes operate with visible light with wavelengths between 400 to 700 nm and thus the resolution of light microscopes is substantially inferior to that of electron microscopes where resolutions can go down to 0.05 nm.

In TEM imaging, thin samples (< 100 nm) placed in vacuum, are illuminated by an electron beam which is mostly transmitted straight through the sample. How-

ever, sample irradiation can also give rise to electrons that are scattered at different angles, either elastically (with undetectable energy loss) or inelastically (with detectable energy loss). Furthermore, a number of secondary signals are also generated from the electron-specimen interaction that can be used to further characterise the sample (Figure 3.1).

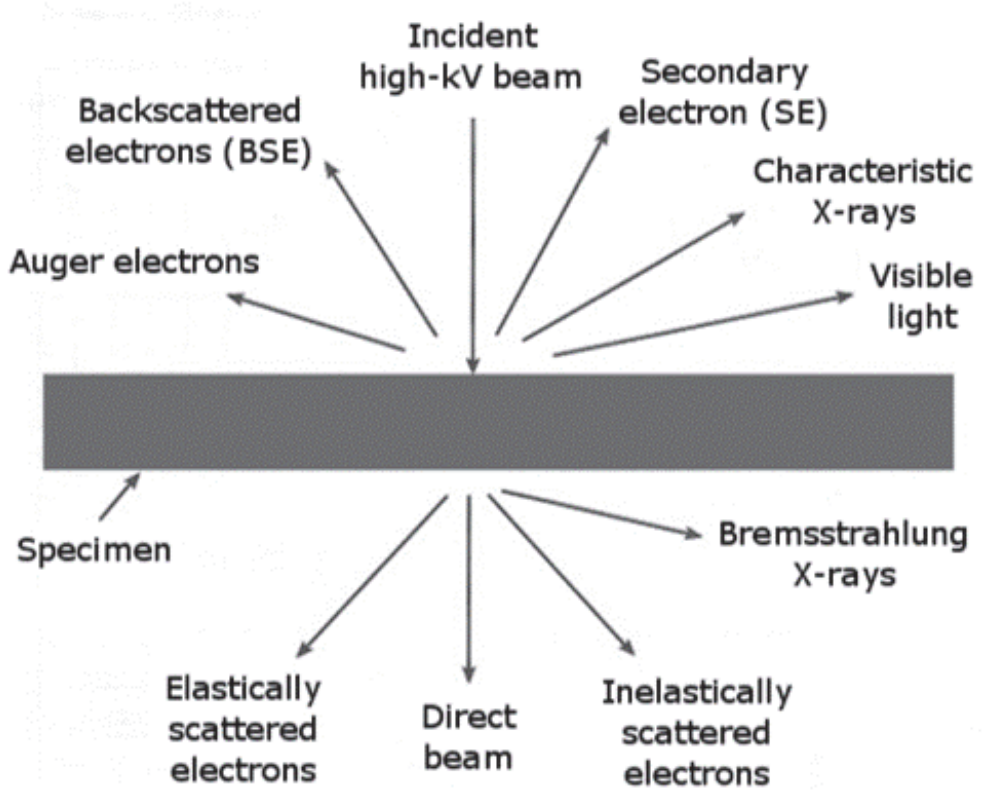


Figure 3.1: Schematic representation of some of secondary signals generated when a beam of high speed electrons interacts with a thin sample. Adapted from (Williams and Carter, 2009)

Elastically scattered electrons, are focused through a system of lens and a TEM image is eventually projected onto a phosphorescence screen. Due to the specific characteristics of the sample including its thickness and the atomic number (Z) of the sample species interacting with the electron beam, the electrons are deflected to different extents. This generates the contrast required to form an image ranging

from the dark areas where the sample has higher density and/or atomic number and brighter regions representing low mass thickness areas where electrons are unscattered (Figure 3.2). The sample contrast can be improved through the use of the objective aperture.

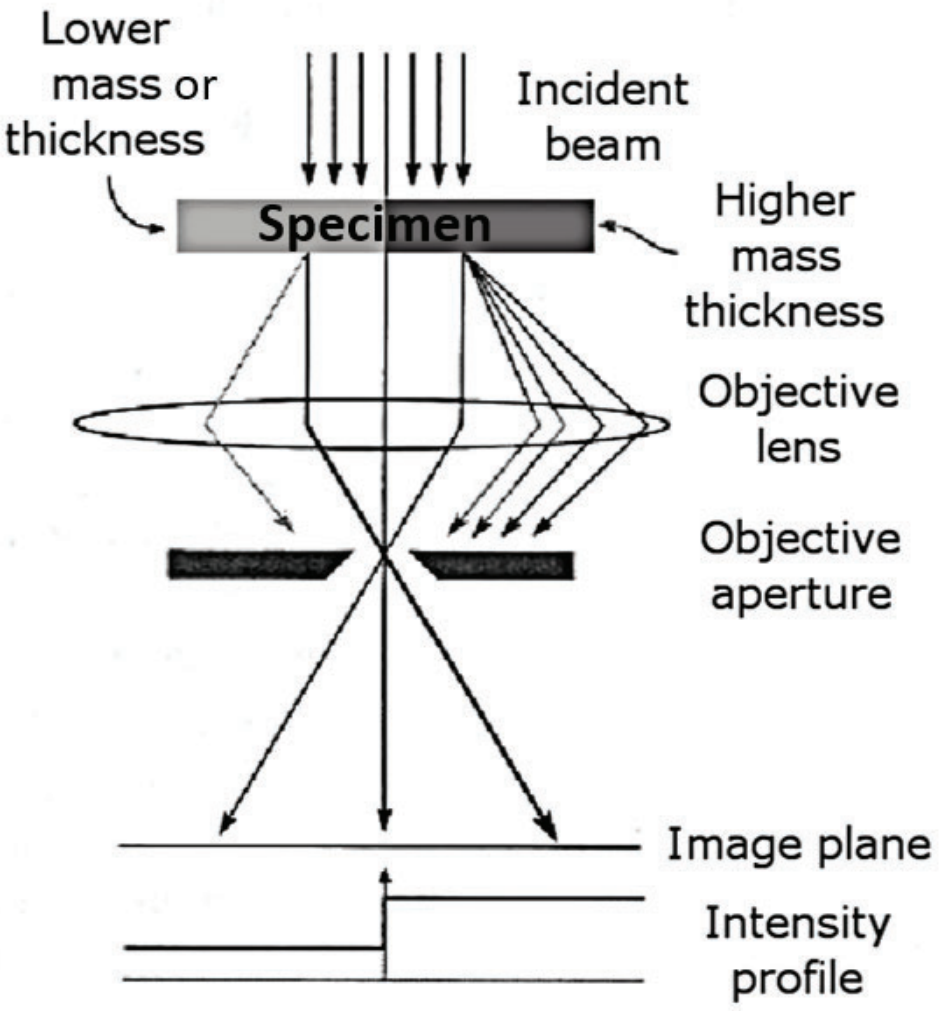


Figure 3.2: Schematic representation of the mechanism by which differences in mass or thickness generate image contrast in a bright field TEM image. Adapted from (Williams and Carter, 2009)

The electron beam is generated, by either thermionic or field emission, by the

electron gun placed at the top of the electron column where a set of electromagnetic lenses are placed to shape and direct the beam through the column. The condenser lenses focus the electrons after the first crossover image onto the specimen and condenser apertures are used below these lenses to decrease spherical aberrations. The electrons emerging from the sample are focused by the objective lens which can also be used to initially magnify the image. Finally, the intermediate lenses further magnify the image from the objective lens followed by the projector lenses that project the image onto the phosphorescent screen.

It is essential to maintain vacuum environment inside the column to decrease the density of contaminant molecules that can interfere with the beam.

Scanning Transmission Electron Microscopy

As previously mentioned, secondary signals can arise from the electron specimen interaction. Scanning trasnmission electron microscopy (STEM) imaging mode is used in correlation to TEM imaging to allow the detection of electron energy loss, X-rays and to detect elastically scattered electrons at low and high angles (Lupini et al., 2015). In STEM, the incident beam is focused through a series of lenses to a probe and scanned across the sample in an area of interest. The differently scattered electrons are collected by detectors present at different post-specimen locations. In particular, electrons that are scattered at relatively high angles, >50 mrad, can be collected by the high angle annular dark field (HAADF) detector. The intensity of the HAADF signal is directly proportional to Z^n (n$\sim$2), since at such high scattering angles nuclear scattering dominates over the effect of the electron cloud on electrons (Lupini et al., 2015). Such property, allow the generation of images with great contrast, where bright features are generated against a dark background (dark-field STEM)(Lupini et al., 2015).

3.1.2 Scanning Electron Microscope

In scanning transmission electron microscopy (SEM) an image is produced by a nanometer sized electron probe that is rastered over an area of interest in the sample. The SEM operates at voltages up to 30 kV and is used for the analysis of a variety of samples including bulk materials, powders and thin films (Erdman and Bell, 2015). Whilst a combination between diameter of the electron probe, lens design and electron source size determine the instrument spatial resolution, beam-specimen interactions can limit the achievable resolution. Nonetheless, the interaction of the electron beam with the sample originates various signals from resulting backscattered, secondary and transmitted electrons. Furthermore, by changing the arrangement of the detectors in the instrument signals like characteristic x-rays and photons can be suitably detected (Erdman and Bell, 2015). In particular, the number of secondary electrons generated depends of the angle at which the beam meets the surface of the sample. Hence, the use of SEM in secondary electron detection mode generates insightful surface topology information (Erdman and Bell, 2015).

3.1.3 Focused Ion beam-SEM

By having the ability to combine both nano and macroscale observations SEM imaging is particularly useful for the observation of cellular samples and their intricate morphological systems whilst allowing tracking the intracellular presence of nanoparticles. SEM instruments can be fitted with a focused ion beam column which allow imaging, milling and specific chemical deposition on substrates surfaces using a finely focused beam of ions. Gallium is conventionally used as an ion source (Ga^{2+}) due to its advantageous properties including its liquid state close to room temperature (30 °C), it is easily ionisable and causes low analytical inter-

ferences (Erdman and Bell, 2015). By rastering a beam of ions across a region of interest on the sample surface, the specimen can be finely milled. FIB-SEM allows for sequential *in situ* cross sectioning of resin embedded sample block followed by SEM imaging. Imaging in SEM mode allows for the highest resolution whilst preserving the sample blockface from ion beam damage. Milling is performed at low beam currents to prevent debris re-deposition onto the imaging surface. This process allows the collection of a tomographic dataset that can be reconstructed in 3D models to provide structural and dimensional sample information.

In chapter 4 FIB-SEM is used for the tomographic reconstructions of BBB endothelial cell monolayers.

3.2 Spectroscopy techniques

3.2.1 Energy Dispersive X-ray Spectroscopy

As electrons pass through the sample X-rays can be generated. The so-called characteristic X-rays have energies that are element specific, hence their analysis allows for quantitative and qualitative analysis of the sample composition. X-rays are produced, when incident electrons interact with inner-shell electrons causing the ejection of the latter when the incident electron transfers enough energy (Williams and Carter, 2009). Following ejection, and electron hole is formed in the inner shell which can be filled by an outer shell electron, thus returning the atom from an excited to a ground state. This electronic transition involves the emission of a characteristic X-ray which energy is equivalent to the energy difference between the two electron shells involved. For instance, K_α X-ray is generated when a hole in the K-shell is filled by an L-shell electron. Ultimately, the elements present in a

sample can be identified by analysing the x-ray energy detected in a semiconductor detector. Finally, EDX spectrum is generated in which the x-ray intensity is plotted against a range of energies (Williams and Carter, 2009). Quantitative information regarding the ratio between elements can be obtained following background subtraction fitting.

3.2.2 Inductively Coupled Plasma-Optical Emission Spectroscopy(ICP-OES)

The use of electromagnetically generated flames or inductively coupled plasmas allows the conversion of trace metals and inorganic analytes in solution into excited atoms and ions (Fassel and Kniseley, 1974). Once generated these ions and atoms can be quantified even at trace levels by using optical emission spectrophotometers. In this technique multiple elements can be analysed simultaneously as elements are determined at characteristic element specific wavelengths. Plasmas are most commonly generated from ignited argon gas which can sustain temperatures of approximately 8000K, thus generating a more inert environment and preventing the generation of contaminants (e.g. oxides) (Fassel and Kniseley, 1974). Samples are injected in a liquid state in the instrument, and the solution is turned to an aerosol in a nebulizer before reaching the central channel of the plasma. Within the plasma, the aerosol is quickly vaporized at such high temperatures liberating the analyte elements as free atoms. Free atoms and ions in the plasma are promoted to excited states due to energy imparted onto them a result of collisional excitation. The spontaneous relaxation of the exited atoms and ions to the ground state is followed by the emission of photons. The energy associated with these photons is quantized and is characteristically associated with the energy level structure of

the originating atom or ion. Consequently, the photon wavelength can be used to identify the element. The elemental concentration can also be determined due to the direct proportionality with the number of photons generated and hence intensity of the signal.

In this thesis, the ICP elemental analysis were performed on a Thermo Scientific iCAP 6000 series Optical Spectrophotometer with an attached CETAC ASX-520 Autosampler, and the data were collected by iTEVA ICP software.

3.2.3 Dynamic Light Scattering (DLS)

Dynamic light scattering is a commonly used optical technique for the determination of particle size down to diameters of 1 nm. DLS operates on the basic principle of scattered coherent light by analytes in a spatially confined volume of sample(Berne and Pecora, 1976). Moreover, the illumination of particles in suspension with monochromatic light gives rise to waves of scatter light that spreads across all directions, ultimately giving rise to a net scattered light intensity. As the particles in the colloidal solution undergo Brownian motion over time, the relative distance between particles fluctuates thus causing fluctuations in the phase of the scattered light that can contribute to or subtract from the stochastic light intensity signal. Thus, the intensity of the scattered light fluctuates over time. These fluctuations are related to the particles diffusion rate in the solution and can be quantified in a intensity correlation function g2(q,τ), with τ being the time delay and q the scattering vector module. By means of this correlation and by relating it to the electric field the diffusion coefficient of the scatters can be determined (Berne and Pecora, 1976).

$$g2(q,\tau) = exp(-\mathscr{T}\tau) \tag{3.4}$$

Where $\mathscr{T}$ is the decay rate. Ultimately, with the use of the diffusion coefficient, the time-variant intensities can be used to determine the hydrodynamic diameter of the particles in solution. This is achieved based on the Stokes-Einstein which relates the particles hydrodynamic diameter (D_h)to their aleatory motion in a solvent with a particular viscosity (n):

$$D_h = \frac{kT}{3\pi D} \tag{3.5}$$

where k is the Boltzmann constant, T is the temperature in Kelvins and D is the diffusion coefficient of the scatters.

This relationship is valid for single scattered light consequently the samples are significantly diluted prior to DLS analysis. In overly concentrated samples, multiple scattering events occur thus rendering the relationship invalid. Considerably large particles and particle aggregates can also cause signal saturation. Nonetheless, hydrodynamic size determinations are formulated for spherically shaped particles and thus is not directly suitable for the evaluation of other particle structures.

In this thesis, samples for DLS analysis were performed using a Malvern Zetasizer Nano. The results are presented as a plot of Number of particles *vs* Size (d,nm).

Chapter 4

Development of AuStr Based Vehicles for BBB Permeation

4.1 Introduction

Nanoparticles are very promising delivery vehicles for biomedical applications. Importantly, it has been recognized that the interaction of these nanomaterials with the body is greatly influenced by the nanoparticle's properties (Nel et al., 2009b; Sau et al., 2010; Alexandridis, 2011). This opens a window of possibilities to specifically design nanoparticles to carry out precise programmed instructions. It is therefore essential to understand how to tailor different nanoparticle related parameters, including shape, morphology and surface chemistry in order to fine tune this response.

In particular, the loading of targeting proteins on the surface of the nanoparticles should be carried out strategically to optimize packing efficiency and increase the chances of an efficient BBB targeting. Gold nanostars (AuStrs) offer high surface are to volume (SA/V) ratios that can accommodate efficient cargo loading since the

synthesis parameters that dictate SA/V ratio and surface biofunctionalisation can be appropriately controlled.

Additionally, the geometry and size of the AuStr candidates needs to be controllably tuned in order to understand, and ultimately optimize, the effect of morphology in BBB penetration ability (described in chapter 5). This chapter reports on the synthesis, functionalization and characterization of AuStrs with complex morphology, coated with transferrin for effective BBB targeting and penetration.

Protein-AuStr constructs have been used for multiple applications, however the way in which the protein binds to the spiky surface was not explored (Li et al., 2015a; Sasidharan et al., 2016; Dam et al., 2014a).

In this study, we aim to synthesise of a matrix of AuStrs with a highly controllable spectrum of properties including size, surface spikiness and spike morphology. After gaining morphological control of the nanoparticle's surface area to volume ratio, we aim to optimize the surface loading of the gold nanostructures through the control of the protein reacting conditions.

As proof-of-concept, surface functionalization with transferrin protein, was carried out to test the level of control over the amount of protein loading, and the protein conformation on the star surface. Tf receptors are typically overexpressed on cancer and brain endothelial cells and is thus a promising molecule for targeting applications (Clark and Davis, 2015). Initially, the procedure is tested on conventional isotropic gold nanospheres (AuNPs) produced by the standard citrate reduction method and finally translated to the anisotropic AuStrs (Turkevich et al., 1951; Frens, 1973).

4.2 Experimental

4.2.1 Materials:

All the chemicals used were purchased from Sigma-Aldrich unless otherwise stated. Milli-Q water was used in all experiments.

4.2.2 Gold nanostructure synthesis:

Standard procedures for seed-mediated synthesis were used to prepare the nanoparticles (Frens, 1973; Cheng et al., 2012; Ramsey et al., 2015). Briefly, 100 mL of a 1 mM $HAuCl_4$ aqueous solution were boiled under stirring followed by the rapid addition of 10 mL of a 38.8 mM solution of sodium citrate trihydrate. Following a series of colour changes the solution stabilised with a deed ruby red colour. This synthesis yielded monodispersed 12 nm gold nanoparticles here on referred to as seed solution. For the synthesis of personalised gold nanostars, different volumes of seed were allowed to react in the presence of $HAuCl_4$, $AgNO_3$ and ascorbic acid in conditions specified in the summary Figure 4.40, Graphs I to V. Gold nanostructures were conjugated with transferrin *via* a thiol group and salt titration was used to test the stability of the resulting bioconstructs.

4.2.3 AuStr and AuNP Characterization:

The size and morphology of the nanoparticles at different synthetic conditions were assessed by using a JEOL JEM-2100F and a FEI Titan TEM, at the acceleration voltage of 200 kV and 300 kV respectively. Negative staining of the nanoparticles was performed using 2% (w/v) solution of uranyl acetate to reveal the presence of a transferrin corona on the surface of the nanoparticle drop-casted onto

300 mesh copper grids (Agar Scientific), coated with holey carbon film. The nanoparticle hydrodynamic diameter was measured in suspension using Dynamic Light Scattering (DLS, Malvern Zetasizer Nano) operated at 25 °C. In this work, Image J was used to manually measure nanoparticles and nanoparticle related parameters following an initial calibration of the pixels from TEM and SEM micrographs into their corresponding length in nm. Image J is an open source imaging processing software designed for multidimensional images.

4.2.4 Elemental Quantification:

The elemental concentration of gold in the samples was measured by inductively coupled plasma optical emission spectrometry (ICP-OES, Thermo Scientific iCAP 6000 series). The nanoparticles were dissolved in Aqua-Regia prepared by mixing hydrochloric acid and nitric acid in a 3:1 ratio. The volume of the solution was brought to a final volume of 10 mL with Milli-Q water.

4.2.5 Chapter contributions

High Performance Liquid Chromatography analysis were performed with the assistance of Dr Lisa Haigh from the Chemistry Department. EDS elemental analysis were performed with the assistance of Dr Mahmoud Ardakani from the Harvey Flowers characterisation suit, Materials Department. Atomic Force Microscopy analysis were performed with the assistance of Dr. Jiahui Qi. Thermogravimetric analysis were performed with the assistance of Dr. Richard Sweeney.

4.3 Results: Nanoparticle Synthesis

In this study, the anisotropic growth of AuStrs was investigated under different reaction conditions. The nanostar size and morphology were tuned through variations of reacting conditions, namely total amount of metal precursor, ratio between metallic species (Au:Ag), reducing agent concentration, seed addition for a mediated synthesis, and hydrochloric acid (HCl) concentration.

4.3.1 Effect of total amount of metal precursor

Initially, the AuStrs were synthesized in a seedless one-pot reaction based on an approach adapted from previous reports (Cheng et al., 2012; Ramsey et al., 2015). Considering the intended application of the AuStrs, our method does not employ potentially cytotoxic surfactants (*e.g.* CTAB), to ensure biocompatibility.

The effect of the total amount of metal precursor on AuStr synthesis was tested whilst maintaining constant the molar ratios between the reactants and the reaction volume. It is known that the optical response of materials in the nanometer range is dependent on their size and shape. UV/Vis spectroscopy and TEM were therefore used in combination to monitor the effects of reacting conditions on nanoparticle synthesis and to characterize changes in particle size and morphology, respectively.

By changing the $HAuCl_4$ concentration, the AuStrs optical response progressively shifted to the NIR (Figure 4.1), indicating changes to the resulting nanostructures. In fact, TEM of the resulting AuStrs (Figure 4.2 a to d) revealed that the average AuStr size increased from 36 ± 2 to 125 ± 6 nm when the concentration of $HAuCl_4$ in the mixture increased from 0.05 to 0.2 mM (Figure 4.2 e).

At $HAuCl_4$ concentrations as low as 0.05 mM, the synthesis yielded mainly spherical nanoparticles with rough surfaces (Figure 4.2 a). When spikes were

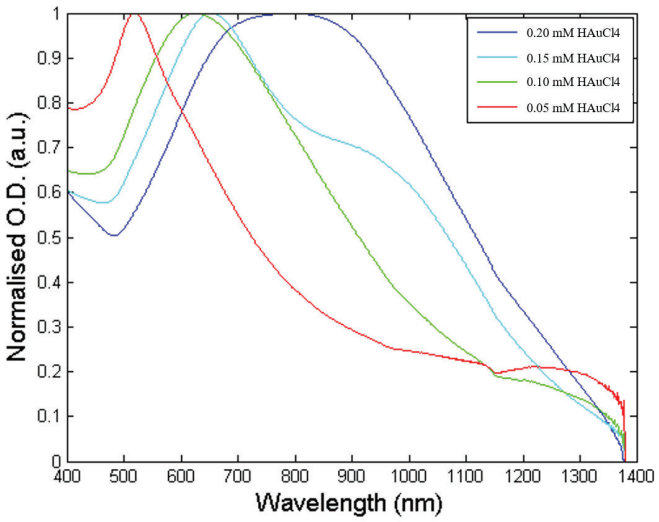


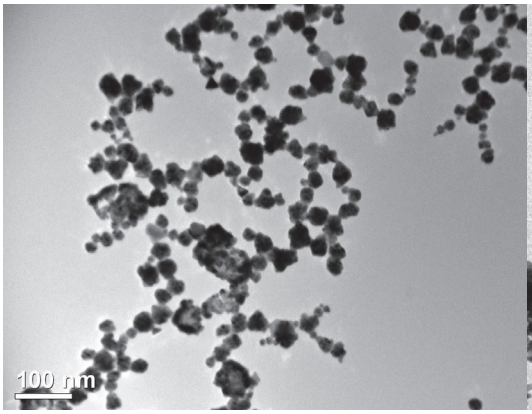
Figure 4.1: UV-VIS spectra of AuStrs synthesised at different $HAuCl_4$ concentrations.

present (here defined as protrusions longer than 7 nm), these did not exceed one spike per particle. For $HAuCl_4$ concentration of 0.1 mM, the resulting particles showed several spikes with mainly round tips (Figure 4.2 b). Increasing the concentration of gold from this critical point generated AuStrs with a more pronounced morphology and spikes of higher aspect ratio (Figure 4.2 c and d).

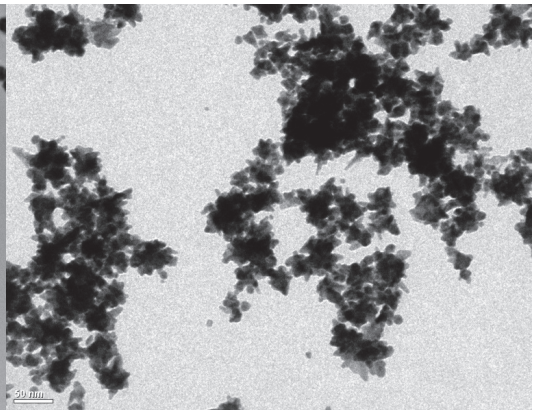
However, due to the inherent variability associated with this synthesis method, the AuStrs are subject to size dispersity (Figure 4.2 a to d). To confirm that the average AuStr size could be controlled by varying the $HAuCl_4$ concentration, the mean size of the samples were statistically analyzed using ANOVA (Figure 4.2 e). The test showed sufficient evidence indicating that the mean size of the AuStrs is statically different between the samples reacted at different $HAuCl_4$ concentrations ($p<0.05$). A tukey-kramer *post hoc* comparison test was used to complement the ANOVA to understand which samples differed from one another. The test revealed that all sample means were statistically different from each other.

These results indicate that $HAuCl_4$ concentration can be varied to control AuStr

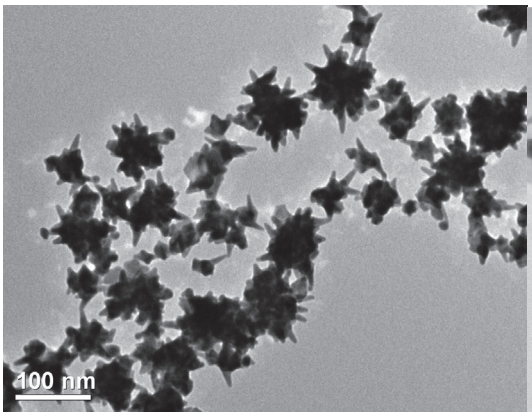
size. However, the main limitation of the one-pot synthesis method is the sample polydispersity. Monodispersity is particularly important in the nanometer regime as the size of the nanostructure has a considerable effect on its optical/physical properties. Additionally, for biomedical applications in which nanoparticles are required to pass through the cell membrane, size uniformity is of great importance.



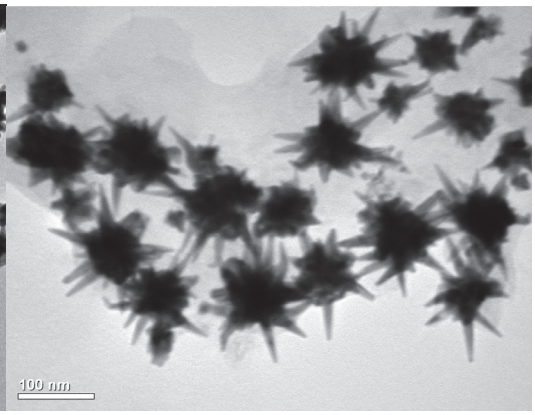
(a) 0.05 mM $HAuCl_4$



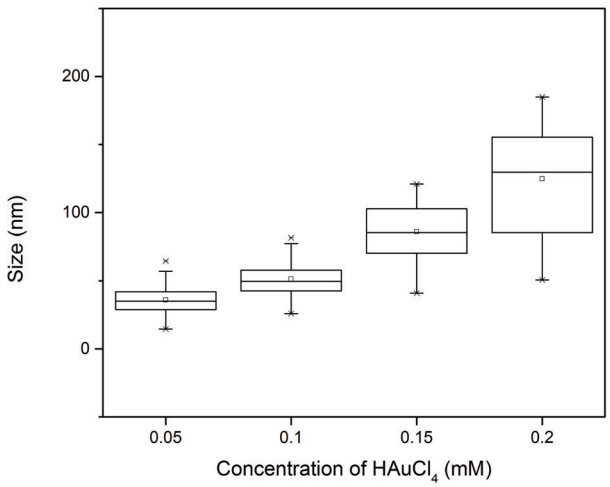
(b) 0.10 mM $HAuCl_4$



(c) 0.15 mM $HAuCl_4$



(d) 0.20 mM $HAuCl_4$



(e) Size of nanoparticles as a function of $HAuCl_4$

Figure 4.2: TEM images of AuStrs synthesized with different concentrations of $HAuCl_4$: (a) 0.05, (b) 0.10, (c) 0.15 and (d) 0.20 mM. Graph (e) shows the AuStr size distribution as a function of $HAuCl_4$ concentration. The size of the nanoparticles was determined using the image J software.

4.3.2 Effect of metallic precursor ratio (Au:Ag)

Subsequently, the effect of changing the Au:Ag ratio was studied. The Au:Ag ratio was varied across a range of values, and the reaction was studied by UV/Vis spectroscopy as shown in Figure 4.3.

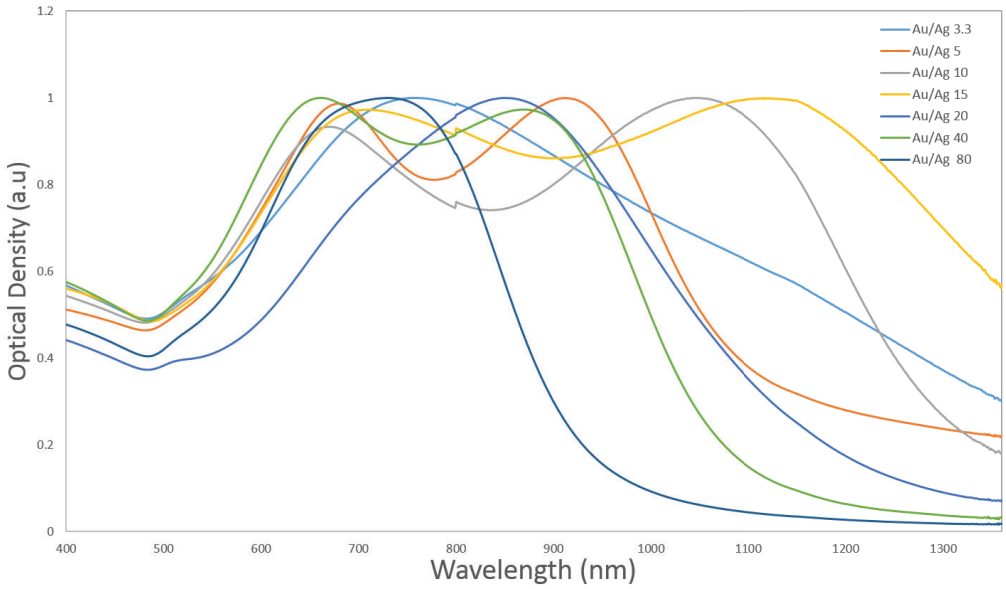
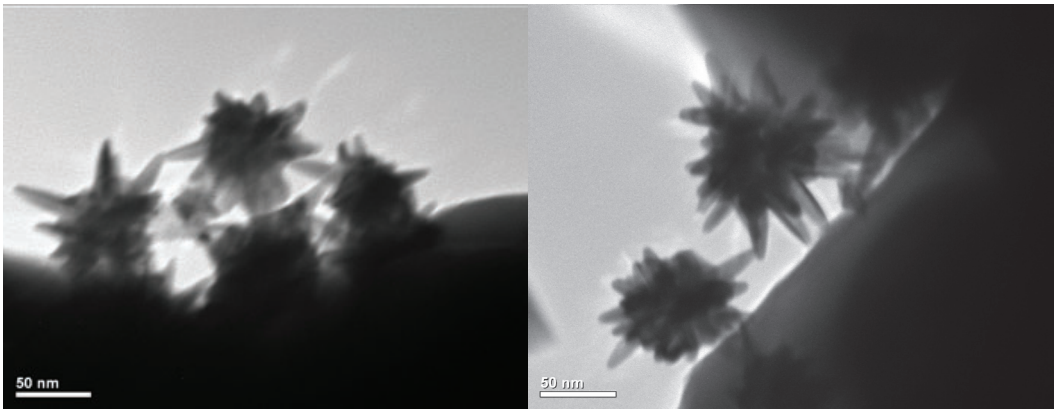


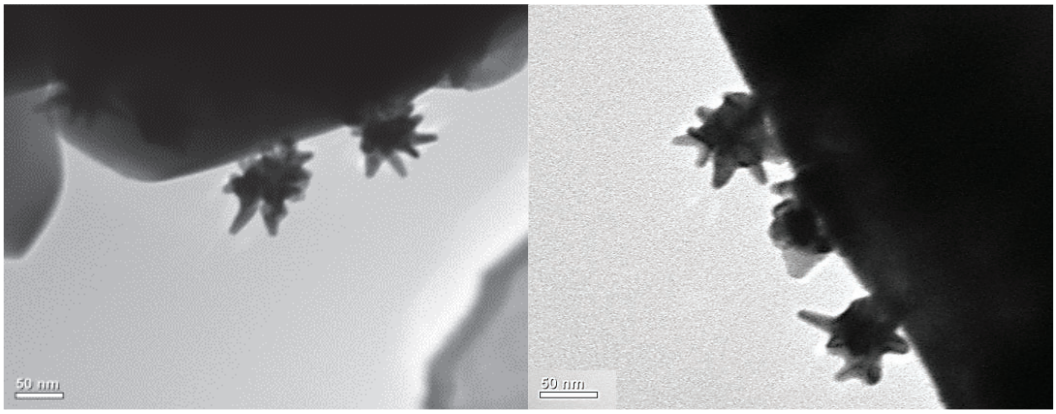
Figure 4.3: UV-Vis spectra of nanostars synthesised at different gold to silver ratios.

When increasing the Au:Ag ratio from 3.3:1 to 5:1, two surface plasmon resonance (SPR) peaks were observed in the spectra of the AuStrs, which correspond to the transverse and longitudinal modes of the core and elongated AuStr tips (Xie et al., 2017), respectively. Increase of the Au:Ag ratios to 10:1 and 15:1, caused the spectra to red-shift. Above the ratio of 15, the AuStr spectra blue-shifted. Previous studies have shown that longitudinal plasmonic mode red-shifts can be linked to changes in the particle morphology (El-Brolossy et al., 2008).

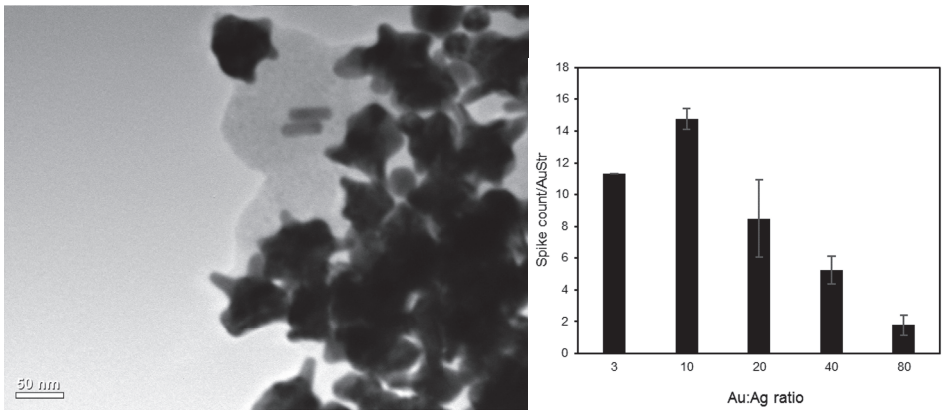
The morphology of the nanostars was investigated by TEM revealing that increasing the proportion of silver in the reaction mixture increased the spike density per particle (Figure 4.4 f). Stars synthesized at Au:Ag of 10:1 (Figure 4.4 b) were particularly spiky with an average of 14 spikes counted per AuStr, measured on the 2D TEM images using Image J. Conversely, when the Au:Ag ratio increased above 10:1, the number, size and aspect ratio of the spikes on the AuStr surface decreased dramatically. At the maximum Au:Ag ratio of 80:1 (Figure 4.4 e), AuStrs with a less irregular shape were observed containing less than 2 cross-sectional spikes per AuStr.



(a) Au:Ag of 3:1 (b) Au:Ag of 10:1



(c) Au:Ag of 20:1 (d) Au:Ag of 40:1



(e) Au:Ag of 80:1 (f) Spike count per AuStr

Figure 4.4: Bright field TEM images of AuStrs synthesised at different Au:Ag ratios of 3 (a), 10 (b), 20 (c), 40 (d) and 80:1 (e). Graph (f) shows the spike count per AuStr as a function of Au:Ag ratio. The nanostructures spike count was analysed using the image J software.

4.3.3 Effect of seed addition for a mediated synthesis

Whilst the one pot synthesis approach provides a high yield of star shaped nanoparticles, these vary in size and are not trivially separated by centrifugation.

Subsequently, pre-formed 12 nm gold citrate seeds were introduced to restrict the nucleation events, and encourage subsequent particle growth onto the surface of the gold seeds (Frens, 1973; Jana et al., 2001). The reaction was monitored by UV-Vis spectroscopy, as shown in figure 4.5. TEM of AuStr samples before (Figure 4.6 a) and after (Figure 4.6 b) seed addition revealed that the seeds clearly contributed towards the size homogenization of the nanostars, indicating that prolonged nucleation in the 1 pot method was responsible for the polydispersity (Figure 4.6 c).

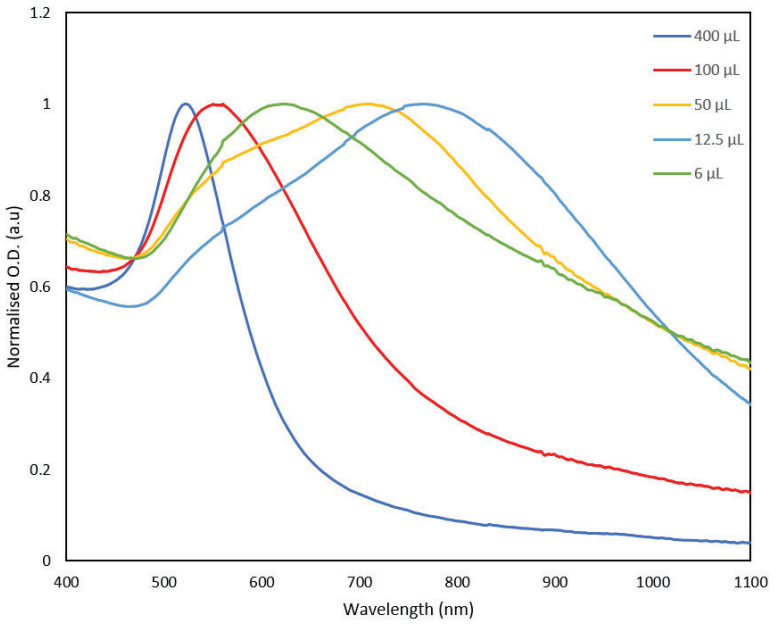
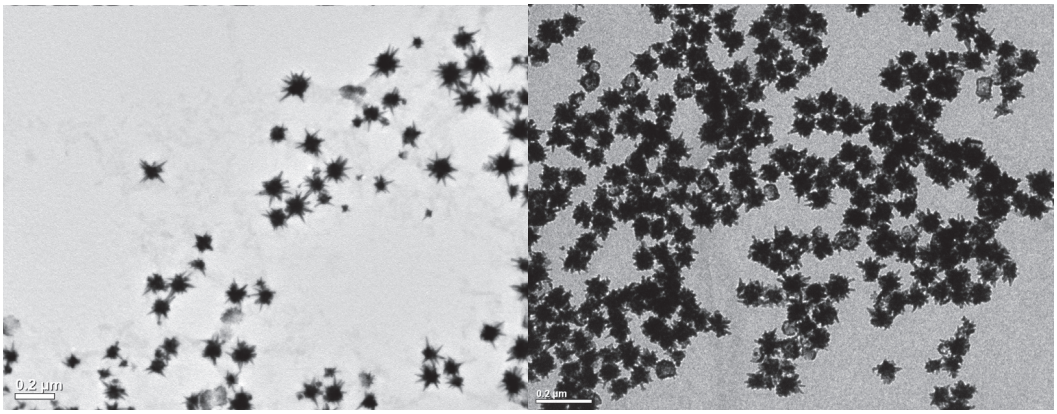
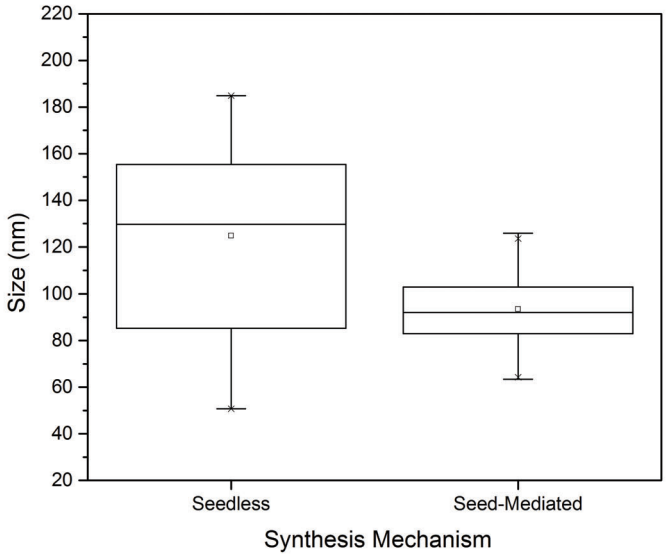


Figure 4.5: UV-Vis spectra of AuStrs synthesised with different volumes of seed



(a) 0.20 mM $HAuCl_4$ (b) 0.20 mM $HAuCl_4$+seeds

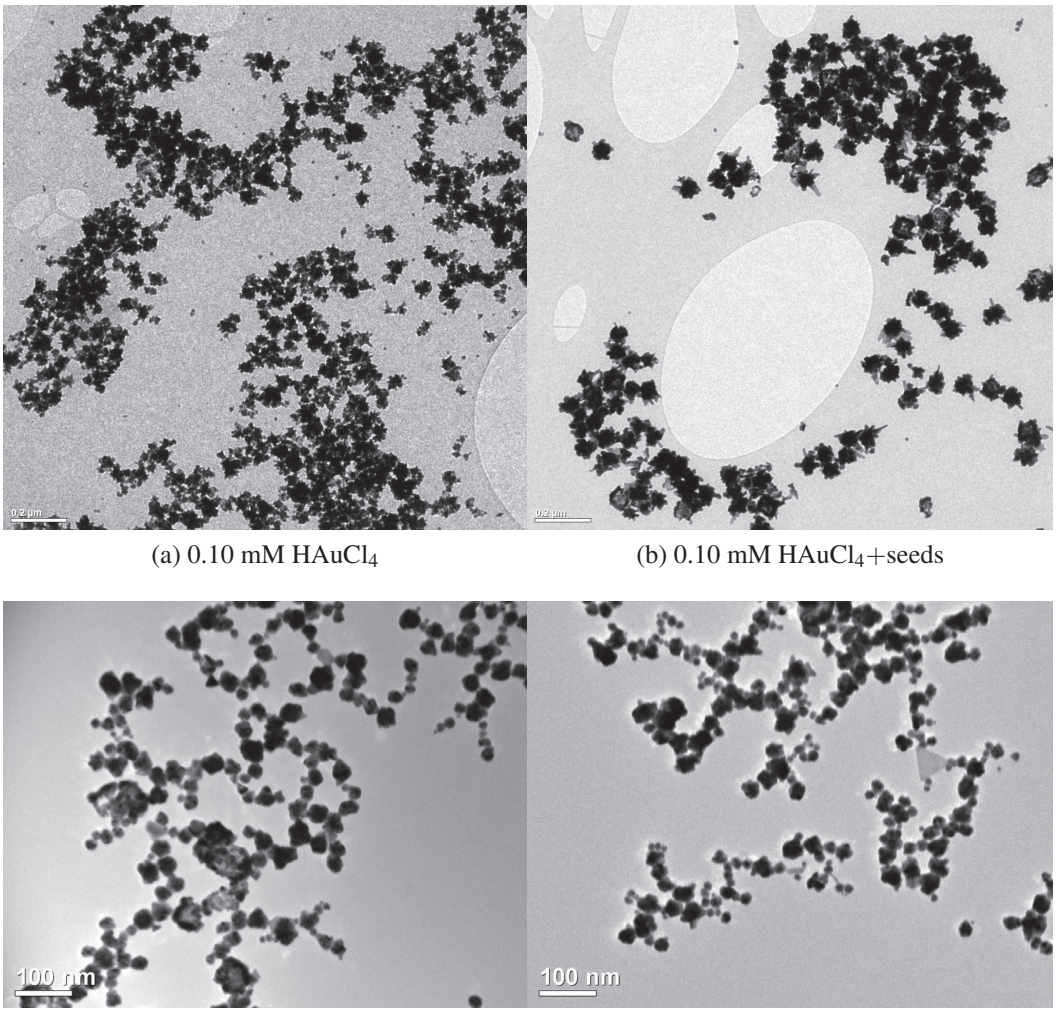


(c) size distributions

Figure 4.6: Bright field TEM images of AuStrs synthesised at 0.2 mM $HAuCl_4$ concentration in the absence (a) or presence (b) of gold seeds. Graph (c) shows the size distribution of nanostructures as a function of the seedless or seed-mediated synthesis mechanism . The nanostructures size distribution was analysed using the image J software.

The addition of seeds had a similar effect in improving the sample homogeneity for AuStrs synthesised at lower gold concentrations (0.10mM $HAuCl_4$ a and b)as shown in (Figure 4.7). However, for $HAuCl_4$ concentrations below 0.10 mM the

sample homogeneity did not improve, possibly due to the low amounts of metal precursor. TEM micrographs of AuStrs synthesised at very low $HAuCl_4$ concentrations of 0.05 mM are shown in Figure 4.7 before (Figure 4.7 c) and after (Figure 4.7 d) seed addition .

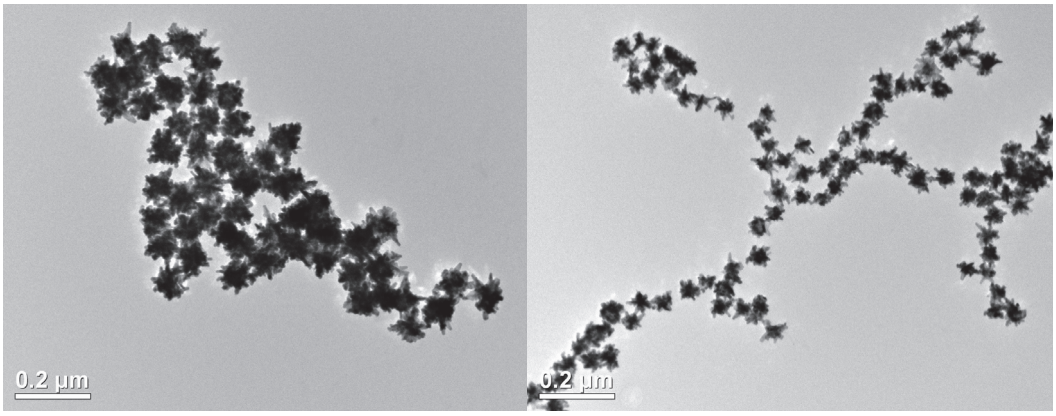


(a) 0.10 mM $HAuCl_4$ (b) 0.10 mM $HAuCl_4$+seeds

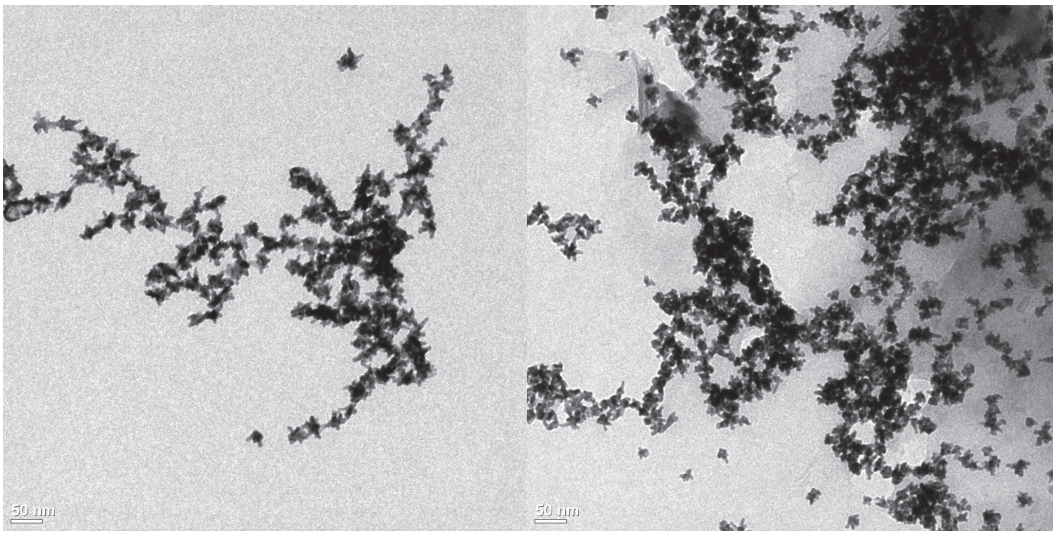
(c) 0.05 mM $HAuCl_4$ (d) 0.05 mM $HAuCl_4$+seeds

Figure 4.7: Bright field TEM images of AuStrs synthesised at 0.1 mM $HAuCl_4$ concentrations in the absence (a) or presence (b) of gold seeds. TEM images AuStrs synthesised at 0.05 mM $HAuCl_4$ concentrations in the absence (c) or presence (d) of gold seeds.

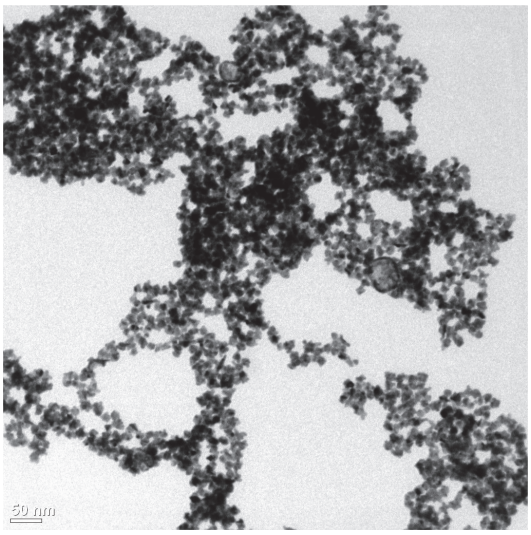
The nanostructure size was effectively tuned by varying the ratio of seeds to metal precursor (Figure 4.8). This size tunability reached a limit when the AuStr size approached the size of the seed. Thus, indicating that the availability of the metal precursors becomes a limiting factor in the reaction with increasing amount of seeds.



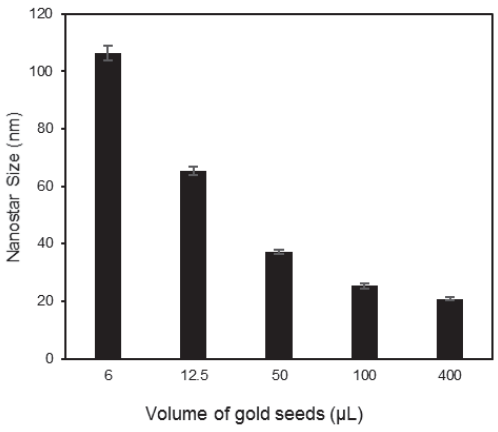
(a) 6 μL of seeds (100 nm AuStr) (b) 12.5 μL of seeds (50 nm AuStr)



(c) 50 μL of seeds (35 nm AuStr) (d) 100 μL of seeds (25nm AuStr)



(e) 400 μL of seeds (20 nm AuStr)



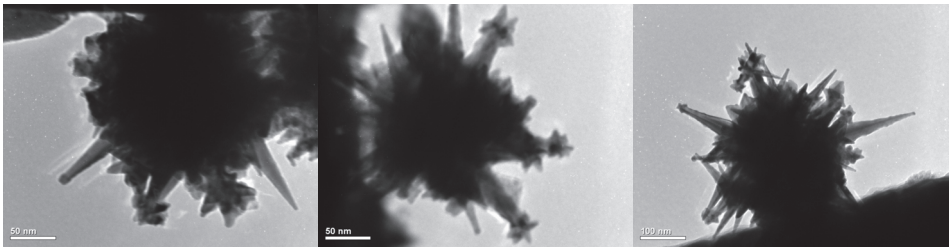
(f) Size distribution of the AuStrs

Figure 4.8: Bright field TEM images of AuStrs synthesised with increasing seed solution volumes of 6 (a), 12.5 (b), 50 (c), 100 (d) and 400 (e) μL. Graph (f) shows the size distribution of the AuStrs as a function of the seed volume. The nanostructures size distribution was analysed using the image J software.

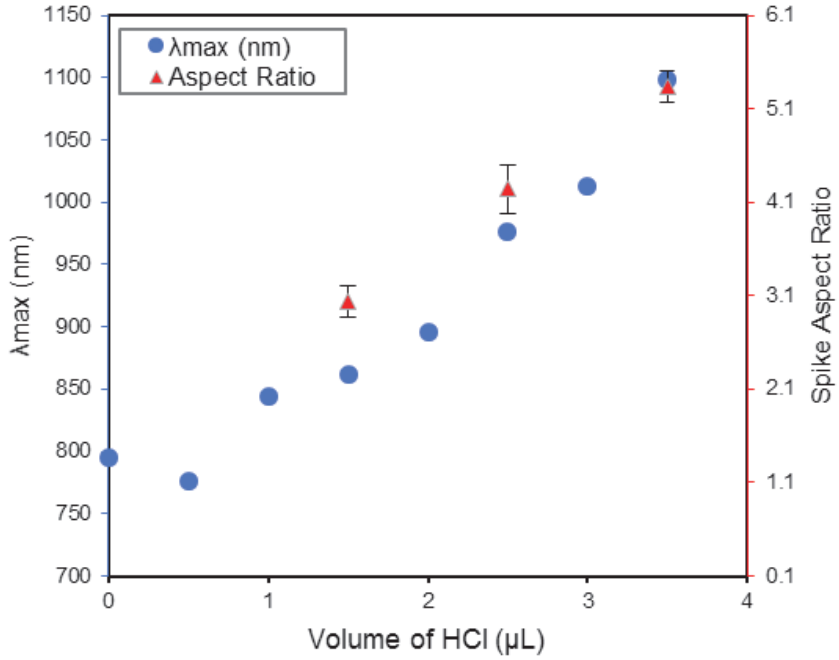
4.3.4 Effect of hydrochloric acid (HCl) concentration

Finally, hydrochloric acid (HCl) was introduced to the reaction to further fine tune the crystalographic growth (Grzelczak et al., 2008). The nanostar synthesis reaction was performed in the presence of increasing volumes of HCl and the resulting samples were analysed by TEM and UV-Vis (Figure 4.9).

The presence of HCl significantly changed the spike morphology (Figure 4.9 a, b and c). In the absence of HCl (Figure 4.4 a), the nanostars contained monocrystal branches that protruded from the core and became gradually thinner, forming spikes. In the presence of HCl (Figure 4.9 b), the spike morphology is altered and some monocrystals exhibit secondary spikes with a "crown-like" morphology. The spike *aspect ratio* also increases in the presence of HCl (Figure 4.9 a -c) and noticeably the maximum absorbance wavelength (λ_{max}) shifted towards the near infrared region (Figure 4.9 d).



(a) 1.5 μL HCl (b) 2.5 μL HCl (c) 3.5 μL HCl



(d)

Figure 4.9: Bright field TEM images of AuStrs synthesised with increasing volumes of 1N Hydrochloric acid of 1.5 (a), 2.5 (b) and 3.5 (c) μL. Graph (d) shows the peak wavelength of the AuStr (λmax) and spike *aspect ratio* as a function of volume of HCl. The nanostructures spike aspect ratio was analysed using the image J software.

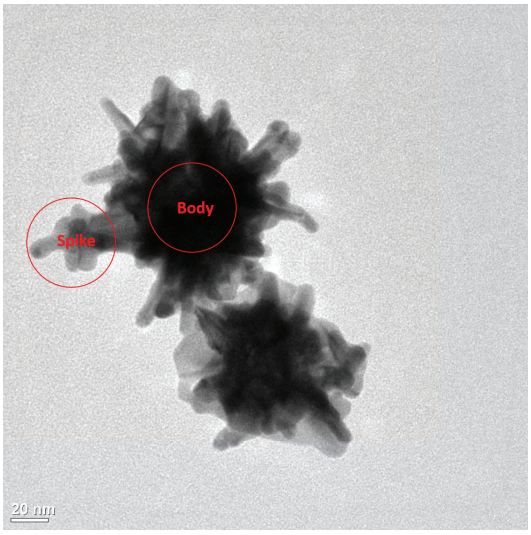
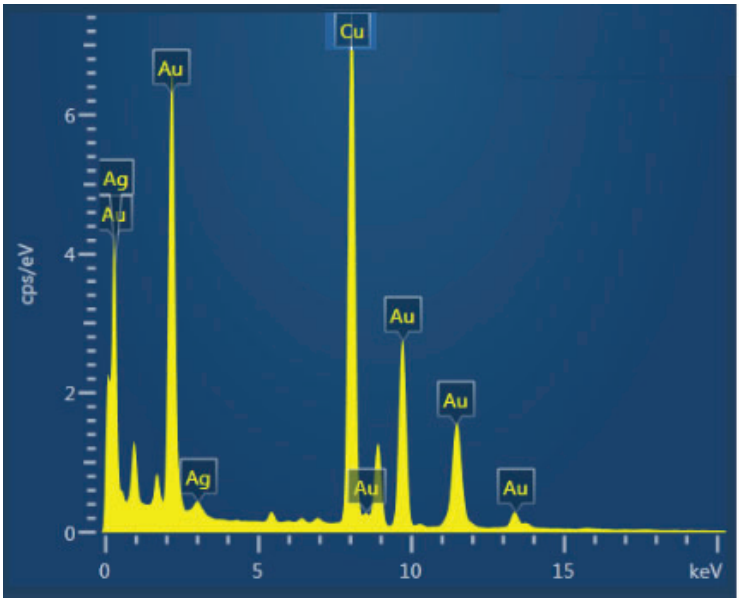


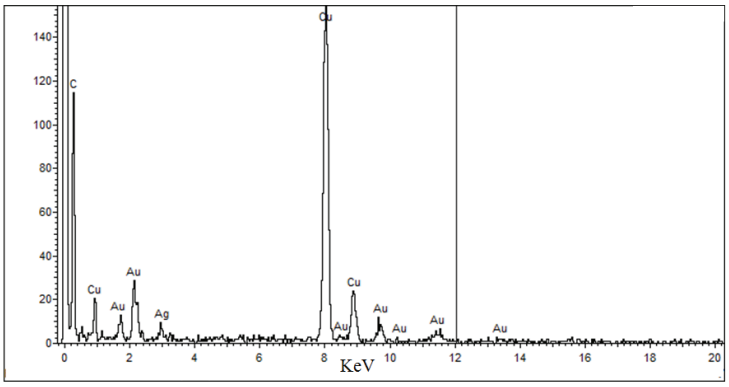
Figure 4.10: Bright field TEM images of AuStrs depicting both the secondary spike and body regions.

4.3.5 Nanostar Elemental Analysis

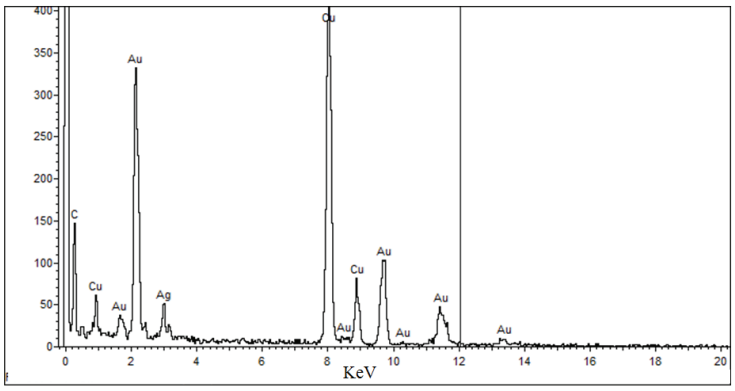
The elemental composition of the AuStr spike and body regions (Figure 4.10) were analyzed by using spatially resolved Energy Dispersive X-Ray Spectroscopy (EDS) in the TEM. The results revealed that the AuStr body, primary and secondary spikes are all primarily composed of gold (93.17 $\pm$ 0.65 atomic %) with silver making up the minor component (6.83 $\pm$ 0.65 atomic %) (Figure 4.11). The percentage of silver of the AuStr branches was similar to that reported in the percent composition of nanorods (2-4.5%) synthesised in the presence of silver and gold precursors (Orendorff and Murphy, 2006). This elemental analysis was performed for the optimum 100 nm AuStrs and future systematic analysis may be performed to understand how the atomic composition varies with the different reaction parameters.



(a) AuStr



(b) Secondary Spike



(c) Body

Figure 4.11: EDS spectra of AuStrs (a) AuStr spike(b) and AuStr body (c) synthesised in the presence of HCl. Both spike and body regions have a similar composition of gold and silver. The samples are supported in a TEM copper grid as indicated by the presence of a Cu peak

To further elucidate the elemental distribution within the nanoparticle, an elemental mapping was carried out in STEM mode (Figure 4.12). In accordance to the atomic quantitative analysis, the map shows a higher density of gold atoms in comparison to that of silver. Both silver and gold can be found in the nanoparticles body as well as on its spikes.

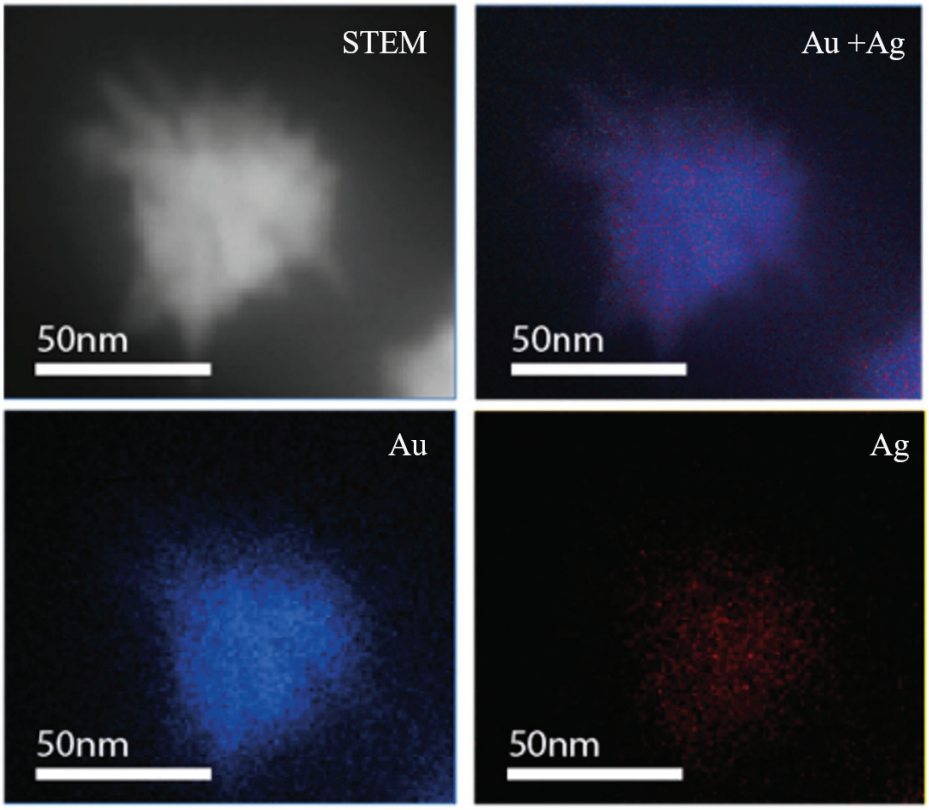


Figure 4.12: STEM-EDS elemental mapping of AuStrs showing the spatial distribution of Au (blue) and Ag (red) elements in the nanostructure.

4.3.6 Experimental characterization of nanostar Au mass

Given the irregular shape of the nanostars there is no easy method to convert the particles dimensions into their equivalent mass. Hence, we proceeded to develop an experimental method to determine the amount of gold per star to thoroughly characterize the nanovehicle. For the reported complex shape nanoparticles we produced a self-assembled monolayer of nanostars in MPTMS (mercaptopropyl trimethoxysilane) silanized glass substrates.

Formation of a nanostar monolayer on 3-Mercaptopropyl)trimethoxy silane (MPTS) functionalised glass Initially the substrate is modified by silanization with an alkoxysilane which provides functionality to the glass surface according to its terminal group. This functionalisation allows the glass to establish a chemical link with the gold nanostars. For silanisation MPTS (3-Mercaptopropyl)trimethoxy silane) was used.

Prior to silanization, the glass is thoroughly cleaned with piranha solution. This is believed to increase the surface density of hydroxyl groups (Bai and Cheng, 2008). The glass substrates were modified by immersing them vertically in 5% MPTS solution (Sigma). MPTS is composed by an organofunctional group and a hydrolysable group which can interact with hydroxyl terminated substrate (Figure 4.13).

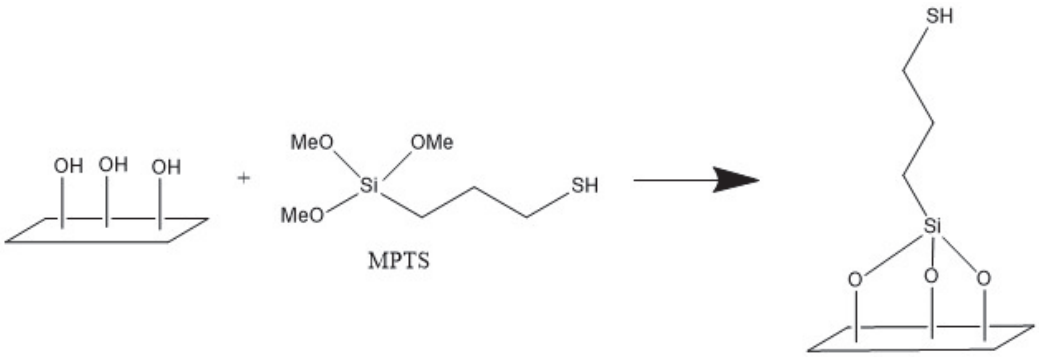


Figure 4.13: Schematic representation of the substrate silanization with MPTS molecules. Scheme drawn in ChemDraw software

The substrates were subsequently incubated in a nanostar solution to promote binding of the nanoparticles to the substrates surface (Figure 4.14).

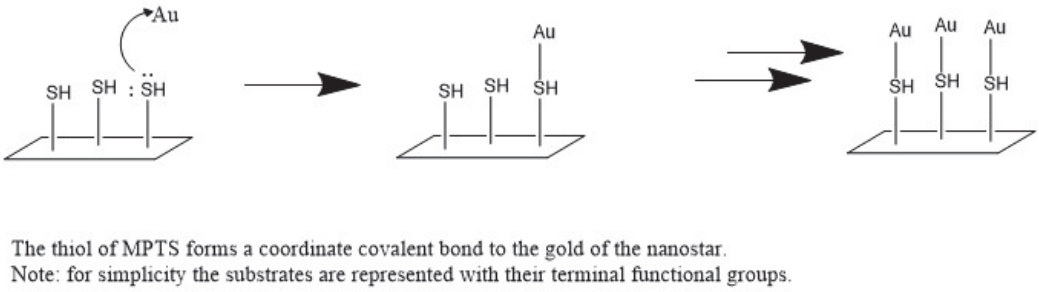
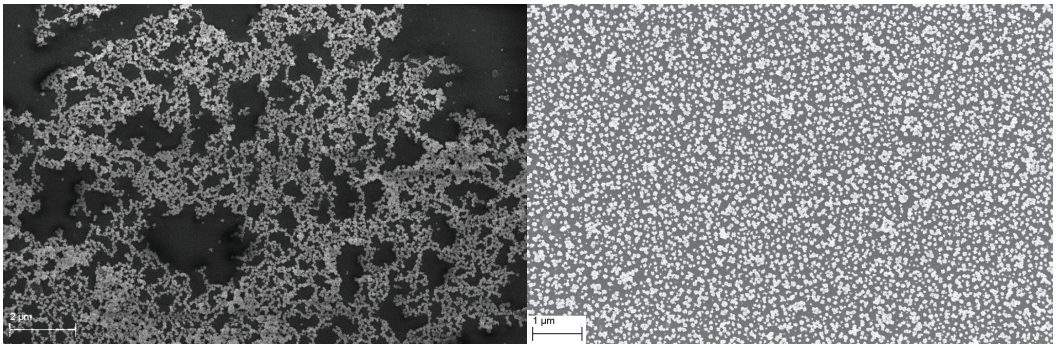
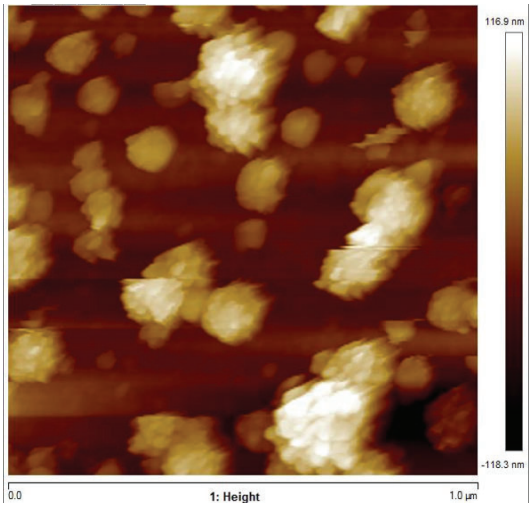


Figure 4.14: Schematic representation of the self-assembly of gold nanoparticles on the thiol functionalized substrate.Scheme drawn in ChemDraw software

AuStrs successfully self-assembled on to the glass substrates as shown by SEM imaging (Figure 4.15 a). It was possible to change the density of the gold film on the substrate by modifying the substrate incubation time in nanostar solution. The best substrate coverage with AuStrs was obtained when incubation in nanostar solution, was allowed to occur for 48hours (Figure 4.15 b). The density of star coverage following 48 hours was determined to be as high as 30%. Further systematic analysis including more incubation periods may be performed in future work to understand how surface coverage varies as a function of time.



(a) 24 hours (b) 48 hours



(c) AFM of Nanostars on MPTS layer

Figure 4.15: Surface characterization of 100nm AuStr substrates. SEM images of 100 nm AuStr monolayers formed on glass following 24 (a) and 48 (b) hours incubation in nanoparticle solution. Atomic Force Micrograph (AFM) of the 48 hour substrate surface.

Finally, to determine the amount of gold per AuStr, the assemblies were dissolved in Aqua-regia and the amount of gold on the substrates was assessed by inductively coupled plasma optical emission spectrometry (ICP-OES). The gold mass per AuStr was obtained by dividing the total amount of gold dissolved from the substrate by the number of particles in the surface of the substrate obtained from imaging. Using this method, it was determined that the average gold mass for the optimum 100 nm AuStrs was $2.4 \pm 0.1 \times 10^{-9} \mu$g per nanostar.

4.4 Results: Nanoparticle surface stabilization

4.4.1 Passivation of the gold nanoparticles by PEGylation

To minimize aggregation events and maintain the AuStr samples in a highly dispersed state, the as-synthesized gold nanostars were stabilised with polyethylene glycol (PEG)-based thiols. The AuStrs were reacted in the presence of a large excess of PEG molecules. The binding of the polymer was based on the attachment of the PEG thiol group to the gold surface.

To test whether the surface of the nanoparticles was successfully modified by this organic layer thermogravimetric analysis (TGA) was performed for the optimum 100 nm AuStrs (Figure 4.16). In this procedure, a known mass of dry AuStr sample (1.35 mg) is placed in a controlled atmosphere (Nitrogen and oxygen) and the sample mass monitored as the temperature is ramped up to 800 °C at a heating rate of 10°C/min. A 12% mass change was registered and associated to the degradation of the PEG polymer. PEGylation was therefore deemed successfully.

TEM imaging confirmed a highly dispersed state of the PEGylated AuStrs (Figure 4.17).

For active targeting applications the AuStrs need to be conjugated with biomolecules, *e.g.* proteins, capable of recognizing the tissue to be targeted. The following sections describe the bioconjugation of AuNPs and AuStrs with the protein transferrin. Initially, the conjugation was studied in simple spherical gold nanoparticles and subsequently applied to AuStrs.

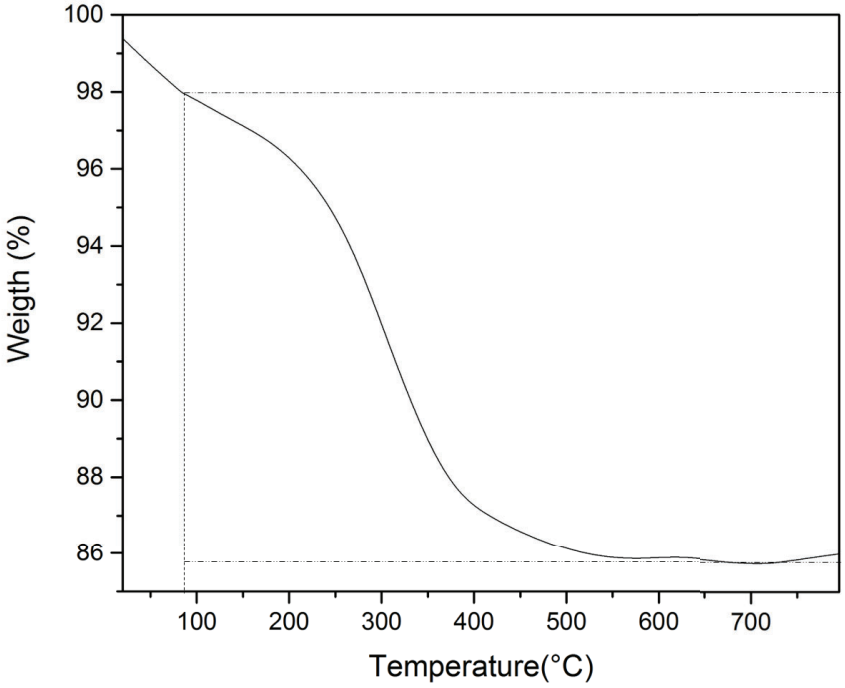


Figure 4.16: TGA curve of 100 nm AuStrs conjugated with polyethylene glycol polymer. The graph shows two mass loss regions, the first (20-90 °C) corresponding to solvent loss and the second (90-650 °C) corresponding to PEG degradation, followed by the plateau of the curve, indicating no further mass changes.

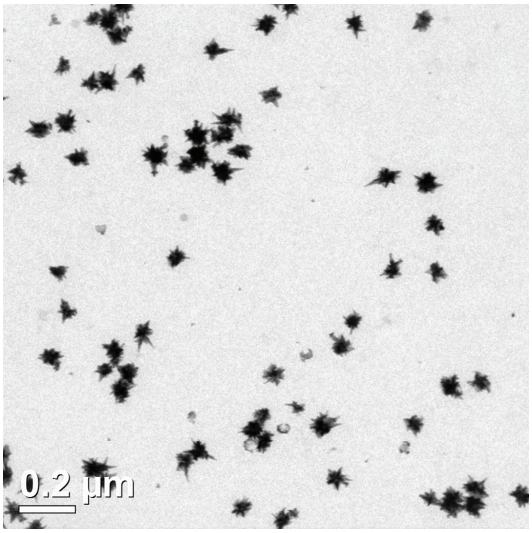


Figure 4.17: Bright field TEM image of monodisperse 100 nm PEG-AuStr.

4.4.2 Bioconjugation of the gold nanoparticles with transferrin protein

Transferrin PEGylation for nanoparticle attachment

AuStrs were modified with transferrin for targeting the transferrin receptors expressed on the surface of the BBB endothelial cells. Transferrin attachment to the surface of the AuStrs has been shown to be achievable by either a passive or covalent manner (Jazayeri et al., 2016). Passive protein adsorption relies mainly on electrostatic interactions between the protein and gold surface. However, proteins adsorbed in this manner can be easily displaced from the Au surface. Hence covalent protein attachment provides a more stable alternative as it relies on a permanent bond to attach the protein the nanoparticle surface.

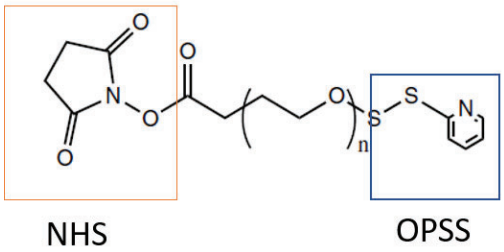


Figure 4.18: Chemical structure of the NHS-PEG-OPSS molecule with the orange square marking the NHS (N-hydroxysuccinimide) group and blue square the OPSS group (orthopyridyl disulfide)

For conjugating the protein to the surface of the nanoparticle, transferrin was directly modified with the heterobifunctional PEG linker (PEG containing two different end groups) alpha-Pyridyl-2-disulfid-omega-carboxy succinimidyl ester poly(ethylene glycol) (NHS-PEG$_{5K}$-OPSS) with a molecular weigth of 5 kDa (Figure 4.18). Modification of the protein with PEG not only allows the immobilization of the protein to the nanoparticle surface but may also maximise the accessibility

of surface receptors to the immobilised protein.

Initially, PEG is attached to the protein *via* the reaction of the transferrin primary amines on lysine groups with the PEG's N-hydroxysuccinimide (NHS) ester group (Bellocq et al., 2003). The remaining PEG terminal group, orthopyridyl disulfide (OPSS), attaches to the nanoparticles surface *via* gold thiol dative bonding.

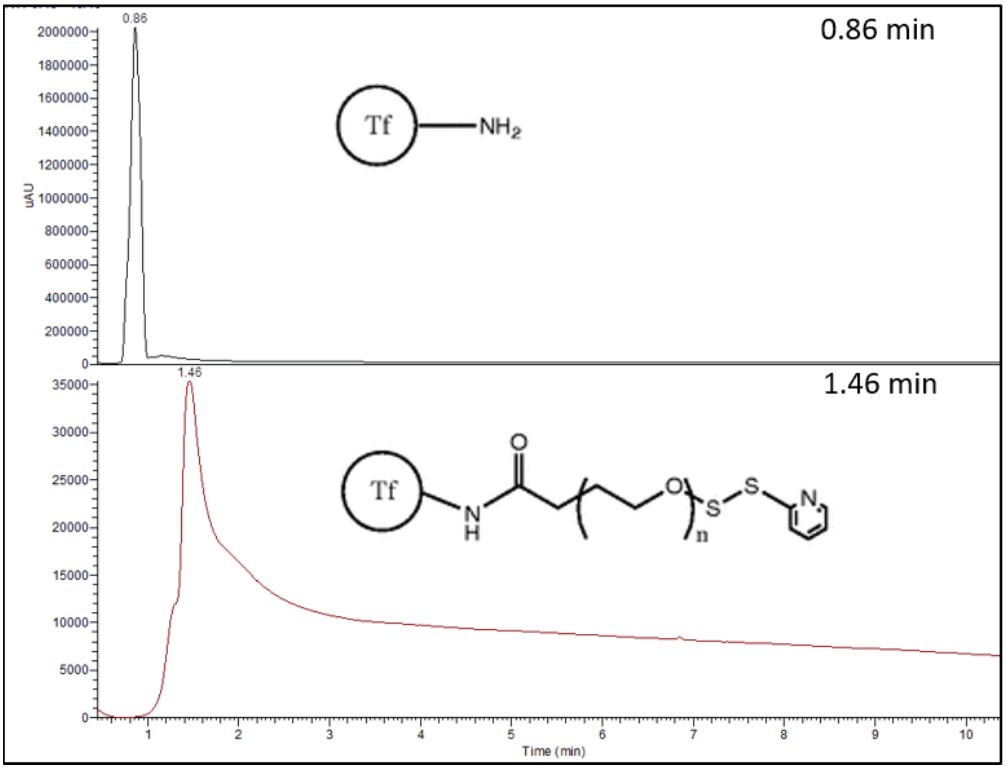


Figure 4.19: High perfomace liquid chromatography (HPLC) analysis showing successful protein PEGylation. Top graph shows the elution time of non PEGylated transferrin control and bottom graph shows the elution time of PEGylated Tf samples. The signal was recorded at 280 nm using a UV-Vis detector.

Prior to nanoparticle attachment, the outcome of protein PEGylation reaction is confirmed and characterised by high performance liquid chromatography analysis. The modified transferrin was run against an unmodified transferrin reference under the same operating conditions and the signal was recorded at 280 nm using a UV-Vis detector. The elution times of the control and reference samples are expected to

differ when the PEGylation reaction is successful. Conversely, if the modification procedure is unsuccessful the retention time of the samples should coincide. Figure 4.19 demonstrates that not only were the elution times between the sample and the reference different but also the modified protein elution profile was consistent with a mono-pegylated protein profile (Wiley et al., 2013). The PEGylation state is important as higher states (*e.g.* di-PEGylation) can induce a small degree of aggregation (Wiley et al., 2013).

Following the successful protein preparation for nanoparticle attachment, it is important to determine how much protein is needed in a bioconjugation reaction to form stable transferrin-gold nanostructures bioconjugates.

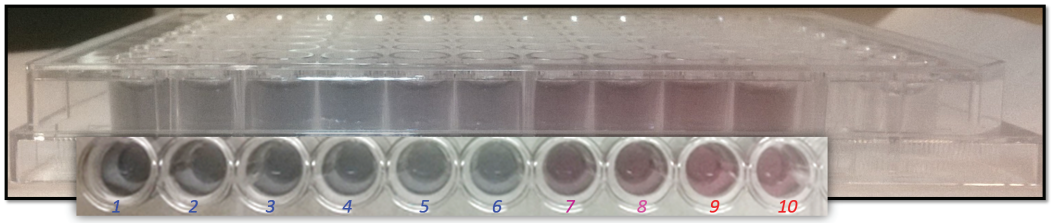
Determining critical tranferrin concentration for bioconjugation with AuNPs

Spherical gold nanoparticles are extensively characterized systems making them suitable models for the study of bioconjugation reactions in the absence of surface spikiness. The bioconjugation reaction of transferrin with nanospheres is conducted in aqueous solution at room temperature under constant stirring to allow the protein to adsorb homogeneously to all the nanoparticles. Transferrin itself is soluble in aqueous solutions, which aids in the prevention of flocculation events. Hypothesizing that appropriately coating nanoparticles with protein can minimize aggregation events, transferrin-gold bioconjugates were prepared, *via* thiol-gold chemistry, at different protein to gold ratios. The bioconjugates stability were evaluated in a high ionic strength solution tested to aggregate control AuNPs, being that the biological environment in which the AuNPs are to be used is also of high ionic strength. In the presence of salt, the electrostatic repulsion between nanoparticles is shielded as the salt ions bind to the particle surface. The neutralization of the surface charges halts particle repulsion, predisposing them to aggregation.

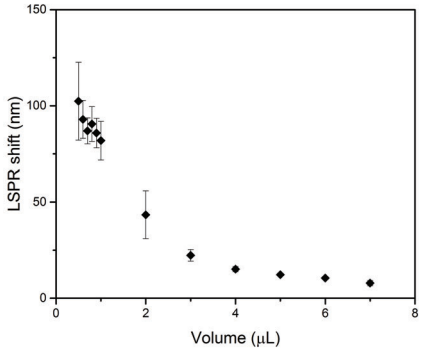
Conversely, an appropriate protein coating is expected to minimize these events because it provides steric hindrance to aggregation as opposed to stabilization based on electrostatic repulsion.

Monodisperse gold nanoparticles have a characteristic ruby red colour, and when aggregated reflect a characteristic blue colour. These changes in colorimetric state can be used to grossly evaluate the stability of the Tf-AuNP conjugates reacted at different protein concentrations (Figure 4.20 a). After stability is reached, the characteristic gold red colour is preserved and from this point, further colorimetric changes are not perceptibly to the naked eye.

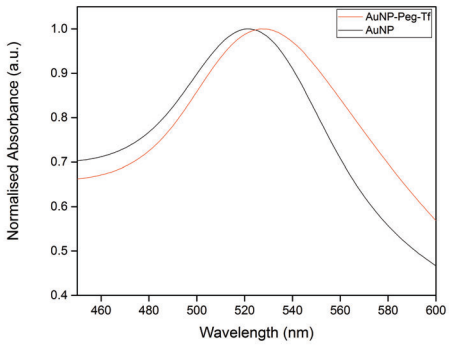
Additionally, the stability of the Tf-AuNP complexes was finely monitored based on how well the complexes were able to preserve their characteristic localized surface plasmon resonance (LSPR) in aggregating salt conditions (Figure 4.20 b). Gold citrate nanoparticles with a size of 12 nm possess a very distinct LSPR peak at 520 nm, allowing changes associated with aggregation events to be easily identified in their spectra (Frens, 1973). Thus, the λ_{max} was used as a measure of stability. The greater the shift in λ_{max}, the more unstable the Tf-AuNP complex. As expected, uncoated AuNP were the most unstable species, showing a $\Delta\lambda_{max}$ of more than 100 nm. The stability of Tf-AuNP complexes increased with increasing volumes of stock protein (Figure 4.20 b). At optimal protein concentrations, only a small 6-8 nm shift was observed (Figure 4.20 c); this is indicative not of aggregation but of the formation of nanoparticle-protein complexes resulting in the modification of the refractive index of the nanoparticle.



(a) Determination of minimum protein concentration required to form of stable AuNP-Tf constructs. Tf concentration increases from well 1 to well 10.



(b) Determination of the stability of various Tf-AuNP constructs based on LSPR shift.



(c) Absorbance spectra of unconjugated (AuNP) and transferrin conjugated (Tf-Peg-AuNP). The λ max shifted by 6nm from 521 to 527.

Figure 4.20: NaCl based titration of Tf-AuNPs synthesised at different Tf concentration (a).(b) Spectrophotometric evaluation of Tf-AuNP stability. Tf-AuNP bioconstructs dispersed in water were read across a range of wavelengths and the wavelength at which the signal is the highest is identified as the peak wavelength position (λmax). The wavelength spectra peaks were fitted to filter out interfering background noise. The λmax of the different Tf-AuNP bioconstructs dispersed in water is taken as a reference and is subtracted from that of Tf-AuNP biconstructs reacted in the presence of NaCl to obtain the LSPR shift. (c) UV-VIS spectra of AuNPs before and after bioconjugation with Tf.

Confirmation of Tf corona on the AuNP surface Finally, the presence of transferrin on the surface of the AuNPs was confirmed by negative staining of Tf-AuNPs drop-casted onto TEM carbon grids. Negative staining was performed because the amorphous protein layer is relatively ineffective in scattering electrons and hence provides insufficient contrast to detect its presence at the particle surface. Uranyl acetate is known to strongly stain proteins, nucleic acids and phospholipids (Hayat,

2000). To generate contrast, the sample was stained using 2% aqueous solution of the heavy metal uranyl acetate.

Moreover, in negative staining, the sample background is stained, with the stain surrounding the sample but being however excluded from the volume occupied by the sample itself. Figure 4.21 shows the negatively stained unconjugated nanoparticles. As expected, there was no clear formation of a bright halo around the AuNPs due to the absence of Tf. It is therefore expected that in the presence of a Tf corona, a brighter region forms between the stain and the AuNP surface. In fact, this can be observed in Figure 4.22. In Figure 4.22 a), AuNPs are found at the edge of a stain patch on the carbon film thus facilitating the identification of the protein at the AuNP surface due to the frontier of non-interaction between the stain and these nanoparticles. Consequently, the stain boundary line becomes irregular only in the proximity to the AuNPs (Figure 4.22 a). For particles fully surrounded by the stain, a Tf corona halo around the nanoparticles is observed (Figure 4.22 b, c, d).

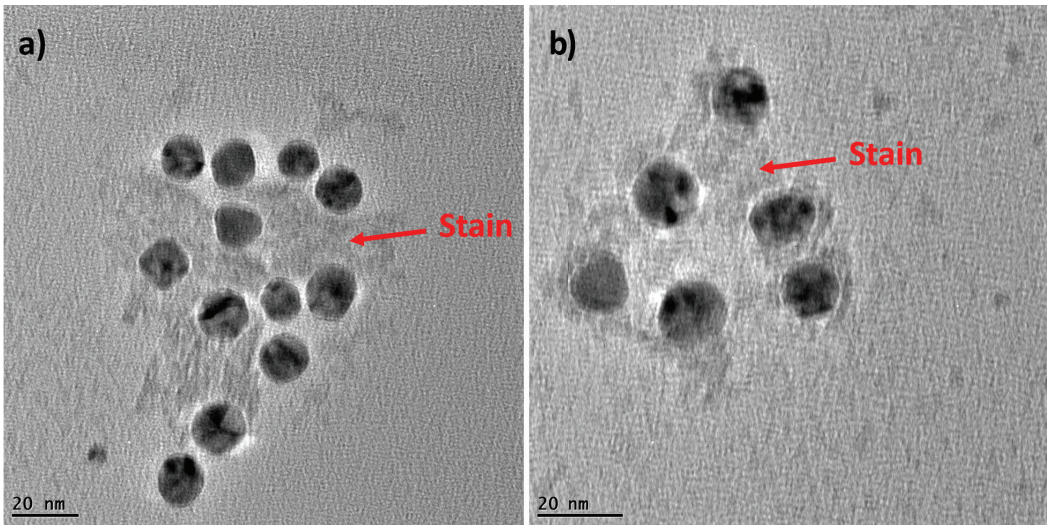


Figure 4.21: Bright field TEM images (a) and (b) showing negatively stained unconjugated AuNP

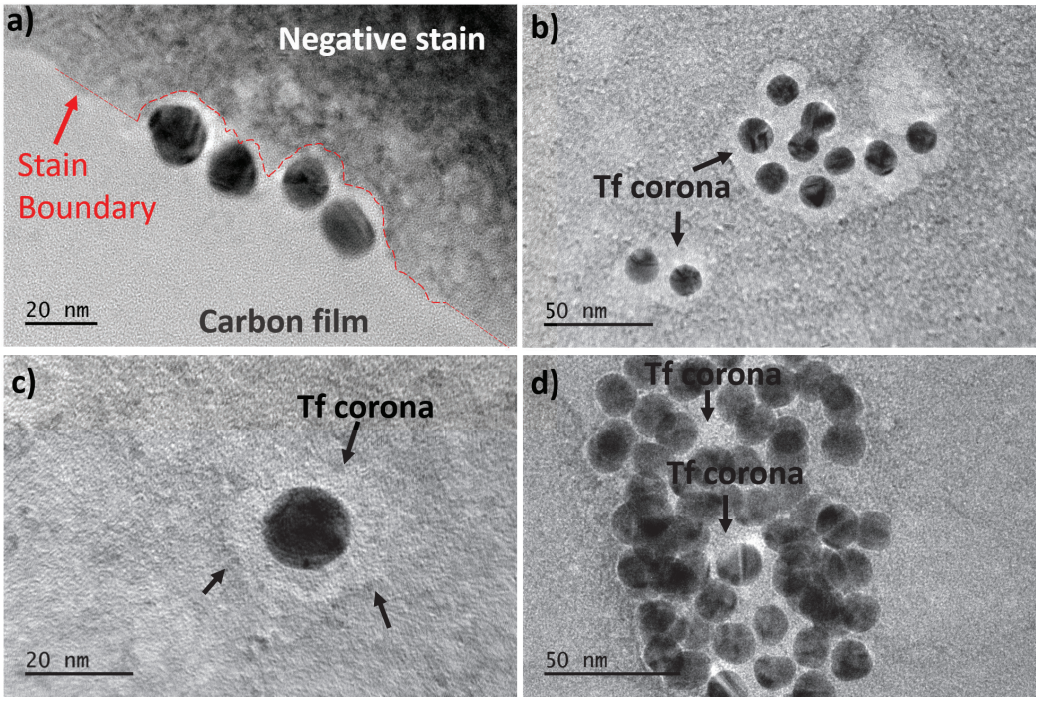


Figure 4.22: Bright field TEM images (a-d) showing negatively stained Tf-AuNPs with black arrows pointing to Tf coronas.

The surface presence of transferrin is therefore confirmed, and the bioconjugation methodology used is therefore deemed successful.

Determining Critical Transferrin concentration for Bioconjugation with AuStrs

The colorimetric and optical analysis of the AuNP allowed the successful identification of the critical protein concentration required to generate stable Tf-AuNPs bioconstructs. For comparison purposes, the Tf:Au ratio identified will be preserved for the bioconjugation reaction with the AuStrs. By using the same Tf:Au ratio, it is possible to normalise the AuStrs and AuNP reaction systems which ultimately allows to compare and study the effect of morphology in protein loading.

To validate this mass normalization, it is important to demonstrate that the

amount of Tf to be used is sufficient to generate stable AuStr constructs. To this purpose, AuStrs were submitted to different salt concentrations to determine their aggregation profile. Fully monodispersed AuStrs have a λmax at approximately 850 nm. Successive addition of salt causes the spectra λmax to redshift to 858, 965, 967 and 972 nm in the presence of 0.6, 0.8, 1.0 and 2 M NaCl, respectively (Figure 4.23 a). NaCl concentrations above 0.8 M were therefore found suitable to induce AuStr aggregation (Figure 4.23 b).

Subsequently, the AuStrs were conjugated with different amounts of Tf (Figure 4.23 c) and the stability of the different conjugates was challenged in aggregating conditions (Figure 4.23 d). It was found that the AuStrs achieved a similar minimum LSPR shift to the AuNPs of 7.6 nm when reacted with 2 μL of Tf (Figure 4.23 e). It is therefore confirmed that the critical amount of Tf required to create stable Tf-AuStr conjugates is met and that mass normalization is therefore valid.

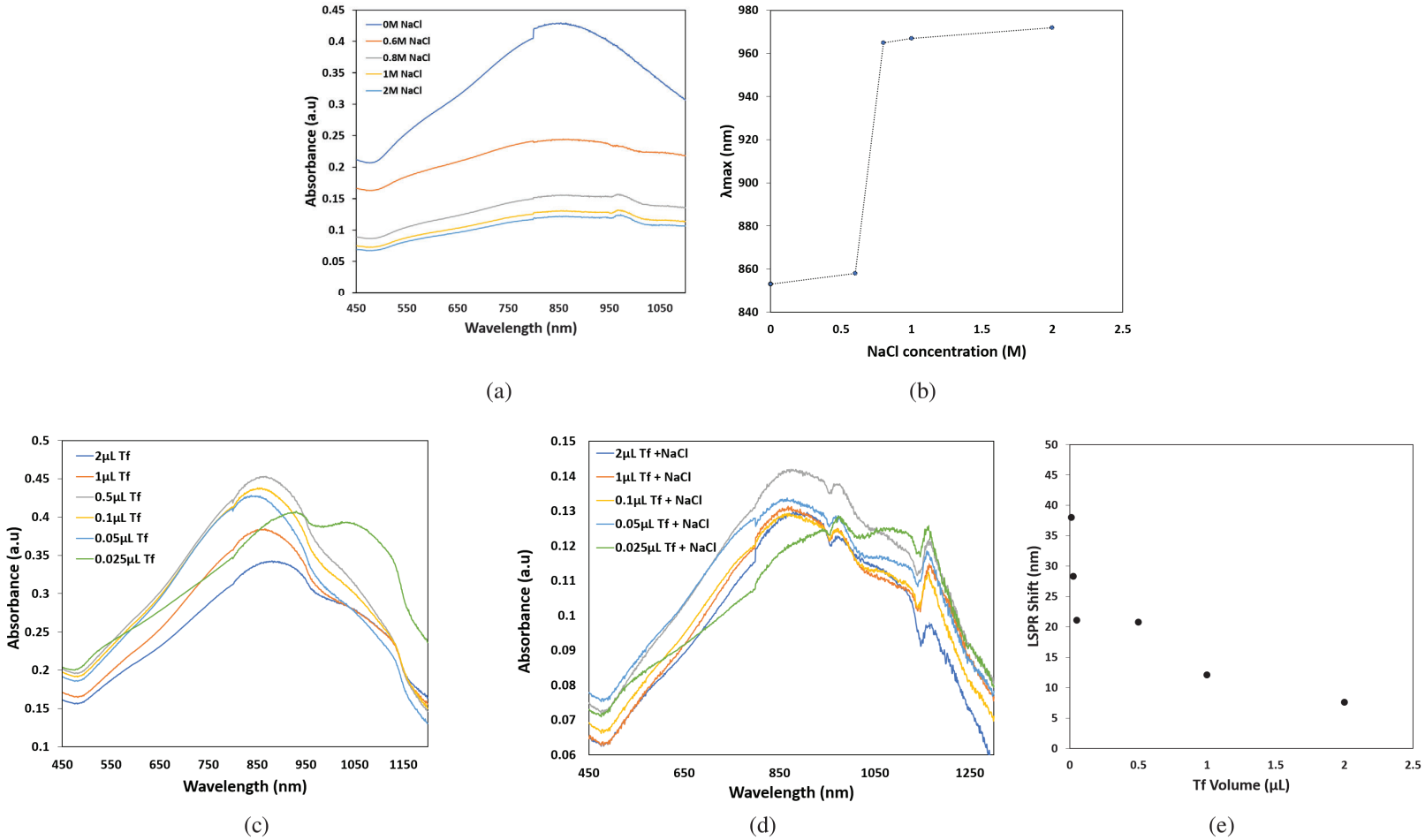


Figure 4.23: NaCl based titration of 100 nm Tf-AuStrs synthesised at different Tf concentration. (a) UV-VIS spectra of AuStrs reacted at different NaCl concentrations (b) Graph of AuStr λ max as a function of NaCl concentration, (c) UV-VIS spectra of Tf-AuStrs synthesised with different volumes of Tf, (d) Uv-Vis spectra of different Tf-AuStr constructs in the presence of NaCl and (e) Graph of LSPR shift as a function of Tf-AuStrs sysntehsised with increasing volumes of Tf.

4.5 Results: Monitoring and Quantification of controlled protein attachment to AuNP

For bionanotechnology applications, it is important to appropriately characterise protein-nanoparticle conjugates. In this section, a non-destructive approach to quantify protein attachment to Au nanostructures was explored (Figure 4.24).

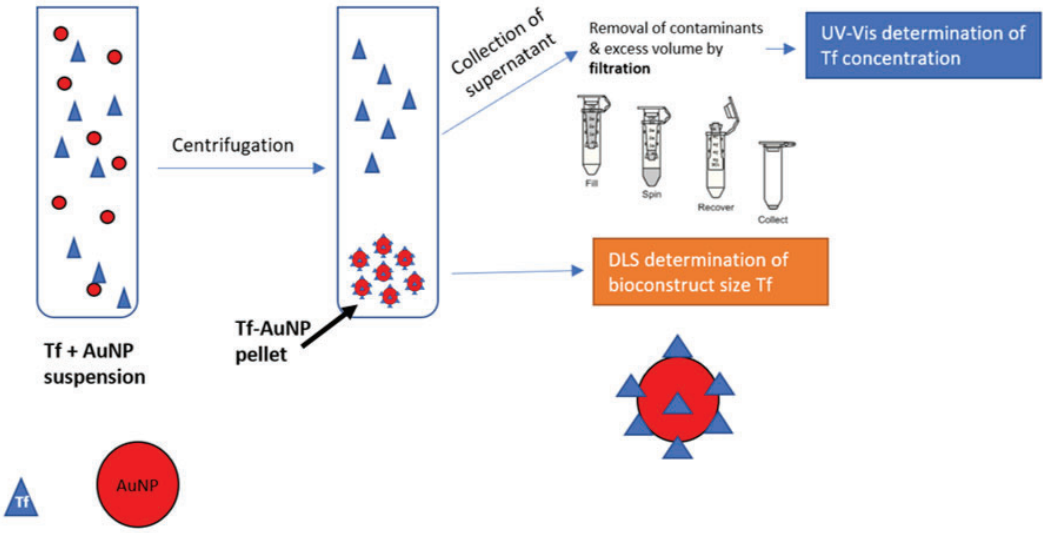


Figure 4.24: Schematic illustration of the procedure used quantify Tf binding to AuNPs. Tf (blue triangles) react with AuNPs (red spheres) for 18 hours following which the solution is centrifuged to separate the unreacted protein from the Tf-AuNPs pellet. The unreacted Tf in the supernatant is concentrated in spin columns and the recovered volume is measured by UV-VIS spectroscopy to determine the protein concentration in solution. The formed Tf-AuNP constructs are further characterised by dynamic light scattering (DLS).

The amount of protein adsorbed to the gold nanoparticles was determined through UV/Vis spectroscopy. Briefly, Au nanoparticles were reacted with Tf following which the unreacted Tf excess is separated from the protein-nanoparticle conjugates through several cycles of centrifugation, until no more protein is detected on the supernatant. The recovered unreacted Tf supernatant is concentrated in ultrafiltration columns (thermofisher) and the absorbance of the recovered Tf fraction measured at 269 nm. The amount of bound protein is thus obtained indirectly by means of a calibration curve of known standard protein solutions. At 269 nm, a linear relationship (where R was >0.98) between absorption and protein concentration was found in the concentration range of 0-8 μg/mL.

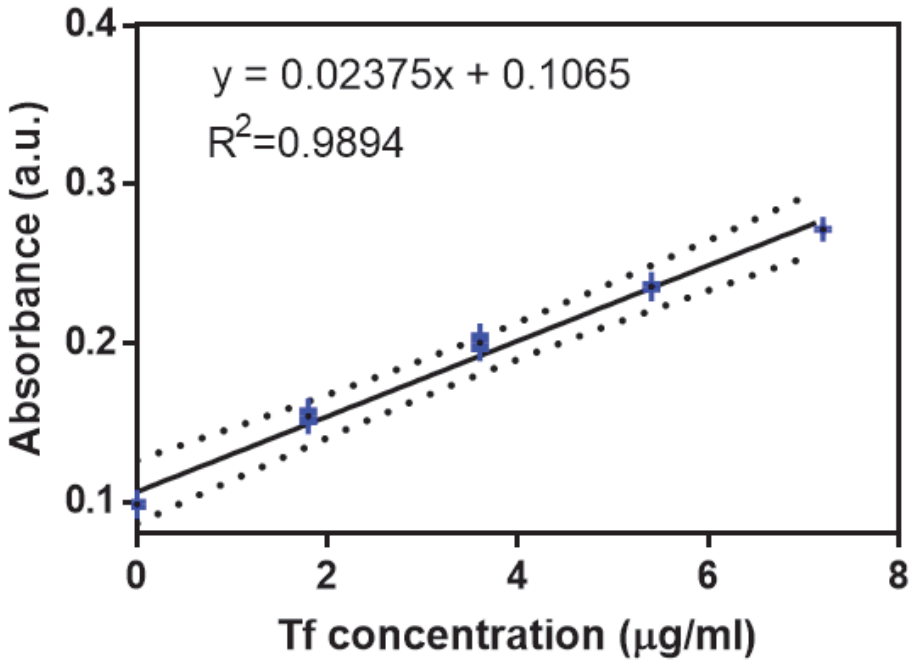


Figure 4.25: UV-VIS calibration curve of transferrin taken at 269 nm

Formation of tunabligthe protein coronas on the AuNPs

The amount of protein successfully attached to the nanoparticles was obtained by subtracting the amount of unreacted protein, recovered in the sample, from that of a control reacted in identical conditions to the sample but in the absence of particles. The unreacted protein in the supernatant was spectrophotometrically measured against a protein calibration curve (Figure 4.25).

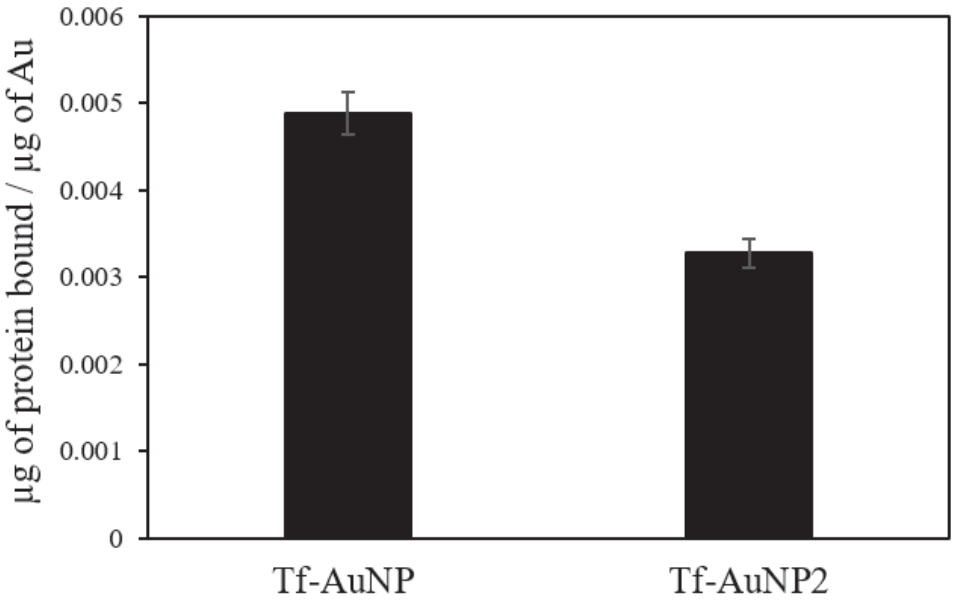


Figure 4.26: Quantification of Tf loading for biconstructs reacted at fixed Tf concentrations but with different amounts of AuNPs. Tf-AuNP2 were reacted with double the amount of gold to that of standard Tf-AuNP constructs. The graph shows that decreasing the Tf to AuNP ratio decreases protein binding.

On average, for the standard bioconjugation reaction, we estimated the binding of approximately 0.226 μg of Tf to 46.36μg of gold nanoparticles (Figure 4.26). This corresponds to a binding of approximately 654 proteins per each of the 2.64×10^{12} gold nanoparticles reacted. Additionally, when double the amount of gold nanoparticles (5.31×10^{12}) reacted in the same volume with the same amount

	Tf-AuNP	Tf-AuNP2
Number of particles reacted	2.65E+12	5.31E+12
Total Mass of gold reacted (µg)	4.63E+01	9.27E+01
Total mass of protein bound (µg)	0.226 ± 0.013	0.319 ± 0.013
Number of proteins per nanoparticle	654 ± 37	461 ± 19

Figure 4.27: Figure summarising the Tf-AuNP reactions that affect protein binding

of protein, a binding of about 440 proteins per particle was observed (Figure 4.27). Hydrodynamic diameter measured through Dynamic Light Scattering (DLS) for uncoated AuNP (Figure 4.28 a), Tf-AuNP2 (Figure 4.28 b) and Tf-AuNP (Figure 4.28 c). Figure 4.28 d shows the superimposed size distribution curve of the three nanoparticle formulations

To establish whether protein binding correlated with a change in particle size, DLS was used to characterize Tf-AuNP complexes (Figure 4.28 c) reacted in the presence of excess protein. Tf-AuNP constructs synthesized in identical conditions, but in the presence of double the amount of gold particles (Tf-AuNP2), resulted in a significantly smaller hydrodynamic size compared to the Tf-AuNP constructs synthesized with the standard amount of spherical AuNPs. Thus, by restricting the reaction time, it was possible to control the hydrodynamic bioconstruct size by changing the protein to nanoparticle ratio.

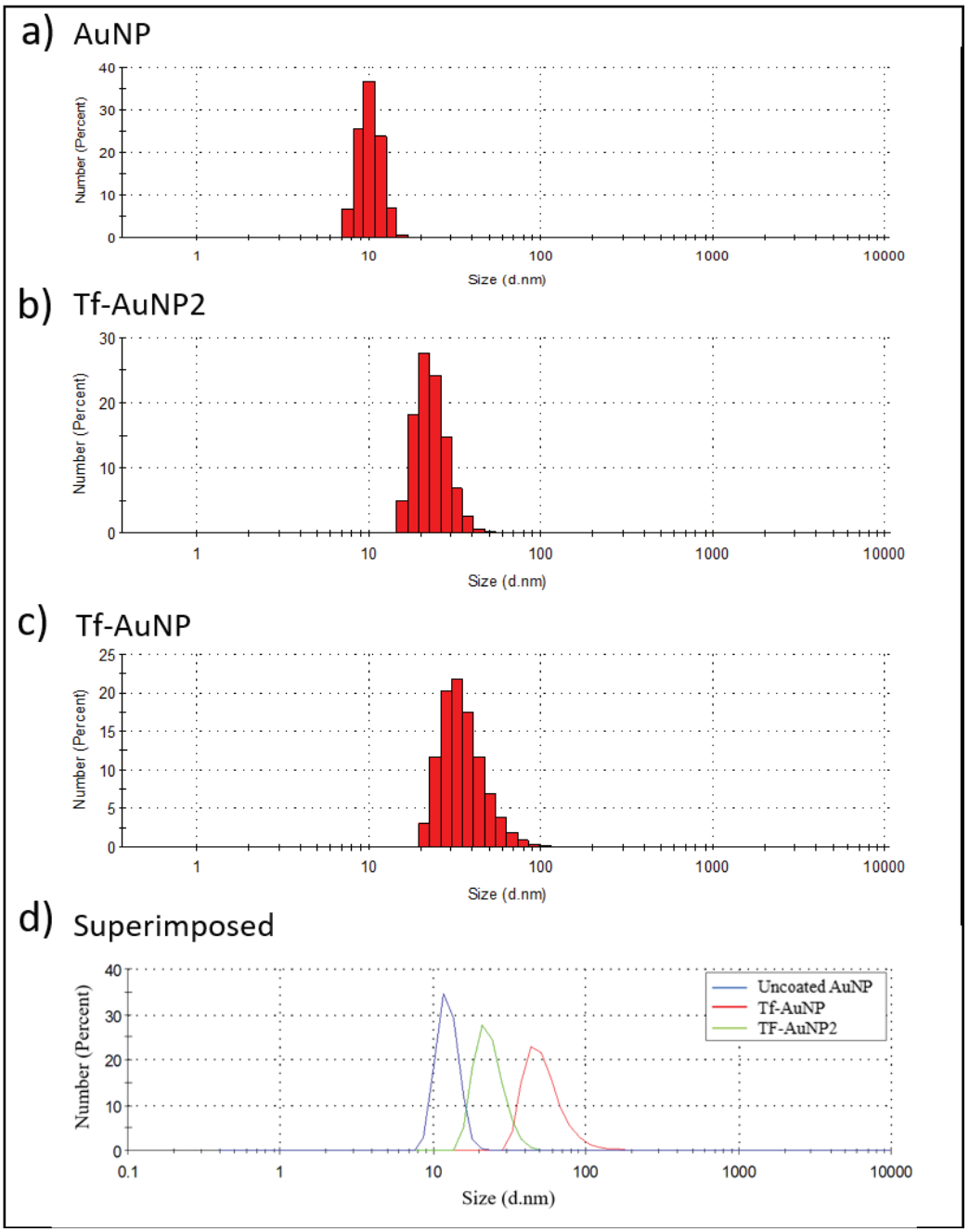


Figure 4.28: Hydrodynamic diameter measured through Dynamic Light scattering (DLS) for uncoated AuNP (a), Tf-AuNP2 (b) and Tf-AuNP (c). Figure (d) shows the superimposed size distribution curve of the three nanoparticle formulations.

Influence of reaction time in formation of protein corona To evaluate the direct influence of reaction time on the formation of the protein corona, Tf and gold

nanoparticles were allowed to react for either 2 or for 18 hours. Following the respective reaction times, the nanoparticles' hydrodynamic diameters and amount of protein binding were measured. It was found that the amount of protein bound to the AuNPs did not vary when the reaction time increased (Figure 4.29). This indicates that the binding occurs rapidly and thus differences in protein binding may be detectable at shorter times. Being that the protein binding remained constant in both cases, the hydrodynamic size of the bioconstructs was the same (40 nm) as demonstrated by the overlap between the hydrodynamic size frequency curves (Figure 4.30). The obtained results suggest that the majority of the protein binding events occur during the first two hours of the reaction. Additional reaction time did not contribute to increasing protein binding.

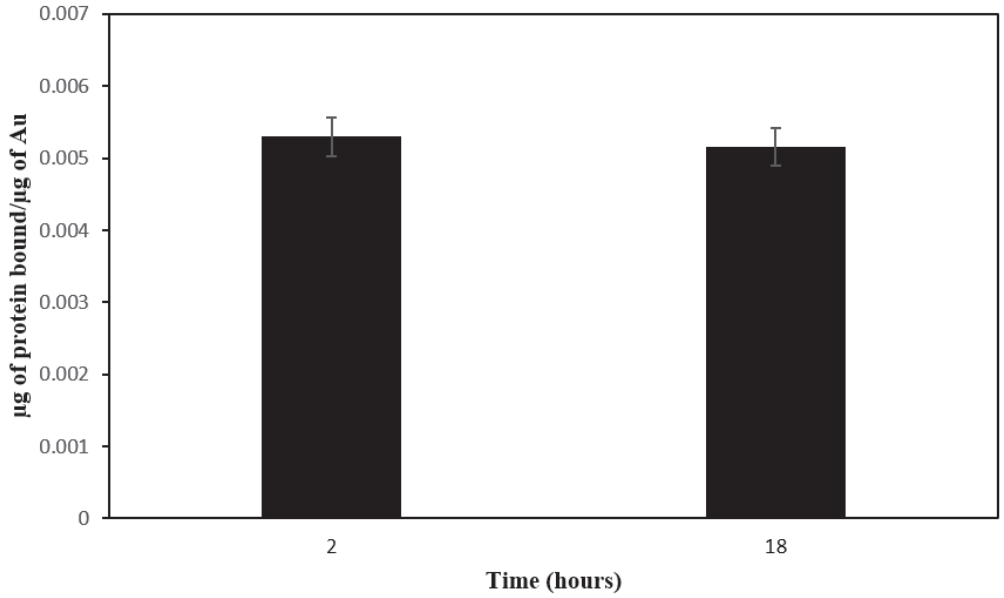


Figure 4.29: Quantification of Tf loaded to AuNPs following a 2 hour and a 18 hour reaction. The graph shows similar protein loading for both reaction times.

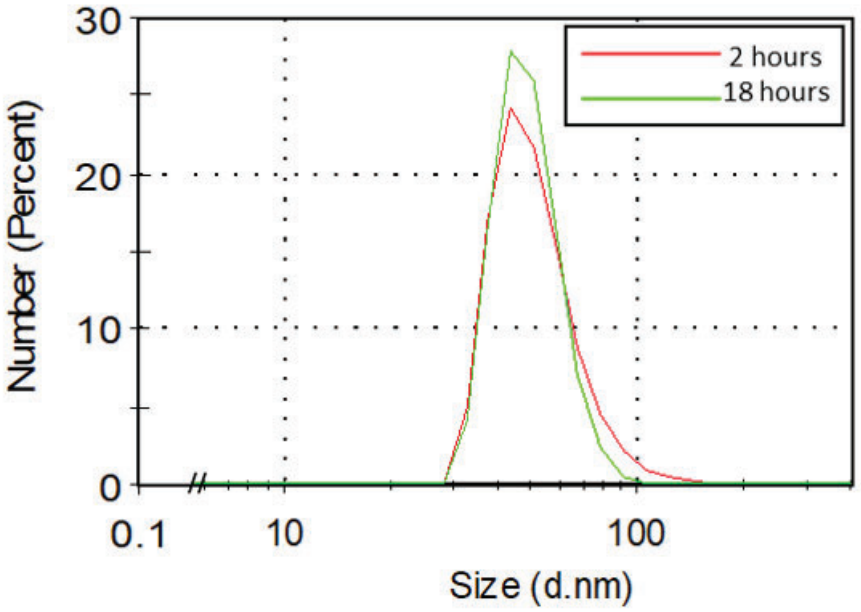


Figure 4.30: Evaluation of Tf-AuNP bioconstruct hydrodynamic size as a function of reaction time measured by dynamic light scattering.

Figure 4.31 shows the TEM image of the negatively stained Tf-AuNP (hydrodynamic size of 40nm) reacted at standard reaction conditions.

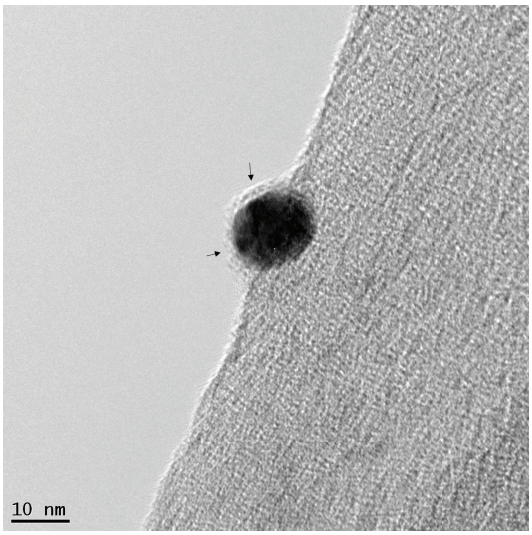


Figure 4.31: TEM of a Tf-AuNP biocunstruct with black arrows showing the presence of surface protein layer with an average thickness of 2.15 $\pm$ 0.29 nm.

Formation of tunable protein coronas on the AuStrs

Finally, we tested the previously described method for the conjugation of Tf to the optimum 100 nm AuStrs, whose complex morphology includes branches of high aspect ratio, separated by valleys radially arranged on a gold core. In particular, we aim to clarify whether particle anisotropy affects the conjugation reaction and formation of the protein corona. To study the protein nanoparticle interface, we used high resolution TEM at 300 kV on negatively stained Tf-AuStr samples. Figure 4.32 shows TEM images of the negatively stained Tf-AuStr conjugates. It was found that transferrin binds to the surface of the 100 nm gold nanostars in a conformal manner, tracing all of the AuStr morphology and leading to the formation of a 2.28 nm thick protein film.

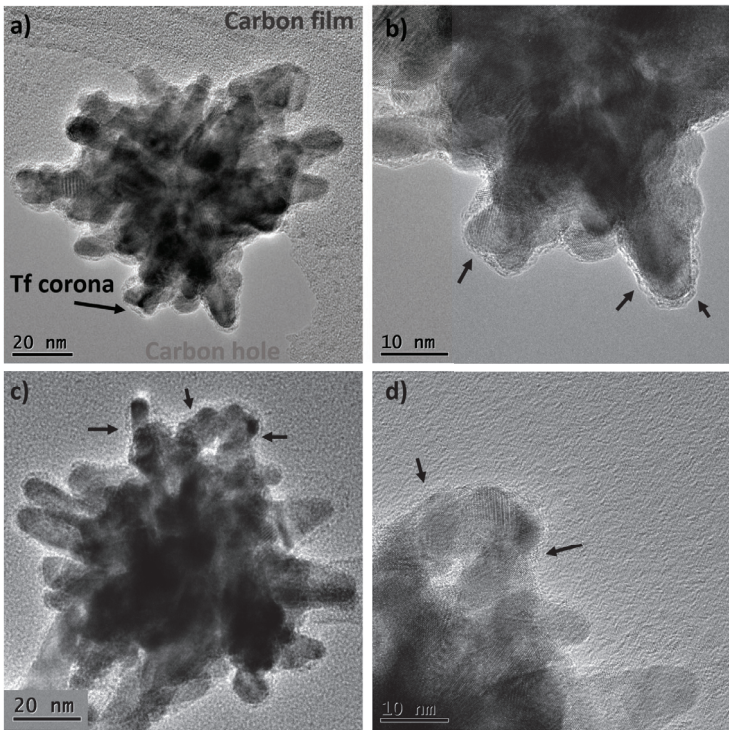


Figure 4.32: Bright field TEM micrographs of negatively stained 100 nm Tf-AuStrs with black arrows showing the presence of a surface protein layer with an average thickness of 2.28 nm

This conformal coating occurred irrespective of the AuStr diameter, as confirmed for the 25 nm (Figure 4.33) and 50 nm ((Figure 4.34)) Tf-AuStrs.

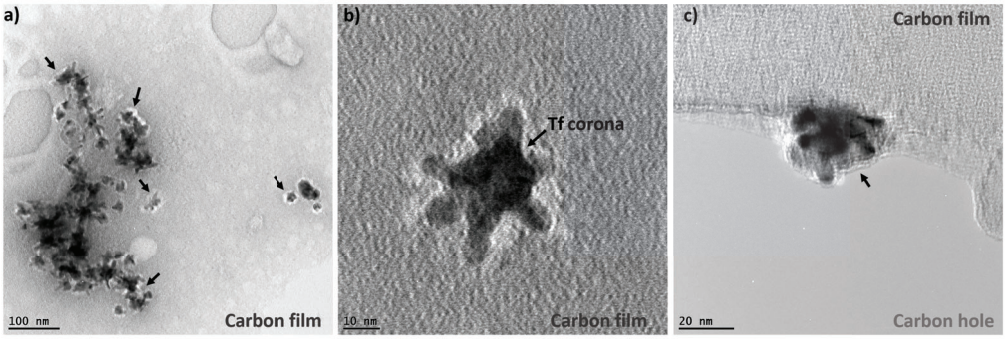


Figure 4.33: Bright field TEM micrographs of negatively stained 25 nm Tf-AuStrs with black arrows pointing at Tf protein coronas on the nanoparticles surfaces

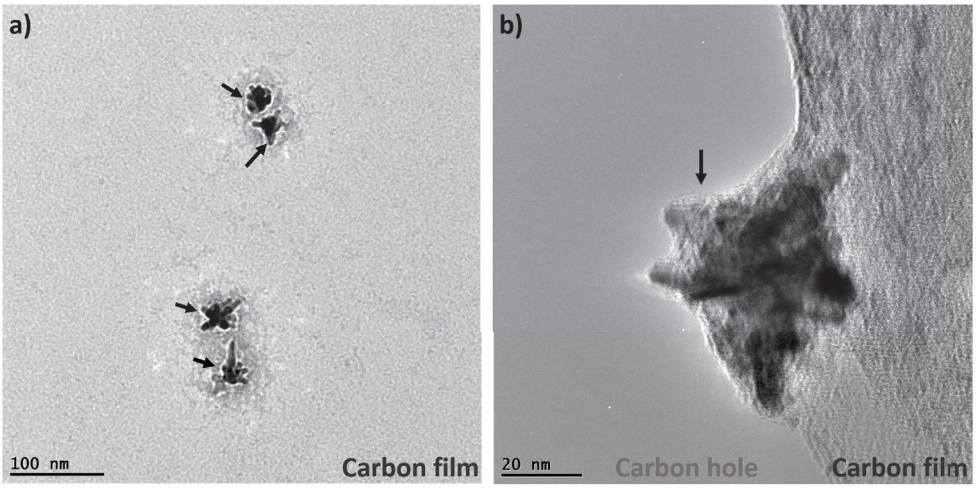


Figure 4.34: Bright field TEM micrographs of negatively stained 50 nm Tf-AuStrs with black arrows pointing at Tf protein coronas on the nanoparticles surfaces.

In order to assess the effects of excess protein, we proceeded to substantially increase the amount of reacting protein by a factor of 10 to test whether the conformal arrangement of the 100 nm AuStrs could be challenged. At this extreme condition (Figure 4.35), the thickness of the protein coating along the side of the nanostars spikes almost doubled, increasing from 2.28 nm to 5.24 nm. The overall

conformal behaviour of the coating remained, however multilayer protein packing bridging particularly small inter-spike distances was occasionally observed. Interestingly, the thickness of the protein layer at the tip of the nanostar's spikes remained undisturbed, irrespective of protein concentration (Figure 4.36).

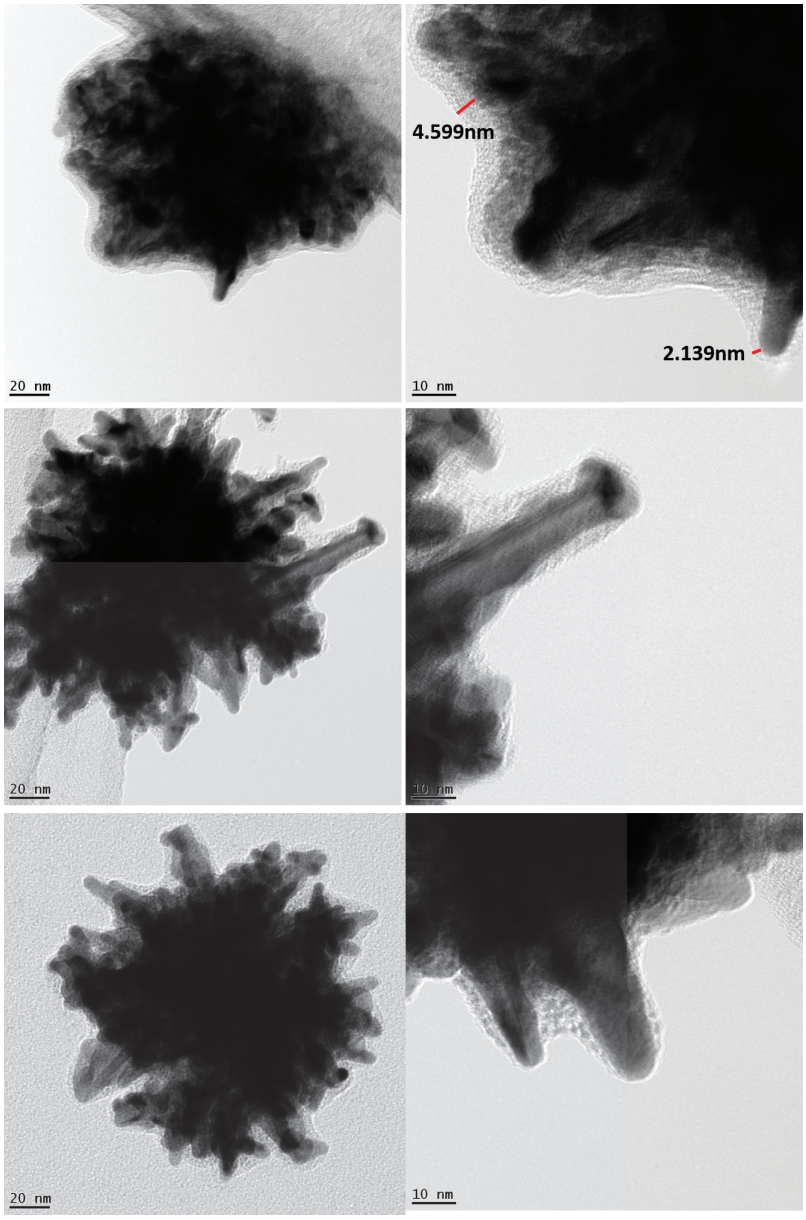


Figure 4.35: Bright field TEM micrographs of negatively stained 100 nm Tf-AuStrs conjugated at high Tf to AuStr ratios [10x].

Corona thickness	Tf-AuStr [1]	Tf-AuStr [10]
Tip of spike (nm)	2.077±0.01	2.769±0.12
Side of the spike (nm)	2.283±0.11	5.24425±0.51

Figure 4.36: Corona thickness on the surface of AuStrs reacted in standard protein concentrations [1Tf] and at high protein concentrations [10Tf]. Thickness measurement analysis were performed in Image j.

In fact, this was consistent with the hydrodynamic size measurements of the of the Tf-AuStrs showing that both biconstructs share the same diameter of about 100 nm (Figure 4.37)

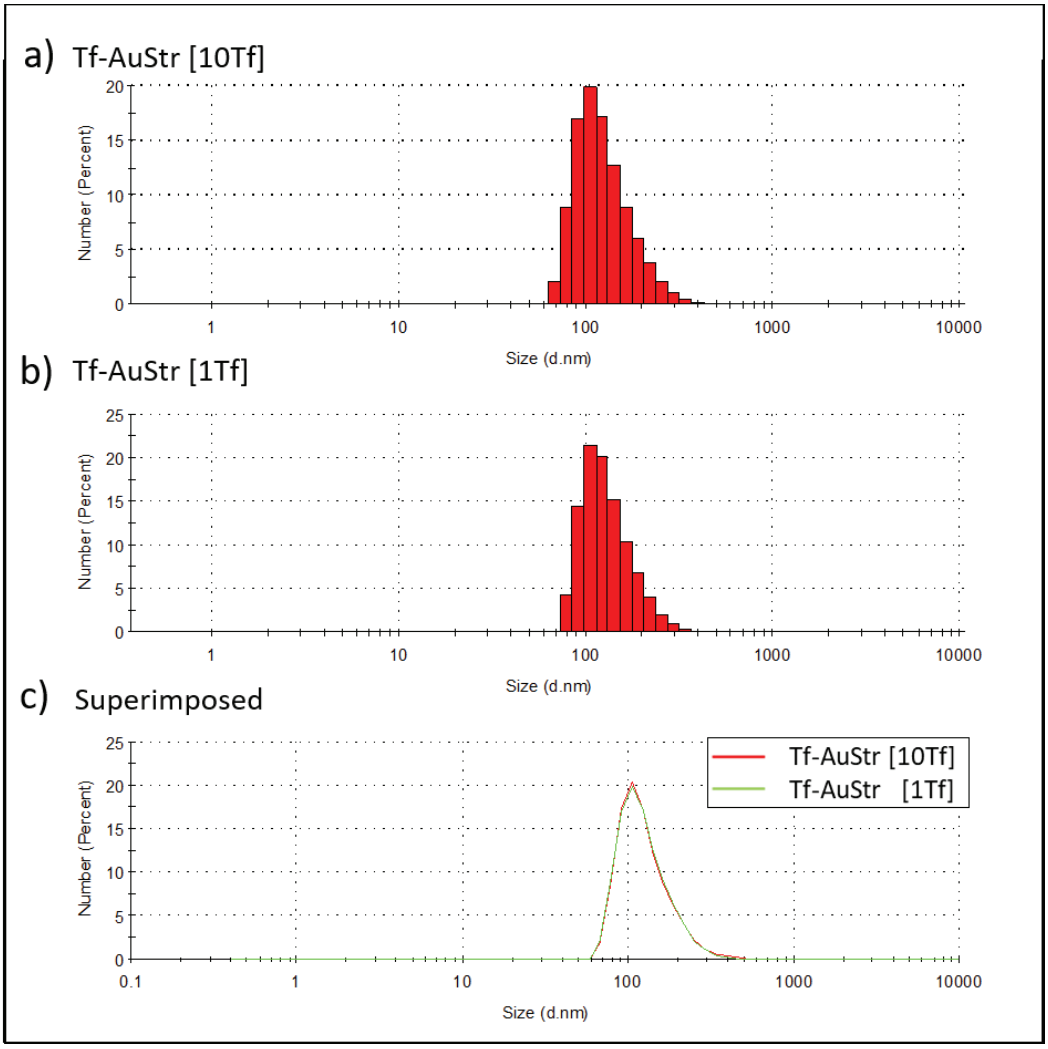


Figure 4.37: Hydrodynamic diameter measured through Dynamic Light scattering (DLS) for AuStrs reacted at high tf concentrations Tf-AuStr[10Tf] (b) and standards tf concentrations Tf-AuStr [1Tf]. Figure (c) shows the superimposed size distribution curve of the two AuStr formulations. The graphs show that changing the Tf to AuStr ratio did not affect bioconstruct size.

A difference in nanoparticle surface corona thickness between AuStrs reacted at standard (Figure 4.38 a and b) and high (Figure 4.38 c and d) transferrin concentrations is consistent with an increased surface binding of the protein. The amount of protein that binds to the AuStrs surface in the presence of the high protein concentration was quantified as 78.25 $\pm$ 5.08 μg of protein when the same 229 μg of gold were reacted (Figure 4.39).

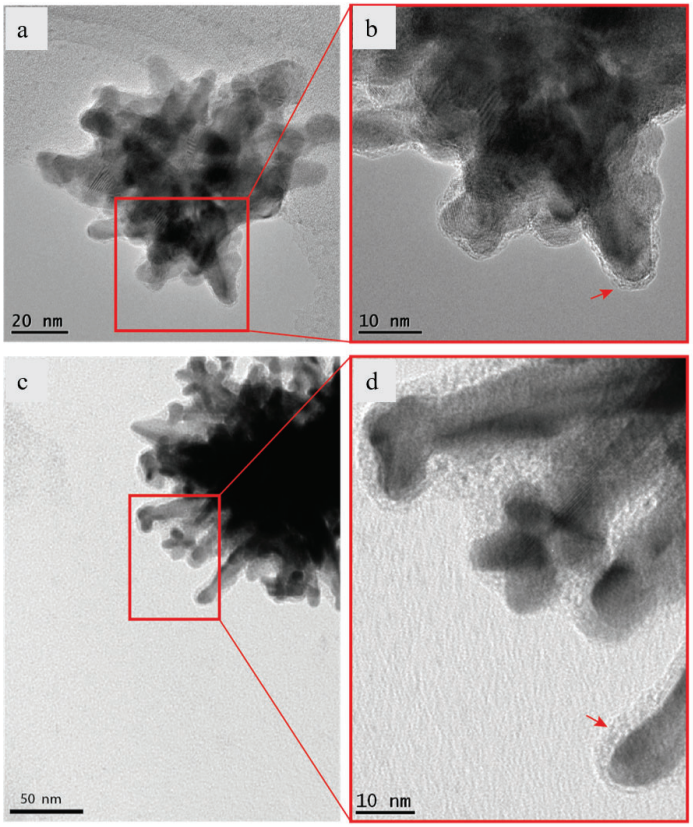


Figure 4.38: TEM image showing the presence of a conformal protein coating surrounding the AuStr reacted at standard Tf concentration [1Tf] (a and b). The thickness of this coating (c and d) increased when the standard amount of reacting protein is raised by a factor of ten [10Tf]. At the tip of the spikes the protein thickness remained unaltered.

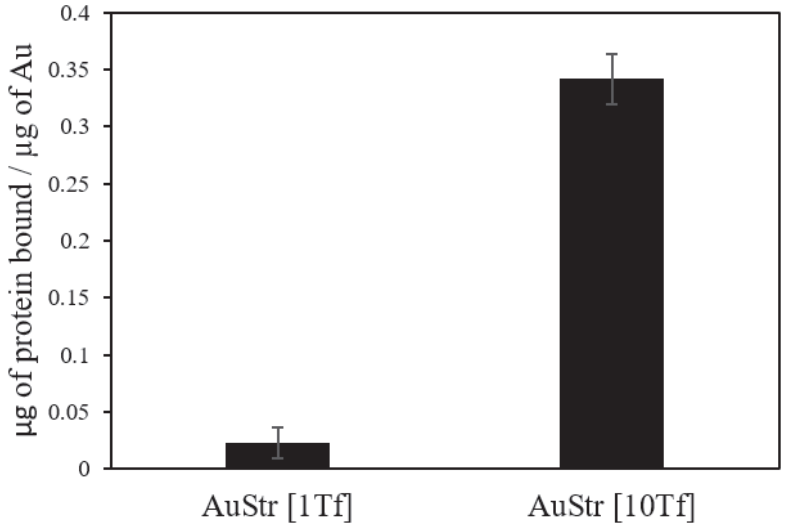


Figure 4.39: Graph showing Tf loading on AuStrs increased when the standard amount of reacting protein [1Tf] is raised by a factor of ten [10Tf].

4.6 Discussion

4.6.1 Controlled synthesis of AuStrs

The production of nanostructures with controlled size and shape is commonly achieved through the reduction of solution phase metal salts in the presence of stabilizers (surfactants or polymers). In solution-phase chemical synthesis, thermodynamic and kinetic parameters dictate the final nanocrystal shape through the control of the nucleation and growth stages of the nanocrystals. Hence, by manipulating these factors, crystallographic and morphological control may be achieved.

The influence of different reactant concentrations on AuStr growth in the presence or absence of pre-formed seeds was explored in order to be able to *controllably tune* the particle's size and morphology. Initially the AuStrs were synthesised based on a seedless one-pot approach. Briefly, $HAuCl_4$ is reduced by ascorbic acid in the presence of silver nitrate to produce AuStrs.

Effect of total amount of metal precursor

It was found that by varying the total amount of metal precursor the size of the AuStrs could be controlled between 36 $\pm$ 2 nm and 125 $\pm$ 6 nm. At $HAuCl_4$ concentrations below 0.1 mM the synthesis resulted mainly in spherical particles with rough surfaces with little to no spikes, whilst in the presence of increasing amounts of $HAuCl_4$ the AuStrs progressively attained a more pronounced 'spiky' morphology.

The formation of a AuStr includes formation of the core and formation of the spikes. These events could occur either simultaneously or consecutively. Our data shows that the gold core is formed first, followed by the spikes. At low gold concentrations of 0.05 mM, spherical gold particles are formed almost exclusively

(Figure 4.2 a); indicating that the spikes do not form simultaneously to (or before) the core. If the amount of metal post-core formation is sufficient, spikes will form on to the core (Figure 4.2 c). Higher availability of gold will contribute further to spike growth, increasing the probability that they become sharp (Figure 4.2 d). The presence of silver ions promote anisotropic growth in certain crystallographic facets on the gold core thus preventing the formation of simply bigger single particles.

Effect of metallic precursor ratio (Au:Ag)

It was found that by changing the Au:Ag ratio the spikiness of the nanoparticle could be altered. In particular, increasing the amount of silver increased the AuStrs spike count. The optical spectrum of the nanostars synthesized at Au:Ag of 10:1 is significantly red-shifted when compared to the nanostars synthesized at Au:Ag ratio of 80:1. The spectra of the latter particles assimilates to that of more spherical morphologies and thus the NIR plasmonic shift of the Au:Ag of 10:1 AuStrs could be attributed to the increased presence of spikes, as shown by TEM.

Previous publications support the role of silver ions in asymmetrical growth of particles. (Ahmed et al., 2010; Yuan et al., 2012b, 2007) These effects were also observed in this study.

It is believed that silver ions act to direct the growth of Au branches rather than forming Ag branches. In the synthesis of nanorods, low amounts of silver ions have been shown not only to improve the yield of gold nanorods but also improved their aspect ratio (Sau and Murphy (2004); Khoury and Vo-Dinh (2008)). Silver nitrate ($AgNO_3$) is believed to trigger both the nucleation and growth of multispiked Au nanoparticles (Sau et al., 2011).

Even though a few theories have been used to explain the branching mechanism

for spike formation, it remains unclear which factor ultimately drives this mode of growth. It has been proposed that, in spike growth, gold may act to displace silver similarly to the synthesis mechanism of cubic Ag/Au alloy nanocages (Hrelescu et al., 2009). However, one of the most accepted arguments is the underpotential deposition (UDP) of silver on the different facets of an initial gold nuclei(Yuan et al. (2012a) ; Sau et al. (2011) ; Cheng et al. (2012)). A silver monolayer is expected to deposit on to particular gold facets as silver has a lower work function than gold. This deposition may occur preferentially on the gold (110) crystalline facets as these have a higher number of neighboring gold atoms causing the silver adatom to experience a stronger attractive potential. (Yu et al., 2013) (Sun and Xia, 2002) This process acts as a symmetry breaking mechanism, as the growth rate of gold is considerably slowed down on the (110) facets whilst faster growth occurs on facets that are only partially covered with silver. (Ahmed et al., 2010; Liu and Guyot-Sionnest, 2005) This growth mechanism is consistent with our study where varying the silver concentration changed the number of spikes.

Effect of seed addition for a mediated synthesis

To improve the sample polydispersity, preformed citrate capped 12 nm gold seeds (Frens, 1973) were introduced to the standard one-pot nanoparticle synthesis. In general, two stages are assumed during the synthesis of nanoparticles, namely nucleation and growth stages. It is believed that by separating these two events in time, one can achieve a more controlled size-distribution of the product nanoparticles (Kuo and Huang, 2005). The addition of seeds to the reaction system provided preformed and uniform nucleation points. As a result, subsequent particle growth occurred on the surface of these seeds thus yielding homogenous AuStr samples as opposed to those obtained in the seedless approach.

The introduction of seed provided an additional point of control over the AuStr size. It is commonly assumed that in the presence of more seeds the size of the resulting nanoparticle decreases due to the even distribution of the metal precursor per seed (Sau et al., 2001). In fact, by decreasing the Au:Seed ratio (Figure 4.40 IV), the AuStr size could be tuned between 103 and 28 nm, which also decreased the spike size and number of spikes per particle.

Jana et al. (2001) investigated upon the mechanism of seed mediated nucleation on the formation of gold nanoparticles. It was found that in the presence of high seed concentrations there was a better control over the nanoparticle growth, in concentration limited growth conditions.

Effect of hydrochloric acid (HCl) concentration

Finally, hydrochloric acid (HCl) was added to the reaction to contribute to the controlled growth of the spikes nanocrystals. This resulted in the appearance of secondary spikes and increased spike aspect ratio.

The altered spike morphology may be attributed to the chloride ion capping particular nanoparticle facets, alteration of the redox potential of the gold precursor in the presence of halides and even change the degree of UPD of silver on the surfaces of nanocrystals (Lohse et al., 2014). Other halides such as iodide (I-) and bromide (Br-) have previously been reported to influence the shape development of nanostructures (Grzelczak et al., 2008).

Figure 4.9 d shows the optical response of the nanostars previously synthesized in the presence of hydrochloric acid. It is observed that the nanostar plasmon shifts to the red with increasing concentration of HCl acid. One could conjecture that the morphology of the stars' spikes synthesized with HCl acid is responsible for the plasmon shifts observed in figure 4.9 d. Besides the number of spikes, spike

morphological factors known to influence the plasmon frequency and intensity are length, angle of the spike on the core and aspect ratio (Yuan et al., 2012b). The appearance of these secondary spikes may interplay with the previous factors.

In summary, the data show that being able to modify the number and shape of the spikes offers a possibility to change the nanoparticles surface area without significantly changing their volume. Finally, as a consequence of this morphological fine-tuning, we are able to modulate particular optical responses (Figure 4.40 V) in the near infra-red window, a medically relevant spectral region for its deep tissue imaging potential (Smith et al., 2009).

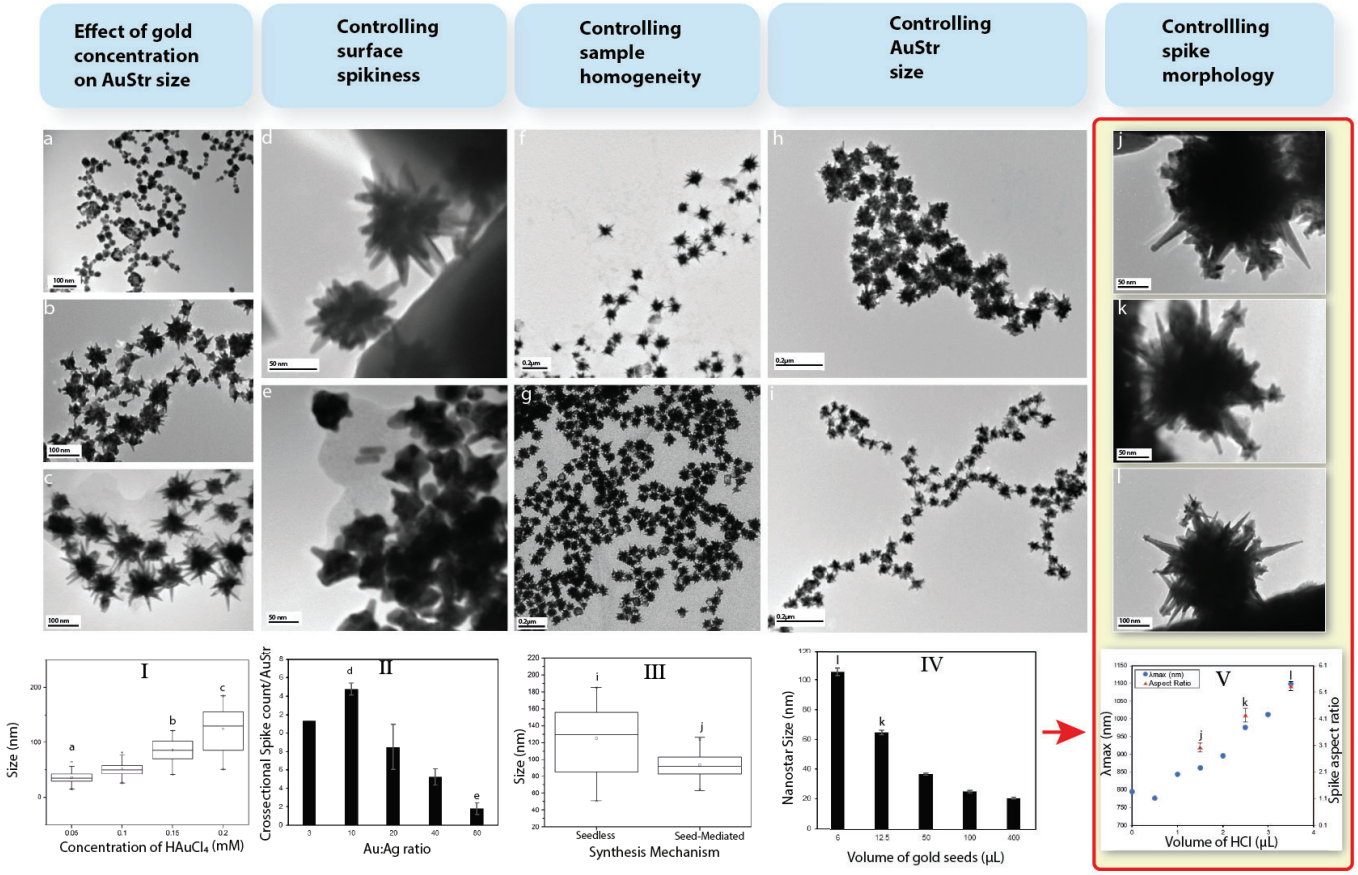


Figure 4.40: Summary of the systematic tailoring of AuStrs to identify the synthesis parameters responsible for particle size and structure. All TEM images are representative of the resulting samples and are individually identified in the corresponding graphs of reaction conditions vs effects on the nanoparticle (I-V). AuStr synthesis was performed in the presence or absence of gold seeds. In absence of gold seeds, nanoparticle size control (I) was achieved by varying the total amount of metal precursor (a-c). Spike count per AuStr (II) was controlled by increasing the Au:Ag ratio (from d to e). Introducing seeds in the reaction dramatically improved the AuStr size homogeneity (III) as evidenced by images taken before (f) and after (g) seed addition. Further varying the seed concentrations (IV) proved effective in fine tuning the AuStr final size (k-l). Spike morphology (III) was tailored by increasing HCl in the reaction system (j-l). By changing spike morphology the nanoparticles λ_{max} was tuned in the NIR (V).

4.6.2 Nanostar elemental analysis

The elemental composition of the 100 nm AuStrs was analaysed by EDS. The analysis revealed that both metallic elements, Au and Ag are evenly distributed through the nanostar core and spikes. This further supports a UPD type of mechanism for branch formation. Since EDS is qualitative in nature, a new approach was developed to attempt to convert the AuStr morphology into their equivalent mass. Due to the challenging morphology of the AuStrs (*i.e.* multiple spike hierarquies) mass values cannot be easily computed based on geometry. Hence, by using a combination of approaches and techniques including self-assembly of nanoparticles, SEM imaging and ICP-OES quantification it was possible to sucessfully determine the mass of gold per AuStr and thoroughly characterize the nanostructures. The value here produced may be useful for future dosing considerations for biomedical applications.

4.6.3 Formation of tunable protein coronas on the AuNPs

For BBB targetting applications, the nanoparticles were modified with the targetting protein transferrin The bioconjugation reaction was first optimised in non-spiky spherical nanoparticles and later applied to the complex nanostars. Different Tf-AuNP bioconjugates were synthesised and their stability evaluated based on a NaCl titration to find a critical protein concentration for the assembly of stable bioconstructs. After optimizing the concentration, the amount of protein loading per nanoparticle was tuned. It was found that, for the AuNPs, the surface loading of transferrin could be controlled by altering the number of nanoparticles in the reaction under fixed protein concentrations and time. Specifically, Tf binding decreased by 32% when the number of nanoparticles in the reaction mixture doubled.

This change in Tf binding can be explained based on the kinetic factors to which the reaction of gold nanoparticles with protein is subjected to. Here, a higher concentration of the reactants results in a higher probability of particle-protein collisions, thus driving the reaction equilibrium in the direction of bioconstruct formation.

In the condition of *excess* protein, a surface protein coating will occur, the density of which is influenced by the total time of contact between the proteins and the nanoparticle. With a larger number of nanoparticles to be coated, in a fixed reaction time, the total time of contact of a nanoparticle with freely available proteins decreases. Therefore, the density of the coverage also decreases. This explains why doubling the number of gold particles whilst restricting the reaction time decreased the average number of proteins per particle. This may represent an effective way to tailor the amount of protein complexed to the gold nanoparticles.

The changes in surface binding correlated with changes to the bioconstruct size. Thus, by restricting the reaction time, it was possible to control the hydrodynamic bioconstruct size by changing the protein to nanoparticle ratio.

4.6.4 Conformal protein coating of the AuStrs

Despite their different shape, AuStrs can be successfully bioconjugated when reacted at the same protein:Au mass ratio of the AuNPs. The thickness of the protein coating on the nanoparticle surface (Figure 4.32) was 2.28 nm, similar to previously determined ellipsoidal axial measurements of Transferrin of 2.76 nm and 5.52 nm. (Rosseneu-motreff et al., 1971) This indicates that a protein monolayer has successfully formed on the nanoparticles' surface. These nanostars bound about 5.23 μg of protein when 229 μg of gold reacted. This shows that, per *microgram* of gold reacted, the nanostars bind about *4.6* times more protein than

AuNPs. As demonstrated by TEM analysis, the protein conformally *accesses all the nanostar surface and the above binding ratio is consistent with surface area effects*.

In an attempt to challenge the conformal coating on the surface of the AuStr, the protein concentration in the reaction mixture was dramatically increased to 10 times that of a standard synthesis. It was found that, whilst the overall thickness of the coating about doubled and surface binding increased by *14 times*, the thickness of the coating at the spike tip did not change.

This behaviour is likely due to the protein binding being influenced by nanoparticle surface energy, a property that is dependent on the local radius of curvature (Nanda et al., 2003).

It is important to note that whilst the surface binding of protein increased in saturated conditions, the thickness of the corresponding protein coating did not exceed the dimensions of the protein longest axis (5.52 nm), indicating that monolayer behavior is maintained but the Tf orientation is changed (Figure 4.41).

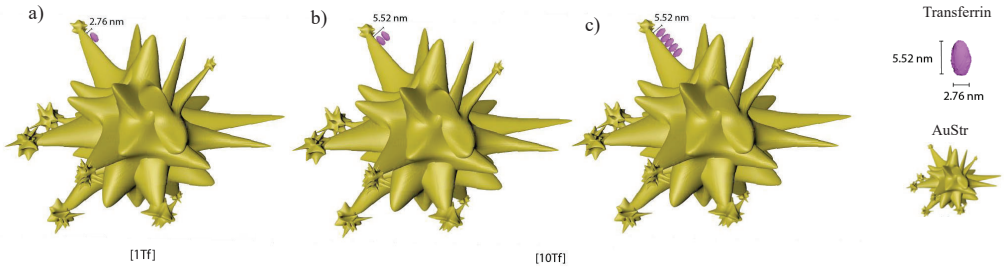


Figure 4.41: Manipulation of the orientation of Transferrin on the surface of AuStrs. Tf changes binding orientation from horizontal (a) at standard Tf concentrations [1Tf] to a double layer (b) or vertical orientation (c) at high Tf concentrations [10Tf].

Transferrin can bind to the surface the gold nanoparticle along its longest or shortest axis. At high Tf concentrations, the thickness of the protein corona is 5.24 nm. The preferential binding of Tf along its longest axis would allow the binding of about two layers of the protein on the surface of the nanoparticle, as the height per layer is 2.76 nm (Tf short axis) (Figure 4.41 b). The *14 times* higher surface binding is however not consistent with a simple bilayer but suggestive of a change in protein orientation, to bind along its shortest axis under the saturation pressures of the environment (Figure 4.41 c). This would enable more proteins to be packed on the surface of the nanomaterial. At the AuStrs branch tips, it is likely that the protein remains bound along its longest axis as independently of the Tf concentration the thickness of the corona in this region did not change. Alternatively, alterations to the protein native conformation upon nanoparticle binding could also alter the complexity of the binding events thus influencing corona thickness (Woods et al., 2016).

4.7 Conclusions

In summary, the flexibility of wet chemistry approaches provides exciting possibilities for the generation of tunable particles. In this study, we demonstrated how gold nanostructures can be finely tailored in a systematic manner to achieve unique morphologies. Transferrin was successfully and conformally conjugated onto AuStrs with a loading efficiency *4.6* higher than that of AuNPs. The resulting corona preserved the nanostructures high index features even at high protein concentrations. The particle protein loading was tuned by controlling the particle to protein ratio for a fixed reaction time. The experimental procedure here studied can be translated and tuned across different nano-topologies and is compatible with applications in which preservation of particle morphology is desired, for example in retention of optical properties or why 'spikiness' is related to uptake. The platform here developed is biocompatible and constitutes an important addition to the thoughtful design of targeted drug delivery nanovehicles.

Chapter 5

In Vitro Evaluation of AuStr based vehicles for BBB crossing

5.1 Introduction

The blood-brain barrier (BBB) is a protective endothelial barrier lining the brain microvasculature that tightly regulates the brain's biochemical environment. Whilst the BBB allows the passage of small lipophilic molecules, carbon dioxide and oxygen (Zlokovic, 2008), it is highly impermeable to other substances due to the presence of complex tight junctions and efflux pumps (Pardridge, 2007). The latter tight junctions and efflux pumps confer protection from pathogens, but also severely impede brain penetration of the majority of therapies into the brain to treat brain diseases.

Conventional strategies used to evade this barrier range from osmotic disruption of the BBB for increasing capillary permeability, to direct intracerebral or cerebrospinal fluid drug injections (Pardridge, 2007). However, such approaches may cause serious risks to patients by allowing immune cells and toxins to access

the brain when the BBB is temporarily opened Pardridge (2012). There is an urgent need to develop new drug delivery vehicles to target and penetrate the BBB.

Several studies have reported the ability of nanoparticle-based systems to cross the BBB and accumulate in the CNS (Andrieux et al., 2009; Kreuter, 2001; Calvo et al., 2001; Kreuter et al., 2002; Ulbrich et al., 2009).

A major focus is currently on the use of gold nanoparticles as these are biocompatible and offer very attractive options for theranostic applications.

These nano-sized particles are advantageous as they fall within the dimensional scale of endothelial endocytic transport mechanisms, their surface characteristics can be tailored to increase circulation times and can improve the bioavailability and stability of therapeutic agents encapsulated onto them or attached to the large surface area of these particles (Mudshinge et al., 2011)

Over the years, nanoparticles with different dimensions and surface chemistries have been investigated with respect to their behaviour/bioreactivity (Etame et al., 2011) and their mechanisms of internalization into cells. For instance, whilst small particles with less than 10 nm may enter the cells *via* passive diffusion (Zhang et al., 2009), bigger nanoparticles (<50 nm) may enter through endocytic pathways (Zhang et al., 2009; Shan et al., 2011). It is known that the size limitation for the crossing of particles across the BBB is <100 nm (Nance et al., 2012). To enable more efficient brain drug delivery it is important to use particles in the upper limit of this size range (100 nm).

In other work using silica nanoparticles it was shown that transport efficiency was also affected by size, with large PEG-Silica NPs crossing less than the smaller NPs which achieved the maximum crossing efficacy of 25% *in vitro* (Liu et al., 2014).

The transport across brain endothelial cells is also influenced by nanoparticles

shape. It was demonstrated that mammalian epithelial cells incubated with nanoparticle with different *aspect ratios* preferentially internalized disk-shaped PEG NPs compared to rod-like and smaller disk-like PEG NPs (Agarwal et al., 2013). Also, high *aspect ratio* carbon nanotubes were shown to have a unique ability to penetrate the BBB (Kafa et al., 2015).

Zeta potential is another important parameter when considering the nanoparticle's design for BBB penetration. Whilst strongly positive nanoparticles have been reported to cause BBB toxicity (Lockman et al., 2004), moderate (- 1 to - 15 mV) (Wiley et al., 2013) to high (- 15 to - 45 mV) (Kreuter et al., 2007) negative zeta potentials were found to have the best transport performance .

Protein-conjugated gold nanoparticles that use receptors overexpressed by the brain endothelium as targets are attractive candidates for controlled BBB targeting. Transferrin is a type of protein capable of entering the BBB by means of receptor mediated endocytosis. Brain blood vessels are highly impermeable due to the presence of tight junctions, thus the overexpressed transferrin receptors on the BBB endothelium (Uchida et al., 2011) represent an attractive target opportunity for selective brain crossing. Following this rationale, nanoparticles containing transferrin molecules have been prepared to target selectively transferrin receptors and consequently enter the brain *via* receptor mediated endocytosis.

Transferrin bioconstructs have been tested in *in vitro* and *in vivo* environments.

It was found that Tf-NP conjugates need specific receptor avidities to allow transcytosis. Wiley et al. (2013) showed that Tf-coated gold nanoparticles could reach the brain of mice by receptor mediated transcytosis following systematic administration. In this study BBB transcytosis was achieved by controlling the avidity of the bioconstructs for the transferrin receptors. Nanoparticle avidity was regulated by tuning the density of Tf in the NP surface and the particle size. It

was found that nanoparticles with high avidity for the transferrin receptor (TfR) remained strongly bounded to the BBB and had reduced accumulation in the brain whilst nanoparticles with very low avidity failed to engage the BBB. Particles with optimised intermediate avidity were able to engage with TfR, transcytose and be released in the brain. Furthermore, the formulation of these Tf-coated gold nanoparticles was later enhanced by using an acid-cleavable linkage to connect Tf to the surface of gold nanoparticles (Clark and Davis, 2015). With such approach Clark and Davis (2015) were able to increase BBB crossing *in vitro* and *in vivo* by facilitating nanoparticle retention in the BBB following receptor-mediated transcytosis. Contrary to these reports of nanoparticle accumulation in the brain following systematic administration, *In vivo* studies by Talamini et al. (2017) reported that PEGylated gold nanoparticles of varying morphologies (spherical, rod and star) were unable to accumulate in the brain of mice. However, no nanostar related data were shown.

Filter based transwell systems are commonly used for *in vitro* BBB models and have now also been adopted for nanoparticle applications. Ye et al. (2013) investigated the transcytotic efficiency of Tf conjugated AuNPs and other nanoparticle formulations across hCMEC/D3 in vitro models of the BBB. It was observed that Tf-AuNPs localised mainly to endosomal vesicles and lysososmes, but a few Tf-AuNPs were observed both in intercellular spaces and in the basal side. Neither the presence of protein nor particle size (5 and 25 nm) appeared to favour the occurrence of transcytosis. This study however was based on TEM observations and therefore qualitative in nature.

A few studies have found that the baseline physical and chemical characteristics of the nanoparticles play an important role on their overall performance. Amongst the strategies employed to achieve nanomaterials transcytosis across the BBB, the

most commonly investigated approach is to control the surface functionalization of the nanoparticle (Bhaskar et al., 2010; Georgieva et al., 2014). This is achieved by the selective attachment of targeting agents to the particles surface to actively target receptor-mediated pathways across the BBB (Xu et al., 2013). However, the role of the nanoparticle underlying features in BBB transcytosis should also be established.

Size and morphology both impact nanoparticle interaction with cells. Whilst it was shown that particle uptake decreases with particle size (for diameters > 50 nm) (Chithrani et al., 2006), this was performed for spherical nanoparticles and others studies show that the size dependency uptake effects can be opposite for different geometries (Nambara et al., 2016).

It is important to establish the optimum nanoparticle morphology to mediate the best transcytotic effect. In particular, there is a lack of the studies on the transcytotic performance of more complex nanoparticle shapes although these may mediate the currently poor transport of large molecules. Gold nanostars (AuStrs) have large surface areas for drug loading, discussed in chapter 4, enabling therapeutic relevant concentrations to cross the BBB to tackle CNS conditions.

Taken together, these studies highlight the need to target selectively transporters that are overexpressed on the BBB and to carefully control the nanomaterials physicochemistry to promote targeted BBB penetration, recognising that trade-offs in performance targets are required.

Initially, we tried to elucidate the effect of geometry, namely surface spikiness, on cellular uptake and transcytosis. The nanostar morphology was chosen as it possesses spikes with high curvature tips and of increasing cross-sectional area anchored onto a gold core. To verify the effect of morphology, the transcytosis efficiency of PEGylated gold stars (PEG-AuStrs) was compared to that of non-

spiky 12 nm gold nanospheres (AuNPs). These AuNPs were selected because the synthesis mechanism is well established (Frens, 1973), controllable and yields high quality monodisperse nanoparticles batches that are highly reproducible.

Subsequently, we investigated the effect of nanostar diameter on uptake and transcytosis. Here, AuStrs were synthesised in three different diameters (25, 50 and 100 nm).

Additionally, we evaluated in parallel experiments to establish whether geometry and diameter effects could be enhanced or negated when the nanoparticles were conjugated with transferrin.

Transcytosis efficiency was evaluated using the well-established hCMEC/D3 cell based *in vitro* model of the BBB (Weksler et al., 2005, 2013). Monolayer cultured human hCMEC/D3 cells in transwell inserts are used as an *in vitro* model of the BBB, as these have been shown to be a robust human BBB model (Weksler et al., 2005, 2013) and to overexpress transferrin receptors (Weksler et al., 2005; Uchida et al., 2011). We hypothesise that the presence of the nanostar sharp features and the spikes' core restricted orientation can enable efficient membrane penetration and transcytosis.

5.2 Experimental

All chemicals were purchased from Sigma-Aldrich unless otherwise stated. Milli-Q water was used in all experiments.

5.2.1 Cell Culture

Immortalised human brain microvascular endothelial cells (hCMEC/D3) derived from human temporal lobe microvessels were cultured in 75 cm^2 CellBIND

culture flasks (Corning Inc.). The cells were cultured in EBM-2 medium (Lonza) supplemented as per manufacturer's instructions with 2.5% (V/V) foetal bovine serum, ascorbic acid, gentamicin, EGF, hydrocortisone, basic fibroblast growth factor, insulin-like growth factor-1 and vascular endothelial growth factor (VEGF). The cells were cultured in humidified chamber at 37 C in 5 % CO_2 and the media replaced every 3 days.

Construction of the BBB Model For the *invitro* BBB model hCMEC/D3 cells were cultured in porous ($\oslash$ = 1 μm) transwell inserts (Millipore) lined with the extracellular matrix fibres collagen and fibronectin (Sigma)in 12 well tissue culture plates. Once the cells reach a confluent state, the culture media was replaced to one without the VEGF supplement to promote cell differentiation into a BBB phenotype whilts avoiding cell overgrowth.

5.2.2 Immunofluorescence Staining

To confirm the expression of tight junctions on the monolayer, the tight junction protein occludin was immune-stained for confocal microscopy observation. Briefly, the cell monolayer was fixed with 4% paraformaldehyde for 10 min and blocked with 1% bovine serum albumin (BSA) for a further 30 minutes. The monolayer was washed thrice with PBS and incubated with a monoclonal rabbit anti-occludin antibody (diluted 1/50 in 1% BSA in PBS overnight. Next, Alex Fluor F488 conjugated mouse anti-rabbit IgG (Invitrogen, UK)(diluted 1/50 in 1% BSA in PBS) was added and incubated for 1 hour. Following washing, the cells were stained with DAPI (1 μ/mL) for 30 min. Finally, the cell monolayer on transwell inserts was clipped and mounted onto glass slides with Prolong Gold.

Transendothelial electrical resistance

The tightness of the cellular monolayer was evaluated by measuring the transendothelial electrical resistance (TEER) with a EVOM ohm meter (World Precision Instruments) (Ragnaill et al., 2011). For the measurement two electrodes were placed on either side of the cell monolayer supported on the pourous filter and the ohmic resistance of the path between the electrodes was recorded. After subtracting the resistance of the porous filter membrane *per se* and multiplying by the surface area of the transwell (1.12 cm^2), the resistance of the monolayer can be obtained in Ωcm^2.

5.2.3 Gold nanostructure toxicity

Cell toxicity was assayed using the LDH (Abcam ab65393) and MTS (Abcam, ab197010 kits) kits. To evaluate the bioconstruct toxicity, hCMEM/D3 cells were exposed to PEGylated and transferrin coated AuStr and AuNPs in a concentration range of 5 -50 μg/mL. Quantification of cytosolic LDH release following 24 hour bioconstruct exposure was measured at 490 nm in a Bio-Rad plate reader in absorbance mode. MTS assay was performed in cells exposed in same concentration range conditions to measure cell viability. The reduction of the MTS tetrazolium reagent to a coloured formazan by metabolic active cells was used as a measure of cell viability and monitored at 490 nm. For both assays, the negative control consisted of the cell wells not exposed to nanoparticles and the positive control wells were treated with 1% Triton-x100 for maximum LDH release and minimum cell viability.Possible colorimetric interferences of the nanostructures with the LDH and MTS reagents were tested in cell-free conditions, however, no dye conversion were observed at these conditions.

5.2.4 Statistical Analysis

Results are presented as mean ± the standard error of the mean. Statistical analyses were performed on GraphPad Prism 6. Differences were considered significant from $p < 0.1$. Sample means were compared with a two way ANOVA and a Sidak multiple comparisons test to determine which groups differed from one another.

Permeability Coefficient

Prior to each transport study the transwells were rinsed with pre-warmed assay medium. Subsequently, the apical and basolateral chambers were respectively filled with 0.5 mL and 1.5 mL of fresh medium and were allowed to equilibrate for 60 minutes. The paracellular permeability of hCMEC/D3 cells to 4 and 70 KDa fluorescein isothiocyanate (FITC)-labelled dextrans (Sigma) was measured as reported by (Weksler et al., 2005). Briefly, 0.5 mL of FITC-dextrans solution (1mg/mL) were added into the apical chamber and the flux of the dextran solution into the basolateral chamber (containing 1.5 mL of assay medium) was sampled at every 10 minutes and immediately replaced with fresh medium. Fluorescence measurement of the sampled basolateral medium was performed at an excitation wavelength of 490 nm and emission wavelength of 510 nm. Subsequently, the dextran concentration in the basolateral compartment was used to calculate the volume of dextran solution cleared from the apical to the basolateral compartment:

$$V_{Cleared} = \frac{C_{basolateral} \times V_{basolateral}}{C_{apical}} \tag{5.1}$$

where V and C stand for volume and concentration,respectively.

As the clearance volume increases linearly over the timecourse of the experi-

ment, it is possible to determine the transport rate (Tr) from the slope of a linear regression of cumulative cleared volume against time.

The transport rate across the cells (Tr_{cell}) was obtained by subtracting the Tr of an empty transwell filter (Tr_f) from that of a transwell containing cells (Tr_{tw}):

$$\frac{1}{Tr_{cell}} = \frac{1}{Tr_{tw}} - \frac{1}{Tr_f} \tag{5.2}$$

Finally, the permeability coefficent (cm/min) across the cells is obtained by dividing Tr_{cell} by the surface area (SA) of the transwell filter:

$$Pe = \frac{Tr_{cell}}{SA} \tag{5.3}$$

5.2.5 Transport assay

For the nanoparticle transport studies, 0.5 mL of the test gold nanostructures solution at a concentration of 50 μ/mL were administered in the apical chamber and incubated for 24 hours (Figure 5.1). The mass of gold recovered in the apical chamber, associated to the cells and in the basolateral chamber were collected in three separate test tubes, dissolved in *Aqua regia* (3:1 HNO_3:HCl) and quantified by ICP-OES. By determining the amount of gold that travells through the barrier, the transport efficiency of the different nanostructures can be ranked.

Sample preparation for TEM imaging

Following exposure to the gold nanostructures, hCMEC/D3 cells were rinsed with 0.1 M HEPES (pH = 7.2) and fixed for 2 hours with 2.5% glutaraldehyde. Subsequently, the cells were post fixed with 1% osmium tetroxide for 1 hour and dehydrated through a series of graded ethanol solutions 50, 70, 95, and 100 per-

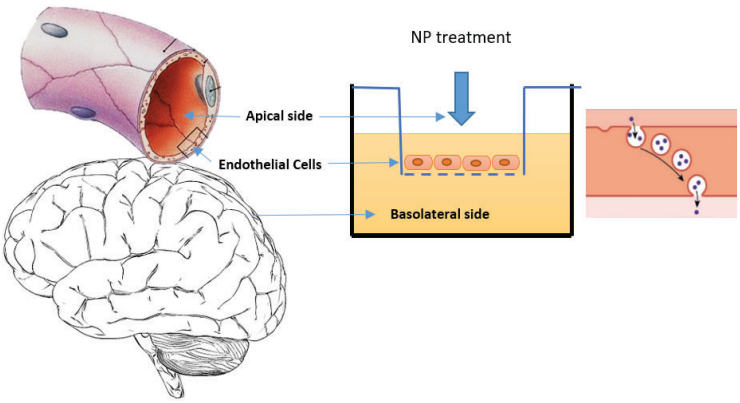


Figure 5.1: Scheme illustrating the transwell based *in vitro* model of the BBB setup.

cent for 15 min in each solution. Each dehydration was performed three times. Finally, the membrane was excised from the filter insert and dehydrated in 100% acetronitrile. The samples were then infiltrated with 50, 75 and 100% of resin in ethanol, in overnight incubations. The samples are subsequently incubated with fresh 100% resin in the presence of the cross linker BDMA under vacuum for 1 hour followed by incubation at 60 °C for 48 hours. The embedded samples were sectioned (80-100) nm using a diamond knife at a 35° angle on a Leica Microtome. The samples were then imaged by transmission electron microscopy set at the accelerating voltage of 80 kV to increase the contrast from the cells organelles.

Chapter contributions

STEM-HAADF imaging was performed with the assistance of Dr Jiahui Qi. Cryo-TEM imaging was performed with the assistance of Dr. Catriona McGilvery. Dr Angela Goode provided assistance with FIB-SEM.

5.3 Results

5.3.1 Nanoparticle Selection for the BBB studies

For the permeability studies, AuStrs were synthesised in a size-controlled manner using the seed-mediated method described in chapter 2. The nanoparticles were monodisperse and with defined diameters of 25, 50 and 100 nm in diameter (Figure 5.2). Nanoparticles were synthesized within a size range that should prevent passive diffusion (> 10 nm) (Zhang et al., 2009) and within the reported limits for the crossing of the BBB (<100 nm) and diffusing in the brain (Nance et al., 2012).

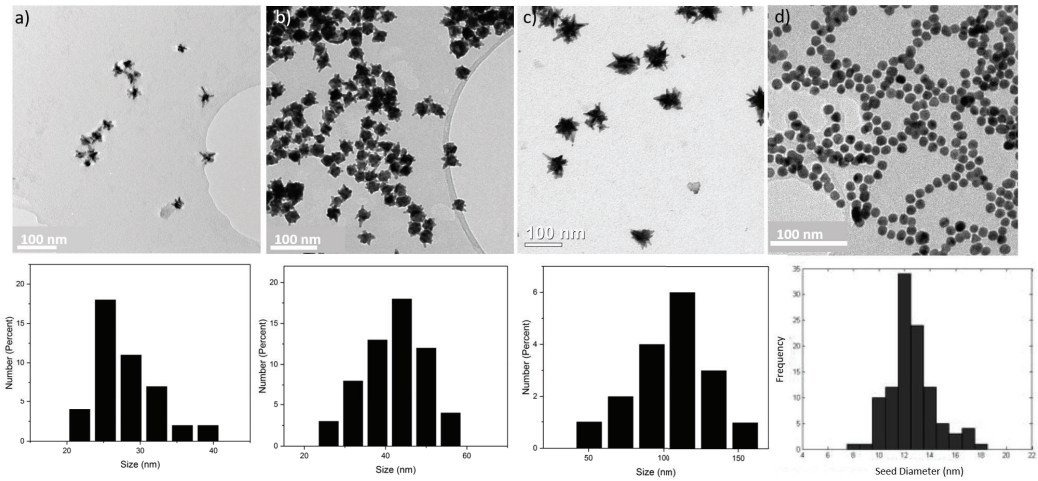


Figure 5.2: Synthesis of gold nanoparticles for transcytosis studies. Monodispersed AuStrs were synthesised with 25 (a), 50 (b) and 100 nm (c) in diameter and AuNPs were 12 nm in diameter (d).

The presence of protein on the surface of the nanostructures was confirmed by transmission electron microscopy (Figure 5.3)

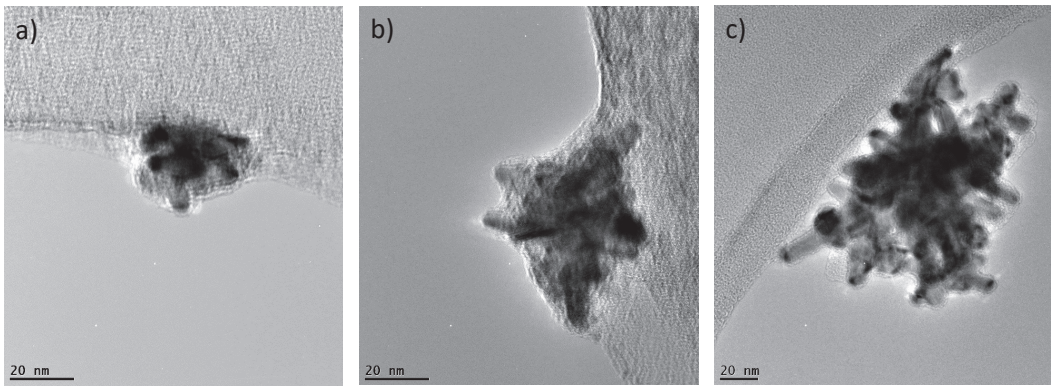


Figure 5.3: Gold nanostars conjugated to transferrin. (a) 25 nm (b) 50 nm (c) 100 nm diameter Tf-AuStr

The nanostructure's Zeta potential was measured in cell culture medium (Table 5.1). It was found that all the nanostructures had negative near-neutral zeta potentials. Zeta potential values in this range are associated with improved transport performance in previous reports (Lockman et al., 2004).

Table 5.1: Zeta potential of gold nanostructures in media+FBS (pH = 7).

Nanostructures	Zeta Potential in Media+FBS (mV)
Peg-AuNP	-10.50 $\pm$ 1.74
Tf-AuNP	-7.08 $\pm$ 3.39
Peg-AuStr 100 nm	-2.27 $\pm$ 0.06
Tf-AuStr 100 nm	-3.25 $\pm$ 0.59
Peg-AuStr 50 nm	-3.52 $\pm$ 1.42
Tf-AuStr 50 nm	-5.67 $\pm$ 2.80
Peg-AuStr 25 nm	-2.82 $\pm$ 0.89
Tf-AuStr 25 nm	-8.47 $\pm$ 3.31

5.3.2 Establishing an *in Vitro* BBB model to study nanoparticle transcytosis

Nanoparticle permeability was tested in a representative *in vitro* transwell model of the brain endothelium (Weksler et al., 2005, 2013). To establish this model,

monolayers of hCMEC/D3 were cultured on the surface of transwell filter inserts coated with collagen and fibronectin fibres. Once the cells were fully grown and differentiated, the monolayer was assessed for it's BBB-like phenotype through the evaluation of cell ability to form tight junctions and measurement of cell permeability.

The *in vitro* BBB successfully acquired a BBB like architecture (Weksler et al., 2005), the brain endothelial cells grew in non-overlapping monolayers (Figure 5.4 a). The cells were joined together by tight junctions, confirmed by the positive immunostaining of the tight junction-marker protein Occludin (Furuse et al., 1994) (Figure 5.4 b). Transmission electron microscopy further showed the formation of tight junction complexes between adjacent cell membranes (Figure 5.4 c).

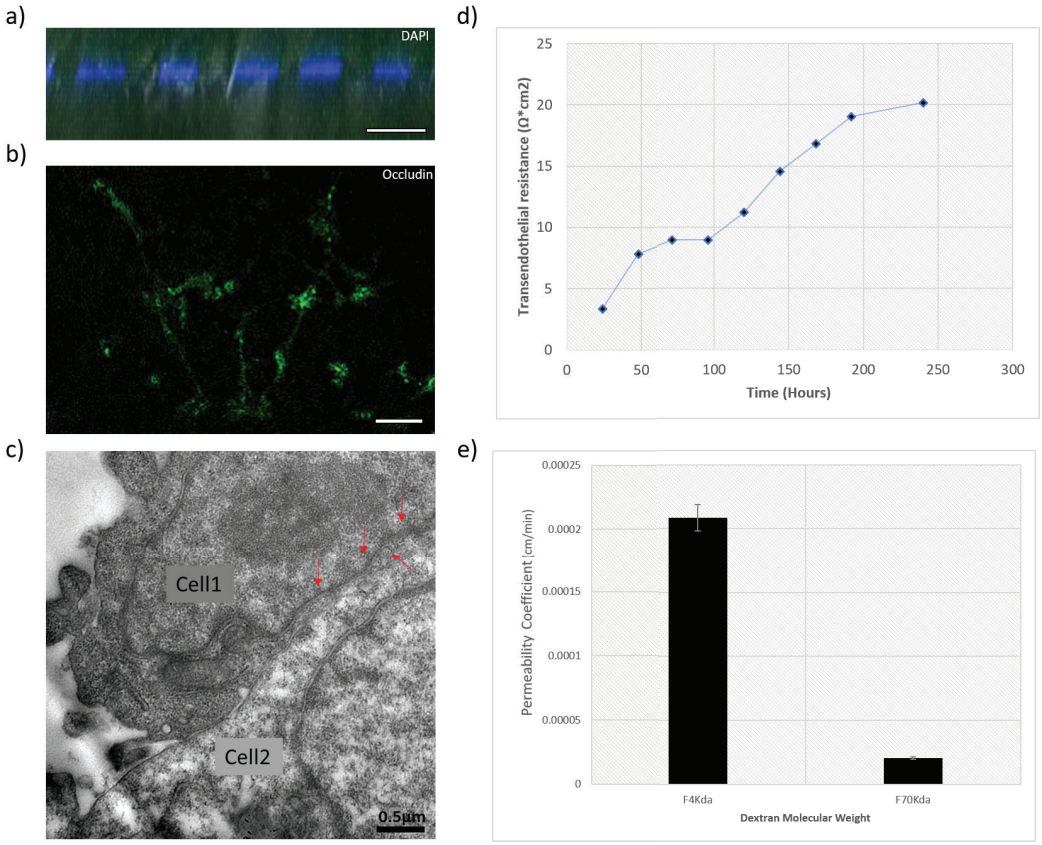


Figure 5.4: Evaluation of the *in vitro* hCMEC/D3 blood brain barrier model. The formation of non overlapping cell monolayers was shown by confocal microscopy of DAPI stained nuclei, shown in blue (a). The formation of tight junctions was confirmed by the positive staining of cells with the tight junction protein Occludin, shown in green (b) and by transmission electron microscopy, indicated by the red arrows (c). (d) Evolution of BBB transendothelial electrical resistance during 200 hours (10 days) of culture. (e) The cells model showed low paracellular permeability as evidenced by both 70kDa and 4 kDa dextran molecules.

The transendothelial electrical resistance (TEER) of the cells was monitored and following the 10 days of culture, the cell resistance registered was about 20 $\Omega.cm^2$. This value fell within the expected range of 9-50 $\Omega.cm^2$ (Biemans et al., 2016; Weksler et al., 2005, 2013).

Furthermore, the ability of fluorescently labelled flux markers with different molecular weights to cross the endothelial cells was used as a measure of paracel-

lular membrane permeability (Figure 5.4 e). Both 4 and 70 kDa FTIC (Fluorescein Isothiocyanate) dextrans revealed low paracellular permeability, comparable with previous BBB *in vitro* models (Weksler et al., 2013) (Förster et al., 2008).

5.3.3 Evaluation of nanoparticle cytotoxicity

The effects of PEGylated and transferrin conjugated nanostructures on hCMEC/D3 cells viability were evaluated. The effect of AuNPs (12 nm) and of AuStrs (25, 50 and 100 nm) was tested in a dose response study by incubating hCMEC/D3 cells with nanostructure concentrations ranging from 5 to 50 μg/mL for 24 hours. The concentration range was chosen based on a previous study on the effect of different sizes of gold nanoparticles in the mice brain microvasculature showing that between 0.8 and 50 μg/mL nanoparticles were biocompatible following 24 hour exposure (Trickler et al., 2011; Yildirimer et al., 2011).

To assess the response of cells, the cellular activity of two markers was evaluated, namely lactate dehydrogenase (LDH) and 3-(4,5-dimethylthiazol-2-yl)-5-(3-carboxymethoxyphenyl)-2-(4-sulfophenyl)-2H-tetrazolium (a MTS tetrazolium compound). MTS was used to assess the cells' metabolic activity and LDH to provide information on damage to the cell membrane.

LDH Assay

LDH is present in all cells and is confined in their cytoplasm. When disrupted, the cell membranes is unable to restrict the leakage of cytoplasmic enzymes, resulting in LDH release to the extracellular environment The concentration of LDH released can therefore be used as a marker for cell membrane damage.

Moreover in the cell culture medium LDH converts lactate to pyruvate, reducing NAD^+ to $NADH/H^+$ in the process (Weyermann et al., 2005). In the presence

of $NADH/H^+$, tetrazolium salts like iodonitrotetrazolium (INT) can be reduced, consequently yielding a characteristic red formazan, indicative of LDH activity. The formed formazan can be readily detected by spectrophotometry at 490 nm.

Initially the cells were permeabilised by the action of a triton X-100 surfactant, a known cytotoxic agent (Borner et al., 1994; Xiong et al., 2009). Following membrane lysis, the LDH released to the extracellular fluid was analysed.

Figure 5.5 shows the LDH release by hCMEC/D3 cells treated with AuNPs and AuStrs, as a function of nanoparticle concentration. Neither spherical nor star shaped Au nanostructures caused significant cellular toxicity following 24 hour exposure.

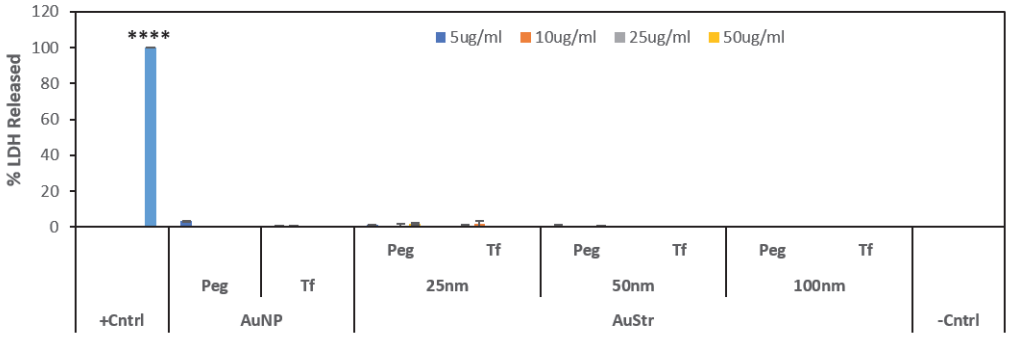


Figure 5.5: LDH viability assay of hCMEC/D3 cell cells treated with increasing doses of gold nanostructures of 5, 10, 25 and 50 μg/mL for 24 hours. hCMEC/D3 cell membrane integrity was unaffected by neither the nanostructures morphologies (AuStr and AuNP) over the treatment period. Triton was used as the positive control for toxicity and untreated cells were used as negative controls.(*p <0.05,**p <0.01,***p <0.001,****p <0.0001, n=3)

MTS assay

A cells metabolic ability can also be used as a control parameter for cellular viability. The MTS assay quantifies the enzymatic reduction of MTS to a coloured

formazan by the mitochondria of viable cells. The amount of formazan formed is directly proportional to the number of living cells in culture.

Figure 5.6 shows the cell viability measured by the conversion of MTS tetrazolium as a function of nanoparticle size and concentration. It was found that the nanoparticle's viability was not statistically lower from that of the negative control, and therefore did not impair the cells viability irrespective of the nanostructure size, surface conjugation, morphology nor concentration. For the $50\mu g/mL$, 100 nm Tf-AuStrs, the cells viability was statistically higher than that of the negative control.

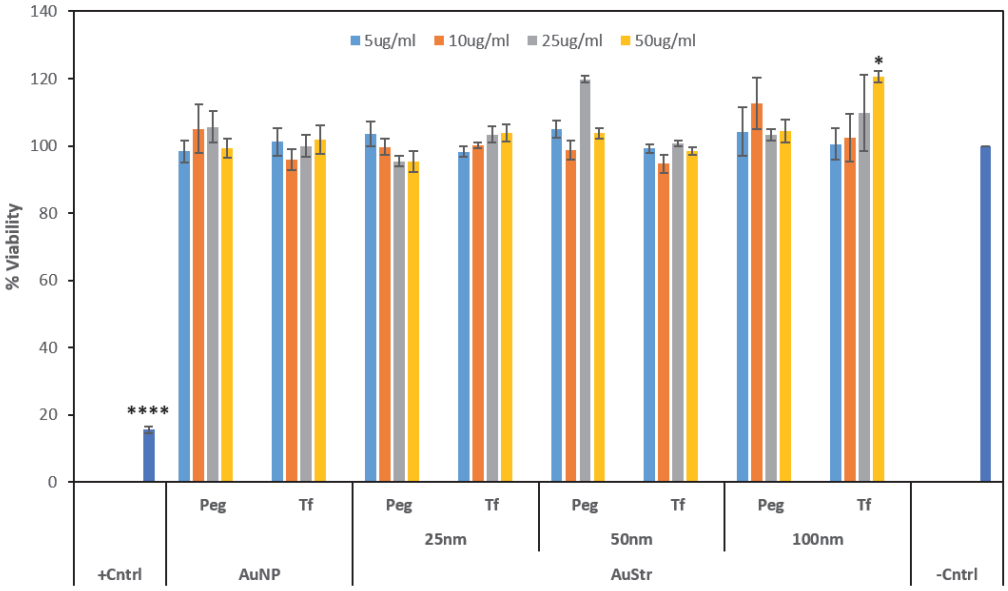


Figure 5.6: MTS viability assay of hCMEC/D3 cells treated with increasing doses of gold nanostructures of 5, 10, 25 and 50 μg/mL for 24 hours. The hCMEC/D3 cell viability was unaffected by the different AuStrs nor AuNP morphologies following 24 hr nanostructure exposure. Triton was used as the positive control for toxicity and untreated cells were used as negative controls.(*p <0.05,**p <0.01,***p <0.001,****p <0.0001, n=3)

5.3.4 TEM Investigation of Nanoparticle Uptake and Transport events

Following treatment with nanoparticles, the cell samples were resin embedded and 80 μm ultramicrotomed sections were produced for transmission electron microscopy analysis at 80 kV. The samples were surveyed to study uptake, intracellular distribution and transcytosis events. The study is initiated with hCMEC/D3 cell exposure to nanoparticles with fully developed high *aspect ratio* surface spikiness, represented by the 100 nm AuStrs modified with PEG or transferrin. Subsequently, the effect of decreasing AuStr diameter and thus decreasing spikiness *aspect ratio* in cellular events were imaged using the smaller AuStrs of 50 and 25 nm. Finally, the cellular processing of completely spherical AuNPs was investigated to elucidate the effect of morphology on hCMEC/D3 uptake, transport and transcytosis.

Effect of 100 nm AuStrs with high *aspect ratio* surface spikiness in hCMEC/D3 cell association and transcytosis

100 nm PEG-AuStr AuStrs anchor to the hCMEC/D3 cell membrane and the spikes protrude to the intracellular space (Figure 5.7 a-c). Cell protrusions were also found interacting with the AuStrs in at the apical surface (Figure 5.7 d). Gold stars were found both in the cytoplasm (Figure 5.7 e and f) and in transport vesicles (Figure 5.7 g), and still exhibited highly structured and sharp morphological features. These transport vesicles were observed both close to the apical membrane (Figure 5.7 g and h) and close to the basolateral side of the cell (Figure 5.7 g and i). A single particle was observed in the cytoplasm, near the basolateral side, in close proximity to a transport vesicle containing several nanoparticles (Figure 5.7 i). A gold nanostar cluster was found inside a large vesicle with a central narrowing

and with different electronic densities in each side of the narrowing (Figure 5.7 j). Close to the basolateral membrane, AuStrs were also found inside round vesicles of high electron density and in the cytoplasm in close proximity to these vesicles (Figure 5.7 k and i). At the basolateral membrane, PEG-Austrs were found in the cytoplasm, in very close contact with the filter surface (Figure 5.7 m) nearby a vesicle containing AuStrs, close to a filter pore. AuStrs were found in between the cell membrane and the transwell filter (Figure 5.7 n), on the basolateral side of the cell (Figure 5.7 o), and inside a filter pore.

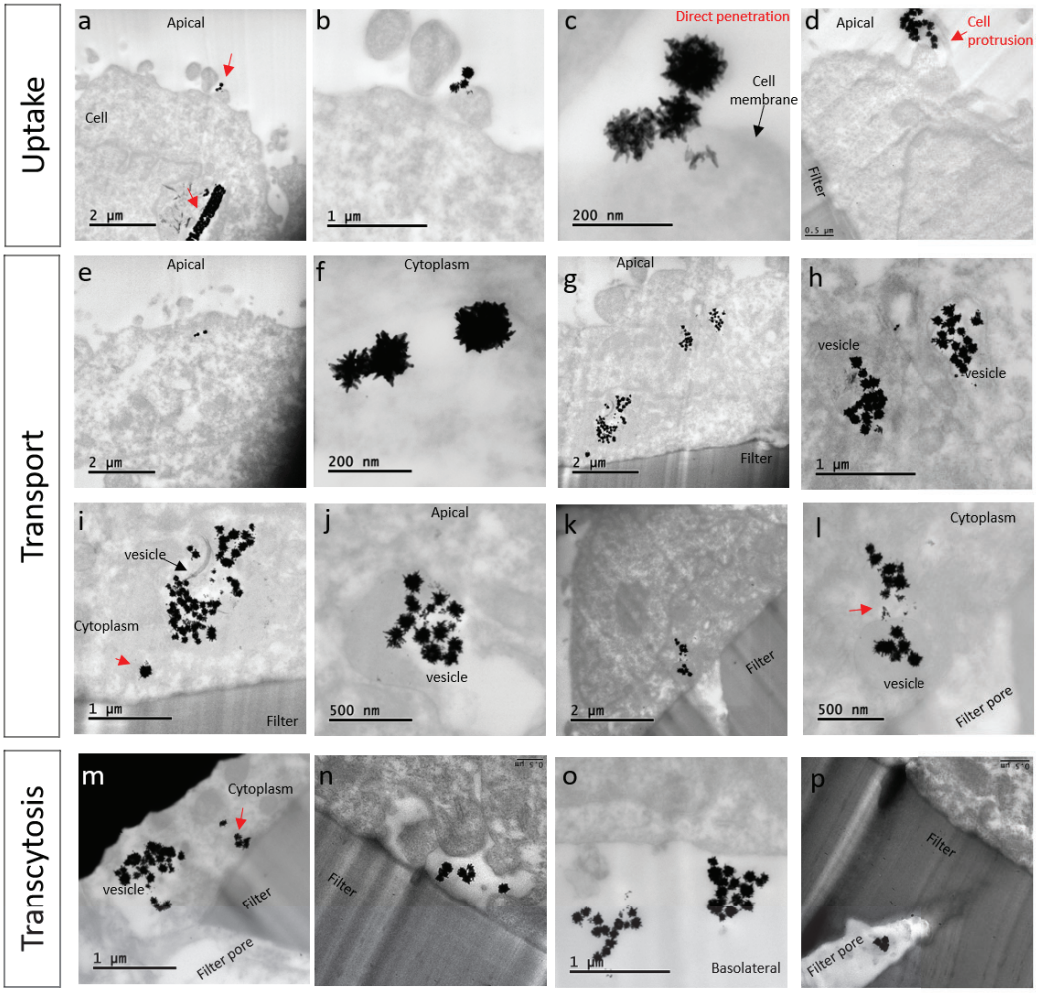


Figure 5.7: Bright field TEM images of uptake, transport and transcytosis events of 100 nm PEG-AuStrs in hCMEC/D3 cells monolayers. Cells were exposed to 50 μg/mL in assay medium containing 2.5% FBS for 24 hours. Panels a-d are representative images uptake events. Red arrows in panel a shows three AuStrs inserted into the cell membrane and a large cylindrical vesicle inside the cell. Panel b and c are higher magnification images of panel a. Panel d shows a AuStr aggregate interacting with cellular membrane protrusions (red arrow) prior to uptake. Panels e-l are representative images of intracellular transport events, with red arrows showing nanoparticles in the cytoplasm close to transport vesicles. Panels m-t are representative images of transcytosis events, with red arrows showing AuStrs in the cytoplasm close to the filter surface.

100 nm Tf-AuStr AuStrs were also found anchored to the cell surface, with the spikes facing the cell membrane (Figure 5.8 a and b). Nanostructure clusters were observed in the vicinity of the cell membrane, associated with protruding cell membrane structures (Figure 5.8 c). AuStrs clusters were also found apically, in association with the previously identified cell membrane structures (Figure 5.8 d). The plasma membrane shape grooved under the shape of the nanoparticles cluster (Figure 5.8 e). Tf-AuStrs were also found inside the cell within vesicles (Figure 5.8 f-l). Inside the vesicles the AuStrs are found attached to and aligned along the vesicle wall (Figure 5.8 f)-l). AuStr containing vesicles were observed close to the basolateral membrane (Figure 5.8 m). AuStrs were found in the space between the cell and the filter (Figure 5.8 n and o).

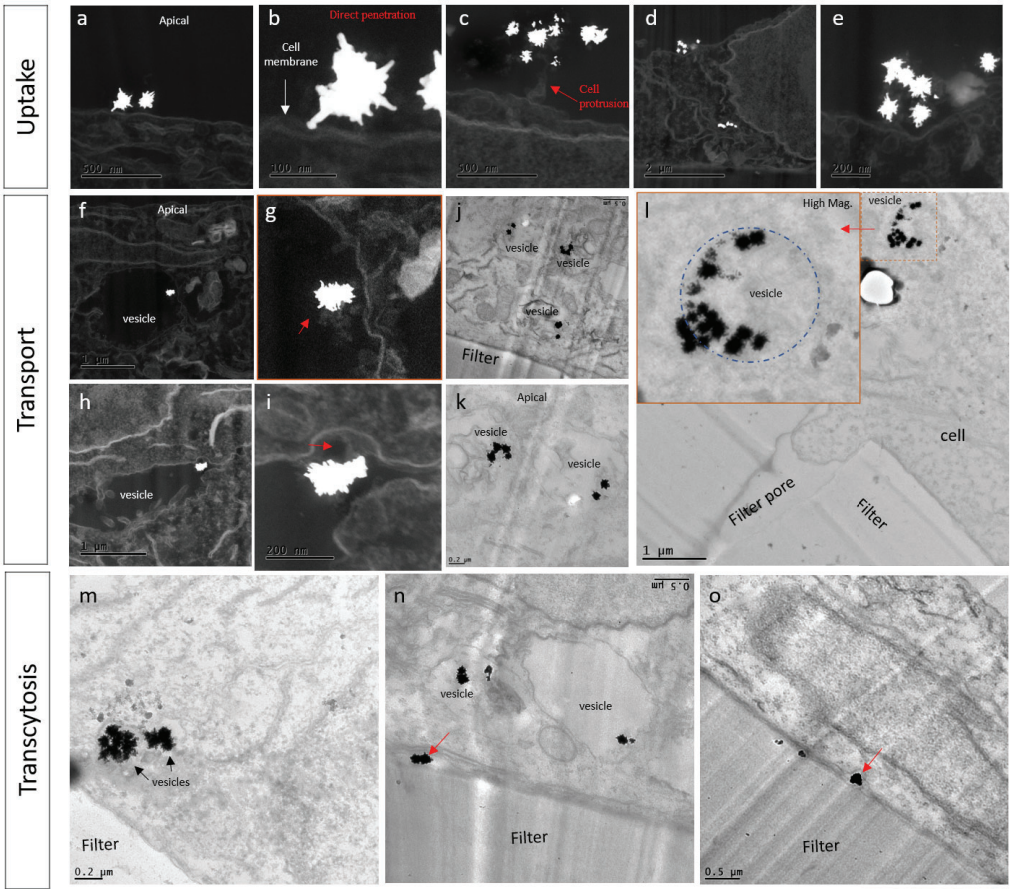


Figure 5.8: TEM images of uptake, transport and transcytosis events of 100 nm Tf-AuStrs in hCMEC/D3 cells monolayers. Panels a-i were obtained in HAADF-STEM mode and panels j-o were obtained in bright field mode. Cells were exposed to 50 μ g/mL in assay medium containing 2.5% FBS for 24 hours. Panels a-e are representative images of uptake events. Panel b and e are higher magnification images of the AuStr entry events observed in panel a and d respectively. Panels f-i are representative images of intracellular transport events, with red arrows showing nanoparticles attached to the vesicle wall. Panels m-o are representative images of transcytosis events, with red arrows showing nanoparticles between the basolateral membrane and the filter surface.

Effect of decreasing AuStr diameter on hCMEC/D3 cell association and transcytosis

50 nm PEG-AuStr AuStr aggregates were observed in the apical side in the vicinity of the cells (Figure 5.9 a and b). AuStrs were internalized by the cells and

the vesicles containing nanostructure aggregates are found close to the basolateral membrane 5.9 c-f). AuStr aggregates and individual AuStrs were released in the pore of the transwell filter (Figure 5.9 g). Nanoparticles were found between the filter and the basolateral membrane (Figure 5.9 h).

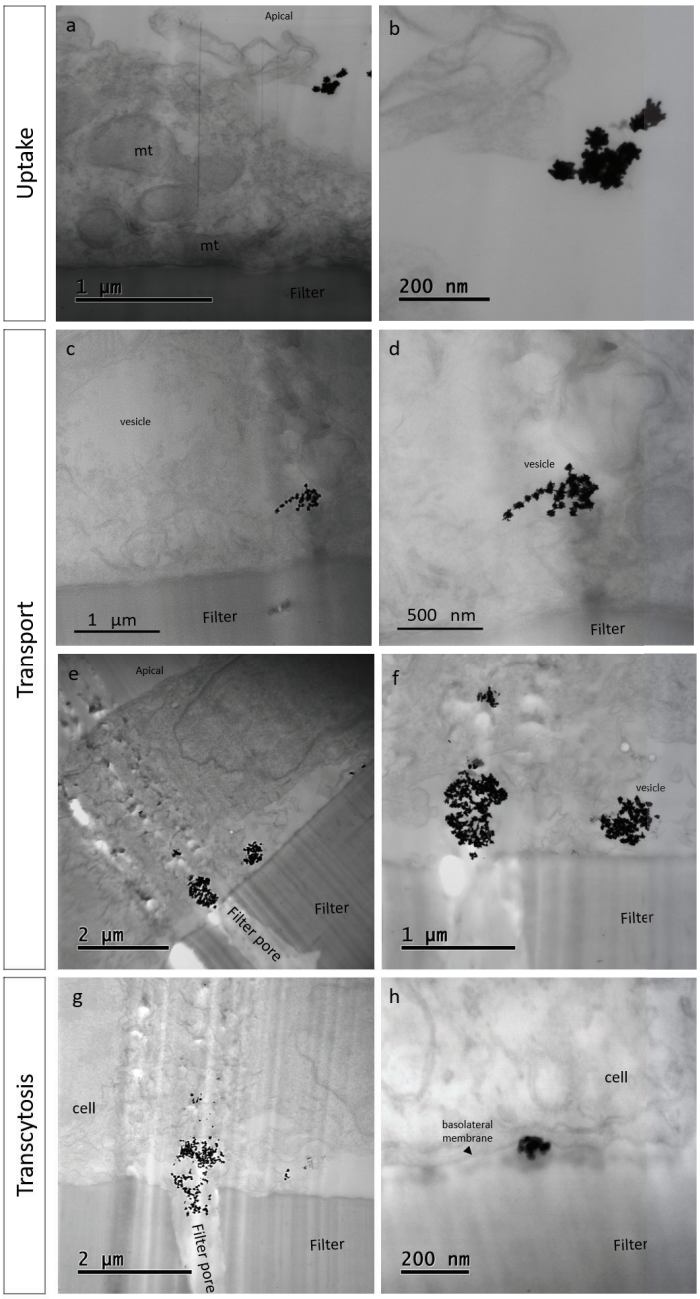


Figure 5.9: Bright field TEM images of uptake, transport and transcytosis events of 50 nm PEG-AuStrs in hCMEC/D3 cells monolayers. Cells were exposed to 50 μg/mL in assay medium containing 2.5% FBS for 24 hours. Panel a and b are representative images of uptake events, with panel b being a higher magnification image of panel a. Panels c-f are representative images of intracellular transport events, with panels d and f being higher magnification images of panels c and e, respectively. Panels g and h are representative images of transcytosis events.

It was observed that AuStrs in between the filter and basolateral membrane were surrounded by a dark halo (Figure 5.10 a-c). EDS analysis of these nanostructures is presented in Figure 5.10 d).

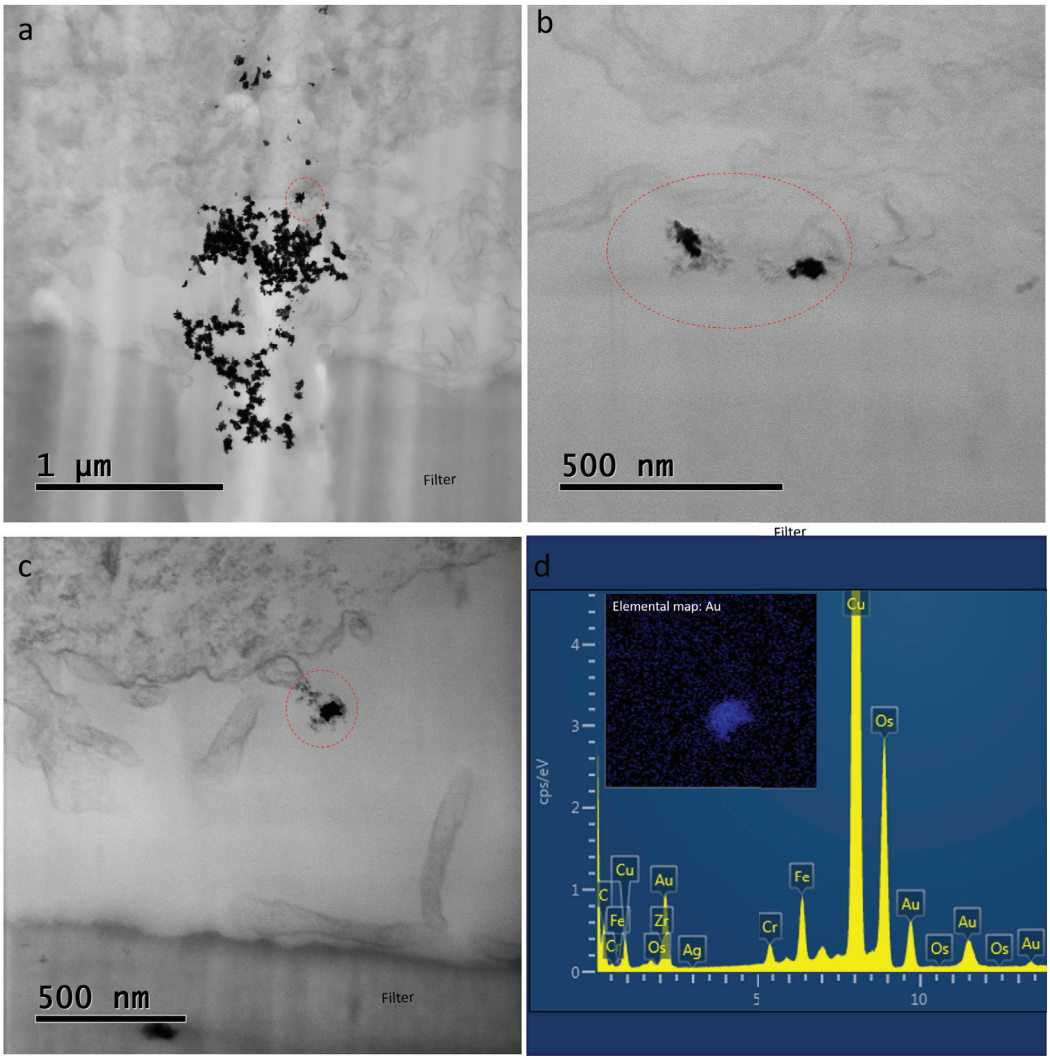


Figure 5.10: Bright field TEM images of transcytosis events of 50 nm PEG-AuStrs in hCMEC/D3 cells monolayers. In panel a-c red circles highlight nanoparticles surrounded in a dark halo following crossing of the basolateral membrane. Panel d shows the EDS spectra of the nanoparticle in panel c. The detected osmium signal is due to the AuStr proximity to the osmium stained cells.

Tf-AuStr 50 nm 50 nm Tf-AuStrs with spikes interacted directly with the apical cell membrane (Figure 5.11 a and b). 50 nm Tf-AuStrs aggregate interacted with the cell membrane at the apical side next to a small cell protrusion (Figure 5.11 c and d). Gold star cluster were observed in close association with the apical membrane covered by a protruding cell membrane structure (Figure 5.11 e and f). Gold clusters were also found inside vesicles in close association with the vesicles' membranous components in the vicinity of the basolateral side of the hCMEC/D3 cells (Figure 5.11 g-i). AuStr clusters were observed inside transport vesicles inside the cell and close to the basolateral membrane (Figure 5.11 j-l).

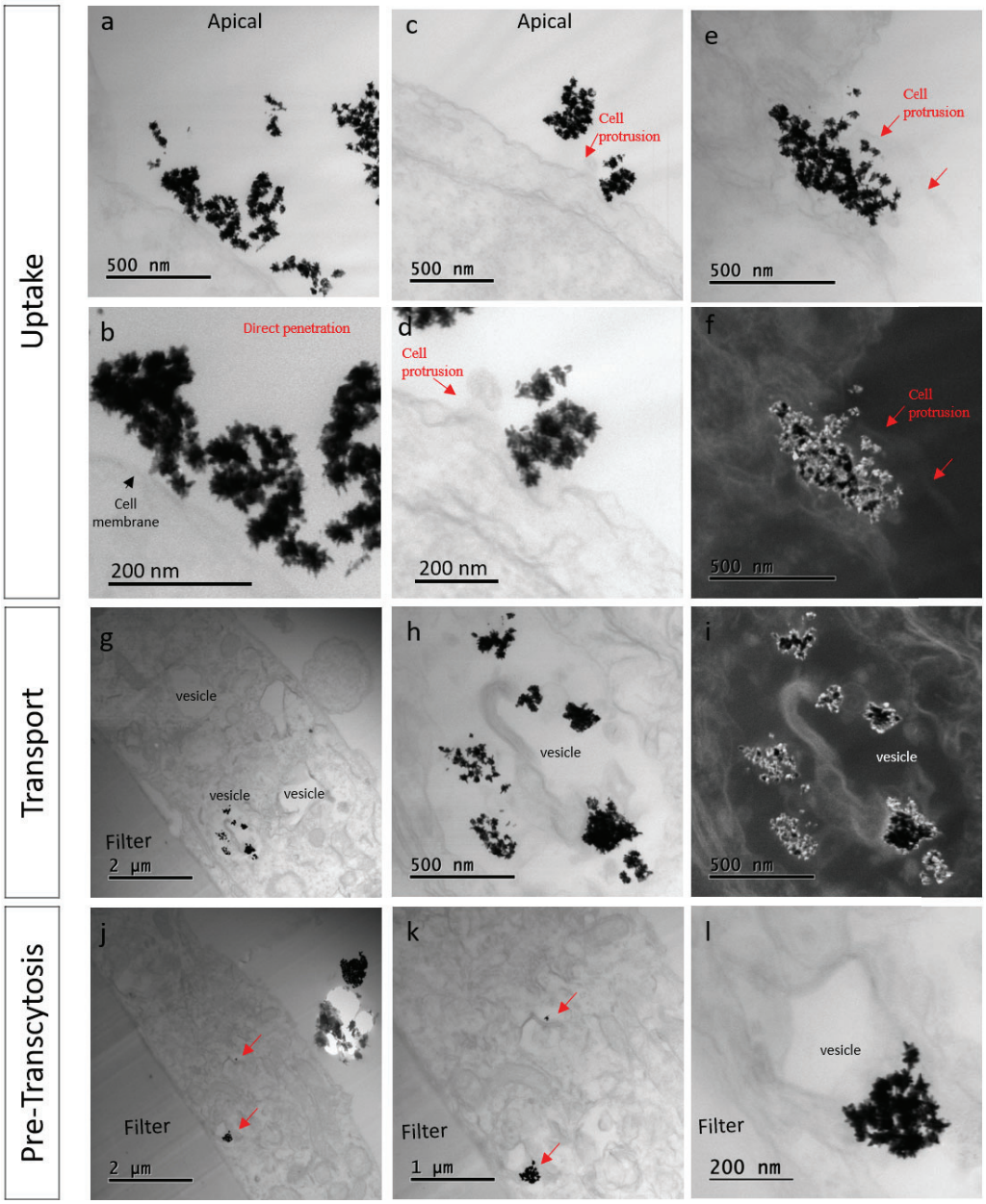


Figure 5.11: TEM images of uptake and transport events of 50 nm Tf-AuStrs in hCMEC/D3 cells monolayers. All panels except f and i were obtained in bright field mode and panels f and i were obtained in HAADF-STEM mode. Cells were exposed to 50 μg/mL in assay medium containing 2.5% FBS for 24 hours. Panel a-f are representative images of uptake events, with panels b and d being a higher magnifications images of panels a and c, respectively. Panel f is a representative HAADF-STEM image of panel e. Panels g-i are representative images of intracellular transport events, with panels h and i being higher magnification images of panels g in bright field and HAADF-STEM modes, respectively. Panel j is a representative image of pre-transcytotic events with panel k and l being higher magnification images of panel j.

25 nm PEG-AuStr Aggregates of 25 nm Peg-AuStrs were found anchored to the cell membrane with sharp edges penetrating the cell membrane (Figure 5.12 a-c). Aggregates of 25 nm PEGylated AuStrs were observed in close association with cells' apical surface and enveloped in membranous structures (Figure 5.12 d-f). AuStrs were found inside heavily loaded vesicles intracellularly. Individual gold nanoparticles were also found in the cytoplasm in proximity to these vesicles (Figure 5.12 g-i).

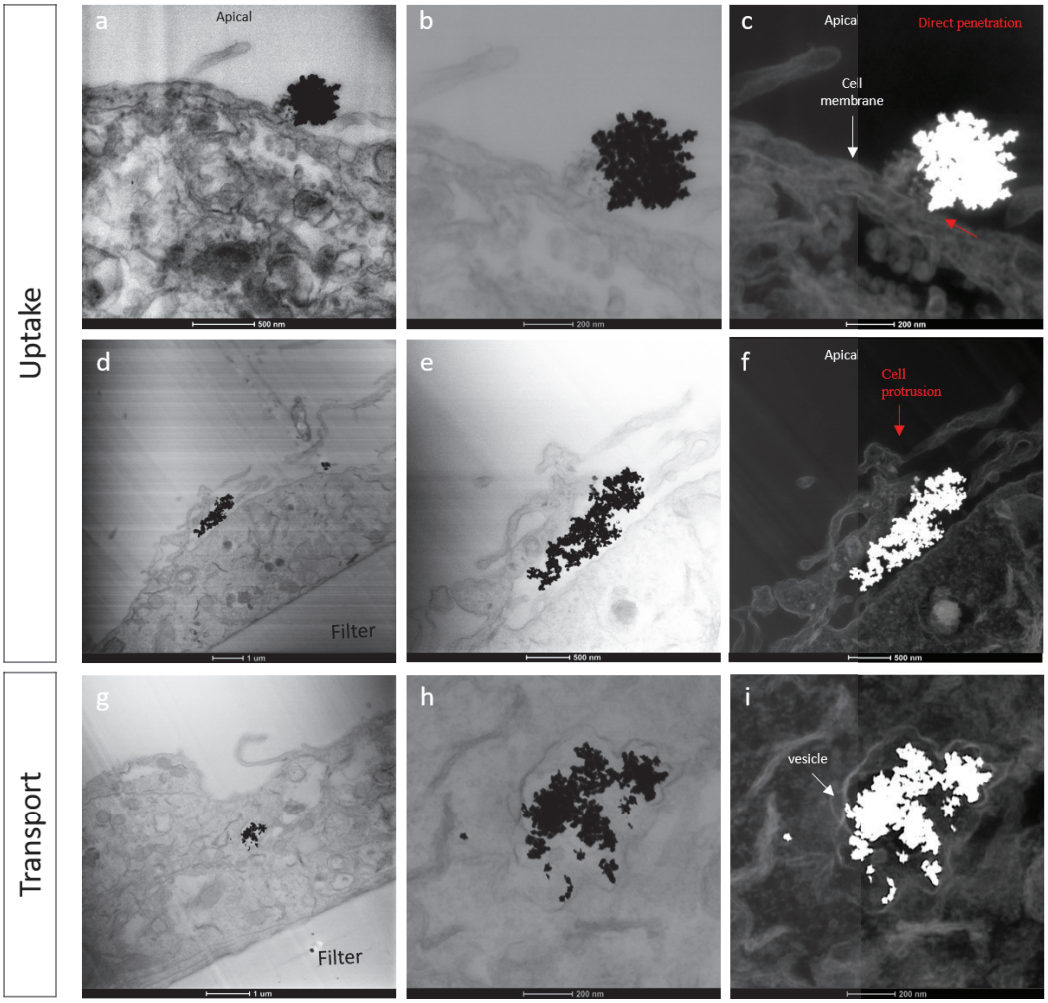


Figure 5.12: TEM images of uptake and transport events of 25 nm PEG-AuStrs in hCMEC/D3 cells monolayers. Panels c, f and i were obtained in HAADF-STEM mode, with the remaining panels being obtained in bright field mode. Cells were exposed to 50 μg/mL in assay medium containing 2.5% FBS for 24 hours. Panel a-f are representative images of uptake events. Panels b and c are higher magnifications images of panel a in bright field and HAADF-STEM modes, respectively. Panels g-i are representative images of intracellular transport events, with panels h and i being higher magnification images of panel g in bright field and HAADF-STEM modes, respectively.

25 nm Tf-AuStr AuStrs were found inside vesicles close to the apical membrane (Figures 5.13 a-b). Numerous AuStrs were found inside transport vesicles both as individual particles and as aggregates (Figures 5.13 c and d). Nanoparticles successfully crossed the cells and were found between the cell and the transwell filter in a linear arrangement (Figures 5.13 e and f) and also as aggregates (Figure 5.13 g and h).

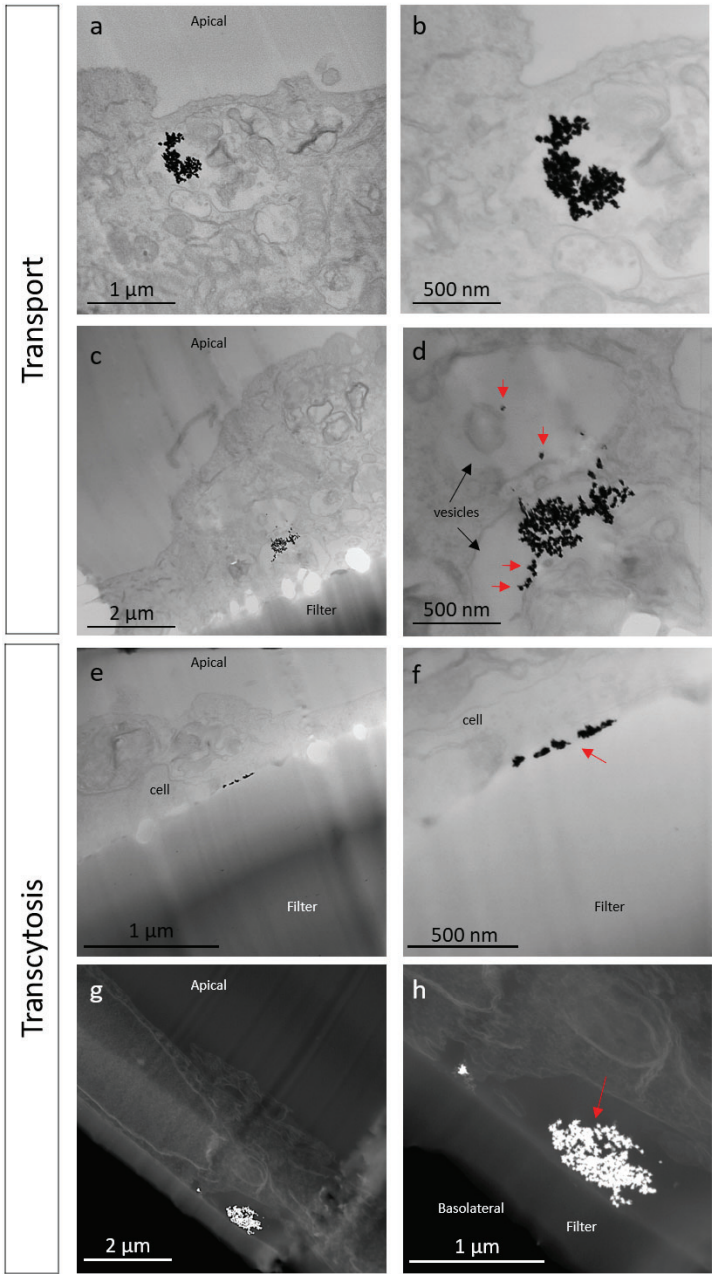


Figure 5.13: TEM images of uptake, transport and transcytosis events of 25 nm Tf-AuStrs in hCMEC/D3 cells monolayers. Panels a-f were obtained in bright field mode, with panels g and h being obtained in HAADF-STEM mode. Cells were exposed to 50 μg/mL in assay medium containing 2.5% FBS for 24 hours. Panel a and b are representative images of uptake events, with panel b being a higher magnification image of panel a. Panels c and d are representative images of intracellular transport events, with panel d being a higher magnification images of panel c. Panels e-h are representative images of transcytotic events. Panels f and h are higher magnification images of panels e and g, respectively.

Effect of smooth spherical morphology in hCMEC/D3 cell association and transcytosis

PEG-AuNP Unlike the gold nanostars, AuNPs were mainly found as individual entities inside intracellular compartments 5.14 (a-d). Occasionally, vesicles containing a larger amount of spherical gold nanoparticles were identified 5.14 e and f).

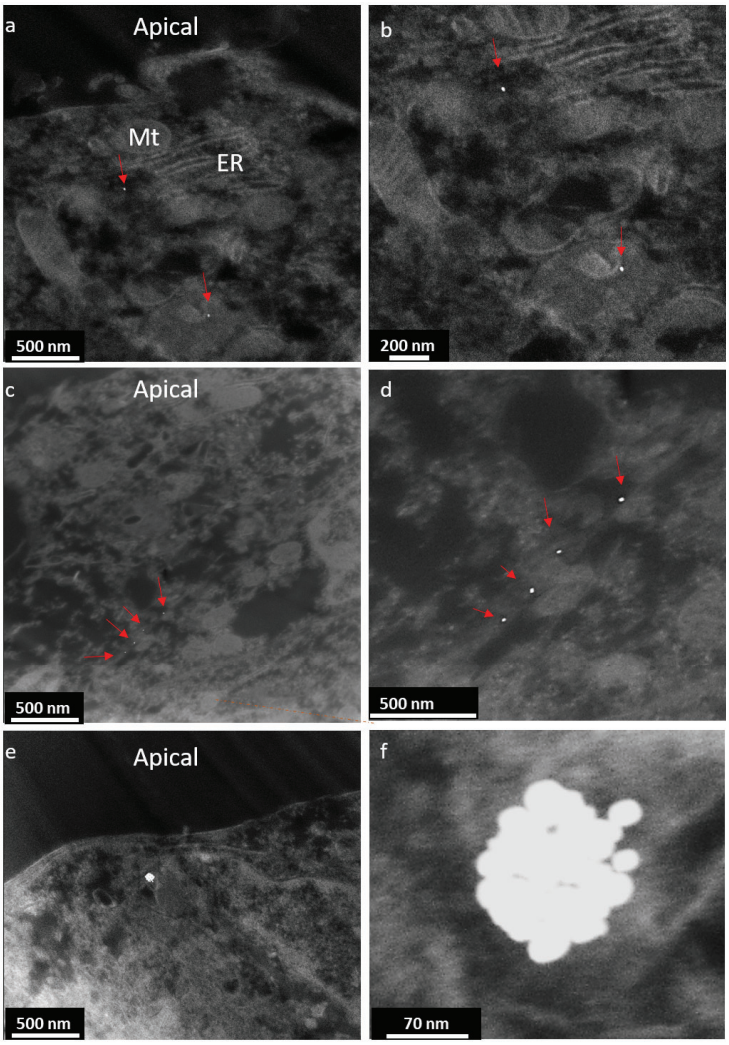


Figure 5.14: HAADF-STEM images of PEG-AuNPs in hCMEC/D3 cells monolayers. Cells were exposed to 50 μg/mL in assay medium containing 2.5% FBS for 24 hours. Panels a-f are representative images of transport events and intracellular distribution of the nanoparticles. Panels b, d and f are higher magnification images of panels a, c and e, respectively.

Tf-AuNP Tf-AuNPs were found intracellularly inside transport vesicles of low electronic density 5.15 a). These vesicles were found close to the apical and basolateral membranes. In between two neighbouring cells, a small plasma membrane indentation was found in the proximity of an internalized AuNP 5.15 b). In these vesicles the NPs aligned along the wall either directly or interacting with a vesicle wall component 5.15 c and d). This event also occurred for Tf-AuNP aggregates that were observed engaging with the vesicular wall components 5.15 c and d). Several single nanoparticles were imaged inside electronically dense vesicles 5.15 f).

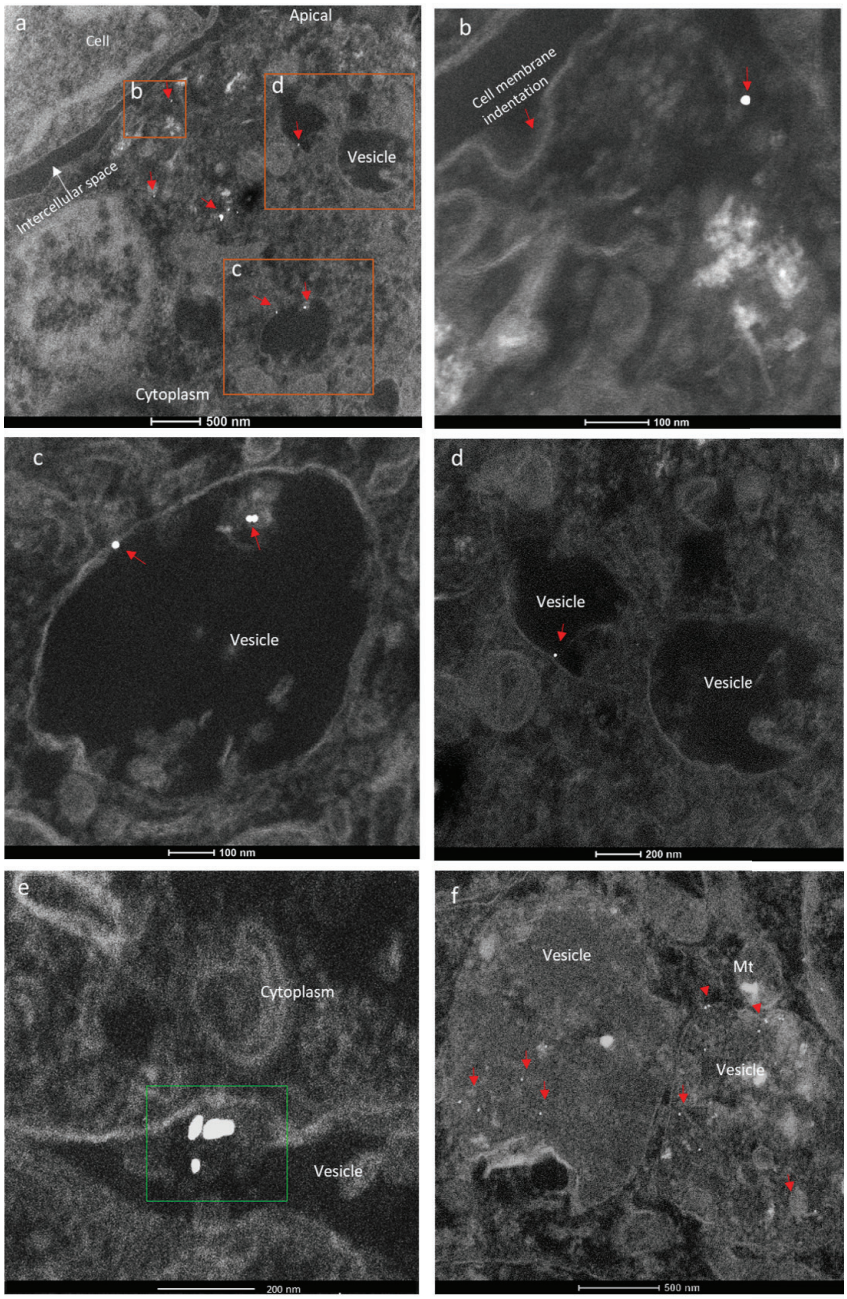


Figure 5.15: HAADF-STEM images of uptake and transport events of Tf-AuNPs in hCMEC/D3 cells monolayers. Cells were exposed to 50 μg/mL in assay medium containing 2.5% FBS for 24 hours. Panel a is a representative image of uptake and transport events. Panel b is a higher magnification image of panel a, showing a cell membrane indentation. Panel c and d are higher magnification images of panel a, showing vesicular transport. Panels e and f are representative images of transport events.

Tomography of hCMEC/D3 cells exposed to 100 nm PEG-AuStrs The previously presented images were obtained by transmission electron microscopy which generates two-dimensional (2D) projections of the sample being imaged. However, one of the disadvantages of imaging samples in 2D is the superimposition of the features of the sample present at different depths and thus it is not possible to assess the sample position along the direction of the electron beam. In focused ion-beam (FIB)-SEM tomography, sequential 2-D images of the area of interest in the sample are acquired at a 52 degree angle and the information collected is used to reconstruct a three-dimensional (3D) volume to represent the original object. FIB tomography was used in this section to gain further insights into the intracellular distribution of the gold nanostructures and map transcytosis events. The collection of data for tomography was performed for the 100 nm PEG-AuStrs in an attempt to further understand the effect of surface spikiness in cell events.

Figure 5.16 a) shows the 3D reconstructed monolayer of hCMEC/D3 cells exposed to 100 nm PEG-AuStr. A large number of AuStrs were found both on the surface of the endothelial cells and intracellularly, inside a vesicle close to the basolateral membrane (Figure 5.16 b and d). Figure 5.16 d) shows a side view of the monolayer where multiple transcytotic points can be observed.

Figure 5.17 shows the different stages of interaction of the 100 nm PEG-Austrs with the hCMEC/D3 cells, and in particular emphasises sites of nanostructure transcytosis. The nanostructures were found associated to the cell membrane (Figure 5.17 a and I). A group of AuStrs was found possibly in an early stage of uptake, the nanostructures were found enveloped in the apical surface of the plasma membrane in an enclosure that sits above the cell level (Figure 5.17 b and II). A large group of nanostructures was observed inside the cell close to the basolateral membrane (Figure 5.17 b). Vesicles containing AuStrs fuse with the basolateral membrane

(Figure 5.17 c and III). Several sites of transcytosis were identified in the basolateral side of the cell monolayer, marked by the red arrows in Figures 5.17 a), c), d), IV and V.

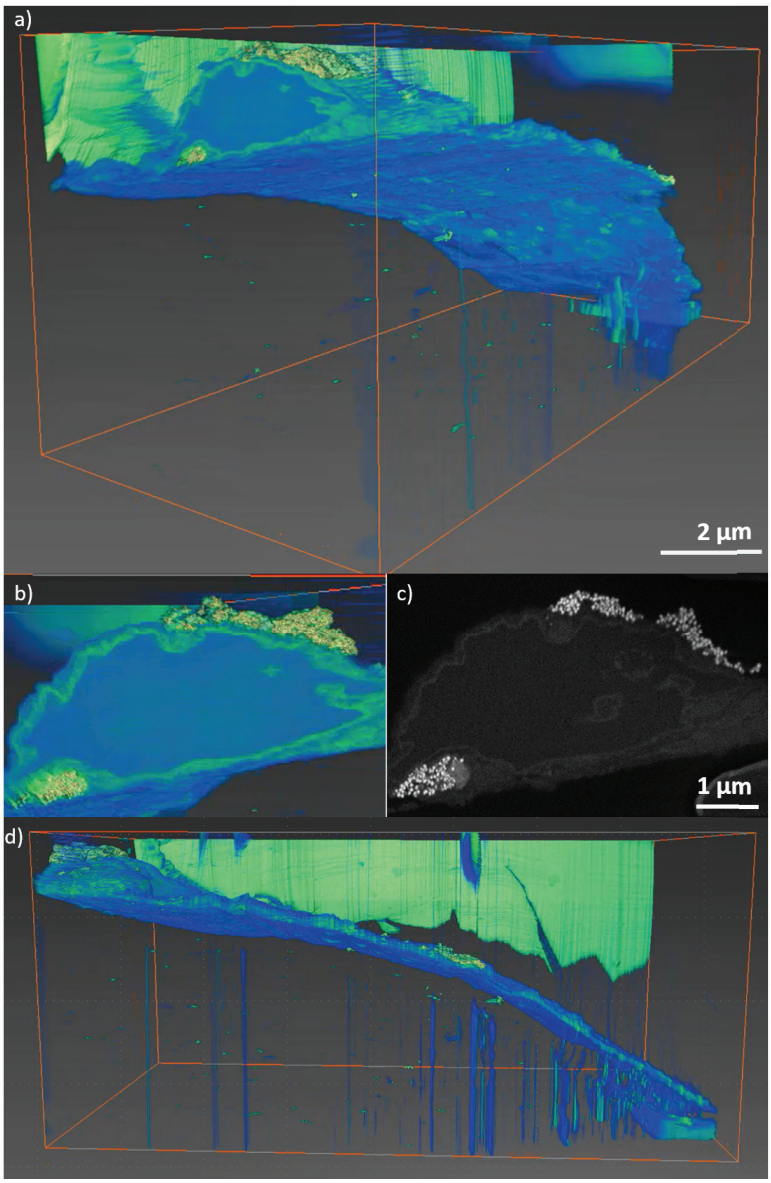


Figure 5.16: (a) 3D tomographic reconstructution model of hCMEC/D3 monolayers exposed to 50 μg/mL of 100 nm PEG-AuStr for.The cells are shown in blue and the areas of high intensity corresponding to the AuStrs are shown in gold. (b) A large cell in the monolayer with AuStrs aggregates on the cell membrane surface and inside the cell close to the basolateral membrane. (c) SEM image of the cell in planel (b). (d) Lateral view of the 3D cell monolayer model.

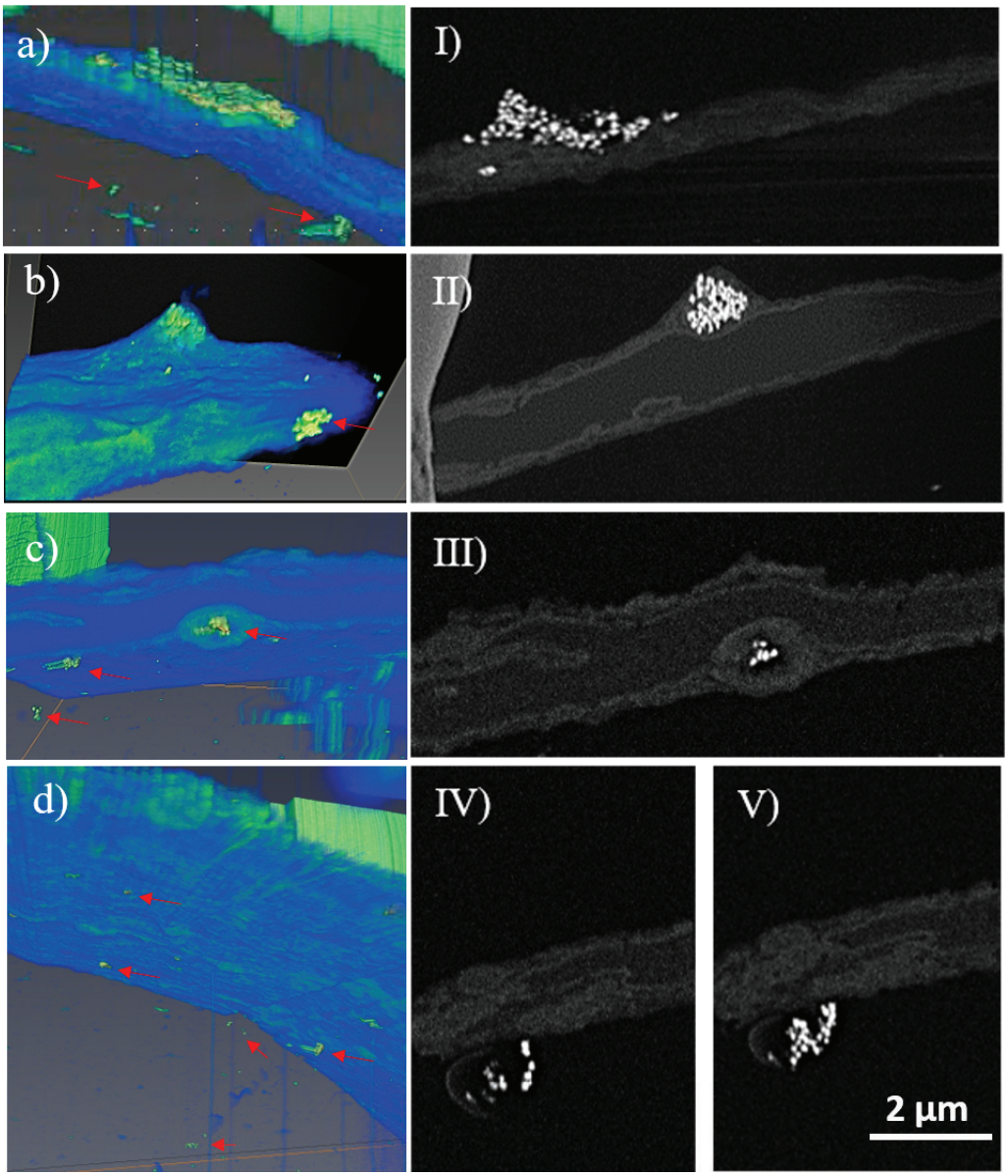
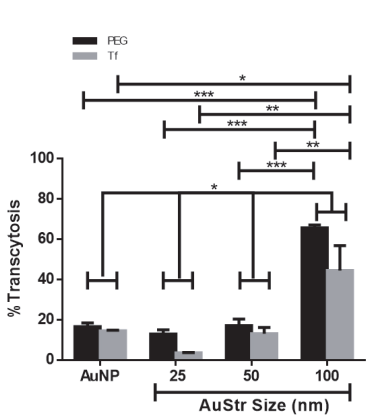


Figure 5.17: Tomographic investigation of uptake, transport and transcytosis of 100 nm PEG-AuStrs across hCMEC/D3 cells following 24 hour exposure. The 3D reconstrution was performed in the software Avizo lite. Panels (a) to (d) show 3D volume reconstructions of the cell monolayer (I) to (V) show the corresponding FIB-SEM images of the depicted 3D events. The 3D volume reconstructions and the FIB-SEM images revealed AuStrs at different stages of interaction with the cells. (a) and (I) nanoparticles closely engaged with the apical side of the blood brain barrier and crossing the cell monolayer (a). b) and II) Nanoparticles are observed enveloped in the plasma membrane lipid bilayer. A group of AuStrs can also was also found intracellularly close to the basolateral membrane (b). (c) and (III) Nanoparticles enclosed in transport vesicle.AuStr transcytotic events can also be observed in the volume reconstruction (c). (d) and (III- IV) Nanoparticles successfully found on the basolateral side of the blood brain barrier The red arrows in 3D BBB volume reconstruction represent the multiple transcytosis events. The cell cytoplasm is shown in blue and the areas of high intensity shown in yellow represent the AuStrs.

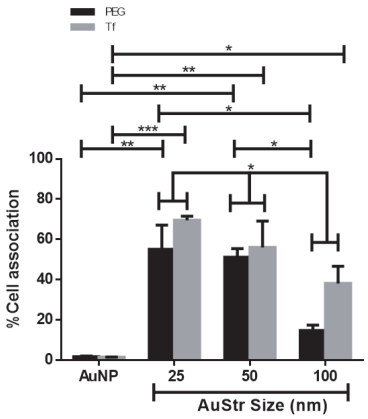
5.3.5 Quantification of nanostructure transcytosis across the BBB

To understand the influence of nanoparticle geometry and surface functionalisation (transferrin and PEG) on the nanostructures ability to complete transcytosis, endothelial cell monolayers cultured on porous transwell inserts were incubated with different nanostructure formulations for 24 hours. The nanoparticles' cell association and transport across the hCMEC/D3 cells were analysed by quantifying the recovered amount of gold from three different compartments in the transwell cell model: apical, cell and basolateral using ICP-OES. The apical fraction consists of gold nanoparticles recovered in the cell culture medium. The cell associated fraction consists of gold nanostructures that are bound to the cell membrane and inside the cells. Finally the transcytosed fraction consists of gold nanostructures that had successfully crossed the cells, diffused through the pores and reached the basolateral compartment. It is important to note that the basolateral fraction does not account for nanoparticles entrapped between the cells and the filter, or attached to the 1 μm filter pores.

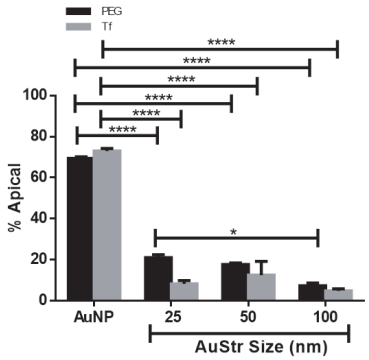
Figure 5.18 presents the Au content measured in the apical, cell and basolateral compartments, for AuNPs and AuStrs with both PEG and Transferrin surface coatings. The sample means were compared with a two way ANOVA and a Sidak multiple comparisons test was performed with a 90% confidence interval. The following sections will focus on the effect of morphology, AuStr diameter and transferrin coating on cell association and transport.



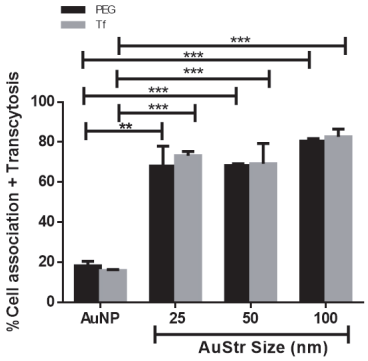
(a) Au recovered in basolateral fraction



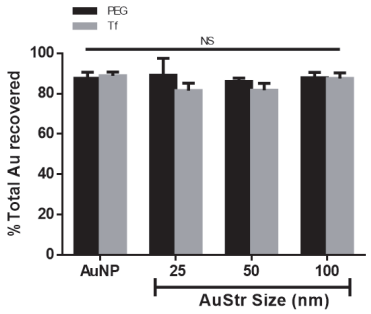
(b) Au recovered in cells



(c) Au recovered in apical fraction



(d) Summed cell association and transport



(e) Total gold recovered

Figure 5.18: Transcytosis of PEGylated and transferrin conjugated gold nanostructures across hCMEC/D3 monolayers cultured on transwell filters. Graphs showing the effect of particle morphology, diameter and surface conjugation (Tf or PEG) in: (a) transcytosis, (b) cell association, (c) apical, (d) summed cell association and transport and (e) total Au recovered (*p<0.1, **p<0.01, ***p<0.001, ****p<0.0001). Nanoparticles were added to the apical compartment and incubated for 24 hours. Cells were treated with 50 μg/mL nanostructure solution for 24 hours. The amount of gold in the apical, cellular and basolateral compartments were quantified by ICP-OES. The values are expressed as percentage of the administered dose of gold.

Effect of Morphology on cell association and transport

To study the effect of nanoparticle morphology on both cell-association and transcytosis, PEG-AuNPs were compared to 100 nm PEG-AuStrs. It was found that over the 24 hour experimental period, the 100 nm PEG-AuStrs transcytosed across the hCMEC/D3 cells in a significantly higher percentage than PEG-AuNPs (***p<0.001, Figure 5.18a). Specifically, $65.7 \pm 1.4\%$ of the administered dose of 100 nm PEG-AuStrs reached the basolateral compartment comparatively to $16.6 \pm 1.9\%$ of the PEG-AuNPs. The 100 nm PEG-AuStrs showed a higher cell association percentage ($14.8 \pm 2.7\%$) than the PEG-AuNPs ($1.71 \pm 0.37\%$), however this difference was not statistically significant. When the percent cell association and transcytosis are summed, there is a statistically significant difference between 100 nm PEG-AuStrs ($80.5 \pm 1.3\%$) and PEG-AuNPs ($18.3 \pm 2.2\%$) (***p<0.001, Figure 5.18d)), thus showing that the change in morphology had an overall significant effect. A significantly lower percentage of 100 nm PEG-AuStrs were recovered apically ($7.4 \pm 1.3\%$) comparatively to PEG-AuNPs ($69.34 \pm 0.76\%$) (****p<0.0001, Figure 5.18c). Subsequently, we proceeded to investigate how these trends varied for different AuStr diameters.

Effect of AuStr diameter on cell association and transport

To evaluate the effect of AuStr diameter on both cell association and transcytosis, hCMEC/D3 cells were incubated with AuStrs of increasing diameters (25, 50 and 100 nm). The percent nanoparticles that undergo transcytosis changed significantly with AuStr diameter. Decreasing the PEG-AuStr size from 100 to 50 nm decreased the percentage transcytosis from $65.7 \pm 1.4\%$ to $17.1 \pm 3.3\%$ (***p<0.001, Figure 5.18a). Further decreasing the PEG-AuStr size from 100 to

25 nm caused transcytosis to decrease further to $12.9 \pm 2.1\%$ (***p<0.001, Figure 5.18a). Whilst the average percentage of transcytosis decreased with decreased PEG-AuStr diameter, no statistically significant difference was found between the two small PEG-AuStr diameters of 25 and 50 nm. In fact, there was no statistically significant differences between the percentage of transcytosis of spherical PEG-AuNPs and that of the 25 nm and 50 nm PEG-AuStrs. This indicates that only the 100 nm PEG-AuStrs had statistically significant percent transcytosis to the PEG-AuNPs.

The decrease in transcytosis with decreasing PEG-AuStr diameter was complementary to the percentage of the cell association fraction. Specifically, the nanostructure cell association increased significantly from $14.8 \pm 2.7\%$ to $55 \pm 12\%$ when the Peg-AuStr diameter decreased from 100 nm to 25 nm (*p<0.1, Figure 5.18b). In contrast to transcytosis, the percent cell association for 25 nm and 50 nm AuStrs was significantly higher than that of PEG-AuNPs (**p<0.01, Figure 5.18b).

Overall the summed cell associated and transcytosis fractions were similar for all the PEG-AuStr diameters, being on average $72.3 \pm 3.7\%$ with no statistical differences between AuStr sizes. The percentage of gold resulting from the summed cell-associated and transcytosis fractions was significantly lower for the PEG-AuNPs comparatively to 25 nm (**p<0.01, Figure 5.18d), 50 nm (***p<0.001, Figure 5.18d) and 100 nm ((***p<0.001, Figure 5.18d) diameter PEG-AuStrs.

The percentage of gold recovered apically was significantly higher for AuNPs comparatively to all AuStr diameters (****p<0.01, Figure 5.18c).

Effect of transferrin on cell association and transport

Furthermore, the effect of transferrin conjugation on transport and cell association was evaluated for the spherical and star morphologies and for the different diameters. In general, transferrin conjugated Au nanostructures followed the same trends of their PEGylated counterparts. The transcytosis of Tf-AuStrs decreased from $45 \pm 12\%$ to $3.66 \pm 0.11\%$ when the Tf-AuStr diameter decreased from 100 to 25 nm.

The transcytosis of transferrin conjugated nanostructures was significantly different to that of PEGylated counterparts (*p<0.1, Figure 5.18a). In particular, in the presence of transferrin, the transcytosis efficiency of the best performing 100 nm PEG-AuStrs decreased from $65.7 \pm 1.4\%$ to $45 \pm 12\%$. The Tf-AuNP transcytosis efficiency ($14.56 \pm 0.32\%$) also decreased comparatively to PEG-AuNP ($16.6 \pm 1.9\%$).

Overall, Tf-AuStrs had a significantly higher cell-association compared to the PEG-AuStrs (*p<0.1). Specifically, transferrin conjugation increased cell association from $14.8 \pm 2.7\%$ to $38.1 \pm 8.5\%$ for 100 nm AuStrs, from $51.2 \pm 4.3\%$ to $56 \pm 13\%$ for the 50 nm Tf-AuStr. The cell association of Tf-AuNPs ($1.42 \pm 0.15\%$) was similar to that of the PEG-AuNPs ($1.71 \pm 0.37\%$).

There were no statistically significant differences for the amount of gold recovered in the assay between the PEGylated and transferrin conjugated nanostructures (Figure 5.18 e). Similarly, the summed cell association and transcytosis was not significantly different between PEGylated and transferrin conjugated nanostructures (Figure 5.18 d).

In summary, it was found that transferrin increased the association of AuStrs to the brain endothelium (cell surface bound or intracellularly) but this did not

correlate with increased transcytosis. In fact, Tf-AuStrs transcytosed less than their PEGylated counterparts for all AuStr diameters.

Validation of the transwell transport assay

The observed nanostructure transport differences are unlikely to be due to filtrations effects as bigger nanoparticles would be expected to suffer greater difficulty crossing the filter than smaller ones. Furthermore, the integrity of the monolayers following nanoparticle exposure were assessed. After 24 hrs nanoparticle exposure, the cell monolayer dextran permeability did not increase (Figure 5.19). This confirmed that the nanoparticles did not increase membrane permeability, confirming there was no loss of membrane integrity and thus invalidading a paracellular route of transport. In fact, Figure 5.20 shows that AuStrs do not open tight junctions.

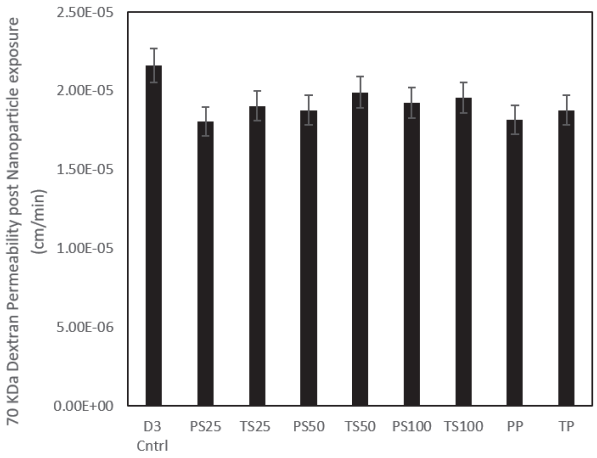


Figure 5.19: Graph showing the paracellular permeability (cm/min) of 70 KDa dextran across hCMEC/D3 cells following 24 hour nanostructure exposure at a concentration of 50 μg/mL. The D3 control group consists of untreated hCMEC/D3 cell samples. Where, PS25 is 25 nm PEG-AuStr, TS25 is 25 nm Tf-AuStr,PS50 is 50 nm PEG-AuStr, TS50 is 50 nm Tf-AuStr, PS100 is 100 nm PEG-AuStr, TS100 is 100 nm Tf-AuStr, PP is PEG-AuNP and TP is Tf-AuNP

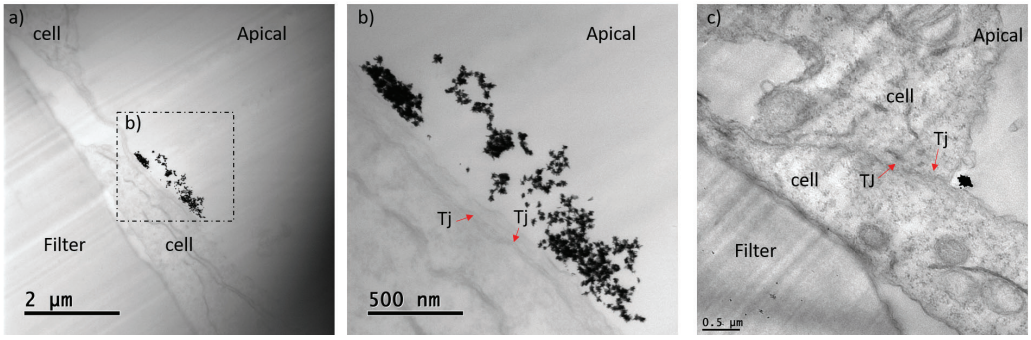


Figure 5.20: Brigth field TEM images showing AuStrs found apically above cell regions containing intact tight junctions. Panel shows (a) 50 Tf-AuStrs and panel b is a high magnification image of panel a. Panel c shows 100 nm Tf-AuStr.

Finally, the dispersity of the nanoparticles in cell media was analysed to test whether the observed size transcytosis effects were due to the extent of particle aggregation in media. PEGylated AuStrs (25, 50 and 100) and Pegylated AuNPs were suspended in FBS supplemented cell culture media and freeze-dried for TEM examination (Figure 5.21) . Freeze drying fixes the nanoparticles samples in a state resembling the one the nanoparticles have in solution. Conventional drop casting onto TEM grids may cause sample disturbances (e.g. aggregation) linked to sample preparation and not representative of the nanoparticle's dispersion state. The number of aggregates per total amount of particles analysed was counted and presented as percent aggregation (% aggregation) in Figure 5.22 a. Cryo-TEM analysis revealed that the degree of aggregation across the different sample sizes was below 5%. In fact, Figure 5.22 b shows that the majority of the nanostructures reside in solution as single entities. When present, the aggregates of 25nm PEG-AuStr were on average composed of more nanoparticles than the aggregates found in the other samples (Figures 5.21 e and 5.22 b) .

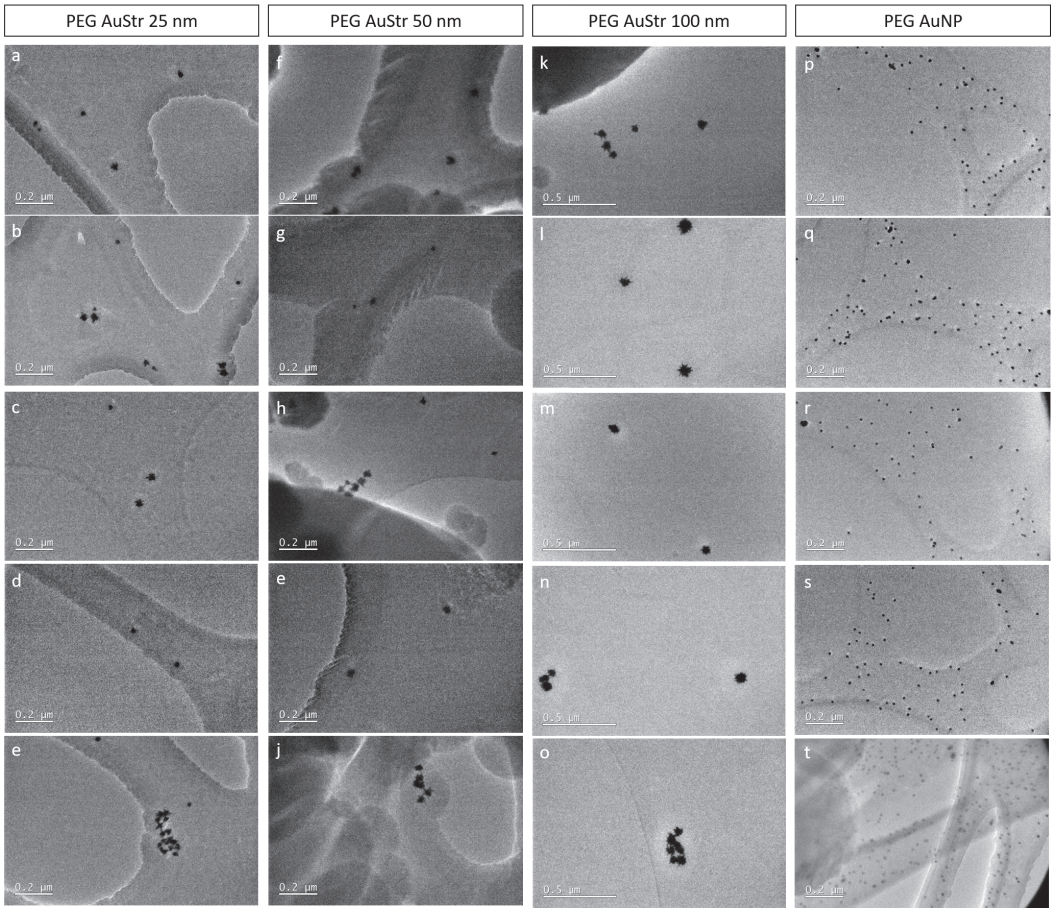


Figure 5.21: Representative cryo-TEM images of the dispersity state of PEGylated AuStrs of 25 (a-e) 50 (f-j) and 100 nm (k-o) in diameter and PEG-AuNPs (p-t) in cell culture media supplemented with 2.5 % FBS. The gold nanostructures were found mainly as single particles in cell culture medium. Gold nanostructure aggregates were occasionally observed (e, j and o)

Limitations of transwell system

Whilst transwell *in vitro* models are widely used for transport studies they are linked to a few limitations. This system does not distinguish between nanoparticles internalised by the cells and those bound to the cell surface. Additionally, nanoparticles may bind to and be entrapped on the filter pores (1μm). It is therefore important to correlate the measured quantitative findings with qualitative analysis of the nanoparticles crossing through the BBB monolayer to obtain representat-

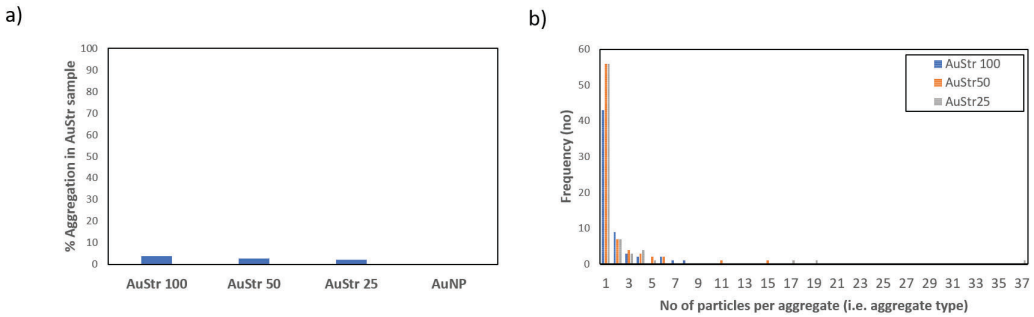


Figure 5.22: Evaluation of nanoparticle aggregation in cell culture media. (a)Graph of percent aggregation as a function of gold nanostructure type. The percent aggregation was below 5% for all the nanoparticle samples.(b) Graph showing the aggregation profile of 25, 50 and 100 nm diameter AuStr samples in the form of a frequency distribution. The majority of the stars exist in the form of single particles independently of AuStr diameter.

ive data of the nanoparticles cellular fate. It was found that transmission electron microscopy was a powerful complementary technique to ICP-OES.

5.4 Discussion

This study was structured to elucidate the influence of nanostructure's morphology and size on their ability to successfully penetrate cells and complete transcytosis. Additionally, we sought to evaluate whether this effect could be enhanced or changed when the bio-identity of the nanoparticle is changed by attachment of transferrin. The transferrin receptor was selected for nanostar targeting to the BBB as its expression is limited to the endothelium of the brain as opposed to the peripheral endothelium. Here, gold nanoparticles of two different morphologies, non-spiky nanospheres and spiky nanostars, were synthesised and their uptake and ability to cross the blood brain barrier in a safe and targeted manner were evaluated. The extensively characterised hCMEC/D3 cell line was used as a model of the blood brain barrier for these studies.

Monodispersed gold nanoparticles were synthesised in a size controlled manner, with nanostars having diameters of 25, 50 and 100 nm and gold nanospheres having 12 nm in size, as determined by TEM. Both morphologies were successfully conjugated with transferrin in a conformal manner.

5.4.1 Establishing an *in Vitro* BBB model to study nanoparticle transcytosis

In vitro models of the BBB constitute a fundamental tool for the study of the BBB and development of penetrating nanoparticle-based delivery vehicles to the brain. The brain microvasculature endothelial cell line hCMEC/D3 represents a suitable model for BBB studies as it retains many of the cellular and molecular signatures of *in vivo* endothelial cells and can be cultured in a reproducible manner. hCMEC/D3 cells were derived from microvessels of a human temporal lobe. When grown under specified conditions the cells can sustain a stable growth and characteristic endothelial markers for up to 35 cell passages.

The cells were cultured in culture plate lined with the extracellular matrix fibres collagen and fibronectin. This was done as hCMEC/D3 cells show adhesion-dependent growth under which they are able to form contact inhibited monolayers. In fact, fluorescence staining of the cells nuclei showed that the cells did not overlap in the monolayer thus indicating contact inhibition. The culture conditions also proved suitable for the cells to acquire a BBB like phenotype and express tight junction proteins. Amongst the tight junction proteins known to be expressed by hCMEC/D3 cells is occludin. The expression of occludin is optimal when the cells grow in the presence of an anti-inflamatory steroids like hydrocortisone believed to have modulatory role over tight junctions (Förster et al., 2008). Moreover, the

formation of tight junctions requires the cells to achieve full differentiation. This was achieved by stimulating a non-proliferating state (*i.e.* cellular quiescence) through the removal of a key growth factor namely vascular endothelial growth factor (VEGF) from the culture medium. However, other growth factors like the basic fibroblast growth factor (bFGF) were maintained in culture as they are known to enhance the expression of tight junctions (Weksler et al., 2013).

For the present model, the cells were allowed to grow to confluence, taking on average between 76 and 100 hours after which VEGF was removed from the culture media. As Figure 5.4 d) shows, from 100 hours onwards the transendothelial electrical resistance increased linearly and after 200 hours it started to stabilised. Transendothelial electrical resistance provides a quantitative indication of tight junction integrity or membrane tightness in an non-invasive manner (Srinivasan et al., 2015). This indicates that in between 100 and 200 hours the tight junctions successfully develop and mature, resulting in a progressively higher ohmic resistance as the cells differentiate. For *in vitro* hCMEC/D3 BBB models, cultured under static conditions, the reported TEER value is only between low and medium (9-50 $\Omega.cm^2$) (Biemans et al., 2016; Weksler et al., 2005, 2013). The maximum TEER achieved was about 20 $\Omega.cm^2$ thus falling within the above mentioned range. Previous reports indicate that TEER values increase in co-culture models with other CNS cells (*e.g.* astrocytes and pericytes) (Förster et al., 2008) and under sheer flow (Cucullo et al., 2008). Allowing further cell growth after confluency is not advisable due to cell overgrowth (Biemans et al., 2016).

Following differentiation, the cell's periphery stained positive for the tight junction protein occludin. This is consistent with this protein's location in the cell, as occludin is a known transmembrane protein located peripherally at the intercellular junctions.

Finally the permeability of the membrane to paracellular tracers was tested. hCMEC/D3 cells showed limited permeability to low and high molecular weight dextrans. The reported values for dextrans permeability are $0.72 \pm 0.07 \times 10^{-3}$ cm/min and $0.09 \pm 0.01 \times 10^{-3}$ cm/min for 4 kDa- and 70 kDa-dextrans, respectively (Weksler et al., 2013; Förster et al., 2008). The values obtained here were 0.2×10^{-3} cm/min and 0.02×10^{-3} cm/min for 4 kDa- and 70 kDa-dextrans, respectively, thus validating the BBB model.

5.4.2 Evaluation of nanoparticle cytotoxicity

Disruption of the cell's membrane occurs as a result of induced necrosis and results in the release of cytoplamic LDH into the medium (Decker and Lohmann-Matthes, 1988). The effect of PEGylated and transferrin conjugated AuStrs and AuNPs on plasma membrane permeability of hCMEC/D3 cells was evaluated using the LDH assay. The cells were treated nanoparticles at a concentration range from 5-50 μg/mL for 24 hours. The cells did not show a dose response toxicity following the exposure period.

For the MTS assay, the viability of the cells was not reduced for any of the concentrations. In fact, only the cells treated with 100 nm Tf-AuStr at a concentration of 50 μg/ml showed increase in cell viability comparatively to that of untreated cells, with statistical significance ($p<0.05$). This difference in viability between the untreated and 100 nm Tf-AuStr treated hCMEC/D3 cells could be due to differences in the metabolic activity of the treated endothelial cells. The metabolic rate (metabolic redox activity) may be stimulated in the presence of this nanoparticle formulation. Differences could also be due to differences in number of cell between the control well and this particular cell well due to volume dispensing differences or particle induced proliferation. On the other hand, the fact the coun-

terpart PEGylated 100 nm AuStr did not cause an increase in cellular activity could indicate that the presence of the iron carrier transferrin on the surface of the 100 nm star bioconstruct can affect the cell metabolism as the cells process the iron. Overall, it was found that toxicity was not dose dependent in the concentration range tested, and was not dependent on particle size or morphology.

5.4.3 TEM Investigation of Nanoparticle Uptake and Transport events

Effect of 100 nm AuStrs with high *aspect ratio* surface spikiness in hCMEC/D3 cell association and transcytosis

100 nm PEG-AuStr Individual nanoparticles were found directly interacting with the cell surface with their spikes protruding through the cell membrane (Figure 5.7 c). Successful internalization could have been facilitated by the AuStrs surface roughness at the bio-interface. Studies have shown that ensuring a perpendicular angle between areas of high curvature (spikes) and the cell membrane may facilitate cell penetration (Yang and Ma, 2010; Ding et al., 2012). Cell membrane structures that are resembling of membrane protrusions were imaged interacting with the PEGylated AuStrs at the plasma membrane (Figure 5.7 d). These protrusions resembling of cell membrane pseudopods are associated with a macropynocytotic uptake mechanism (Lim and Gleeson, 2011). Macropinocytosis is a mechanism used by the cells for the uptake of a large amount of substances in solution at the same concentration as in the surrounding medium. In fact, a large number of nanoparticles were found in large cylindrically shaped vesicles (Figure 5.7 a). Large cylindrical vesicles are observed during the maturation (tubulation) of macropynosomes which is consistent with a macropynocytic uptake (Lim and

Gleeson, 2011). Whilst clatherin-dependent endocytic vesicles are approximately 100 nm, macropinosomes by being clatherin independent, and by lacking any other type of structural coating structures, can reach sizes in between the range of 0.2 to 5μm in diameter (Lim and Gleeson, 2011).

Ye et al. (2013) reported the presence of cell protrusions in the uptake of 50 nm SiO_2 nanoparticles by hCMEC/D3 cells, thus resembling macropinocytic uptake. A macropinocytic uptake mechanism has also been reported in an *in vitro* BMVEC based model for the uptake of human immunodeficiency virus type 1 by brain macrovascular cells (Liu et al., 2002).

Following complete particle enveloping, the nanoparticles reside inside vesicles possibly entering the endosomal sorting system (Figure 5.7 g). Intracellularly, the AuStrs reside inside endosomal vesicles located both close to the apical and basolateral membranes, suggesting an apical to basolateral pathway (Figure 5.7 g). In particular, single AuStrs were found in the cytoplasm in close proximity to nanoparticle transport vesicles (Figure 5.7 i). It is possible that these single entities were able to escape into the cytoplasm from the transport vesicle by benefiting from their preserved sharp morphology (Chu et al., 2014).

Different types of vesicles could be identified inside the cells based on their electron density, due to the fact that lysosomes are characteristically electron dense vacuoles and endosomes are electron lucent vacuoles (Eskelinen, 2008), (Ye et al., 2013). During transport, the AuStrs may enter the endolysosomal pathway when endosomes containing AuStrs fuse with lysosomes. Figure 5.7 j) could illustrate the fusion between an electron-dense lysosome and an electron-lucent endosome (endolysosome). Additionally, sharp 100 nm Peg-Austrs were found in the cytoplasm in proximity to these vesicles of high electronic density (lysosomes) containing AuStrs (Figure 5.7 l). Importantly, a multispiked morphology could have

allowed the PEG-AuStrs to successfully escape endolysosomal entrapment, allowing the particle to evade the lytic pathway and resume its journey to the basolateral membrane (Figure 5.7 m).

Despite the different trafficking challenges the nanostars successfully complete transcytosis when vesicles containing 100 nm PEGylated AuStrs possibly fuse with the basolateral membrane (Figure 5.7 n) and release the nanostructures (Figure 5.7 o and p).

100nm Tf-AuStr Similarly to the their PEGylated 100nm Austr counterpart, cell membrane protrusions are observed extending from the cell surface to engage with AuStrs in the viccinity of the apical cell membrane. Specifically, the cell membrane protrusions were observed bridging the gap (50-200 nm) between the AuStrs and the cell surface (Figure 5.8 c). Above the cells the nanoparticles seem to be found in an aggregated state. As the AuStrs are negatively charged, agglomeration could occur as a result of electrostatic repulsion between the negatively charged cell glycocalyx and the AuStrs surface (Möckl et al., 2017). AuStrs were also found directly anchored onto the apical cell membrane with spikes facing the cell membrane possibly in the preliminary stages of penetration (Figure 5.8 b). Figure 5.8 e) shows a more advanced stage of internalization involving AuStrs entangled in membrane protrusions, and apical membrane topology grooved to accommodate the entry of the Tf-AuStrs.

Within the cells, 100 nm Tf-AuStrs are found inside vesicles, similarly to PEGylated 100 nm AuStrs (Figure 5.8 f-l). However, within these electron lucent vesicles (endosomes), the Tf-AuStrs were aligned along the vesicle wall (Figure 5.8 f, h and l). This engagement with the endosome could occur as a result of transferrin in the surface of the nanostars attaching to their corresponding transfer-

rin receptors on the endosomal wall (Wiley et al., 2013). This strong avidity for the endosomal wall may hinder the disengaging of the bioconstruct from the cell wall during exocytosis, thus decreasing the amount of Tf-AuStrs that can reach the basolateral compartment (Clark and Davis, 2015).

Gold stars were found between the cell and the filter (Figure 5.8 n and o), indicating successful transcytosis.

Comparison Cell membrane protrusions were identified in the uptake of both PEGylated and Tf coated AuStrs. Both types of AuStrs were also found directly anchored to the cell membrane possibly initiating penetration, indicating an additional entry route to macropinocytosis.

Alternatively to being cell protrusions, the cell structures observed could be linked to the cells glycocalyx. The internalization of the nanoparticles is subject to the interaction between the nanoparticles and the enothelial glycocalyx (eGCX) layer at the apical surface of the cell membrane. The eGCX layer is a network of membrane bound glycosaminoglycans, proteoglycans, glycoproteins, sialic acid and plasma proteins (Reitsma et al., 2007; Weinbaum et al., 2007). The eGCX has vasculoprotective properties, functioning to maintain fluid balance and in the regulation of vascular permeability (Becker et al., 2010), coagulation (Kolářová et al., 2014) and constituting a physical barrier to the interaction of blood componenents (radi $>$ 5.7 nm) (Vink and Duling, 2000) with the vascular wall (Alphonsus and Rodseth, 2014; Lipowsky, 2012).

Möckl et al. (2017) investigated the role of the endothelial glycocalyx on the uptake of 50 nm polystyrene nanoparticles in human umbilical vein endothelial cells. It was found that the glycocalyx acted as a barrier for the internalization of nanoparticles. In fact, it was possible to significantly increase the uptake of

nanoparticles into the endothelial cells when the glycocalyx was enzymatically degraded to enable the nanoparticles to reach the cell membrane. Furthermore, in the presence of the eGCX, the nanoparticles' native charge was an important determinant for their cell internalization despite particle size. Positively charged nanoparticles were able to interact with the negatively charged eGCX resulting in significantly higher uptake than that of negatively charged nanoparticles that are possibly electrostatically repelled by the eGCX. However, such charge interactions are complex events due to the presence of oppositely charged species in the media and formation of the protein corona (Pino et al., 2014).

The interaction between the negatively charged nanostructures with the positively charged glycocalyx could cause the nanostructures to aggregate at the cell surface as observed in Figure 5.8 c).

PEGylated and Tf conjugated Star shaped nanoparticles successfully iternalised hCMEC/D3 cells. Both AuStr formulations were found intracellularly inside vesicles. PEGylated AuStrs were found evenly distributed within these vesicles and also in the cytosol in the vesicles' vicinity. Tf-AuStrs, on the other hand, aligned to the endosomal wall and were not found in the cytosol close to vesicles. PEG-AuStrs cytososlic presence possibly reflects the ability of PEG-AuStrs to escape to the cytosol during vesicular transport. The morphology of the 100 nm AuStrs, with both PEG and Tf coatings, within the intracellular environment was not altered. Even though Tf-AuStrs share the same sharp geometrical features to PEGylated AuStrs, Tf-AuStrs attachment to the endothelium could halt their escape from the vesicles, thus explaining the lack of transferrin particles in the cytosol close to transport vesicles.

Both formulations showed the ability of successfully completing transcytosis, having been found in between the basolateral membrane and the filter.

Effect of decreasing AuStr diameter in hCMEC/D3 cell association and transcytosis

50 nm PEG-AuStr 50 nm PEGylated AuStrs were found next to protruding cell membrane structures in an aggregated state in the apical side (Figure 5.9 a) possibly due to electrostatic interaction with glycocalyx (Möckl et al., 2017). Inside the cells the AuStrs aggregates were densely packed inside vesicles (Figure 5.9 f). 50 nm PEGylated AuStrs are released in the basolateral side both as single particles and as aggregates (Figure 5.9 g). This indicates that nanoparticles can be transported in both forms inside the vesicles.

Additionally, individual AuStrs were also observed successfully completing transcytosis. Some of these AuStrs were surrounded by a dark halo in BF-TEM micrographs (Figure 5.9 d) indicating the presence of surrounding biomolecules (e.g. lipids). It is possible that the nanoparticles cause some lipid loosening on their exit from the cell. This phenomena has been previously identified by Taraska and Almers (2004) and Chithrani and Chan (2007) that following content release from vesicles the membrane lipids were loosened. Importantly, this possible loosening did not compromise the integrity of the membrane as confirmed by the non significant levels of LDH released by the treated cells (Figure 5.5).

Alternatively, a protein corona may have formed on the surface of this AuStrs before or during transport through the BBB. In fact, Cox et al. (2018) demonstrated that the surface of the nanoparticles undergoes dynamic molecular modifications upon crossing the BBB.

Tf-AuStr 50 nm Small cell protrusions were observed next to Tf-AuStr aggregates at the cell membrane surface (Figure 5.11 d). This could represent the early formation of macropinocytic membrane ruffles during the preliminary stage of in-

ternalization (Lim and Gleeson, 2011). In fact, possibly in a more advanced stage of macropinocytic uptake, membrane ruffles were found enveloping most of a nanoparticle aggregate (Figure 5.11 f). The AuStrs also interacted with the cell membrane direactely via their spikes (Figure 5.11 b). Once inside the cell, the nanoparticle enclosed in vesicles moved towards the basolateral membrane to complete transcytosis (Figure 5.11 j). Like for the 100 nm Tf-AuStrs, here the aggregates of 50 nm Tf-AuStrs are observed in close proximity to the vesicle wall, possibly due to Tf-Tf receptor linkages (Figure 5.11 k). These bioconstructs were also closely associated with the vesicles membranous structures (Figure 5.11 h).

25 nm PEG-AuStr AuStrs aggregates were also found anchored to the cell and penetrating the membrane surface (Figure 5.12 c). AuStrs at the cell vicinity were also found captured by a large protrusion of the plasma membrane (Figure 5.12 d). Thus, consistent with the previous nanoparticle sizes, 25 nm PEGylated stars also seem to be taken up by macropinocytosis (Lim and Gleeson, 2011). The formation of the pseudopod-like structures allows the internalization of a bulk amount of gold nanostars, and thus numerous AuStrs can be found intracellularly (Figure 5.12 g and h). Interestingly, one AuStr was also found next to a transport vesicle, suggesting that these particles were also capable of crossing the vesicle into the cytoplasm.

25 nm Tf-AuStr Internalised nanoparticles were enclosed within vesicles and move towards the basolateral side of the membrane (Figure 5.13 c). AuStrs were found in vesicles as individual particles, which again attached to the vesicles membranous wall (Figure 5.13 d). Vesicles also transported AuStrs as aggregates, however, the AuStrs that did not integrate this main aggregate structure attached to the

vesicle wall (Figure 5.13 d, red arrows). This occurrence highlights once more transferrin to transferrin receptor (Tf:TfR) interactions for the small AuStrs (Wiley et al., 2013). Post-transcytosis, AuStrs were found as aggregates (Figure 5.13 h) or aligned along the basolateral membrane (Figure 5.13 f). These configurations may be consistent with the pre-transcytotic particle architecture during transport, with individual particles corresponding to the vesicle wall linearly attached AuStrs and aggregates to vesicles transporting aggregates.

Comparing the effect of diameter Particles of smaller diameter showed behaviours in common with the 100 nm AuStrs. In summary, both PEG and Tf coated AuStrs were uptaken in an aggregated state and found mostly as aggregates inside vesicles. Similarly to the 100 nm Tf-AuStrs, smaller Tf-AuStrs were not observed outside of vesicles and also engaged with the vesicles' walls. However, there were relatively fewer instances of small PEGylated AuStrs in the cytoplasm, in comparison to 100 nm PEG-AuStrs.

Vesicles containing Tf or PEG AuStrs of smaller diameter carried relatively more nanoparticles than vesicles transporting 100 nm AuStrs. This higher packing of smaller AuStrs can be explained if on average the transport vesicles had relatively similar dimensions across the samples, limiting the maximum number of AuStrs that can be transported per vesicle, given the comparable vesicle dimensions.

Whilst the transport vesicles contained more smaller particles, this did not translate into more transcytosis as shown by the ICP transport data. In fact, the transcytosis fraction decreased for smaller particle sizes (Figure 5.18). Vesicle transport was predominantly observed on all cell samples. Following the transport of vesicles across the cell, transcytosis can occur either by direct vesicle fusion with

the basolateral membrane or by Austr escape from vesicle followed by transcytosis.

For being polarized cells, vesicular transport in the BBB endothelium can occur either in a blood-to-brain or brain-to-blood direction, in accordance to the cellular needs (Barar et al., 2016). By supporting this bidirectional movement, the cells are able to constantly recycle endocytosed receptors back to the apical membrane unless the transport vesicles contain specific signals for degradation or transcytosis (Barar et al., 2016). Particle escape is particularly important for vesicles that may be retained by the cell and recycled back to the apical cell membrane (Roberts et al., 1993) instead of exocytosing basolateraly. In these instances particle escape could be a non-negligible source of nanoparticles for transcytosis.

It is known that the majority of monodisperse AuNP formulations are found in intracellular vesicles in an aggregated state (Chithrani et al., 2006; Chithrani and Chan, 2007; Albanese and Chan, 2011). It is possible that as more AuStrs become aggregated inside vesicles, their escape becomes more difficult due to a decrease in aggregate *aspect ratio* (Chu et al., 2014) in comparison to single particles (same spike length to induce the escape of a bigger aggregate core). Interestingly, ICP data showed that the cell associated fraction was larger for smaller AuStrs, which formed larger aggregates inside vesicles than bigger AuStrs. This is consistent with Albanese et al. (2012) in which the uptake of aggregates by MDA-MB-435 cells led to aggregate accumulation inside vesicles. However, this behaviour was cell type dependent (Albanese et al., 2012).

Also, geometrically, smaller AuStrs have lower *aspect ratios* than larger AuStrs, which could further reduce the ability of small AuStrs to escape from vesicles and complete transcytosis. Both the increase in AuStr aggregation inside vesicles and the decrease in *aspect ratio* of smaller AuStrs may justify the higher cell association fraction and the lower transcytosis fraction as a consequence of decreased

AuStr diameter.

Effect of smooth spherical morphology in hCMEC/D3 cell association and transcytosis

PEG-AuNP Since AuNPs were found at different intracellular locations as individual particles and only occasionally as aggregates, it is possible that the cell uptake occurred through endocytosis. In fact, Liu et al. (2017) used real-time visualization studies to show that, following the uptake of DNA-coated gold nanoparticles, the AuNPs appeared mostly as single particles during the early stages of endocytosis and clustered during vesicular transport and maturation. The presence of individual and clustered AuNPs could therefore be an indication of the stage of endocytic vesicle maturation.

Tf-AuNP Similarly to PEGylated AuNP, transferrin AuNPs were also found inside endosomes, given the low electronic density of these vesicles (Eskelinen, 2008; Ye et al., 2013). Transferrin AuNPs attached to the endosomal wall similarly to previous transferrin bioconstructs in this study, suggesting Tf-TfR interactions (Wiley et al., 2013). The electronically dense vesicles in which AuNPs were found probably correspond to lysosomes (Eskelinen, 2008; Ye et al., 2013).

Uptake and transport of AuNPs in comparison to that of AuStrs Tf-AuNP were able to enter the cells, however to a lower extent than the star shaped nanoparticles. Once inside the endosomes the transferrin coated nanoparticles are found attached to the endosomal wall, due to their possible engagement with the transferrin receptor. Some of the bioconstructs were observed inside lysosomes. Unlike the AuStrs, AuNP were not observed escaping this organelle. AuNPs were not

found in the cytoplasm near any of the vesicles imaged.

Tomography of hCMEC/D3 cells exposed to 100 nm PEG-AuStrs The tomographic datasets presented in this chapter were acquired from a section of cells that were exposed to PEG-AuStrs for 24 hours before fixation (Figures 5.16 and 5.17). In these datasets PEG-AuStrs can be seen associated with the outer surface of the cell's plasma membrane. Evaluation of the reconstructed volume reveals that the nanostructures were also indeed located inside the cell. The AuStrs were distributed throughout the entire monolayer. In fact, multiple points of PEG-AuStr transcytosis were mapped in the 3D reconstructed model. These findings correlate with the 2-D TEM images confirming that the 2D observations were not artefacts from the sheering during the ultramicrotomy process.

5.4.4 Quantification of nanostructure transcytosis across the BBB

Effect of Morphology on cell association and transport

It was found that after incubation for 24 hours at 37°C the 100 nm PEG-AuStrs showed an outstanding summed cell association and transcytosis ($80.5 \pm 1.3\%$) over that of PEG-AuNPs ($18.3 \pm 2.2\%$). This effect was observed for all AuStr diameters comparatively to the spherical AuNPs and was statistically significant. Thus, hCMEC/D3 cells show preferential uptake of PEG AuStrs over the spherical AuNP counterparts, strongly suggesting that the nanostructure's morphology played a crucial role. This difference in the extent of cellular uptake may result from the interplay between several factors including surface contact area (including SA/V and surface spikiness), and the preferred biological pathways of entry (Kuo and Huang, 2005).

Being that prior to their internalization the nanoparticles need to adhere to the

cell membrane, it is important to consider the cell membrane to nanoparticle contact area. The PEG-AuStrs have a larger surface area to volume ratio than AuNPs, being that spheres have the smallest surface area to volume ratio of all other morphologies. This indicates that the AuStrs may be able to support more multivalent interactions and thus have stronger adhesion force to the membrane (Mammen et al., 1998) than the PEG-AuNPs to drive internalisation. Gao et al. (2005) reported that the docking of single bioparticles with sizes below 50 nm did not engage with the critical receptor density at the cell membrane wrapping front required to generate enough free energy to trigger their complete enclosement by the cell membrane.

Additionally, in contrast to the PEG-AuNP, PEG-AuStrs contain several areas of high local curvature (surface spikiness), which are reported to accelerate cellular internalization when the particle angle is perpendicular to the cell membrane (Yang and Ma, 2010; Ding et al., 2012). Nambara et al. (2016) showed that both surface area to volume ratio and the presence of vertices allowed the better performance of triangular gold nanoparticles over spherical particles in HeLa cells by 20-fold. In particular, Champion and Mitragotri (2006) reports that the particle shape at the point of contact with the membrane determine their internalisation rate rather than the particle's overall size. In fact, the needle-like morphology of carbon nanotubes allows them to cross biological membranes by direct translocation and thus evading conventional endocytic processes (Kafa et al., 2015).

The TEM images provided valuable information on the possible preferred pathway of nanostructure entry into the cells. Whilst the spherical nanoparticles were mainly found in the cells as individual entities (Figure 5.14 a), the nanostars were frequently observed inside the cells as aggregates inside vesicles (Figure 5.7 a and g). The AuStrs are possibly internalised by macropinocytic pathway as indicated

by the presence of pseudopods surrounding AuStrs (Figure 5.7 d). This uptake pathway allows the internalization of a large amount of nanoparticles and may thus be a great contributor to the observed enhanced uptake of star shaped particles compared to nanospheres.

Importantly, this study also shows that the star morphology was the most efficient for BBB transcytosis. The 100 nm PEG-AuStrs showed a significantly higher transcytotic capacity comparatively to the spherical nanoparticles (***p<0.001, Figure 5.18a). Peg-AuStrs translocated the membrane with an impressive $65.7 \pm 1.4\%$ efficiency whilst only $16.6 \pm 1.9\%$ of the PEG-AuNP dose translocated to the basolateral compartment.

Effect of AuStr diameter on cell association and transport

The summed cell associated and transcytosis fractions following 24 hours treatment were on average $72.3 \pm 3.7\%$ for all PEG-AuStr diameters, with no statistical differences between them. When the cell associated gold fraction is deconvoluted from transcytosis, it is found that the % cell association decreases with AuStr size (Figure 5.18b). More specifically, particle retention decreases from $55 \pm 12\%$ to $14.8 \pm 2.7\%$ when the gold star size increases from 25 to 100 nm. The decrease in particle retention with increase in particle size can be due to a decreased particle residence time in cell, as larger particles seem to be more easily released from the cells (Figure 5.18a). The fact that larger AuStrs had a higher transcytosis fraction than smaller AuStrs indicates that bigger AuStrs either have a smaller residence time on the cells or that they get transported preferentially to the basolateral membrane rather than entering a different trafficking pathway.

Whilst it was conventionally thought that particles should be smaller than 64 nm for brain penetration (Thorne and Nicholson, 2006), Nance et al. (2012) showed

in *ex vivo* human and mouse brain tissue and *in vivo* mouse brain that particles up to 114 nm in diameter were able to penetrate the brain given that they are densely PEGylated, unlike 200 nm particles. This effect was due to the great presence of brain extracellular space pores bigger than 100 nm (28%) but low presence of pores above 200 nm. Irrespective of the size, the penetration of uncoated nanoparticles in the brain were limited by hydrophobic and electrostatic interactions. Heavily PEGylated nanoparticles had near neutral zeta surface charge ($<$ -4 mV) which was correlated with greater rat brain tissue penetration. For PEGylated nanoparticles to successfully penetrate the brain, the PEG layers should be in a brush arrangement occurring when roughly with 9 PEG molecules (5 kDa) per 100 nm^2. The formation of PEG coating in this regime possibly limits nanoparticle adhesion to the brain extracellular space and facilitates particle diffusion. Like Nance et al. (2012) all of the 100 nm PEG-AuStrs in this study had a near neutral zeta surface charge ($<$ -4 mV) in the culture medium (Table 5.1).

Furthermore, in this study it was shown that by changing the AuStr diameter it was possible to significantly change the extent of nanostructure transcytosis from $12.9 \pm 2.1\%$ to $65.7 \pm 1.4\%$ (***p<0.001), when particle size was increased from 25 nm to 100 nm, respectively. Hence, whilst the summed cell association and transcytosis fraction were similar across the AuStrs with different diameters (Figure 5.18e), the AuStrs ability to complete basolateral transcytosis increased with particle size.

This effect may be justified based on the nanostructures geometrical features. As the size of the AuStrs increases to 100 nm, their shape becomes more prominent, the spikes become longer (Figure 5.23 a), and the spike *aspect ratio* increases (Figure 5.23 b). These features proved to be beneficial to the AuStrs ability to complete their path across the cell. In fact, TEM images suggested that 100 nm

spiky AuStrs were able to pierce and escape both endosomal and lysosomal compartments and move towards the basolateral membrane (Figure 5.7 m). This escape from the endolysosomal pathway (Figure 5.7 l) together with the successful docking of transport vesicles to the basolateral membrane (Figure 5.7 n) contribute to the successful transcytosis of the 100 nm AuStrs with high *aspect ratio* surface spikiness.

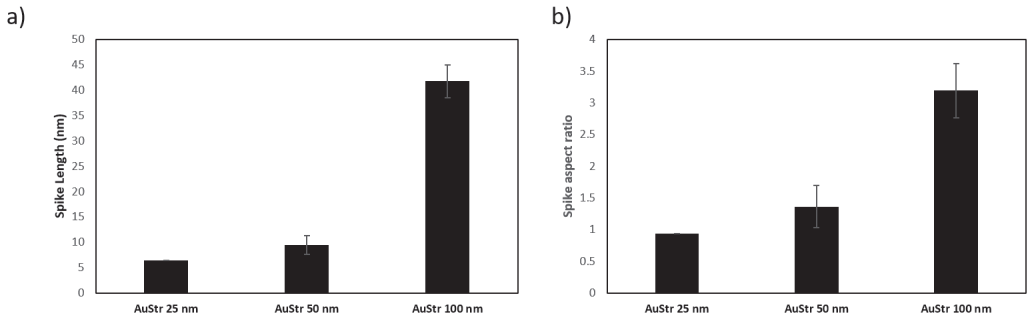


Figure 5.23: Graphs showing the average spike length (a) and average spike *aspect ratio* as a function of AuStr diameter. The AuStr spike measurements determined using the image J software.

Size dependency of nanoparticle transport across the BBB has previously been identified for lactofferin (Song et al., 2017) and PEG (Liu et al., 2014) conjugated spherical silica nanoparticles. Here, the particle size showed a negative correlation with BBB transport, with 25 nm particles crossing more than 50 nm particles whilst 100 nm particles crossed the least. Unlike Liu et al. (2014), Song et al. (2017) was not able to demonstrate size dependence for the spherical PEGylated nanoparticles.

In our study it is shown for the first time that the transcytosis of nanostars increases with gold star diameter. Thus, the reverse size dependence effects previously reported between isotropic and anysotropic nanoparticles (Nambara et al., 2016; Agarwal et al., 2013) seem to hold for the transport between anisotropic and spherical nanoparticles across the BBB.

Effect of transferrin on cell association and transport

Overall, the Tf-AuStrs followed the previously observed uptake and transcytosis trends observed for PEG-AuStrs, with increased particle size resulting in lower cell retention and increased nanostructure transcytosis. Furthermore, it was found that whilst the cell associated fraction of Tf-AuStrs was higher than that of PEGylated AuStrs (*p<0.1, Figure 5.18b) the transcytosis of the Tf-AuStrs was lower (*p<0.1, Figure 5.18a). The difference in transcytosis between PEGylated AuStrs and Tf-AuStrs could be attributed to receptor ligand (Tf-TfR) interactions. The transferrin receptor is known to internalize transferrin *via* receptor mediated endocytosis, with subsequent transcytosis across the endothelial cell (Pardridge et al., 1987). The presence of transferrin on the surface of the nanoparticles may therefore increase the binding of the bioconstructs to the cell membrane leading to increased nanoparticle entry by transferrin receptor mediated endocytosis.

The effects of ligand receptor interactions have been reported in previous stud-

ies and strategies to improve the transcytosis of bioconstructs are currently being investigated. Clark and Davis (2015) group tackled the entrapment of high-avidity Tf-AuNP conjugates within the endothelium by adding a cleavable group that releases AuNP from Tf-TfR complexes when the endosomal pH decreases. This modification increased by 10-fold the amount of nanoparticles reaching the basolateral compartment. Furthermore, Cui et al. (2018) investigated the bypass of the endolysosomal entrapment by accelerating basolateral exocytosis as a way of promoting transcytosis of nanoparticles in epithelial cells.

AuStrs bioconstructs are densely conjugated in a conformal coat of transferrin (chapter 3). The release of the nanostars on the basolateral side is dependent on the dissociation of the ligand coated nanoparticles from the membrane receptors. As showed by Clark and Davis (2015), the multivalent interactions of Tf-AuStrs with the cell membrane may make it more difficult for the nanostructures to disengage from the basolateral membrane comparatively to the PEGylated nanostructures. TEM shows that Tf-AuStrs (Figure 5.8 g) and Tf-AuNPs (Figure 5.15 c) are engaged with the vesicular wall during transport. Whilst the AuStrs' sharp features are favourable for endosomal escape, the physical attachment of the Tf-AuStrs to these organelles hinders their escape compared to PEG-AuStrs. The above-mentioned factors increase the residence of the Tf nanoparticles within the cells comparatively to PEGylated nanostructures, thus decreasing the transcytosis amount of the bionconstructs.

Alternatively the observed results are possibly in agreement with an alternative mechanism for transferrin's role in the iron transport cycle in the BBB. Roberts et al. (1993) demonstrated in *murine* models that, unlike other epithelial cells, transferrin receptors are highly polarized at the BBB and are localized only at the apical membrane. The results indicated that iron transport occurred in three main

stages: holo-transferrin binding to surface TfR, iron release in endosomes and iron transcytosis to the brain by unknown mechanisms with TfR being recycled back to the apical membrane. Later studies by Skjørringe et al. (2015) agreed with Roberts et al. (1993) findings and proposed that iron is pumped to the cytosol by a metal transporter (divalent metal transporter 1) present on the endosomal membrane and finally transported across the basolateral membrane, possibly by ferroportin (iron export protein) (Figure 5.24). According to this proposed mechanism, Tf endocytosis allows for iron transcytosis but the protein is recycled back to the luminal side (Moos et al., 2006).

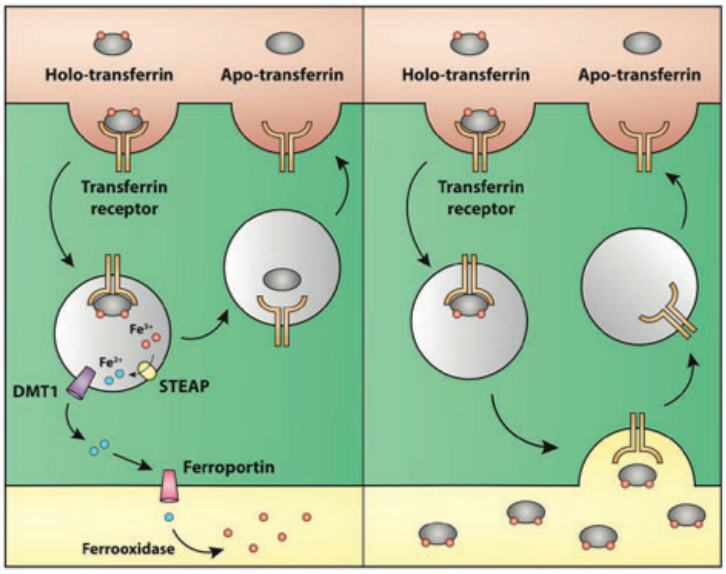


Figure 5.24: Image showing two proposed models of iron transport through the BBB without (left) or with (rigth)transcytosis of transferrin (Skjørringe et al., 2015).Copyright 2015 Skjorringe, Burkhart, Johnsen and Moos.

If iron transport in fact happens through this alternative mechanism, the presence of transferrin on the surface on the AuStrs and AuNPs would not necessarily guarantee their transcytosis. If these vesicles are destined to be recycled back to the apical membrane then vesicle escape would be beneficial to transcytosis.

Also, Gunduz et al. (2017) studies revealed that intracellular nanoparticle ac-

cumulation following prolonged AuNP exposure caused HUVEc cells to inhibit further AuNP uptake by macropinocytosis when an intracellular AuNP concentration threshold level was achieved. In this way cells were able to actively regulate nanoparticle uptake. Interestingly, AuNP accumulation did not interfere with the clatherin nor calveoly-mediated endocytic uptake of transferrin proteins and choleratoxin, respectively Gunduz et al. (2017).

The findings presented in the previous study support the observation in this chapter that Tf-AuStrs are retained more within the endothelium than PEG-AuStrs. Being that the summed cell association and transcytosis fraction was relatively constant across the different AuStr diameters (Figure 5.18d) it could be postulated that hCMEC/D3 cells are defined by a threshold of the total percent of gold that can be processed by the cells in 24 hours, for the star morphology. Thus, in this study this threshold value would be around $72.3 \pm 3.7\%$. Therefore, according to Gunduz et al. (2017), once this threshold is achieved, further AuStr uptake by the endothelial cells through macropynocytosis would be inhibited whilst the cellular uptake through transferrin-receptor mediated endocytosis would still be permitted. Under these conditions, only AuStrs that enter the cell *via* transferrin-receptor mediated endocytosis would continue to enter the cells, *i.e.* Tf-AuStrs. This additional Tf-AuStr entry beyond the threshold point would therefore account for the extra 2.7% of the found Tf threshold comparatively to the PEG-AuStr threshold.

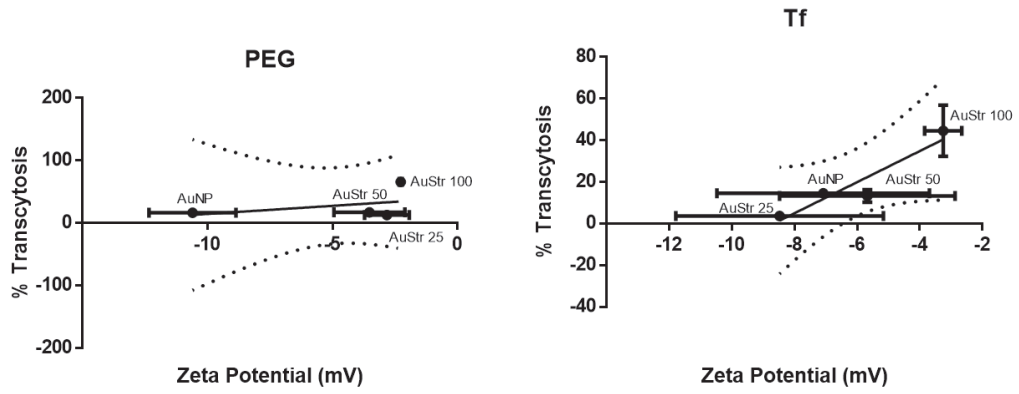
Furthermore, the amount of Tf-AuStrs that would be permitted to enter the cells *via* Tf-receptor mediated transcytosis would depend on the nanostructure dispersity state at the point immediately before internalization. It has been shown that multiwalled carbon nanotubes are found in epithelial cells in endocytic cups when taken up as individual entities whilst larger aggregates were found inside macropynosomes (Ruenraroengsak et al., 2016).

In the transwell culture model, the nanostructures are introduced in the apical side of the BBB endothelial cells. Before the nanostructures interact with the cell membrane, they first encounter the endothelial glycocalyx layer at the apical surface of the cell membrane (Möckl et al., 2017).

Being that all the nanoparticle formulations in this study have near neutral to negative charge (Figure 5.27), it is possible that their interaction with the negatively charged glycocalyx causes them to aggregate at the cell surface to exclude the interaction with the glycocalyx by electrostatic repulsion. As Figure 5.8 c shows, most of the Tf-AuStrs in close proximity to the cell membrane are in an aggregated state. Therefore, even though the Tf-AuStrs are targeted to the BBB, the nanostructure aggregation at the apical cell surface could affect their entry (Ruenraroengsak et al., 2016) by receptor mediated endocytosis because aggregation increases the overall size of the nanostructures to be internalised. Therefore, Tf-AuStrs would have limited access to a receptor mediated route.

5.4.5 Evaluation transcytosis efficiency in correlation with geometry

To understand the parameters that ultimately influence the transcytotic behaviour of the different gold nanostructures, the effect of surface charge (zeta potential), geometry and surface coating were evaluated in respect to transcytotic efficiency. It was verified that all nanostructures had near neutral zeta potential as expected due to PEG stabilization , and there were no statistically significant effect of the small differences in zeta potential on transcytosis (Figure 5.25). The effect of different zeta potentials in nanostructure transcytosis was not explored in this this study as highly charged particles are less stable in the biological media and would therefore not fit with the current design strategy.



(a) (b)

Figure 5.25: Transcytosis as a function of zeta potential for PEGylated (a) and Tf coated nanostructures (b), with slope deviation from zero being not significant (p=0.6 and p=0.06, for graphs a and b respectively.

Overall, geometry had a statistically significant effect on transcytosis (Figure 5.26). Spike *length* showed the most direct correlation to transcytotic efficiency for PEGylated AuStrs (p=0.004). However, in the presence of transferrin, the effect of

length was not significant, and AuStr *diameter* and spike *aspect ratio* were the only statistically significant variables to affect transcytosis. However, it is worth noting that spike *length* and aspect ratio are co-dependent variables, and therefore have to be considered in combination.

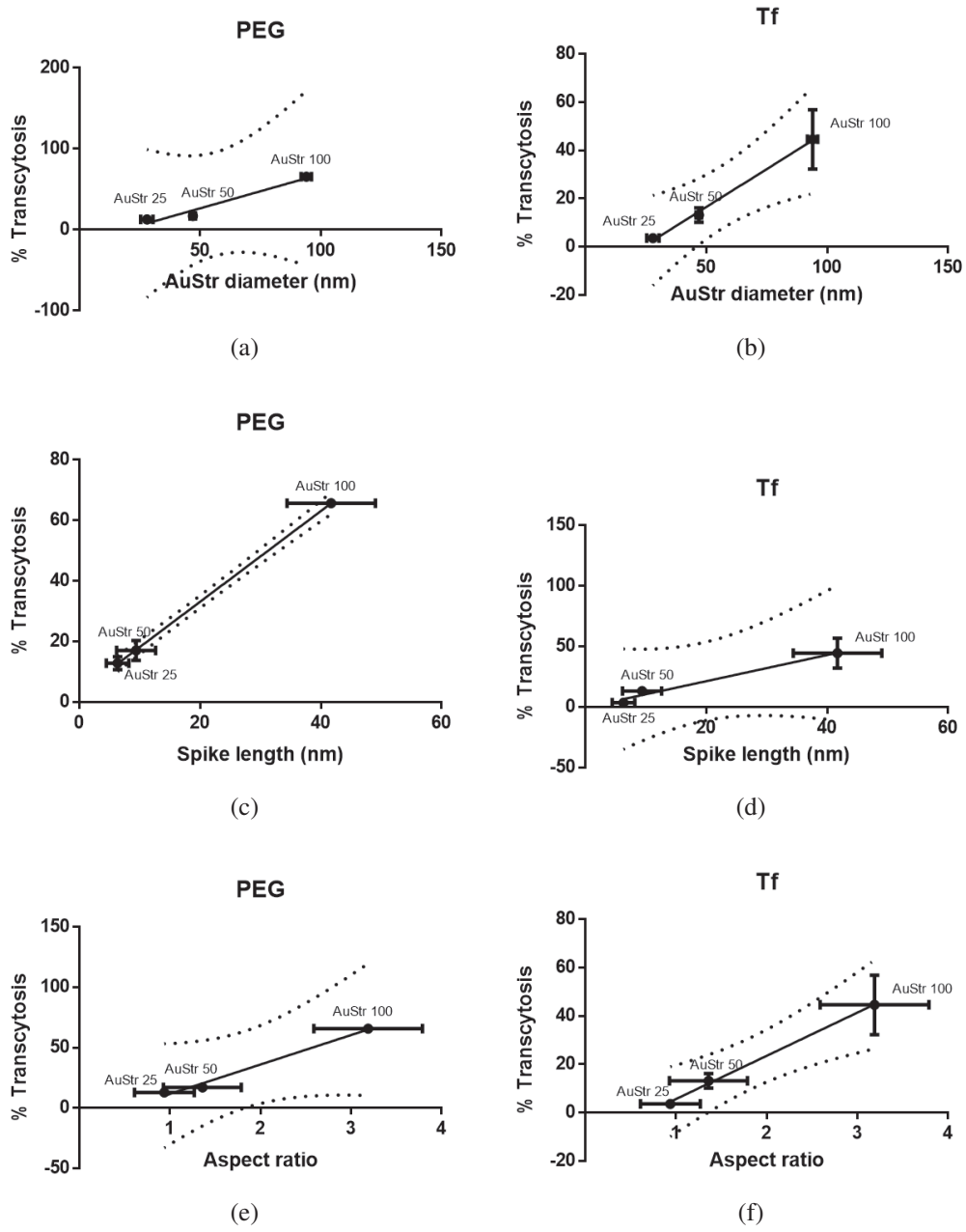


Figure 5.26: Transcytosis as a function of AuStr diameter for PEGylated (a) and Tf coated nanostructures (b), with slope deviation from zero only being significant for Tf coated nanostructures (p=0.13 and p=0.04, for graphs a and b respectively). Transcytosis as a function of spike *length* for PEGylated (c) and Tf coated nanostructures (d), with slope deviation from zero only being significant for PEGylated nanostructures (p=0.004 and p=0.09, for graphs c and d respectively). Transcytosis as a function of spike aspect ratio for PEGylated (e) and Tf coated nanostructures (f), with slope deviation from zero being significant for Tf coated nanostructures (p=0.06 and p=0.03, for graphs e and f respectively).

5.5 Conclusions

A hCMEC/D3 cell based *in vitro* model of the BBB was successfully established and implemented to evaluate the effect of particle geometry, diameter and surface coating in nanostructure transcytotic efficiency. It was found that the nanostars were about 50% more efficient than nanospheres in crossing the BBB (Table 5.27).

	Geometry (TEM analysis)			Zeta Potential (mV)				% Trancytosis	
	Diameter (nm)	Spike Parameters		ddH2O		Media +FBS			
Morphology		Length (nm)	Aspect ratio	PEG	Tf	PEG	Tf	Peg	Tf
AuNP	12	N/A	N/A	-23.43 ± 2.7	-23.2 ± 0.9	-10.59 ± 1.74	-7.08 ± 3.39	16.6±1.9	14.56±0.32
AuStr 25	28	6.35 ± 1.87	0.94 ± 0.33	-23.33 ± 2.8	-47.4 ± 0.43	-2.82± 0.89	-8.47 ± 3.31	12.9±2.1	3.66±0.11
AuStr 50	47	9.42 ± 3.22	1.36 ± 0.43	-24.5 ± 1.8	-29.1 ± 0.44	-3.52± 1.42	-5.67 ± 2.80	17.1±3.3	13.2±3.0
AuStr 100	94	41.73 ± 7.33	3.19 ± 0.6	-20.53 ± 3.8	-22.33 ± 5.37	-2.27± 0.06	-3.25 ± 0.59	65.7±1.4	45±12

Figure 5.27: Summary of nanostructures geometrical features and their effect in transcytosis.

The maximum transcytotic efficiency, 65.7 $\pm$ 1.4 %, was achieved for 100 nm PEGylated AuStrs and the extent of transcytosis diminished with decreased AuStr diameter. All the gold nanostructures had near neutral zeta potentials in the testing cell media which did not significantly correlate with the different transcytotic efficiencies.

Moreover, increasing AuStr size was linked to a well-developed spiky surface morphology with long spike *lengths* and of greater aspect ratio. As the AuStrs get smaller and their shape closer assimilates that of a spherical morphology, the effect of AuStr morphology in transcytosis is lost. It is postulated that the high aspect ratio features in AuStrs are beneficial for transcytosis for allowing the AuStrs to efficiently penetrate the cells, escape endolysososomal entrapment, and reduce cell retention. Transferrin based bioconstructs engaged strongly with the basolateral

cell membrane during transcytosis and thus did not contribute to enhance transcytosis efficiency. However, Tf bioconstructs increased cell association and cell residence.

Taken together, the analysis show that the transcytotic efficiency was strongly influenced by geometrical factors, specifically spike *length*, *aspect ratio* and *AuStr diameter*. It is therefore concluded that a spiky surface topology is key for nanoparticle transcytosis, and can therefore be considered in the future design of BBB penetrating nanoparticles.

Chapter 6

Conclusions and Future work

The work has highlighted the promising use of a nanostar based morphology for successful crossing of the BBB. Characterisation of the nanostructures revealed that the presence of a multispiked surface topology on the synthesised nanoparticles allows for preferential cell uptake by the brain endothelium, and for a high loading capacity with the ligand of interest Tf comparatively to nanoparticles of less structured topology.

Specifically, the synthesis of three different sizes of AuStrs, namely 25, 50 and 100 nm in diameter, through a solution based seed mediated method, were demonstrated to change the nanostructure association to the cells, and extent of transcytosis across the BBB *in vitro*. The observed effects were obtained for PEGylated AuStrs and thus a PEG coating has proven to be an applicable stabilising ligand for effective AuStr transcytosis.

The biconjugation of the AuStrs was highly efficient with the formation of a conformal Tf coating on the nanostar surface. Additionally the AuStrs had high loading capacity and the protein packing was concentration dependent. Furthermore, the bio-functionalization of the gold nanostructures with the Tf increased

the nanostructures association to the brain endothelium but did not translate into enhanced trasncytotic ability. These observations highlight that following surface bio-functionalization, the complexity of the nanostructure trafficking events increase.

Further experiments could be performed aimed at understanding bio-functionalisation factors and their effect in cell trafficking. Specifically, it would be important to identify in a systematic study the optimal Tf surface density for each nanoparticle morphology and diameter that leads to the bioconstructs' best transcytotic performance. Similarly it is important to fully understand the structure and loading behaviour of the protein on the surface of the nanostructures as a quality control analysis of the bioconstructs (Kelly et al., 2005); techniques such as circular dichroism could be applied to yield this information.

The hCMEC/D3 *in vitro* model of the BBB was an essential tool in the validation of the design of nanoparticles for BBB crossing. The culturing of the cells in a porous transwell set-up allowed for the successful quantification of transcytotic events of the different nanostructure formulations by using ICP-OES. However, this approach has some limitations. Specifically, when it came to analysing the amount of cell-associated gold, ICP-OES was not able to distinguish between intracellular gold content and that solely anchored to the cell surface. Therefore, correlative confocal microscopy analysis of live-cell systems could provide an estimation of the proportion of surface bound nanostructures to those that have been internalised.

The imaging of resin preserved cell samples by transmission electron microscopy provided valuable information on the uptake and intracellular distribution of the gold nanostructures in the brain endothelium. Furthermore, confocal fluorescence microscopy could complement the hypothesis that sharp 100 nm AuStrs escape organelle entrapment and contribute to transcytosis. The immunofluores-

cent tagging of the different cell organelles and vesicles can allow the unambiguous colocalization analysis of the nanostructures in the intracellular environment. Such study would provide further insights into the interaction of the nanoparticles within cells. Live cell imaging studies can also be carried out in order to visualise the uptake trafficking and transcytosis of different nanostructure formulations in live cells to complement the TEM studies.

Future work could also be aimed at elucidating the pathways involved in the uptake of the different nanoparticle formulations by the hCMEC/D3 cells. Cell inhibition studies with substances known to selectively inhibit particular transport pathways would be a complementary experiment to this work. Ultimately, murine models could be used to extensively study the ability of the promising nanoparticle formulations to cross the BBB *in vivo*.

Ultimately, the gold nanostar based platform developed here is versatile and can be specifically adapted to enable brain targeting for therapeutic or diagnostic purposes. Future work should extend on the application of the developed system. Specifically, other proteins or peptides can be explored to target and translocate the BBB. Furthermore, owing to the large surface area conferred by the gold star morphology, a multiplexed platform could be built, with the simultaneous incorporation of targeting therapeutic and diagnostic agents for the management of conditions in a holistic manner.

Publications and presentations

Publications

1. Rodrigues, R., Xie, F., Porter, A.E. and Ryan, M.P. (2018) Towards Efficient Nanovehicle Drug Dosing: Conformal Protein Loading of Gold Nanostructures with highly Tailored Surface Morphology. (ready for submission)

2. Rodrigues, R., Qi, J., Ruenraroengsak, P., Goode, A., Porter, A.E. and Ryan, M.P. (2018) Gold star based vehicles for blood-brain-barrier crossing: *in Vitro* permeability evaluation of BBB targeted bioconstructs. (in preparation)

Oral presentations

1. 21/07/2016 Rodrigues, R., Porter, A.E. and Ryan, M.P. The Use of Smart Nanoparticles for Crossing the Blood-Brain Barrier, Year 2 PhD seminar, Materials Department, Imperial College, London (UK)

2. 29/06/2018 Rodrigues, R., Porter, A.E. and Ryan, M.P. Synthesis of Gold Nanovehicles for Controlled Drug Delivery Applications, The 4th edition of Nanotech France 2018 International Conference and Exhibition, Paris (France)

Appendix

The toxicity of nanostars in neuron cells was evaluated to test the potential fo AuStrs as BBB drug delivery vehicles (Figure 1).

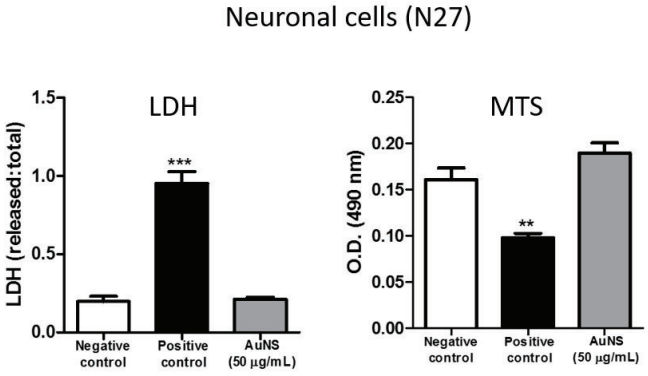


Figure 1: LDH and MTS cytotoxicity assays of N27 cells exposed to 100 nm PEG AuStrs at the concentration of 50 μg/mL. The figure shows that the nanostars were not toxic in neuronal cells with statistical significance.

Bibliography

Agarwal, R., Singh, V., Jurney, P., Shi, L., Sreenivasan, S. V., and Roy, K. (2013). Mammalian cells preferentially internalize hydrogel nanodiscs over nanorods and use shape-specific uptake mechanisms. *Proceedings of the National Academy of Sciences*, 110(43):17247–17252.

Ahmed, W., Kooij, E. S., Silfhout, A. v., and Poelsema, B. (2010). Controlling the morphology of multi-branched gold nanoparticles. *Nanotechnology*, 21(12):125605.

Aisen, P. and Listowsky, I. (1980). Iron transport and storage proteins. *Annual Review of Biochemistry*, 49:357–393.

Albanese, A. and Chan, W. C. (2011). Effect of Gold Nanoparticle Aggregation on Cell Uptake and Toxicity. *ACS Nano*, 5(7):5478–5489.

Albanese, A., Tang, P. S., and Chan, W. C. (2012). The Effect of Nanoparticle Size, Shape, and Surface Chemistry on Biological Systems. *Annual Review of Biomedical Engineering*, 14(1):1–16.

Alexandridis, P. (2011). Gold Nanoparticle Synthesis, Morphology Control, and Stabilization Facilitated by Functional Polymers. *Chemical Engineering & Technology*, 34(1):15–28.

Allen, T. M. (2002). Ligand-targeted therapeutics in anticancer therapy. *Nature Reviews Cancer*, 2(10):750–763.

Alphonsus, C. S. and Rodseth, R. N. (2014). The endothelial glycocalyx: a review of the vascular barrier. *Anaesthesia*, 69(7):777–784.

Alzheimer's Research UK (2018). Deaths due to dementia.

Andrews, N. C. (2000). Iron homeostasis: insights from genetics and animal models. *Nature Reviews Genetics*, 1(3):208–217.

Andrieux, K., Garcia-Garcia, E., Kim, H. R., and Couvreur, P. (2009). Colloidal Carriers: A Promising Way to Treat Central Nervous System Diseases.

Araya, E., Olmedo, I., Bastus, N. G., Guerrero, S., Puntes, V. F., Giralt, E., and Kogan, M. J. (2008). Gold Nanoparticles and Microwave Irradiation Inhibit Beta-Amyloid Amyloidogenesis. *Nanoscale Research Letters*, 3(11):435–443.

Bai, T. and Cheng, X. (2008). Preparation and characterization of 3-mercaptopropyl trimethoxysilane self-assembled monolayers. *Journal of University of Science and Technology Beijing, Mineral, Metallurgy, Material*, 15(2):192–196.

Bakr, O. M., Wunsch, B. H., and Stellacci, F. (2006). High-Yield Synthesis of Multi-Branched Urchin-Like Gold Nanoparticles. *Chemistry of Materials*, 18(14):3297–3301.

Banerjee, J., Shi, Y., and Azevedo, H. S. (2016). In vitro blood-brain barrier models for drug research: state-of-the-art and new perspectives on reconstituting these models on artificial basement membrane platforms. *Drug Discovery Today*, 21(9):1367–1386. WOS:000384863500004.

Barar, J., Rafi, M. A., Pourseif, M. M., and Omidi, Y. (2016). Blood-brain barrier transport machineries and targeted therapy of brain diseases. *BioImpacts : BI*, 6(4):225–248.

Barbosa, S., Agrawal, A., Rodriguez-Lorenzo, L., Pastoriza-Santos, I., Alvarez-Puebla, R. A., Kornowski, A., Weller, H., and Liz-Marzan, L. M. (2010). Tuning Size and Sensing Properties in Colloidal Gold Nanostars. *Langmuir*, 26(18):14943–14950.

Barrett, G. L., Trieu, J., and Naim, T. (2009). The identification of leptin-derived peptides that are taken up by the brain. *Regulatory Peptides*, 155(1–3):55–61.

Becker, B. F., Chappell, D., and Jacob, M. (2010). Endothelial glycocalyx and coronary vascular permeability: the fringe benefit. *Basic Research in Cardiology*, 105(6):687–701.

Bellocq, N. C., Pun, S. H., Jensen, G. S., and Davis, M. E. (2003). Transferrin-Containing, Cyclodextrin Polymer-Based Particles for Tumor-Targeted Gene Delivery. *Bioconjugate Chemistry*, 14(6):1122–1132.

Berne, B. J. and Pecora, R. (1976). *Dynamic light scattering. With applications to chemistry, biology, and physics.*

Bhaskar, S., Tian, F., Stoeger, T., Kreyling, W., de la Fuente, J. M., Grazú, V., Borm, P., Estrada, G., Ntziachristos, V., and Razansky, D. (2010). Multifunctional Nanocarriers for diagnostics, drug delivery and targeted treatment across blood-brain barrier: perspectives on tracking and neuroimaging. *Particle and Fibre Toxicology*, 7(1):3.

Biemans, E. A., Jäkel, L., de Waal, R. M., Kuiperij, H. B., and Verbeek, M. M.

(2016). Limitations of the hCMEC/D3 cell line as a model for Aβ clearance by the human blood-brain barrier. *Journal of Neuroscience Research*, pages n/a–n/a.

Booth, R. and Kim, H. (2012). Characterization of a microfluidic in vitro model of the blood-brain barrier (μBBB). 12(10):1784–1792.

Borner, M. M., Schneider, E., Pirnia, F., Sartor, O., Trepel, J. B., and Myers, C. E. (1994). The detergent Triton X-100 induces a death pattern in human carcinoma cell lines that resembles cytotoxic lymphocyte-induced apoptosis. *FEBS Letters*, 353(2):129–132.

Butt, A. M., Jones, H. C., and Abbott, N. J. (1990). Electrical resistance across the blood-brain barrier in anaesthetized rats: a developmental study. *The Journal of Physiology*, 429:47–62.

Calvo, P., Gouritin, B., Chacun, H., Desmaële, D., D'Angelo, J., Noel, J. P., Georgin, D., Fattal, E., Andreux, J. P., and Couvreur, P. (2001). Long-circulating PEGylated polycyanoacrylate nanoparticles as new drug carrier for brain delivery. *Pharmaceutical Research*, 18(8):1157–1166.

Champion, J. A., Katare, Y. K., and Mitragotri, S. (2007). Making polymeric micro- and nanoparticles of complex shapes. *Proceedings of the National Academy of Sciences*, 104(29):11901–11904.

Champion, J. A. and Mitragotri, S. (2006). Role of target geometry in phagocytosis. *Proceedings of the National Academy of Sciences*, 103(13):4930–4934.

Chen, H., Zhang, X., Dai, S., Ma, Y., Cui, S., Achilefus, S., and Gu, Y. (2013). Multifunctional Gold Nanostar Conjugates for Tumor Imaging and Combined Photothermal and Chemo-therapy. *Theranostics*, 3(9):633–649.

Chen, J., Saeki, F., Wiley, B. J., Cang, H., Cobb, M. J., Li, Z.-Y., Au, L., Zhang, H., Kimmey, M. B., Li, and Xia, Y. (2005). Gold Nanocages: Bioconjugation and Their Potential Use as Optical Imaging Contrast Agents. *Nano Letters*, 5(3):473–477.

Chen, Y. and Liu, L. (2012). Modern methods for delivery of drugs across the blood–brain barrier. *Advanced Drug Delivery Reviews*, 64(7):640–665.

Cheng, L.-C., Huang, J.-H., Chen, H. M., Lai, T.-C., Yang, K.-Y., Liu, R.-S., Hsiao, M., Chen, C.-H., Her, L.-J., and Tsai, D. P. (2012). Seedless, silver-induced synthesis of star-shaped gold/silver bimetallic nanoparticles as high efficiency photothermal therapy reagent. *Journal of Materials Chemistry*, 22(5):2244–2253.

Chithrani, B. D. and Chan, W. C. W. (2007). Elucidating the Mechanism of Cellular Uptake and Removal of Protein-Coated Gold Nanoparticles of Different Sizes and Shapes. *Nano Letters*, 7(6):1542–1550.

Chithrani, B. D., Ghazani, A. A., and Chan, W. C. W. (2006). Determining the Size and Shape Dependence of Gold Nanoparticle Uptake into Mammalian Cells. *Nano Letters*, 6(4):662–668.

Chu, Z., Miu, K., Lung, P., Zhang, S., Zhao, S., Chang, H.-C., Lin, G., and Li, Q. (2015). Rapid endosomal escape of prickly nanodiamonds: implications for gene delivery. *Scientific Reports*, 5:11661.

Chu, Z., Zhang, S., Zhang, B., Zhang, C., Fang, C.-Y., Rehor, I., Cigler, P., Chang, H.-C., Lin, G., Liu, R., and Li, Q. (2014). Unambiguous observation of shape effects on cellular fate of nanoparticles. *Scientific Reports*, 4.

Chung, M. C.-M. (1984). Structure and function of transferrin. *Biochemical Education*, 12(4):146–154.

Clark, A. J. and Davis, M. E. (2015). Increased brain uptake of targeted nanoparticles by adding an acid-cleavable linkage between transferrin and the nanoparticle core. *Proceedings of the National Academy of Sciences of the United States of America*, 112(40):12486–12491.

Corrada, M. M., Brookmeyer, R., Paganini-Hill, A., Berlau, D., and Kawas, C. H. (2010). Dementia Incidence Continues to Increase with Age in the Oldest Old The 90+ Study. *Annals of Neurology*, 67(1):114–121.

Cox, A., Andreozzi, P., Dal Magro, R., Fiordaliso, F., Corbelli, A., Talamini, L., Chinello, C., Raimondo, F., Magni, F., Tringali, M., Krol, S., Jacob Silva, P., Stellacci, F., Masserini, M., and Re, F. (2018). Evolution of Nanoparticle Protein Corona across the Blood–Brain Barrier. *ACS Nano*, 12(7):7292–7300.

Cucullo, L., Couraud, P.-O., Weksler, B., Romero, I.-A., Hossain, M., Rapp, E., and Janigro, D. (2008). Immortalized human brain endothelial cells and flow-based vascular modeling: a marriage of convenience for rational neurovascular studies. *Journal of Cerebral Blood Flow and Metabolism: Official Journal of the International Society of Cerebral Blood Flow and Metabolism*, 28(2):312–328.

Cui, Y., Shan, W., Zhou, R., Liu, M., Wu, L., Guo, Q., Zheng, Y., Wu, J., and Huang, Y. (2018). The combination of endolysosomal escape and basolateral stimulation to overcome the difficulties of "easy uptake hard transcytosis" of ligand-modified nanoparticles in oral drug delivery. *Nanoscale*, 10(3):1494–1507.

Dam, D. H. M., Culver, K. S. B., and Odom, T. W. (2014a). Grafting Aptamers onto Gold Nanostars Increases in Vitro Efficacy in a Wide Range of Cancer Cell Types. *Molecular Pharmaceutics*, 11(2):580–587.

Dam, D. H. M., Lee, R. C., and Odom, T. W. (2014b). Improved in Vitro Efficacy of Gold Nanoconstructs by Increased Loading of G-quadruplex Aptamer. *Nano Letters*, 14(5):2843–2848.

Daniel, M.-C. and Astruc, D. (2004). Gold Nanoparticles: Assembly, Supramolecular Chemistry, Quantum-Size-Related Properties, and Applications toward Biology, Catalysis, and Nanotechnology. *Chemical Reviews*, 104(1):293–346.

De Jong, W. H., Hagens, W. I., Krystek, P., Burger, M. C., Sips, A. J. A. M., and Geertsma, R. E. (2008). Particle size-dependent organ distribution of gold nanoparticles after intravenous administration. *Biomaterials*, 29(12):1912–1919.

Decker, T. and Lohmann-Matthes, M.-L. (1988). A quick and simple method for the quantitation of lactate dehydrogenase release in measurements of cellular cytotoxicity and tumor necrosis factor (TNF) activity. *Journal of Immunological Methods*, 115(1):61–69.

Decuzzi, P., Godin, B., Tanaka, T., Lee, S. Y., Chiappini, C., Liu, X., and Ferrari, M. (2010). Size and shape effects in the biodistribution of intravascularly injected particles. *Journal of Controlled Release*, 141(3):320–327.

Ding, H.-m., Tian, W.-d., and Ma, Y.-q. (2012). Designing Nanoparticle Translocation through Membranes by Computer Simulations. *ACS Nano*, 6(2):1230–1238.

El-Brolossy, T. A., Abdallah, T., Mohamed, M. B., Abdallah, S., Easawi, K., Negm, S., and Talaat, H. (2008). Shape and size dependence of the surface plasmon resonance of gold nanoparticles studied by Photoacoustic technique. *The European Physical Journal Special Topics*, 153(1):361–364.

Erdman, N. and Bell, D. C. (2015). Scanning Electron and Ion Microscopy of Nanostructures. pages 300–350.

Eskelinen, E.-L. (2008). To be or not to be? Examples of incorrect identification of autophagic compartments in conventional transmission electron microscopy of mammalian cells. *Autophagy*, 4(2):257–260.

Etame, A. B., Smith, C. A., Chan, W. C. W., and Rutka, J. T. (2011). Design and potential application of PEGylated gold nanoparticles with size-dependent permeation through brain microvasculature. *Nanomedicine: Nanotechnology, Biology, and Medicine*, 7(6):992–1000.

Fassel, V. A. and Kniseley, R. N. (1974). Inductively coupled plasma. Optical emission spectroscopy. *Analytical Chemistry*, 46(13):1110A–1120a.

Fischer, H., Gottschlich, R., and Seelig, A. (1998). Blood-brain barrier permeation: molecular parameters governing passive diffusion. *The Journal of Membrane Biology*, 165(3):201–211.

Frens, G. (1973). Controlled Nucleation for the Regulation of the Particle Size in Monodisperse Gold Suspensions. *Nature*, 241(105):20–22.

Förster, C., Burek, M., Romero, I. A., Weksler, B., Couraud, P.-O., and Drenckhahn, D. (2008). Differential effects of hydrocortisone and TNFα on tight junction proteins in an in vitro model of the human blood–brain barrier. *The Journal of Physiology*, 586(7):1937–1949.

Furuse, M., Itoh, M., Hirase, T., Nagafuchi, A., Yonemura, S., Tsukita, S., and Tsukita, S. (1994). Direct association of occludin with ZO-1 and its possible involvement in the localization of occludin at tight junctions. *The Journal of Cell Biology*, 127(6 Pt 1):1617–1626.

Gao, H., Shi, W., and Freund, L. B. (2005). Mechanics of receptor-mediated endocytosis. *Proceedings of the National Academy of Sciences*, 102(27):9469–9474.

Geng, Y., Dalhaimer, P., Cai, S., Tsai, R., Tewari, M., Minko, T., and Discher, D. E. (2007). Shape effects of filaments versus spherical particles in flow and drug delivery. *Nature Nanotechnology*, 2(4):249–255.

Georgieva, J. V., Hoekstra, D., and Zuhorn, I. S. (2014). Smuggling Drugs into the Brain: An Overview of Ligands Targeting Transcytosis for Drug Delivery across the Blood–Brain Barrier. *Pharmaceutics*, 6(4):557–583.

Giljohann, D. A., Seferos, D. S., Patel, P. C., Millstone, J. E., Rosi, N. L., and Mirkin, C. A. (2007). Oligonucleotide Loading Determines Cellular Uptake of DNA-Modified Gold Nanoparticles. *Nano Letters*, 7(12):3818–3821.

Gratton, S. E. A., Ropp, P. A., Pohlhaus, P. D., Luft, J. C., Madden, V. J., Napier, M. E., and DeSimone, J. M. (2008). The effect of particle design on cellular internalization pathways. *Proceedings of the National Academy of Sciences*, 105(33):11613–11618.

Grzelczak, M., Pérez-Juste, J., Mulvaney, P., and Liz-Marzán, L. M. (2008). Shape control in gold nanoparticle synthesis. *Chemical Society Reviews*, 37(9):1783–1791.

Guerrero, S., Araya, E., Fiedler, J. L., Arias, J. I., Adura, C., Albericio, F., Giralt, E., Arias, J. L., Fernández, M. S., and Kogan, M. J. (2010). Improving the brain delivery of gold nanoparticles by conjugation with an amphipathic peptide. *Nanomedicine*, 5(6):897–913.

Gunduz, N., Ceylan, H., Guler, M. O., and Tekinay, A. B. (2017). Intracellular

Accumulation of Gold Nanoparticles Leads to Inhibition of Macropinocytosis to Reduce the Endoplasmic Reticulum Stress. *Scientific Reports*, 7:40493.

Hainfeld, J. F., Slatkin, D. N., Focella, T. M., and Smilowitz, H. M. (2006). Gold nanoparticles: a new X-ray contrast agent. *The British Journal of Radiology*, 79(939):248–253.

Hamidi, M., Azadi, A., and Rafiei, P. (2006). Pharmacokinetic Consequences of Pegylation. *Drug Delivery*, 13(6):399–409.

Hao, N., Li, L., Zhang, Q., Huang, X., Meng, X., Zhang, Y., Chen, D., Tang, F., and Li, L. (2012). The shape effect of PEGylated mesoporous silica nanoparticles on cellular uptake pathway in Hela cells. *Microporous and Mesoporous Materials*, 162:14–23.

Harris, D. C., Rinehart, A. L., Hereld, D., Schwartz, R. W., Burke, F. P., and Salvador, A. P. (1985). Reduction potential of iron in transferrin. *Biochimica et Biophysica Acta (BBA) - General Subjects*, 838(3):295–301.

Harush-Frenkel, O., Debotton, N., Benita, S., and Altschuler, Y. (2007). Targeting of nanoparticles to the clathrin-mediated endocytic pathway. *Biochemical and Biophysical Research Communications*, 353(1):26–32.

Hatherell, K., Couraud, P.-O., Romero, I. A., Weksler, B., and Pilkington, G. J. (2011). Development of a three-dimensional, all-human in vitro model of the blood–brain barrier using mono-, co-, and tri-cultivation Transwell models. *Journal of Neuroscience Methods*, 199(2):223–229.

Hayat, M. A. (2000). *Principles and Techniques of Electron Microscopy: Biological Applications*. Cambridge University Press. Google-Books-ID: 8bH5ngEACAAJ.

Helms, H. C., Abbott, N. J., Burek, M., Cecchelli, R., Couraud, P.-O., Deli, M. A., Förster, C., Galla, H. J., Romero, I. A., Shusta, E. V., Stebbins, M. J., Vandenhaute, E., Weksler, B., and Brodin, B. (2016). In vitro models of the blood–brain barrier: An overview of commonly used brain endothelial cell culture models and guidelines for their use. *Journal of Cerebral Blood Flow & Metabolism*, page 0271678X16630991.

Hervé, F., Ghinea, N., and Scherrmann, J.-M. (2008). CNS Delivery Via Adsorptive Transcytosis. *The AAPS Journal*, 10(3):455–472.

Herz, J. and Marschang, P. (2003). Coaxing the LDL Receptor Family into the Fold. *Cell*, 112(3):289–292.

Hrelescu, C., Sau, T. K., Rogach, A. L., Jäckel, F., and Feldmann, J. (2009). Single gold nanostars enhance Raman scattering. *Applied Physics Letters*, 94(15):153113.

Huang, X., Teng, X., Chen, D., Tang, F., and He, J. (2010). The effect of the shape of mesoporous silica nanoparticles on cellular uptake and cell function. *Biomaterials*, 31(3):438–448.

Ivask, A., H. Pilkington, E., Blin, T., Käkinen, A., Vija, H., Visnapuu, M., F. Quinn, J., R. Whittaker, M., Qiao, R., P. Davis, T., Chun Ke, P., and H. Voelcker, N. (2018). Uptake and transcytosis of functionalized superparamagnetic iron oxide nanoparticles in an in vitro blood brain barrier model. *Biomaterials Science*, 6(2):314–323.

Jain, K. K. (2012). Nanobiotechnology-based strategies for crossing the blood–brain barrier. *Nanomedicine*, 7(8):1225–1233.

Jana, N. R. (2005). Gram-scale synthesis of soluble, near-monodisperse gold nanorods and other anisotropic nanoparticles. *Small (Weinheim an Der Bergstrasse, Germany)*, 1(8-9):875–882.

Jana, N. R., Gearheart, L., and Murphy, C. J. (2001). Evidence for Seed-Mediated Nucleation in the Chemical Reduction of Gold Salts to Gold Nanoparticles. *Chemistry of Materials*, 13(7):2313–2322.

Jazayeri, M. H., Amani, H., Pourfatollah, A. A., Pazoki-Toroudi, H., and Sedighimoghaddam, B. (2016). Various methods of gold nanoparticles (GNPs) conjugation to antibodies. *Sensing and Bio-Sensing Research*, 9:17–22.

Kafa, H., Wang, J. T.-W., Rubio, N., Venner, K., Anderson, G., Pach, E., Ballesteros, B., Preston, J. E., Abbott, N. J., and Al-Jamal, K. T. (2015). The interaction of carbon nanotubes with an in vitro blood-brain barrier model and mouse brain in vivo. *Biomaterials*, 53:437–452.

Kedia, A. and Kumar, P. S. (2013). Controlled reshaping and plasmon tuning mechanism of gold nanostars. *Journal of Materials Chemistry C*, 1(30):4540–4549.

Kedia, A. and Senthil Kumar, P. (2012). Precursor-Driven Nucleation and Growth Kinetics of Gold Nanostars. *The Journal of Physical Chemistry C*, 116(2):1679–1686.

Kelly, S. M., Jess, T. J., and Price, N. C. (2005). How to study proteins by circular dichroism. *Biochimica et Biophysica Acta (BBA) - Proteins and Proteomics*, 1751(2):119–139.

Khoury, C. G. and Vo-Dinh, T. (2008). Gold Nanostars For Surface-Enhanced Raman Scattering: Synthesis, Characterization and Optimization. *The Journal of Physical Chemistry. C, Nanomaterials and Interfaces*, 2008(112):18849–18859.

Kolhar, P., Anselmo, A. C., Gupta, V., Pant, K., Prabhakarpandian, B., Ruoslahti, E., and Mitragotri, S. (2013). Using shape effects to target antibody-coated nanoparticles to lung and brain endothelium. *Proceedings of the National Academy of Sciences*, 110(26):10753–10758.

Kolářová, H., Ambrůzová, B., Švihálková Šindlerová, L., Klinke, A., and Kubala, L. (2014). Modulation of Endothelial Glycocalyx Structure under Inflammatory Conditions.

Kreuter, J. (2001). Nanoparticulate systems for brain delivery of drugs. *Advanced Drug Delivery Reviews*, 47(1):65–81.

Kreuter, J., Hekmatara, T., Dreis, S., Vogel, T., Gelperina, S., and Langer, K. (2007). Covalent attachment of apolipoprotein A-I and apolipoprotein B-100 to albumin nanoparticles enables drug transport into the brain. *Journal of Controlled Release: Official Journal of the Controlled Release Society*, 118(1):54–58.

Kreuter, J., Shamenkov, D., Petrov, V., Ramge, P., Cychutek, K., Koch-Brandt, C., and Alyautdin, R. (2002). Apolipoprotein-mediated transport of nanoparticle-bound drugs across the blood-brain barrier. *Journal of Drug Targeting*, 10(4):317–325.

Kuhn, D. A., Vanhecke, D., Michen, B., Blank, F., Gehr, P., Petri-Fink, A., and Rothen-Rutishauser, B. (2014). Different endocytotic uptake mechanisms for nanoparticles in epithelial cells and macrophages. *Beilstein Journal of Nanotechnology*, 5(1):1625–1636.

Kuhn, M., Letunic, I., Jensen, L. J., and Bork, P. (2016). The SIDER database of drugs and side effects. *Nucleic Acids Research*, 44(D1):D1075–D1079.

Kumar, A., Ma, H., Zhang, X., Huang, K., Jin, S., Liu, J., Wei, T., Cao, W., Zou, G., and Liang, X.-J. (2012). Gold nanoparticles functionalized with therapeutic and targeted peptides for cancer treatment. *Biomaterials*, 33(4):1180–1189.

Kumar, C. S. S. R. (2010). *Microfluidic Devices in Nanotechnology: Applications*. John Wiley & Sons. Google-Books-ID: k4CAWOzG31gC.

Kumar, P. S., Pastoriza-Santos, I., Rodriguez-Gonzalez, B., Abajo, F. J. G. d., and Liz-Marzan, L. M. (2008). High-yield synthesis and optical response of gold nanostars. *Nanotechnology*, 19(1):015606.

Kumari, A. and Yadav, S. K. (2011). Cellular interactions of therapeutically delivered nanoparticles. *Expert Opinion on Drug Delivery*, 8(2):141–151.

Kuo, C.-H. and Huang, M. H. (2005). Synthesis of Branched Gold Nanocrystals by a Seeding Growth Approach. *Langmuir*, 21(5):2012–2016.

Kusuhara, H. and Sugiyama, Y. (2005). Active efflux across the blood-brain barrier: role of the solute carrier family. *NeuroRx: The Journal of the American Society for Experimental NeuroTherapeutics*, 2(1):73–85.

LaMer, V. K. and Dinegar, R. H. (1950). Theory, Production and Mechanism of Formation of Monodispersed Hydrosols. *Journal of the American Chemical Society*, 72(11):4847–4854.

Lawrence Steinman, M. D. (1996). Multiple Sclerosis: A Coordinated Immunological Attack against Myelin in the Central Nervous System. *Cell*, 85(3):299–302.

Levin, V. A. (1980). Relationship of octanol/water partition coefficient and molecular weight to rat brain capillary permeability. *Journal of Medicinal Chemistry*, 23(6):682–684.

Lewis, F., Karlsberg Schaffer, S., Sussex, J., O'Neill, P., and Cockcroft, L. (2014). The Trajectory of Dementia in the UK - Making a Difference.

Li, J., Cai, R., Kawazoe, N., and Chen, G. (2015a). Facile preparation of albumin-stabilized gold nanostars for the targeted photothermal ablation of cancer cells. *Journal of Materials Chemistry B*, 3(28):5806–5814.

Li, N., Zhao, P., and Astruc, D. (2014). Anisotropic Gold Nanoparticles: Synthesis, Properties, Applications, and Toxicity. *Angewandte Chemie International Edition*, 53(7):1756–1789.

Li, Y., Kröger, M., and Kam Liu, W. (2015b). Shape effect in cellular uptake of PEGylated nanoparticles: comparison between sphere, rod, cube and disk. *Nanoscale*, 7(40):16631–16646.

Lim, J. P. and Gleeson, P. A. (2011). Macropinocytosis: an endocytic pathway for internalising large gulps. *Immunology and Cell Biology*, 89(8):836–843.

Lin, J., Zhang, H., Chen, Z., and Zheng, Y. (2010). Penetration of Lipid Membranes by Gold Nanoparticles: Insights into Cellular Uptake, Cytotoxicity, and Their Relationship. *ACS Nano*, 4(9):5421–5429.

Lipowsky, H. H. (2012). The endothelial glycocalyx as a barrier to leukocyte adhesion and its mediation by extracellular proteases. *Annals of Biomedical Engineering*, 40(4):840–848.

Liu and Guyot-Sionnest, P. (2005). Mechanism of Silver(I)-Assisted Growth of Gold Nanorods and Bipyramids. *The Journal of Physical Chemistry B*, 109(47):22192–22200.

Liu, D., Lin, B., Shao, W., Zhu, Z., Ji, T., and Yang, C. (2014). In Vitro and in Vivo Studies on the Transport of PEGylated Silica Nanoparticles across the Blood–Brain Barrier. *ACS Applied Materials & Interfaces*, 6(3):2131–2136.

Liu, M., Li, Q., Liang, L., Li, J., Wang, K., Li, J., Lv, M., Chen, N., Song, H., Lee, J., Shi, J., Wang, L., Lal, R., and Fan, C. (2017). Real-time visualization of clustering and intracellular transport of gold nanoparticles by correlative imaging. *Nature Communications*, 8:15646.

Liu, N. Q., Lossinsky, A. S., Popik, W., Li, X., Gujuluva, C., Kriederman, B., Roberts, J., Pushkarsky, T., Bukrinsky, M., Witte, M., Weinand, M., and Fiala, M. (2002). Human immunodeficiency virus type 1 enters brain microvascular endothelia by macropinocytosis dependent on lipid rafts and the mitogen-activated protein kinase signaling pathway. *Journal of Virology*, 76(13):6689–6700.

Lockman, P. R., Koziara, J. M., Mumper, R. J., and Allen, D. D. (2004). Nanoparticle surface charges alter blood-brain barrier integrity and permeability. *Journal of Drug Targeting*, 12(9-10):635–641.

Lohse, S. E., Burrows, N. D., Scarabelli, L., Liz-Marzán, L. M., and Murphy, C. J. (2014). Anisotropic Noble Metal Nanocrystal Growth: The Role of Halides. *Chemistry of Materials*, 26(1):34–43.

Longmire, M., Choyke, P. L., and Kobayashi, H. (2008). Clearance Properties of Nano-sized Particles and Molecules as Imaging Agents: Considerations and Caveats. *Nanomedicine (London, England)*, 3(5):703–717.

Lupini, A. R., Rashkeev, S. N., Varela, M., Borisevich, A. Y., Oxley, M. P., Benthem, K. V., Peng, Y., Jonge, N. D., Veith, G. M., Pennycook, T. J., Zhou, W.,

Ishikawa, R., Chisholm, M. F., Pantelides, S. T., and Pennycook, S. J. (2015). Scanning Transmission Electron Microscopy. pages 30–79.

MacGillivray, R. T. A., Mendez, E., Sinha, S. K., Sutton, M. R., Lineback-Zins, J., and Brew, K. (1982). The Complete Amino Acid Sequence of Human Serum Transferrin. *Proceedings of the National Academy of Sciences of the United States of America*, 79(8):2504–2508.

Maeda, H., Wu, J., Sawa, T., Matsumura, Y., and Hori, K. (2000). Tumor vascular permeability and the EPR effect in macromolecular therapeutics: a review. *Journal of Controlled Release*, 65(1):271–284.

Mammen, M., Choi, S.-K., and Whitesides, G. M. (1998). Polyvalent Interactions in Biological Systems: Implications for Design and Use of Multivalent Ligands and Inhibitors. *Angewandte Chemie International Edition*, 37(20):2754–2794.

Möckl, L., Hirn, S., Torrano, A. A., Uhl, B., Bräuchle, C., and Krombach, F. (2017). The glycocalyx regulates the uptake of nanoparticles by human endothelial cells in vitro. *Nanomedicine*, 12(3):207–217.

Mellman, I. (1996). Endocytosis and Molecular Sorting. *Annual Review of Cell and Developmental Biology*, 12(1):575–625.

Mensch, J., Melis, A., Mackie, C., Verreck, G., Brewster, M. E., and Augustijns, P. (2010). Evaluation of various PAMPA models to identify the most discriminating method for the prediction of BBB permeability. *European Journal of Pharmaceutics and Biopharmaceutics*, 74(3):495–502.

Mer, V. K. L. (1952). Nucleation in Phase Transitions. *Industrial & Engineering Chemistry*, 44(6):1270–1277.

Moos, T., Skjoerringe, T., Gosk, S., and Morgan, E. H. (2006). Brain capillary endothelial cells mediate iron transport into the brain by segregating iron from transferrin without the involvement of divalent metal transporter 1. *Journal of Neurochemistry*, 98(6):1946–1958.

Mudshinge, S. R., Deore, A. B., Patil, S., and Bhalgat, C. M. (2011). Nanoparticles: Emerging carriers for drug delivery. *Saudi Pharmaceutical Journal*, 19(3):129–141.

Nair, L. V., Nair, R. V., Shenoy, S. J., Thekkuveettil, A., and Jayasree, R. S. (2017). Blood brain barrier permeable gold nanocluster for targeted brain imaging and therapy: an in vitro and in vivo study. *Journal of Materials Chemistry B*, 5(42):8314–8321.

Nambara, K., Niikura, K., Mitomo, H., Ninomiya, T., Takeuchi, C., Wei, J., Matsuo, Y., and Ijiro, K. (2016). Reverse Size Dependences of the Cellular Uptake of Triangular and Spherical Gold Nanoparticles. *Langmuir*, 32(47):12559–12567.

Nance, E. A., Woodworth, G. F., Sailor, K. A., Shih, T.-Y., Xu, Q., Swaminathan, G., Xiang, D., Eberhart, C., and Hanes, J. (2012). A Dense Poly(ethylene glycol) Coating Improves Penetration of Large Polymeric Nanoparticles within Brain Tissue. *Science translational medicine*, 4(149):149ra119.

Nanda, K. K., Maisels, A., Kruis, F. E., Fissan, H., and Stappert, S. (2003). Higher surface energy of free nanoparticles. *Physical Review Letters*, 91(10):106102.

Nations, U. (2017). World Population Prospects - Population Division - United Nations.

Nehl, C. L., Liao, H., and Hafner, J. H. (2006). Optical Properties of Star-Shaped Gold Nanoparticles. *Nano Letters*, 6(4):683–688.

Nel, A. E., Mädler, L., Velegol, D., Xia, T., Hoek, E. M. V., Somasundaran, P., Klaessig, F., Castranova, V., and Thompson, M. (2009a). Understanding biophysicochemical interactions at the nano–bio interface. *Nature Materials*, 8(7):543–557.

Nel, A. E., Mädler, L., Velegol, D., Xia, T., Hoek, E. M. V., Somasundaran, P., Klaessig, F., Castranova, V., and Thompson, M. (2009b). Understanding biophysicochemical interactions at the nano–bio interface. *Nature Materials*, 8(7):543–557.

Neurology, T. L. (2013). Joining forces to fight neurodegenerative diseases. *The Lancet Neurology*, 12(2):119.

Niu, W. and Xu, G. (2011). Crystallographic control of noble metal nanocrystals. *Nano Today*, 6(3):265–285.

Nutt, D. J. (2011). The full cost and burden of disorders of the brain in Europe exposed for the first time. *European Neuropsychopharmacology*, 21(10):715–717.

Oldenburg, S. J., Averitt, R. D., Westcott, S. L., and Halas, N. J. (1998). Nanoengineering of optical resonances. *Chemical Physics Letters*, 288(2):243–247.

Oldendorf, W. H., Hyman, S., Braun, L., and Oldendorf, S. Z. (1972). Blood-brain barrier: penetration of morphine, codeine, heroin, and methadone after carotid injection. *Science (New York, N.Y.)*, 178(4064):984–986.

Orendorff, C. J. and Murphy, C. J. (2006). Quantitation of Metal Content in the Silver-Assisted Growth of Gold Nanorods. *The Journal of Physical Chemistry B*, 110(9):3990–3994.

Owens, D. E. and Peppas, N. A. (2006). Opsonization, biodistribution, and pharmacokinetics of polymeric nanoparticles. *International Journal of Pharmaceutics*, 307(1):93–102.

Pallavicini, P., Donà, A., Casu, A., Chirico, G., Collini, M., Dacarro, G., Falqui, A., Milanese, C., Sironi, L., and Taglietti, A. (2013). Triton X-100 for three-plasmon gold nanostars with two photothermally active NIR (near IR) and SWIR (short-wavelength IR) channels. *Chemical Communications*, 49(56):6265–6267.

Paolinelli, R., Corada, M., Ferrarini, L., Devraj, K., Artus, C., Czupalla, C. J., Rudini, N., Maddaluno, L., Papa, E., Engelhardt, B., Couraud, P. O., Liebner, S., and Dejana, E. (2013). Wnt Activation of Immortalized Brain Endothelial Cells as a Tool for Generating a Standardized Model of the Blood Brain Barrier In Vitro. *PLOS ONE*, 8(8):e70233.

Pardridge, W. M. (2002). Drug and gene targeting to the brain with molecular trojan horses. *Nature Reviews Drug Discovery*, 1(2):131–139.

Pardridge, W. M. (2005). The Blood-Brain Barrier: Bottleneck in Brain Drug Development. *NeuroRx*, 2(1):3–14.

Pardridge, W. M. (2007). Blood–brain barrier delivery. *Drug Discovery Today*, 12(1–2):54–61.

Pardridge, W. M. (2012). Drug transport across the blood–brain barrier. *Journal of Cerebral Blood Flow & Metabolism*, 32(11):1959–1972.

Pardridge, W. M. (2014). Targeted delivery of protein and gene medicines through the blood–brain barrier. *Clinical Pharmacology & Therapeutics*, 97(4):347–361.

Pardridge, W. M., Eisenberg, J., and Yang, J. (1987). Human blood-brain barrier transferrin receptor. *Metabolism*, 36(9):892–895.

Patel, M. M., Goyal, B. R., Bhadada, S. V., Bhatt, J. S., and Amin, A. F. (2009). Getting into the brain: approaches to enhance brain drug delivery. *CNS drugs*, 23(1):35–58.

Pino, P. d., Pelaz, B., Zhang, Q., Maffre, P., Nienhaus, G. U., and Parak, W. J. (2014). Protein corona formation around nanoparticles – from the past to the future. *Materials Horizons*, 1(3):301–313.

Polte, J., Ahner, T. T., Delissen, F., Sokolov, S., Emmerling, F., Thünemann, A. F., and Kraehnert, R. (2010). Mechanism of Gold Nanoparticle Formation in the Classical Citrate Synthesis Method Derived from Coupled In Situ XANES and SAXS Evaluation. *Journal of the American Chemical Society*, 132(4):1296–1301.

Pong, B.-K., Elim, H. I., Chong, J.-X., Ji, W., Trout, B. L., and Lee, J.-Y. (2007). New Insights on the Nanoparticle Growth Mechanism in the Citrate Reduction of Gold(III) Salt: Formation of the Au Nanowire Intermediate and Its Nonlinear Optical Properties. *The Journal of Physical Chemistry C*, 111(17):6281–6287.

Prades, R., Guerrero, S., Araya, E., Molina, C., Salas, E., Zurita, E., Selva, J., Egea, G., López-Iglesias, C., Teixidó, M., Kogan, M. J., and Giralt, E. (2012). Delivery of gold nanoparticles to the brain by conjugation with a peptide that recognizes the transferrin receptor. *Biomaterials*, 33(29):7194–7205.

Ragnaill, M. N., Brown, M., Ye, D., Bramini, M., Callanan, S., Lynch, I., and Dawson, K. A. (2011). Internal benchmarking of a human blood–brain bar-

rier cell model for screening of nanoparticle uptake and transcytosis. *European Journal of Pharmaceutics and Biopharmaceutics*, 77(3):360–367.

Ramsey, J. D., Zhou, L., Almlie, C. K., Lange, J. D., and Burrows, S. M. (2015). Achieving plasmon reproducibility from surfactant free gold nanostar synthesis. *New Journal of Chemistry*, 39(12):9098–9108.

Reese, T. S. and Karnovsky, M. J. (1967). Fine structural localization of a blood-brain barrier to exogenous peroxidase. *The Journal of Cell Biology*, 34(1):207–217.

Reitsma, S., Slaaf, D. W., Vink, H., van Zandvoort, M. A. M. J., and oude Egbrink, M. G. A. (2007). The endothelial glycocalyx: composition, functions, and visualization. *Pflugers Archiv*, 454(3):345–359.

Ribatti, D., Nico, B., Crivellato, E., and Artico, M. (2006). Development of the blood-brain barrier: a historical point of view. *Anatomical Record. Part B, New Anatomist*, 289(1):3–8.

Richardson, J. J., Choy, M. Y., Guo, J., Liang, K., Alt, K., Ping, Y., Cui, J., Law, L. S., Hagemeyer, C. E., and Caruso, F. (2016). Polymer Capsules for Plaque-Targeted In Vivo Delivery. *Advanced Materials*, 28(35):7703–7707.

Roberts, R. L., Fine, R. E., and Sandra, A. (1993). Receptor-mediated endocytosis of transferrin at the blood-brain barrier. *Journal of Cell Science*, 104(2):521–532.

Rosseneu-motreff, M. Y., Soetewey, F., Lamote, R., and Peeters, H. (1971). Size and shape determination of apotransferrin and transferrin monomers. *Biopolymers*, 10(6):1039–1048.

Ruan, S., Yuan, M., Zhang, L., Hu, G., Chen, J., Cun, X., Zhang, Q., Yang, Y., He, Q., and Gao, H. (2015). Tumor microenvironment sensitive doxorubicin delivery and release to glioma using angiopep-2 decorated gold nanoparticles. *Biomaterials*, 37:425–435.

Ruenraroengsak, P., Chen, S., Hu, S., Melbourne, J., Sweeney, S., Thorley, A. J., Skepper, J. N., Shaffer, M. S. P., Tetley, T. D., and Porter, A. E. (2016). Translocation of Functionalized Multi-Walled Carbon Nanotubes across Human Pulmonary Alveolar Epithelium: Dominant Role of Epithelial Type 1 Cells. *ACS Nano*, 10(5):5070–5085.

Santos, T. d., Varela, J., Lynch, I., Salvati, A., and Dawson, K. A. (2011). Quantitative Assessment of the Comparative Nanoparticle-Uptake Efficiency of a Range of Cell Lines. *Small*, 7(23):3341–3349.

Sasidharan, S., Bahadur, D., and Srivastava, R. (2016). Albumin stabilized gold nanostars: a biocompatible nanoplatform for SERS, CT imaging and photothermal therapy of cancer. *RSC Advances*, 6(87):84025–84034.

Sau, T. K. and Murphy, C. J. (2004). Seeded High Yield Synthesis of Short Au Nanorods in Aqueous Solution. *Langmuir*, 20(15):6414–6420.

Sau, T. K., Pal, A., Jana, N. R., Wang, Z. L., and Pal, T. (2001). Size Controlled Synthesis of Gold Nanoparticles using Photochemically Prepared Seed Particles. *Journal of Nanoparticle Research*, 3(4):257–261.

Sau, T. K., Rogach, A. L., Döblinger, M., and Feldmann, J. (2011). One-Step High-Yield Aqueous Synthesis of Size-Tunable Multispiked Gold Nanoparticles. *Small*, 7(15):2188–2194.

Sau, T. K., Rogach, A. L., Jäckel, F., Klar, T. A., and Feldmann, J. (2010). Properties and Applications of Colloidal Nonspherical Noble Metal Nanoparticles. *Advanced Materials*, 22(16):1805–1825.

Schütz, M., Steinigeweg, D., Salehi, M., Kömpe, K., and Schlücker, S. (2011). Hydrophilically stabilized gold nanostars as SERS labels for tissue imaging of the tumor suppressor p63 by immuno-SERS microscopy. *Chemical Communications (Cambridge, England)*, 47(14):4216–4218.

Shan, Y., Ma, S., Nie, L., Shang, X., Hao, X., Tang, Z., and Wang, H. (2011). Size-dependent endocytosis of single gold nanoparticles. *Chemical Communications*, 47(28):8091–8093.

Shukla, R., Bansal, V., Chaudhary, M., Basu, A., Bhonde, R. R., and Sastry, M. (2005). Biocompatibility of Gold Nanoparticles and Their Endocytotic Fate Inside the Cellular Compartment: A Microscopic Overview. *Langmuir*, 21(23):10644–10654.

Skjørringe, T., Burkhart, A., Johnsen, K. B., and Moos, T. (2015). Divalent metal transporter 1 (DMT1) in the brain: implications for a role in iron transport at the blood-brain barrier, and neuronal and glial pathology. *Frontiers in Molecular Neuroscience*, 8.

Smith, A. M., Mancini, M. C., and Nie, S. (2009). Second window for in vivo imaging. *Nature nanotechnology*, 4(11):710–711.

Snoeys, J., Lievens, J., Wisse, E., Jacobs, F., Duimel, H., Collen, D., Frederik, P., and Geest, B. D. (2007). Species differences in transgene DNA uptake in hepatocytes after adenoviral transfer correlate with the size of endothelial fenestrae. *Gene Therapy*, 14(7):604–612.

Song, Y., Du, D., Li, L., Xu, J., Dutta, P., and Lin, Y. (2017). In Vitro Study of Receptor-Mediated Silica Nanoparticles Delivery across Blood-Brain Barrier. *Acs Applied Materials & Interfaces*, 9(24):20410–20416. WOS:000404090000016.

Srinivasan, B., Kolli, A. R., Esch, M. B., Abaci, H. E., Shuler, M. L., and Hickman, J. J. (2015). TEER measurement techniques for in vitro barrier model systems. *Journal of laboratory automation*, 20(2):107–126.

Sun, Y. and Xia, Y. (2002). Shape-Controlled Synthesis of Gold and Silver Nanoparticles. *Science*, 298(5601):2176–2179.

Talamini, L., Violatto, M. B., Cai, Q., Monopoli, M. P., Kantner, K., Krpetić, e., Perez-Potti, A., Cookman, J., Garry, D., P. Silveira, C., Boselli, L., Pelaz, B., Serchi, T., Cambier, S., Gutleb, A. C., Feliu, N., Yan, Y., Salmona, M., Parak, W. J., Dawson, K. A., and Bigini, P. (2017). Influence of Size and Shape on the Anatomical Distribution of Endotoxin-Free Gold Nanoparticles. *ACS Nano*, 11(6):5519–5529.

Taraska, J. W. and Almers, W. (2004). Bilayers merge even when exocytosis is transient. *Proceedings of the National Academy of Sciences*, 101(23):8780–8785.

Thorne, R. G. and Nicholson, C. (2006). In vivo diffusion analysis with quantum dots and dextrans predicts the width of brain extracellular space. *Proceedings of the National Academy of Sciences of the United States of America*, 103(14):5567–5572.

Trickler, W. J., Lantz, S. M., Murdock, R. C., Schrand, A. M., Robinson, B. L., Newport, G. D., Schlager, J. J., Oldenburg, S. J., Paule, M. G., Slikker, W., Hussain, S. M., and Ali, S. F. (2011). Brain microvessel endothelial cells responses

to gold nanoparticles: In vitro pro-inflammatory mediators and permeability. *Nanotoxicology*, 5(4):479–492.

Träuble, H. (1971). The movement of molecules across lipid membranes: A molecular theory. *The Journal of Membrane Biology*, 4(1):193–208.

Tsinman, O., Tsinman, K., Sun, N., and Avdeef, A. (2011). Physicochemical selectivity of the BBB microenvironment governing passive diffusion–matching with a porcine brain lipid extract artificial membrane permeability model. *Pharmaceutical Research*, 28(2):337–363.

Turkevich, J., Stevenson, P. C., and Hillier, J. (1951). A study of the nucleation and growth processes in the synthesis of colloidal gold. *Discussions of the Faraday Society*, 11(0):55–75.

Uchida, Y., Ohtsuki, S., Katsukura, Y., Ikeda, C., Suzuki, T., Kamiie, J., and Terasaki, T. (2011). Quantitative targeted absolute proteomics of human blood-brain barrier transporters and receptors. *Journal of Neurochemistry*, 117(2):333–345.

Ulbrich, K., Hekmatara, T., Herbert, E., and Kreuter, J. (2009). Transferrin- and transferrin-receptor-antibody-modified nanoparticles enable drug delivery across the blood-brain barrier (BBB). *European Journal of Pharmaceutics and Biopharmaceutics: Official Journal of Arbeitsgemeinschaft Fur Pharmazeutische Verfahrenstechnik e.V*, 71(2):251–256.

Umadevi, S., Lee, H. C., Ganesh, V., Feng, X., and Hegmann, T. (2013). A versatile, one-pot synthesis of gold nanostars with long, well-defined thorns using a lyotropic liquid crystal template. *Liquid Crystals*, 41(3):265–276.

Vink, H. and Duling, B. R. (2000). Capillary endothelial surface layer selectively

reduces plasma solute distribution volume. *American Journal of Physiology. Heart and Circulatory Physiology*, 278(1):H285–289.

Wang, Z., Wu, Z., Liu, J., and Zhang, W. (2018). Particle morphology: an important factor affecting drug delivery by nanocarriers into solid tumors. *Expert Opinion on Drug Delivery*, 15(4):379–395.

Weinbaum, S., Tarbell, J. M., and Damiano, E. R. (2007). The structure and function of the endothelial glycocalyx layer. *Annual Review of Biomedical Engineering*, 9:121–167.

Weksler, B., Romero, I. A., and Couraud, P.-O. (2013). The hCMEC/D3 cell line as a model of the human blood brain barrier. *Fluids and barriers of the CNS*, 10(1):16.

Weksler, B. B., Subileau, E. A., Perrière, N., Charneau, P., Holloway, K., Leveque, M., Tricoire-Leignel, H., Nicotra, A., Bourdoulous, S., Turowski, P., Male, D. K., Roux, F., Greenwood, J., Romero, I. A., and Couraud, P. O. (2005). Blood-brain barrier-specific properties of a human adult brain endothelial cell line. *The FASEB Journal*.

Weyermann, J., Lochmann, D., and Zimmer, A. (2005). A practical note on the use of cytotoxicity assays. *International Journal of Pharmaceutics*, 288(2):369–376.

Wiley, D. T., Webster, P., Gale, A., and Davis, M. E. (2013). Transcytosis and brain uptake of transferrin-containing nanoparticles by tuning avidity to transferrin receptor. *Proceedings of the National Academy of Sciences*, 110(21):8662–8667.

Williams, D. B. and Carter, C. B. (2009). *Transmission Electron Microscopy: A Textbook for Materials Science*. Springer US, 2 edition.

Woods, K. E., Perera, Y. R., Davidson, M. B., Wilks, C. A., Yadav, D. K., and Fitzkee, N. C. (2016). Understanding Protein Structure Deformation on the Surface of Gold Nanoparticles of Varying Size. *The Journal of Physical Chemistry C*, 120(49):27944–27953.

Wronska, M. A., O'Connor, I. B., Tilbury, M. A., Srivastava, A., and Wall, J. G. (2016). Adding Functions to Biomaterial Surfaces through Protein Incorporation. *Advanced Materials*, 28(27):5485–5508.

Xie, J., Lee, J. Y., and Wang, D. I. C. (2007). Seedless, Surfactantless, High-Yield Synthesis of Branched Gold Nanocrystals in HEPES Buffer Solution. *Chemistry of Materials*, 19(11):2823–2830.

Xie, X., Liao, J., Shao, X., Li, Q., and Lin, Y. (2017). The Effect of shape on Cellular Uptake of Gold Nanoparticles in the forms of Stars, Rods, and Triangles. *Scientific Reports*, 7(1):3827.

Xiong, J. S., Branigan, D., and Li, M. (2009). Deciphering the MSG controversy. *International Journal of Clinical and Experimental Medicine*, 2(4):329–336.

Xu, S., Olenyuk, B. Z., Okamoto, C. T., and Hamm-Alvarez, S. F. (2013). Targeting receptor-mediated endocytotic pathways with nanoparticles: Rationale and advances. *Advanced Drug Delivery Reviews*, 65(1):121–138.

Xue, J., Zhao, Z., Zhang, L., Xue, L., Shen, S., Wen, Y., Wei, Z., Wang, L., Kong, L., Sun, H., Ping, Q., Mo, R., and Zhang, C. (2017). Neutrophil-mediated anticancer drug delivery for suppression of postoperative malignant glioma recurrence. *Nature Nanotechnology*, 12(7):692–700.

Yameen, B., Choi, W. I., Vilos, C., Swami, A., Shi, J., and Farokhzad, O. C. (2014). Insight into nanoparticle cellular uptake and intracellular targeting. *Journal of*

controlled release : official journal of the Controlled Release Society, 190:485–499.

Yang, K. and Ma, Y.-Q. (2010). Computer simulation of the translocation of nanoparticles with different shapes across a lipid bilayer. *Nature Nanotechnology*, 5(8):579–583.

Yang, L., Kuang, H., Zhang, W., Aguilar, Z. P., Wei, H., and Xu, H. (2017a). Comparisons of the biodistribution and toxicological examinations after repeated intravenous administration of silver and gold nanoparticles in mice. *Scientific Reports*, 7(1):3303.

Yang, L., Sun, J., Xie, W., Liu, Y., and Liu, J. (2017b). Dual-functional selenium nanoparticles bind to and inhibit amyloid β fiber formation in Alzheimer's disease. *Journal of Materials Chemistry B*, 5(30):5954–5967.

Ye, D., Raghnaill, M. N., Bramini, M., Mahon, E., Åberg, C., Salvati, A., and Dawson, K. A. (2013). Nanoparticle accumulation and transcytosis in brain endothelial cell layers. 5(22):11153–11165.

Yildirimer, L., Thanh, N. T. K., Loizidou, M., and Seifalian, A. M. (2011). Toxicology and clinical potential of nanoparticles. *Nano Today*, 6(6):585–607.

Yin, T., Xie, W., Sun, J., Yang, L., and Liu, J. (2016). Penetratin Peptide-Functionalized Gold Nanostars: Enhanced BBB Permeability and NIR Photothermal Treatment of Alzheimer's Disease Using Ultralow Irradiance. *ACS Applied Materials & Interfaces*, 8(30):19291–19302.

Yin, Y. and Alivisatos, A. P. (2005). Colloidal nanocrystal synthesis and the organic–inorganic interface. *Nature*, 437:664–670.

You, H. and Fang, J. (2016). Particle-mediated nucleation and growth of solution-synthesized metal nanocrystals: A new story beyond the LaMer curve. *Nano Today*, 11(2):145–167.

Yu, Y., Zhang, Q., Yao, Q., Xie, J., and Lee, J. Y. (2013). Guiding Principles in the Galvanic Replacement Reaction of an Underpotentially Deposited Metal Layer for Site-Selective Deposition and Shape and Size Control of Satellite Nanocrystals. *Chemistry of Materials*, 25(23):4746–4756.

Yuan, H., Khoury, C. G., Hwang, H., Wilson, C. M., Grant, G. A., and Vo-Dinh, T. (2012a). Gold nanostars: surfactant-free synthesis, 3d modelling, and two-photon photoluminescence imaging. *Nanotechnology*, 23(7):075102.

Yuan, H., Khoury, C. G., Hwang, H., Wilson, C. M., Grant, G. A., and Vo-Dinh, T. (2012b). Gold nanostars: surfactant-free synthesis, 3d modelling, and two-photon photoluminescence imaging. *Nanotechnology*, 23(7):075102.

Yuan, H., Ma, W., Chen, C., Zhao, J., Liu, J., Zhu, H., and Gao, X. (2007). Shape and SPR Evolution of Thorny Gold Nanoparticles Promoted by Silver Ions. *Chemistry of Materials*, 19(7):1592–1600.

Yuan, H., Ma, W., Chen, C., Zhu, H., Gao, X., and Zhao, J. (2011). Controllable Synthesis of 3d Thorny Plasmonic Gold Nanostructures and Their Tunable Optical Properties. *The Journal of Physical Chemistry C*, 115(47):23256–23260.

Zhang, M., Mao, X., Yu, Y., Wang, C.-X., Yang, Y.-L., and Wang, C. (2013). Nanomaterials for Reducing Amyloid Cytotoxicity. *Advanced Materials*, 25(28):3780–3801.

Zhang, S., Li, J., Lykotrafitis, G., Bao, G., and Suresh, S. (2009). Size-Dependent

Endocytosis of Nanoparticles. *Advanced materials (Deerfield Beach, Fla.)*, 21:419–424.

Zhang, Y. and Pardridge, W. M. (2001). Mediated efflux of IgG molecules from brain to blood across the blood-brain barrier. *Journal of Neuroimmunology*, 114(1-2):168–172.

Zhao, X., Shang, T., Zhang, X., Ye, T., Wang, D., and Rei, L. (2016). Passage of Magnetic Tat-Conjugated Fe<Subscript>3</Subscript>O<Subscript>4</Subscript>@SiO<Subscript>2</Subscript> Nanoparticles Across In Vitro Blood-Brain Barrier. *Nanoscale Research Letters*, 11(1):451.

Zlokovic, B. V. (2008). The blood-brain barrier in health and chronic neurodegenerative disorders. *Neuron*, 57(2):178–201.